



*remote sensing*

# Archaeological Remote Sensing in the 21st Century (Re)Defining Practice and Theory

---

Edited by

Geert Verhoeven, Dave Cowley and Arianna Traviglia

Printed Edition of the Special Issue Published in *Remote Sensing*

# **Archaeological Remote Sensing in the 21st Century: (Re)Defining Practice and Theory**



# Archaeological Remote Sensing in the 21st Century: (Re)Defining Practice and Theory

Editors

**Geert Verhoeven**

**Dave Cowley**

**Arianna Traviglia**

MDPI • Basel • Beijing • Wuhan • Barcelona • Belgrade • Manchester • Tokyo • Cluj • Tianjin



*Editors*

Geert Verhoeven  
Ludwig Boltzmann Institute for Archaeological Prospection and  
Virtual Archaeology  
Austria

Dave Cowley  
Historic Environment Scotland  
UK

Arianna Traviglia  
Ca' Foscari University of Venice  
Italy

*Editorial Office*

MDPI  
St. Alban-Anlage 66  
4052 Basel, Switzerland

This is a reprint of articles from the Special Issue published online in the open access journal *Remote Sensing* (ISSN 2072-4292) (available at: [https://www.mdpi.com/journal/remotesensing/special\\_issues/21archaeological\\_rs](https://www.mdpi.com/journal/remotesensing/special_issues/21archaeological_rs)).

For citation purposes, cite each article independently as indicated on the article page online and as indicated below:

LastName, A.A.; LastName, B.B.; LastName, C.C. Article Title. <i>Journal Name</i> <b>Year</b> , Volume Number, Page Range.
--

**ISBN 978-3-0365-1375-1 (Hbk)**

**ISBN 978-3-0365-1376-8 (PDF)**

© 2021 by the authors. Articles in this book are Open Access and distributed under the Creative Commons Attribution (CC BY) license, which allows users to download, copy and build upon published articles, as long as the author and publisher are properly credited, which ensures maximum dissemination and a wider impact of our publications.

The book as a whole is distributed by MDPI under the terms and conditions of the Creative Commons license CC BY-NC-ND.

# Contents

About the Editors . . . . .	vii
Preface to "Archaeological Remote Sensing in the 21st Century: (Re)Defining Practice and Theory" . . . . .	ix
<b>Dave Cowley, Geert Verhoeven and Arianna Traviglia</b> Editorial for Special Issue: "Archaeological Remote Sensing in the 21st Century: (Re)Defining Practice and Theory" Reprinted from: <i>Remote Sens.</i> 2021, 13, 1431, doi:10.3390/rs13081431 . . . . .	1
<b>César Borie, César Parceró-Oubiña, Youngsang Kwon, Diego Salazar, Carola Flores, Laura Olguín and Pedro Andrade</b> Beyond Site Detection: The Role of Satellite Remote Sensing in Analysing Archaeological Problems. A Case Study in Lithic Resource Procurement in the Atacama Desert, Northern Chile Reprinted from: <i>Remote Sens.</i> 2019, 11, 869, doi:10.3390/rs11070869 . . . . .	5
<b>Włodzimierz Rączkowski</b> Power and/or Penury of Visualizations: Some Thoughts on Remote Sensing Data and Products in Archaeology Reprinted from: <i>Remote Sens.</i> 2020, 12, 2996, doi:10.3390/rs12182996 . . . . .	33
<b>Jane Gallwey, Matthew Eyre, Matthew Tonkins and John Coggan</b> Bringing Lunar LiDAR Back Down to Earth: Mapping Our Industrial Heritage through Deep Transfer Learning Reprinted from: <i>Remote Sens.</i> 2019, 11, 1994, doi:10.3390/rs11171994 . . . . .	57
<b>Alexandre Guyot, Marc Lennon, Nicolas Thomas, Simon Gueguen, Tristan Petit, Thierry Lorho, Serge Cassen and Laurence Hubert-Moy</b> Airborne Hyperspectral Imaging for Submerged Archaeological Mapping in Shallow Water Environments Reprinted from: <i>Remote Sens.</i> 2019, 11, 2237, doi:10.3390/rs11192237 . . . . .	79
<b>Christopher Sevara, Martin Wieser, Michael Doneus and Norbert Pfeifer</b> Relative Radiometric Calibration of Airborne LiDAR Data for Archaeological Applications Reprinted from: <i>Remote Sens.</i> 2019, 11, 945, doi:10.3390/rs11080945 . . . . .	99
<b>Žiga Kokalj and Maja Somrak</b> Why Not a Single Image? Combining Visualizations to Facilitate Fieldwork and On-Screen Mapping Reprinted from: <i>Remote Sens.</i> 2019, 11, 747, doi:10.3390/rs11070747 . . . . .	123
<b>Karsten Lambers, Wouter B. Verschoof-van der Vaart and Quentin P. J. Bourgeois</b> Integrating Remote Sensing, Machine Learning, and Citizen Science in Dutch Archaeological Prospection Reprinted from: <i>Remote Sens.</i> 2019, 11, 794, doi:10.3390/rs11070794 . . . . .	149
<b>Ciara N. McGrath, Charlie Scott, Dave Cowley and Malcolm Macdonald</b> Towards a Satellite System for Archaeology? Simulation of an Optical Satellite Mission with Ideal Spatial and Temporal Resolution, Illustrated by a Case Study in Scotland Reprinted from: <i>Remote Sens.</i> 2020, 12, 4100, doi:10.3390/rs12244100 . . . . .	169

Zoltán Czajlik, Mátyás Árvai, János Mészáros, Balázs Nagy, László Rupnik  
and László Pásztor

Cropmarks in Aerial Archaeology: New Lessons from an Old Story

Reprinted from: *Remote Sens.* **2021**, *13*, 1126, doi:10.3390/rs13061126 . . . . . **189**

## About the Editors

**Geert Verhoeven** graduated in Archaeology in 2002 and completed his PhD in 2009 at Ghent University (UGent, Belgium). Afterwards, he worked for three years as a part-time professor at the UGent to teach archaeological prospection and archaeological IT. In June 2010, Geert moved to Vienna (Austria) to accommodate his job as a senior researcher in the LBI ArchPro, where he has been researching airborne photography and imaging spectroscopy, archaeological image fusion, scientific photography, and image-based modelling. These techniques are explored to improve existing data acquisition and information extraction procedures within archaeology and cultural heritage at large. Geert's work is published in various international peer-reviewed papers and book chapters (all available online at <https://lbi.academia.edu/GeertVerhoeven>). He is also a CIPA expert member and member of AARG, ISAP, and SPIE.

**Dave Cowley** graduated in Archaeology at the University of Newcastle upon Tyne (UK) in 1987 and has been an archaeologist in Scotland since 1989. He has worked as a field surveyor (1989–2005), managed an annual programme of aerial reconnaissance (2005–2019) and now leads on archaeological survey for Historic Environment Scotland, the lead publicly funded body for the historic environment in Scotland. His research is focused on survey practice, especially in airborne contexts, on the archaeology of the landscape and on Iron Age settlement. He is undertaking a part-time PhD at Ghent University (UGent, Belgium) on long-term demographic patterns in south-east Scotland. He has published extensively in journals and book chapters, and edited volumes on remote sensing for archaeology and on Iron Age settlement in Europe (<https://historicenvironment.academia.edu/DAVECOWLEY>). He is a member of AARG and ISAP.

**Arianna Traviglia** is the Coordinator of the Centre for Cultural Heritage Technology (CCHT), part of the Italian Institute of Technology (IIT). Her work is focussed on the intersection of technology and humanities and most of her research focuses on mediating the inclusion of digital practices within the study and management of cultural heritage. Her expertise lies mainly in (close and far range) multi and hyperspectral image processing for the analysis of the cultural landscape and material culture. Dr Traviglia is part of the Executive Steering Committee of the International Computer Application and Quantitative Methods in Archaeology (CAA) association and has chaired the 41st Computer Applications in Archaeology Conference (CAA2013 Perth). She is the Project Officer of ArcLand International initiative and a member of AARG. She is currently a Principal Investigator or Co-Investigator of several projects funded by the European Commission and centred around the use of digital technologies for cultural heritage analysis and protection (NETCHER, REPAIR), and director of a project co-funded by the European Space Agency (ESA) focused on the use of satellite imagery and AI for detecting buried archaeological sites.



# **Preface to "Archaeological Remote Sensing in the 21st Century: (Re)Defining Practice and Theory"**

Despite the many (r)evolutions in remote sensing technology over the past three decades, integration in archaeological practice and theory has sometimes been limited by reliance on practice and theory imported from other disciplines, without questioning or deep understanding. This collection of papers aims to contribute to the exploration of developing practice and theory in remote sensing archaeology for the 21st century. The scope of this volume is the use of remotely sensed data from either air- or spaceborne platforms for the benefit of archaeology and cultural heritage in general, with a specific focus on better defining the roles and contexts that detail why archaeologists may apply remote sensing techniques. With this focus, it is our hope that remotely sensed data will be better and more intrinsically integrated into the symbiosis of archaeological practice and theory.

The editorial for this volume suggests that many aspects of archaeological practice can be characterised as 'beg, borrow and steal'. This collection provides the reader with thoughtful papers that contribute to the development of archaeological remote sensing as a mature interdisciplinary field characterised by explicit and theoretically engaged approaches to understanding the past.

**Geert Verhoeven, Dave Cowley, Arianna Traviglia**

*Editors*





Editorial

# Editorial for Special Issue: “Archaeological Remote Sensing in the 21st Century: (Re)Defining Practice and Theory”

Dave Cowley <sup>1</sup>, Geert Verhoeven <sup>2,\*</sup> and Arianna Traviglia <sup>3</sup>

<sup>1</sup> Historic Environment Scotland, John Sinclair House, 16 Bernard Terrace, Edinburgh EH8 9NX, UK; dave.cowley@hes.scot

<sup>2</sup> Ludwig Boltzmann Institute for Archaeological Prospection and Virtual Archaeology (LBI ArchPro), Ludwig Boltzmann Gesellschaft GmbH, Franz-Klein-Gasse 1, A-1190 Vienna, Austria

<sup>3</sup> Centre for Cultural Heritage Technology, Italian Institute of Technology, via della Liberta' 12, 30178 Venice, Italy; arianna.traviglia@iit.it

\* Correspondence: geert.verhoeven@archpro.lbg.ac.at

“Beg, borrow and steal”: in many ways, this is a strapline for archaeology as a discipline, and perhaps especially so for archaeological remote sensing? The practice of archaeology places it at the intersection of many disciplines, partly in the humanities, partly scientific in orientation, drawing on a range of fields including Earth sciences, philosophy, and computer science, to name just a few. On the one hand, this is an attribute that makes archaeology such an interesting field. However, it can also be observed that archaeological practice has frequently relied on data and tools developed elsewhere, applied without question and with a superficial understanding of underlying principles, and appropriated theory with only shallow appreciation of the intellectual context in which it was developed. Specifically, in archaeological remote sensing, and despite the steady developments in remote sensing technology over the past three decades, the thoughtful integration of data sources and methods into theoretically aware archaeological practice remains relatively underdeveloped. There is a need, therefore, to critically explore developing praxis in 21st century remote sensing archaeology in a context which recognises the need to understand underlying principles, to assess fitness for purpose of approaches, and to develop more mature methodologically and theoretically aware frameworks.

This is the scope for this Special Issue of the journal *Remote Sensing*—to explore the use of remotely sensed data from either air- or spaceborne platforms for archaeology and cultural heritage in general and contribute to better integrating remotely sensed data in the discipline of archaeology. The nine papers in this SI address a range of technical and theoretical issues within this framework—looking at aspects of products and workflows across a range of data acquisition technologies (airborne laser scanning, airborne hyperspectral imaging, traditional aerial photography, satellite imaging). In this regard, there is a persistent focus on understanding the characteristics of the datasets applied, the workflows implemented, the opportunities offered by innovative applications, and the framing of relevant archaeological questions.

In archaeological remote sensing, the focus of much research and publication work on technical issues and exemplars of methods and data, with less focus on understanding the past, is a notable characteristic of the last decade or more. This is an understandable response to new technology, but the importance of addressing archaeological questions is foregrounded in a study of lithic resource procurement in the Atacama Desert, Northern Chile, by Borie et al. [1]. This paper makes use of Landsat 8 satellite images, moving beyond the discovery and documentation of archaeological features and sites to a massive landscape scale and an understanding of environmental resources—in this case, lithic raw material used by hunter–gatherer groups. The role of focused field studies introduces a multi-scalar perspective to archaeological understanding in a challenging physical setting.



**Citation:** Cowley, D.; Verhoeven, G.; Traviglia, A. Editorial for Special Issue: “Archaeological Remote Sensing in the 21st Century: (Re)Defining Practice and Theory”. *Remote Sens.* **2021**, *13*, 1431. <https://doi.org/10.3390/rs13081431>

Received: 23 March 2021  
Accepted: 31 March 2021  
Published: 8 April 2021

**Publisher’s Note:** MDPI stays neutral with regard to jurisdictional claims in published maps and institutional affiliations.



**Copyright:** © 2021 by the authors. Licensee MDPI, Basel, Switzerland. This article is an open access article distributed under the terms and conditions of the Creative Commons Attribution (CC BY) license (<https://creativecommons.org/licenses/by/4.0/>).

The way in which archaeological understanding is generated from airborne and spaceborne remote sensing is considered from a very different perspective in a paper by Rączkowski [2], which presents a critical challenge to any view that assimilating such data into archaeological understanding is through the simple expediency of looking, and that in some way, such “looking” is uncomplicated. The common fixation with visualisations of remotely sensed data, such as airborne laser scanning, is discussed with reference to Heidegger’s understanding of technology, exploring how such outputs are seen as representations of the “real world” and the extent to which those perceptions are culturally and theoretically dependent. This paper contributes to a largely undeveloped consideration of epistemology in remote sensing archaeology, which can otherwise be dominated by an inherently positivist, and largely uncritical, perspective.

If the paper by Rączkowski introduces the necessity for understanding the “thinking” behind aspects of remote sensing archaeology, the paper by Gallwey et al. [3] illustrates the need to understand the foundational aspects of new approaches. In this study of deep learning for the semi-automated detection of historic mining remains, the limited availability of archaeological training datasets is discussed with reference to the potential implications of pre-training convolutional neural networks on “general purpose” (i.e., ImageNet) imagery. On the basis that relict mining remains are expressed in surface topography, this study uses a transfer learning approach in which the initial training of the neural network uses Lunar topographic data—that is to say, a dataset (even if it is “off this world”) that may have more in common with archaeological features than the multi-use imagery routinely used for pre-training.

The need to establish the foundational aspects of remote sensing is also illustrated in a paper by Guyot et al. [4], dealing with the potential for airborne hyperspectral imaging for the mapping of submerged archaeological remains. While applications of hyperspectral data for terrestrial contexts are well established, and airborne laser bathymetry or acoustic soundings are routinely used in submerged contexts, the use of airborne imaging spectroscopy brings new perspectives. By combining noise reduction, the automated detection of features, and characterisation of morphological and spectral attributes of archaeological structures, the basis for the analytical exploration of such environments is significantly broadened.

The potential for applications of tried and tested approaches in new contexts demonstrated by Guyot et al. is also a theme in the paper by Sevara et al. [5], where the focus shifts to fully exploiting the dimensionality of remote sensing data—in this case, the value of radiometric information in airborne laser scanning to provide further insights about archaeological features. This paper describes a desk-based approach to radiometric calibration through the selection of homogenous areas of interest, which allows a raster reflectance map approximating a monochromatic illumination-independent true orthoimage to be generated. Having demonstrated the value of the approach and negating the lack of in-field calibration data for most airborne laser scanning data, a freely available tool to apply this procedure is introduced.

The value of such tools is well known to all users of the Relief Visualisation Toolbox, which provides a set of techniques to visualise raster elevation datasets in an easy-to-use package. In the paper by Kokalj and Somrak [6], the authors discuss what constitutes useful visualisations, and how their characteristics bear on the visibility of archaeological topographic features. The paper also addresses the inherent complexity that multiple visualisations may bring to the interpretative process, proposing an approach that blends different relief visualisation techniques to allow for the simultaneous display of topographic features in a single image. This paper offers an interesting complement to Rączkowski’s [2] and provides the “recipes” for their visualisations and a tool for their computation.

The benefits of integrated workflows and the combination of what might otherwise be distinct areas of archaeological practice are illustrated in the paper by Lambers et al. [7] which reports on the articulation of remote sensing, machine learning, and Citizen Science in a Dutch case study. Underlying this approach is a desire to address the paucity of

labelled archaeological training datasets for machine learning (see also [3]), and the recognition that Citizen Science can help generate and validate detections of hitherto unknown archaeological objects. This paper, too, offers an explicit, well-documented workflow that aims to ensure effective integration and that the character of outputs from the different processes is understood.

Understanding the character of outputs from data collection strategies is a theme common to the last two papers in this Special Issue. By asking the question of what a satellite system designed for archaeological specifications might look like, McGrath et al. [8] discuss the factors that impose inherent limitations on the archaeological applications of existing satellite data. By presenting a high-level mission architecture for a bespoke satellite system designed from an archaeological specification, the paper provides a simulation analysis that foregrounds the archaeological requirements for a satellite constellation design. This provides insights into data characteristics that should be useful to the users of repurposed satellite data and contributes to thinking about how archaeological and heritage management concerns might be incorporated into the future planning of satellite missions. A key point of this paper is that satellite data can be sourced and used without understanding how they were acquired, which may be an inherent limitation on the considered applications.

While the discussion of a satellite for archaeology is innovative, the valuable application of satellite data in archaeology has a long history, with such data from the 1960s and 1970s, for example, providing valuable historical documents of landscapes that may be long gone or dramatically altered. The benefits of a longer-term perspective on aspects of archaeological practice are discussed by Czajlik et al. [9] in this collection's final paper. The value of differential crop development (cropmarks) in the detection of buried archaeology is well-known, but the authors point out that much of the knowledge about how and why such proxies develop is empirical. They identify the significance of the results of a long-term aerial survey—in this case, in Hungary, over more than three decades—to support systematic analysis against factors such as soil properties and weather patterns to better inform future survey strategies. This is important because cropmark prospection needs to be properly targeted, whether that is to define the most cost-effective conditions under which to task a satellite or to put an aircraft in the air.

Returning to the scope of this collection of papers, there is an aspiration to explore (re)defining practice and theory, including critical discussion on the role of remote sensing within archaeological practice, addressing dislocations that may occur with theoretical concerns, and considering the future symbiosis of practice and theory. We note some positive trends, specifically in the better understanding of underlying assumptions, in the explicit definition of workflows, and in the provision of tools and other mechanisms to standardise, and so ensure the replicability, of work. Perhaps less well-developed is the symbiosis of practice and theory in archaeological remote sensing, and this is unsurprising given the weight of interest in the “technical” aspects of the field of study [2].

We hope that the collation of this Special Issue provides the reader with food for thought on these challenges, and so contributes to archaeological remote sensing as a discipline not so much epitomised by “beg, borrow and steal” but rather a mature interdisciplinary field characterised by explicit, thoughtful, and theoretically engaged approaches to understanding the past.

**Acknowledgments:** We thank our contributors for their papers and for thoughtfully engaging with the scope of this SI, and the editorial team at *Remote Sensing*, and specifically Joss Chen, for steering us through the process.

**Conflicts of Interest:** The authors declare no conflict of interest.

## References

1. Borie, C.; Parcero-Oubiña, C.; Kwon, Y.; Salazar, D.; Flores, C.; Olguín, L.; Andrade, P. Beyond Site Detection: The Role of Satellite Remote Sensing in Analysing Archaeological Problems. A Case Study in Lithic Resource Procurement in the Atacama Desert, Northern Chile. *Remote Sens.* **2019**, *11*, 869. [[CrossRef](#)]

2. Rączkowski, W. Power and/or Penury of Visualizations: Some Thoughts on Remote Sensing Data and Products in Archaeology. *Remote Sens.* **2020**, *12*, 2996. [[CrossRef](#)]
3. Gallwey, J.; Eyre, M.; Tonkins, M.; Coggan, J. Bringing Lunar LiDAR Back Down to Earth: Mapping Our Industrial Heritage through Deep Transfer Learning. *Remote Sens.* **2019**, *11*, 1994. [[CrossRef](#)]
4. Guyot, A.; Lennon, M.; Thomas, N.; Gueguen, S.; Petit, T.; Lorho, T.; Cassen, S.; Hubert-Moy, L. Airborne Hyperspectral Imaging for Submerged Archaeological Mapping in Shallow Water Environments. *Remote Sens.* **2019**, *11*, 2237. [[CrossRef](#)]
5. Sevara, C.; Wieser, M.; Doneus, M.; Pfeifer, N. Relative Radiometric Calibration of Airborne LiDAR Data for Archaeological Applications. *Remote Sens.* **2019**, *11*, 945. [[CrossRef](#)]
6. Kokalj, Z.; Somrak, M. Why Not a Single Image? Combining Visualizations to Facilitate Fieldwork and On-Screen Mapping. *Remote Sens.* **2019**, *11*, 747. [[CrossRef](#)]
7. Lambers, K.; Verschoof-van der Vaart, W.B.; Bourgeois, Q.P.J. Integrating Remote Sensing, Machine Learning, and Citizen Science in Dutch Archaeological Prospection. *Remote Sens.* **2019**, *11*, 794. [[CrossRef](#)]
8. McGrath, C.N.; Scott, C.; Cowley, D.; Macdonald, M. Towards a Satellite System for Archaeology? Simulation of an Optical Satellite Mission with Ideal Spatial and Temporal Resolution, Illustrated by a Case Study in Scotland. *Remote Sens.* **2020**, *12*, 4100. [[CrossRef](#)]
9. Czajlik, Z.; Árvai, M.; Mészáros, J.; Nagy, B.; Rupnik, L.; Pásztor, L. Cropmarks in Aerial Archaeology: New Lessons from an Old Story. *Remote Sens.* **2021**, *13*, 1126. [[CrossRef](#)]

Article

# Beyond Site Detection: The Role of Satellite Remote Sensing in Analysing Archaeological Problems. A Case Study in Lithic Resource Procurement in the Atacama Desert, Northern Chile

César Borie <sup>1,\*</sup>, César Parcerro-Oubiña <sup>2</sup>, Youngsang Kwon <sup>3</sup>, Diego Salazar <sup>4</sup>, Carola Flores <sup>5</sup>, Laura Olguín <sup>6</sup> and Pedro Andrade <sup>7</sup>

<sup>1</sup> Programa de Doctorado en Antropología UCN-UTA, Universidad Católica del Norte, Calle R.P. Gustavo Le Paige 380, San Pedro de Atacama, 1410000 Antofagasta, Chile. CONICYT-PCHA/Doctorado Nacional/2015-21150953. FONDECYT 1151203

<sup>2</sup> Instituto de Ciencias del Patrimonio (Incipit), Consejo Superior de Investigaciones Científicas (CSIC), Av. de Vigo, 15705 Santiago de Compostela, Spain; cesar.parcerro-oubina@incipit.csic.es

<sup>3</sup> Earth Sciences Department, University of Memphis, Memphis, 109 Johnson Hall, Memphis, TN 38152, USA; ykwon@memphis.edu

<sup>4</sup> Departamento de Antropología, Facultad de Ciencias Sociales, Universidad de Chile, Ignacio Carrera Pinto 1045, Núñoa, 7800284 Santiago, Chile. FONDECYT 1151203; dsalazar@uchile.cl

<sup>5</sup> Centro de Estudios Avanzados en Zonas Áridas (CEAZA), Ossandón 877, 1781681 Coquimbo, Chile. FONDECYT 3170913, 1151203; carola.flores@ceaza.cl

<sup>6</sup> Programa de Doctorado en Antropología UCN-UTA, Universidad Católica del Norte, Calle R.P. Gustavo Le Paige 380, San Pedro de Atacama, 1410000 Antofagasta, Chile. FONDECYT 1151203; olguinlaura.o@gmail.com

<sup>7</sup> Carrera de Antropología, Universidad de Concepción, Víctor Lamas 1290, 4070386 Concepción, Chile. FONDECYT 1151203; pandradem@udec.cl

\* Correspondence: cbc032@alumnos.ucn.cl

Received: 28 February 2019; Accepted: 5 April 2019; Published: 10 April 2019

**Abstract:** Remote sensing archaeology in recent years has emphasized the use of high-precision and high-accuracy tools to achieve the detailed documentation of archaeological elements (drones, LIDAR, etc.). Satellite remote sensing has also benefited from an increase in the spatial and spectral resolution of the sensors, which is enabling the discovery and documentation of new archaeological features and sites worldwide. While there can be no doubt that a great deal is being gained via such “site detection” approaches, there still remains the possibility of further exploring remote sensing methods to analyse archaeological problems. In this paper, this issue is discussed by focusing on one common archaeological topic: the mapping of environmental resources used in the past and, in particular, the procurement of lithic raw material by hunter-gatherer groups. This is illustrated by showing how the combined use of Landsat 8 images and “ground-truthing” via focused field studies has allowed the identification of a number of potential chert sources, the major lithic resource used by coastal groups between 11,500–1,500 cal. BP, in a vast area of the Atacama Desert covering 22,500 km<sup>2</sup>. Besides discussing the case study, the strength of remote sensing techniques in addressing archaeological questions comprising large spatial scales is highlighted, stressing the key role they can play in the detection and study of specific environmental resources within challenging physical settings.

**Keywords:** archaeology; arid environments; satellite remote sensing; lithological mapping; lithic procurement; chert sourcing; Landsat 8; GIS

## 1. Introduction

Remote sensing in archaeology has grown into a large and varied field. In particular, satellite remote sensing has benefited from an increase in the spatial and spectral resolution of the sensors, an improvement which has enabled the discovery and documentation of new archaeological features and sites worldwide [1–3]. While there can be no doubt that a great deal can be gained from these “site detection” approaches, there is still potential to be explored in using remote sensing methods as tools to analyse archaeological problems, especially on large geographical scales. In this paper, this potential is discussed by focusing on one common archaeological topic: the mapping of environmental resources used in the past, and in particular, the procurement of lithic raw material by ancient hunter-gatherer groups.

Since the 1970s, geological studies have tested the capacity of satellite remote sensing for lithological mapping in different environmental contexts, highlighting the ability of spectral analysis to discriminate between diverse rock and soil units, thus complementing and improving the accuracy of the data provided by conventional geological maps [4–9]. On the other hand, archaeologists have long emphasized the technological and social importance of high-quality rocks for prehistoric hunter-gatherer societies [10–14]. The large geographical ranges involved in the direct or indirect procurement of such rocks and their consistent use over long time spans imply that approaches on regional or landscape-based scales are especially well-suited for tackling these questions [15–18]. There seems to be a “natural” point of convergence here between the capabilities of satellite remote sensing and the research questions raised by some archaeological approaches. However, so far, these techniques have not received much attention from archaeologists concerned with the procurement of lithic resources in the past, despite the remarkable advantages they represent for addressing this problem on large spatial scales [19–22].

In this paper, following the trend of previous research [22], it is argued that satellite remote sensing in archaeology holds a great potential beyond the common (and indeed useful) aims of site detection. In particular, the suitability of remote sensing to overcome some of the major limitations of traditional archaeological methodologies is stressed. This is illustrated via a case study that shows how the combined use of freely accessible satellite images and “ground-truthing” through focused field studies has allowed the identification of a number of primary and secondary sources of chert in a vast area of the Atacama Desert covering 22,500 km<sup>2</sup>. This is a large-scale approach that takes full advantage of the natural conditions of the study area and also of the information contained in the “grey literature” provided by spatially discrete and dispersed CRM reports, offering a cost-effective methodology which can easily be replicated in other contexts.

The benefits and drawbacks of the methodology will be assessed, stressing the need for higher spectral resolution satellite imagery and “ground-truthing” via Visible Near-Infrared (VIS/NIR) and Fourier Transform Infrared (FTIR) reflectance spectroscopy for further refinement of the remote sensing approach, and also the need to conduct lithic provenance studies with a high level of geographical and geological resolution [23]. Finally, the strength of remote sensing techniques in addressing archaeological questions that comprise large spatial scales is discussed, and attention is drawn to the key role which they can play in the detection and study of specific environmental resources, such as lithic source areas, within challenging and poorly studied physical settings.

## 2. Satellite Remote Sensing in Problem-Oriented Research

Broadly speaking, and without any pretensions of being exhaustive, it could be argued that satellite images are used in archaeology in two possible ways: as exploratory tools (aimed at prospecting the landscape in order to find new sites or features of archaeological interest) or as part of problem-oriented research (as tools to answer explicit questions about the past). Although this broad-brush distinction is by no means new [22,24], it is not very clear: finding new archaeological places of interest can be problem-oriented research in itself, for instance, in the case of heritage management bodies, whose purpose is precisely to identify and document the highest number of

archaeological elements in any given area or region [25]. The difference does not imply any hierarchy at all; both approaches are equally useful and productive, at different levels and with different impacts. However, they usually imply a different approach to the use of satellite images and involve different methods and skills.

Exploratory analysis is commonly a general-purpose task, aimed at finding any elements of potential archaeological interest in a region. Consequently, the traces that are to be detected are equally varied (crop marks, soil marks, topographical anomalies, etc.). It follows almost naturally that general-purpose methods, such as visual photointerpretation, which do not require sophisticated processing of the remote sensing data to provide broad, and rather generic, results, are the best suited to such applications; on the contrary, any methods tailored to find certain specific proxies using more sophisticated image processing methods are typically not very good candidates for this [26,27].

It is by no means implied that all the aforementioned general-purpose applications do not involve any kind of expertise or skills [28]. The point to be noticed here is that, within these exploratory approaches, satellite images are typically used just like other types of aerial photos, for visual interpretation. Until recently, the medium to coarse spatial resolution of satellite imagery (especially when compared with aerial photos) strongly limited its use for visual prospection. Even now, despite the increasing availability of images with a higher spatial resolution (even those freely accessible through Google Maps, Bing Maps, and similar sites), it is still true that “satellite reconnaissance is better suited for mapping large-scale and broad landscape features such as paleochannels or detecting upstanding monuments in semi-arid environments, while airborne imaging remains the preferred approach for a detailed study of past geo-cultural activity” [29] (p.5).

In this paper, the focus is placed on the other main use of satellite imagery; spectral analysis. There are two main reasons which have limited the use of satellite spectral analysis in archaeology. Firstly, there is, again, an issue with the spatial resolution of most satellite imagery, which is insufficient to single out the marks of many individual archaeological features. The development of high-spatial resolution sensors has alleviated this limitation to some extent, although the limited spectral resolution of these spatially detailed sensors comes as an unavoidable drawback [22]. Secondly, and perhaps more importantly, there are no general-purpose methods for analysing the spectral information of satellite imagery, because this task is highly dependent on the characteristics of the specific target elements and on the characteristics of the surrounding landscape.

In any case, there are some good examples that prove that, when the conditions are right, remote sensing can fill relevant gaps in archaeological research. It is not surprising that the best examples of this synergy are those related to the delimitation of environmental variables which can be informative of economic or social practices in the past, especially those related to geological and soil mapping. As B. Vining pointed out a few years ago that “while environmental mapping was one of the earliest applications of archaeological remote sensing, the focus on site detection has shifted attention away from this area. Using spectral data to delimit environmental variables is the strong suite of remote sensing” [22] (p. 493). Different examples prove the usefulness of using satellite imagery for the analysis of environmental factors in relation to archaeological problems, such as the development of early agricultural practices [30]; the identification of patterns of settlements and paths [31]; or, similar to our case study, the detection of sources of raw stone material [32].

While such approaches might be equally feasible in any context, the existence of a good state of preservation and visibility of the archaeological evidence is always a factor that increases the chances of a successful remote sensing approach. In this respect, arid regions typically rank very high, since the absence of dense vegetation allows for a more direct observation of the properties of the soils. A first obvious benefit comes when satellite imagery is used for visual interpretation [33,34]. However, spectral analysis also benefits from the absence of dense vegetation. South America, or at least those large parts of it occupied by arid or semi-arid landscapes, represents a geographical context which can be especially suited to these kinds of approaches: the existence of large areas with very low population densities, both in the present and in historical times, implies a low amount of

human-induced alteration of the landscape, thus resulting in a reduced level of “noise” detectable through satellite images. Furthermore, many of these areas are geomorphologically very stable, an aspect which also increases the value of remote observation for the interpretation of past patterns. Finally, and more importantly, these largely unpopulated areas usually pose significant difficulties for traditional archaeological recognition due to their vastness, difficult access, and poor communication (which, for instance, limits the use of GPS and similar devices). All this suggests that spectral analysis of satellite imagery has great potential to be applied in many areas of arid and semi-arid South America, but at the moment, there are few examples of its application in the region [35], particularly if only those cases that go beyond the not-so-uncommon visual interpretation of satellite imagery are considered [36,37].

The increasing availability of free imagery represents a good opportunity to move forward and take advantage of the potential benefits of a problem-oriented use of satellite remote sensing in this region. The case study presented in the following sections attempts to illustrate this in practice.

### 3. Introduction to the Case Study: Research Problem and Background

#### 3.1. Lithic Procurement Strategies in Hunter-Gatherer Societies

Land-use patterns and, particularly, lithic procurement strategies, have long been major topics in the archaeological research of ancient hunter-gatherer societies [11–14,38,39]. In particular, the procurement of high-quality stone (the concept of high quality rocks, as it is used here, stands for the ease of a given lithic raw material for controlled knapping [14], and also for the functional requirements that the artefacts made of such raw material have to meet to achieve their intended use, for instance, in terms of edge strength, requirements that usually prompted the selection of cryptocrystalline toolstone like chert, chalcedony, flint, and jasper in prehistoric times [10,40]) has been considered a key aspect in the technological organization of these kinds of groups and an activity that affected, in diverse and complex ways, the configuration of their settlement and mobility patterns [13,39–41].

The geological occurrence of the most suitable rocks for tool manufacturing is manifested unevenly across the landscape, and there is normally a strong discordance between the spatial distribution of critical subsistence resources and these natural deposits of raw material [10,13,14,39]. Therefore, hunter-gatherer societies had to develop strategies to ensure the availability of adequate toolstone raw materials in the locations where they were required for subsistence activities [13,42,43], investing, in some cases, considerable time and effort in their procurement [12,13,44].

In desert areas such as the Atacama, this discordance is manifested as a stark contrast between the coastal environments, rich in biotic resources, where local hunter-gatherer-fisher communities settled, and the vast barren landscape of the Central Depression, profuse in high-quality lithic resources, where only ephemeral occupations were possible [45–50]. The technological organization of those communities relied heavily on high-quality non-local chert, which comprises between 83% and 95% of the coastal lithic assemblages documented for the period 11,500–1,500 cal. BP [51]. To sustain that, these groups had to organize forays taking them between 40–115 km away from their settlement areas into the hyper-arid core of the Atacama Desert [45,46,48,52–54].

Material evidence for these logistic forays is abundant but widely dispersed in the Atacama Central Depression, just like the chert-bearing geological formations [46,48,53,54]. This scenario imposes challenges for traditional archaeological methodologies, mainly due to the cost in time and human resources that the systematic study of these contexts demands and the extremely complex practical conditions for fieldwork.

In order to deal with these limitations, different research techniques need to be integrated in innovative ways, providing access to the cumulative and continuous expression of the lithic record across space on an appropriate geographical scale [15–18,40,42].

The Atacama Desert, and particularly its hyper-arid Central Depression, has been geologically stable since the end of the Pliocene [55–58]. In exchange for its challenging fieldwork conditions,

this stable, bare earth landscape, offers exceptional conditions for archaeological visibility and preservation, thus making it an ideal setting for the use of satellite remote sensing techniques [53].

### 3.2. Satellite Imagery and the Mapping of Lithic Source Areas

Among the multispectral satellite images available with global coverage and free access, those captured by the Landsat program sensors are among the most widely used in geology and archeology for lithological mapping [9]. Satellites from NASA's Landsat program have been in sun-synchronous orbit since 1972, capturing scenes from the earth's surface with a coverage of  $185 \times 185$  km per single image (USGS). Their sensors provide a moderate spatial and radiometric resolution, covering the visible and near-infrared (VNIR) range with a resolution of 15 to 60 m and also, from the Landsat 4-5 mission onwards, the Thermal Infrared (TIR) range with resolutions of 60 to 120 m.

The wide distribution of their bands in the electromagnetic spectrum makes Landsat images one of the most versatile tools for remote sensing studies in diverse landscape conditions [59]. The geological remote sensing community makes use of them extensively for lithological and mineralogical mapping, especially since the advent of the Landsat Thematic Mapper (TM) sensor [9], following the precept that reflectance characteristics of the different lithological classes (rocks or soil types) are primarily derived from the presence and relative proportion of their mineral components [60,61].

For lithological discrimination, specifically in zones with mineralogical alteration, Landsat bands are commonly combined in RGB composites and are subject to digital enhancement techniques, such as band-ratioing, principal component analysis (PCA), and supervised classification [9]. In general, bands within the visible to SWIR (or VNIR) range ( $0.4\text{--}2.3 \mu\text{m}$ ) are selected for these tasks, due to the presence of diagnostic spectral features of certain minerals, such as clays, carbonates, and iron oxides, which allow zones with hydrothermally altered rocks to be differentiated from those with unaltered rocks [7,9,62].

Archaeological studies on local and regional scales have successfully exploited some of these enhancement techniques in Landsat images for the detection of ancient lithic source areas. A few examples can illustrate this. Carr and Turner [19], in a pioneering study within this line of research, combined field studies, laboratory analysis, and satellite remote sensing on Landsat 5 TM images to locate prehistoric quarries in the Horse Prairie region, in the southwest of Montana, United States. Using "ground truth" data provided by reflective spectroscopic analysis of field samples, these researchers identified distinctive spectral profiles for chert weathered outcrops and soils with dispersions of rocks extracted from these outcrops. The spectral data was incorporated into a supervised classification within which the adjacency of pixels assigned to these two types of deposition contexts proved to be indicative of the location of ancient chert quarries, which had previously been unknown [19].

More than a decade later, Rosendahl (2010) used Landsat 7 ETM+ VNIR bands for a principal component analysis, in conjunction with pedestrian surveys in the Troodos foothills, Cyprus, as training data for a supervised classification. This work identified potential chert-bearing areas within the Lefkara geological formation and was used for the design of targeted pedestrian surveys.

A more recent example is that of Cattáneo, et al. [63] who demonstrated the successful identification of potential prehistoric lithic sources using Landsat 7 VNIR bands in the northeast of the Province of Santa Cruz, in Argentina.

The aforementioned references seek to highlight the relevance and potential of the integration of satellite remote sensing tools for lithic landscape archaeological research. In the following section, the guidelines of a multidisciplinary research strategy benefitting from this integration for the reconstruction of the Southern Atacama prehistoric lithic landscape are detailed.

#### 4. Study Area: Physical and Archaeological Setting

The study area extends between 24.6° and 26° S, comprising the southern part of the Atacama Desert, and stretches from the Pacific coast to the foothills of the Andes, a transect of ca. 150 km. This area of 22,500 km<sup>2</sup> lays within the southern portion of the Antofagasta region, Chile, and is characterized by a complete lack of perennial streams and great altitudinal contrast (Figure 1).

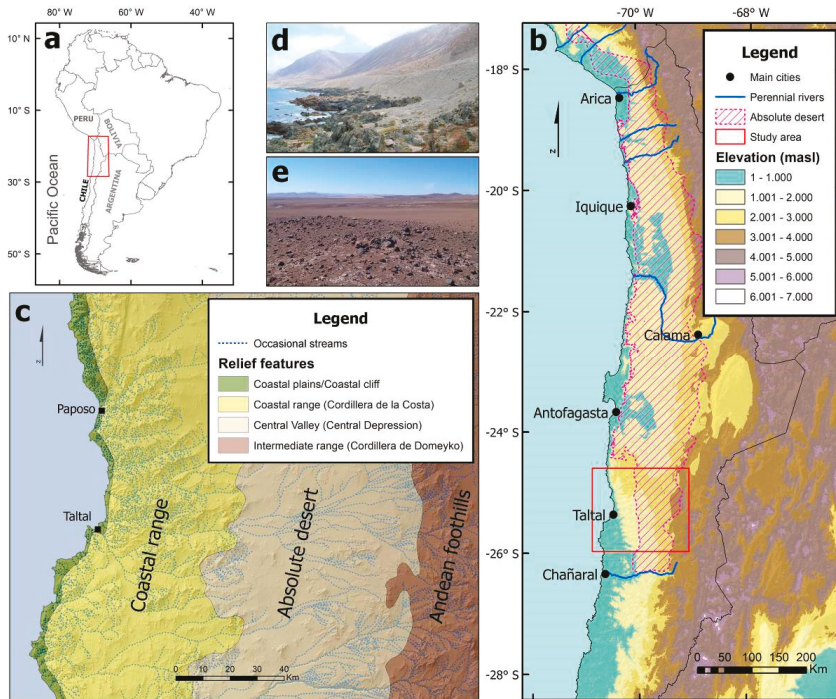


**Figure 1.** (a) Map of South America, red box indicates the extent of (b) altitudinal map showing the location of the absolute desert in northern Chile (hatched polygon), main cities (black dots), and perennial streams (blue lines). Red box in (b) corresponds to the map of study area (c) with the main topographic features and occasional streams (dashed blue lines); (d) panoramic view of the coastal platform and cliffs; (e) panoramic view of the absolute desert of Taltal.

The main relief features correspond to, from west to east, a narrow litoral platform, a steep coastal range (Cordillera de la Costa), a longitudinal central valley or Central Depression, the foothills of the Andes (represented in the area by the Cordillera de Domeyko) and, finally, the higher-level Andes and the Altiplano [64].

On the coast, facing the rich and diverse marine ecosystems of the Pacific [65], dense fogs sustain isolated plant communities of the *lomas* formation, which attract minor fauna species [66]. Fresh water is available from small springs along the litoral platform and in the neighboring coastal range, fed by occasional coastal rains related to ENSO events [67,68]. The cliff-like Cordillera de la Costa, with peaks of 2,000 m.a.s.l., blocks the eastward advance of the coastal fogs and, together with the cold oceanic Humboldt Current and the rain-shadow effect of the Andes, intensifies the hyper-arid conditions of the Central Depression [55,69]. In this 70 km wide Central Valley, with its vast plains, isolated hills, and low-altitude ranges, rainfall averages less than 1 mm per year, solar radiation is extremely high, and strong thermal oscillations occur throughout the day [56,69]. Plant and animal communities are minimal here and are restricted to the scarce and widely scattered locations around groundwater

outcrops [70]. To the east, the streams and wetlands of the Cordillera de Domeyko and the upper Andes offer a relative abundance of water resources, animals, and plants [70].

The extreme and long-standing aridity of the Central Depression [55,56,69,71], except during phases of relatively more humid conditions [72–76], has always hindered stable human occupation. Accordingly, settlement patterns have historically been anchored to the coastal environments, which are richer in biotic resources [45,47,50,77,78].

Nevertheless, the vast wealth of high-quality rock in the Central Valley has attracted sporadic, but recurrent, occupations by the coastal inhabitants of the Atacama for over 10,000 years [45–48,52–54,78]. The abundance of sedimentary microcrystalline and cryptocrystalline silicates, or chert [79], throughout the area is explained by the presence of several spatially restricted hydrothermal alteration zones, which mainly developed in rocks of the Chile-Alemania Formation, part of a continental volcanic chain of the Palaeocene-Middle Eocene age [80]. Igneous rocks intrude this Formation (e.g., quartziferous, tonalitic, and granodioritic porphyries) and, due to the action of geothermal systems, they have gone through silicification, argillization, and propylitization processes of variable intensity and extension [80,81] (Figure 2).

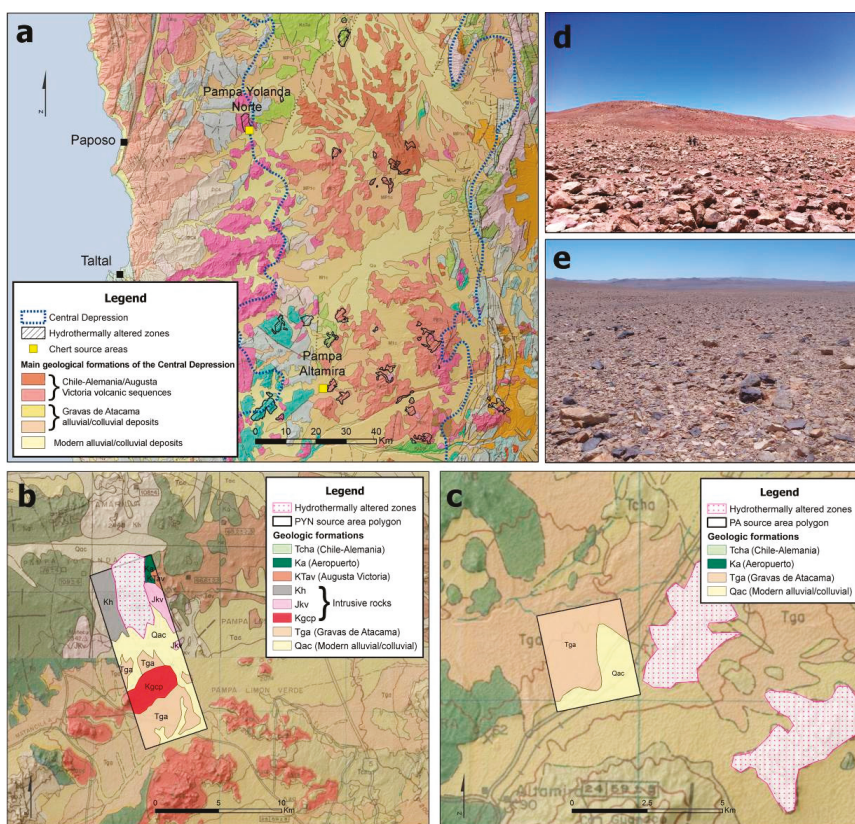


**Figure 2.** (a) Map of the study area showing the main geological formations within the Central Depression (dashed blue lines), hydrothermally-altered zones (black hatched polygons), and chert source areas (yellow squares), data from 1:1,000,000 geological map [82]; (b) and (c) source area of Pampa Yolanda Norte (b) and Pampa Altamira (c), showing associated geological formations and hydrothermally-altered zones (pink dotted polygons), data from 1:250,000 geological maps [80,81]; (d) and (e) panoramic views of Pampa Yolanda Norte and Pampa Altamira, respectively.

Chert source areas occur in the Central Depression as outcrops in hydrothermal alteration zones predominantly associated with the Chile-Alemania Formation, but also as secondary geological deposits in the overlying Gravas de Atacama Formation (Oligocene-Miocene) and in modern (Pleistocene/Holocene) alluvium and colluvium deposits [80,81]. The detritus flows of the latter formations fill low reliefs covering large areas in the Central Valley, where chert nodules carried from different outcrops abound [53,54].

The very low deposition rates documented in the area for the last 10 ka [55,56,69] and the very limited erosion processes during post-Pliocene times [83,84] define a mostly stable landscape in which primary and secondary deposits of chert, as well as evidence of their prehistoric exploitation, are exceptionally well-preserved in old and continuously exposed surfaces (the erosion and incision processes related to rain episodes during post-Pliocene humid phases have been limited to fluvial and alluvial features of a small scale [56,58,83]). Thus, the major geomorphological features between the foothills of the Andes and the coastal range, and the archaeological evidence located on them, have remained mostly unchanged [58,64,84]). This offers a perfect setting for the archaeological research of ancient lithic procurement systems through distributional large-scale approaches.

## 5. Materials and Methods

The methodological strategy proposed by this study integrates techniques from archaeology, geography, and geology. In order to reach its full potential, this approach requires the implementation of a series of linked work stages and specialized analysis techniques. In the following sections, the stages executed to date are presented sequentially, while those that are still in progress will be considered in the Discussion and Conclusions sections.

### 5.1. Construction of a Georeferenced Database

As an initial step, a baseline georeferenced database was constructed in QGIS®. This database included cartographic baseline data at a 1:50,000 scale, acquired from the Military Geographic Institute of Chile (IGM), and freely accessible hydrology, ecology, and topography (ASTER GDEM) geospatial data. The geological maps available for the area at a 1:250,000 scale [80,81] were also digitized and georeferenced in this GIS database.

Using online search tools from the Chilean Environmental Assessment Service (SEA) website, the existing CRM reports containing archaeological data for the interior desert (the area between the coastal range cliffs and the Andean foothills) were identified. The information they contained regarding prehistoric sites and finds was organized and standardized using a tabular database including the following data fields:

- UTM coordinates (WGS84 datum)
- site category
- horizontal extension (area)
- type and number of lithic artefacts recorded
- type of lithic raw materials recorded

This database also included the archaeological findings made by the research team in preliminary inspections of the area (see Figure 3 in Section 6.1. Details of the different datasets used in this research are presented in Supplementary Table S1).

### 5.2. Satellite Image Analysis

The second stage involved the acquisition, pre-processing, and study of Landsat 8 multispectral satellite images using QGIS. Four scenes were needed to cover the study area. These scenes were downloaded with minimum cloud cover (less than 3%) and pre-processed using the Semi-Automatic Classification Plugin (SCP, version 6) in QGIS. The pre-processing operations included atmospheric correction, application of the DOS1 method to the blue and green bands, and conversion to surface

reflectance values of the six spectral bands (bands 2 to 7) of the Landsat 8 OLI sensor, corresponding to a spectral range between the VIS and SWIR (0.45 and 2.35  $\mu\text{m}$ ).

After pre-processing, the Landsat scenes were assembled in a mosaic, from which a polygon of 22,500  $\text{km}^2$  (ca.  $150 \times 150$  km) of the study area was extracted as a subset. This subset, with a 30 m spatial resolution and six spectral bands, constituted the base dataset on which the subsequent analyses were conducted by applying basic image enhancement techniques for their visual interpretation.

False-color RGB composites were generated using different band combinations to highlight geological features. This first approach sought to produce a color image with optimal conditions for geological interpretation at a regional scale, by testing various combinations of Landsat SWIR, NIR, and VIS bands, which included RGB composites suggested by other studies to highlight geological features in arid and semi-arid environments [7,85,86].

Band-ratting techniques were used to suppress variations in the reflectance of the scenes due to topography and grain-size variations, emphasizing differences in the spectral reflectance curves which favor the discrimination of mineral clusters that cannot be seen clearly in single-band examination [6,8,87,88]. Different Landsat band ratios recognized for their utility in mapping hydrothermal alteration zones [7,9,85,86] were tested in RGB false-color composites to enhance the visual discrimination of chert primary and secondary deposits associated with this kind of alteration zone. Finally, a third processed image was obtained from a PCA, with the aim of (1) reducing the redundant spectral data contained in the different Landsat bands to a limited set of new uncorrelated principal components (or PCs) [89] and (2) enhancing the subtle spectral information of new principal component images related to characteristics of lithic raw material that may not be noticeable in original bands' composition. The eigenvalues and eigenvector matrix of the PCA were examined and, together with the generated PCs, various RGB combinations of principal components were tested to identify potential chert-bearing geological formations.

### 5.3. Archaeological Fieldwork

Integration of the data from the two previous stages allowed us to (a) identify certain trends in the spatial organization of the archaeological record and the geology of the area, and (b) define spatially restricted zones of interest for targeted pedestrian surveys. To facilitate the detailed study of these zones, two polygons of  $1 \times 30$  km were selected as sampling zones and placed in order to cover two segments (the Western and Central Segments), which the baseline data signalled as relevant for the lithic provisioning dynamics within the study area [53,54]. Both segments make up an almost continuous altitudinal transect (with a gap of 10 km) covering the interior desert from 12 to 82 km east of the coastline and rising from 930 meters above sea level, in the lower reaches of the Cascabeles ravine, up to 2,275 meters above sea level in Pampa Flor de Chile, in the middle portion of the Central Depression (see Figure 7 in Section 6.3).

This strategy sought to generate a cross-sectional view of the coastal lithic supply systems deployed in the hyper-arid lands which extend between the coastal range and the western slopes of the Cordillera de Domeyko. For this purpose, the Western Segment of the survey transect was located in one of the main natural routes connecting the coastal platform with the Central Depression. In turn, the Central Segment was placed in the core area of the Central Valley, an area highlighted by preliminary studies as having a greater presence of actual and potential chert source areas [53,54]. The design of these segments avoided crossing areas heavily intervened by historic nitrate extraction operations and excluded, as far as possible, areas which had already been subject to archaeological survey by CRM projects.

The two survey polygons were traversed by parallel transects of west-east orientation, regularly spaced at 100 m intervals (the distance of 100 m between transects responds to a compromise between survey intensity and spatial coverage. This methodological decision considered the excellent archaeological visibility of the interior desert, which is favored by the complete absence of vegetation cover and the predominance of flat terrain.). The archaeological finds along these transects were

positioned with handheld GPS devices and their main features recorded as field notes and by digital photography. Additionally, specific archaeological studies were conducted in a targeted manner in discrete areas outside of the survey segments, areas that had been signalled by the baseline data previously collected as potential chert sources.

#### 5.4. GIS Integration

This last stage involved updating the GIS database with the new archaeological field data provided by the systematic pedestrian surveys. When integrated with the baseline information gathered from the available sources and generated by satellite remote sensing techniques, this detailed field data facilitated the assessment of the results of the remote sensing approach, in terms of both the geological (discrimination of types of chert) and geographical (size and location of the sources identified) resolution. All in all, this helped to gain a more thorough vision of the Southern Atacama lithic landscape.

The capabilities of GIS for data integration were exploited in this stage specifically as a means for assessing the accuracy of the remote sensing results by confronting them with the data provided by the conventional 1:250,000 geological maps, in addition to the archaeological field data contained in the “grey literature” and gathered during the aforementioned field studies.

Managing multiple information sources collected at different spatial resolutions is an unavoidable task in the reconstruction of ancient lithic landscapes [18], and GIS have greatly assisted this process in archaeological studies that range from local [90–92] and regional [18,93] to macro-regional scales [94].

## 6. Results

### 6.1. From the “Grey Literature” to the GIS Database

The review of the SEA database found 15 reports containing data of prehistoric archaeological findings within the interior desert. These findings were identified through systematic surveys in various patches of land comprising an area of ca. 390 km<sup>2</sup> [54]. The 1,193 records obtained from these sources were complemented by 37 new archaeological sites detected during preliminary inspection of the main ravines that dissect the Central Depression and the coastal range.

These 1,230 points of archaeological interest were systematized and integrated into the GIS geo-referenced database. All of them consist of locations with surface lithic scatters, only occasionally (3.3% of the records) associated with the remains of circular stone structures of very low architectural investment. The lithic categories reported in these locations are nodules, cores, hammerstones, flakes, and debris. Macroscopically diverse chert varieties, described as flint, chalcedonies, jaspers, and quartz, are the dominant raw materials (97.8% of records). Non-siliceous and coarse-grained silicified raw materials (quartzite, andesite, basalt, and tuff) are markedly less represented, occurring at a low frequency in assemblages with chert (in only 12 locations) and in 24 locations exclusively (2.2% of records) (Figure 3).

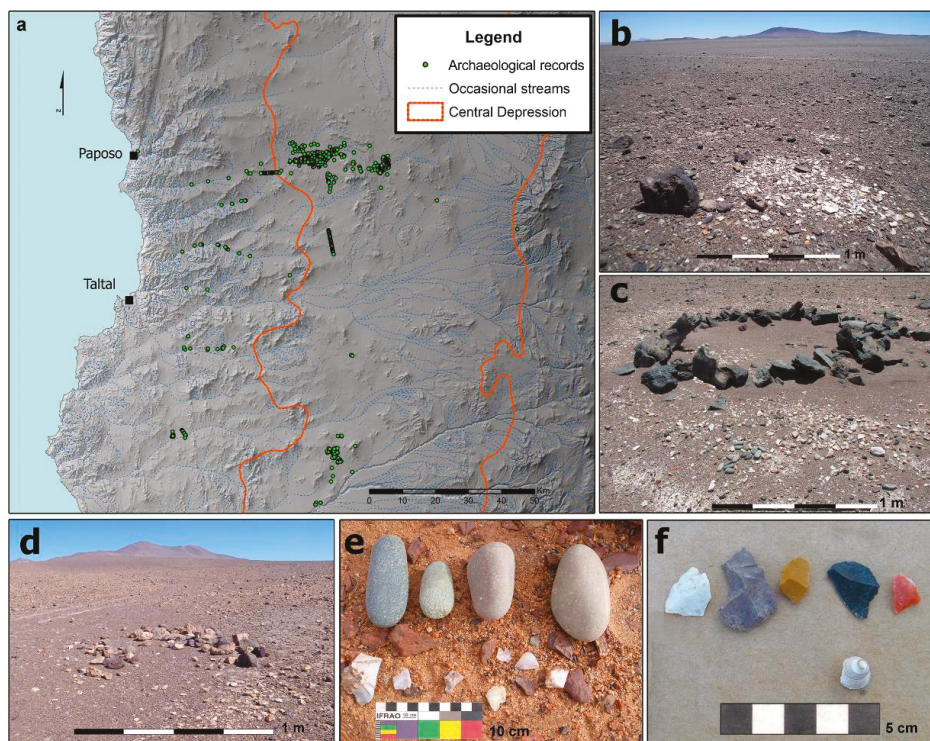


**Figure 3.** DEM of the study area showing the points of archaeological interest of the interior desert (green dots), the limits of the Central Depression (orange lines), and occasional streams (blue lines); (b) to (f) material assemblages of ephemeral prehistoric occupations in the core of the Atacama Desert.

The baseline data recovered from the “grey literature” and our initial inspections of the area allowed us to obtain an overview of the archaeological record of the interior desert. These georeferenced data, when incorporated into the GIS database with other thematic layers, provided key information for evaluating the potential of satellite remote sensing techniques, as will be described below. GIS integration of the results of these different lines of work was crucial for the planning of systematic fieldwork focused on specific areas of interest, the main results of which are presented in Section 6.3.

## 6.2. Satellite Remote Sensing the Lithic Landscape

In this subsection, the main results of the spectral analysis techniques applied to Landsat 8 multispectral imagery are summarized. More details about this preliminary analysis, including the use of complementary techniques of digital interpretation (material mapping and supervised classification), can be consulted in [53].

### 6.2.1. Band Combinations

Different band combinations were tested with the pre-processed Landsat 8 image of the study area, with the false-color composite of 7-6-2 (RGB) providing a greater visual contrast of the actual and potential chert-bearing geological formations. These formations are highlighted in light green, showing spatial correspondence with hydrothermal alteration zones registered in the geological 1: 250,000 charts [80,81], as well as with the two source areas of this raw material detected in preliminary field inspections (Pampa Yolanda Norte and Pampa Altamira). Meanwhile, the surrounding environment

is dominated by two other shades: blue, mainly in the area of mountains and plains of the Central Depression, and yellow, which generally coincide with the mountain ranges of both the coastal range in the west and the Cordillera de Domeyko in the east (Figure 4).

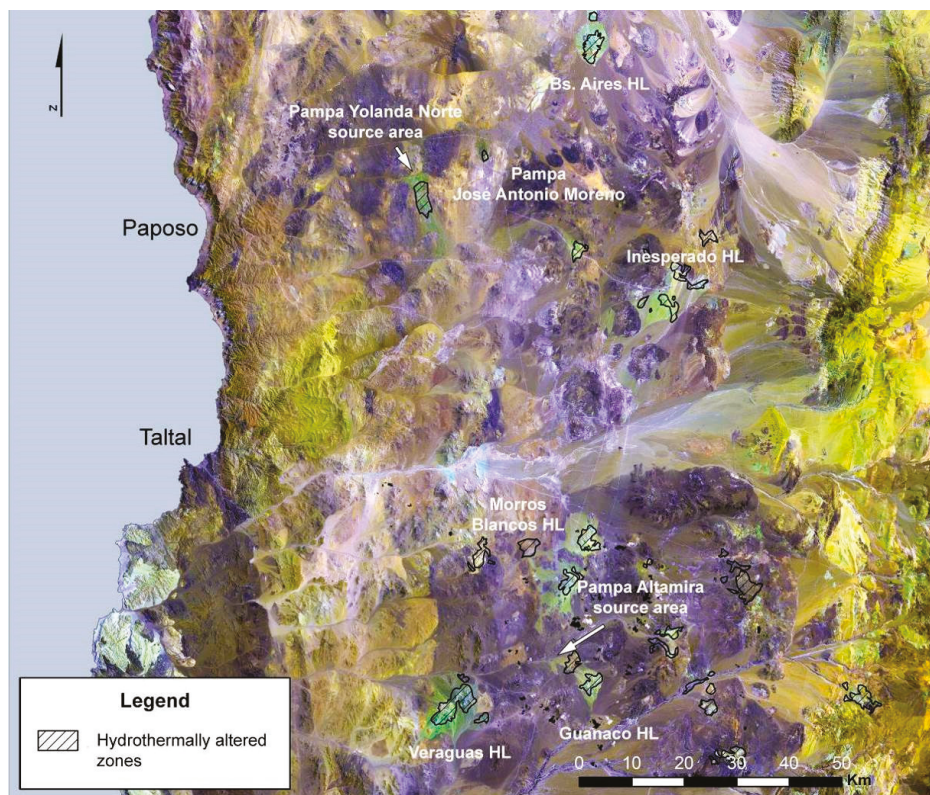


**Figure 4.** Landsat 8, bands 7-6-2 (RGB) false-color composite. Potential and actual chert source areas are highlighted in light green, and hydrothermally-altered zones are shown as black hatched polygons.

This first composite allowed us to observe a pattern of grouping of potential chert-bearing lithological units within the Central Depression, which broadly coincide with the location of the main hydrothermal alteration zones mapped on the geological charts. In the northern section of the Central Depression, the somewhat dispersed group formed by Cerro Punta Amarilla (Pampa Yolanda Norte), Pampa José Antonio Moreno, and the Inesperado and Buenos Aires hills stands out. In the southern section, the Veraguas, Guanaco, and Morros Blancos hills, together with Pampa Altamira, form a more compact grouping of extensive areas with the possible presence of chert-bearing deposits, together with other minor hydrothermal alteration zones towards the east.

#### 6.2.2. Band Ratios

Band ratios reported as informative in identifying hydrothermal alteration zones with Landsat scenes [6,7,9,85,86] were calculated and manipulated in the RGB guns of QGIS to determine the most appropriate combinations to effectively distinguish the lithological units of interest. The composite of ratios that best highlighted the spectral features of the different soil covers of the study area was  $R = 4/2$ ,  $G = 6/7$ ,  $B = 5$  [9,86] (Figure 5).

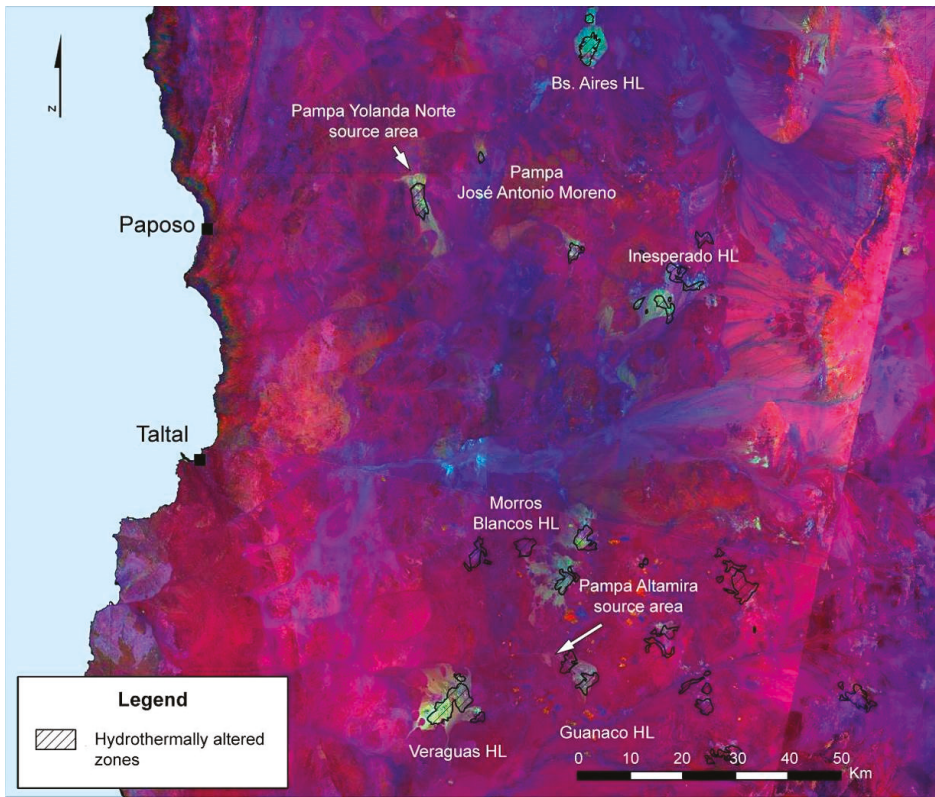


**Figure 5.** Landsat 8, band ratio 4/2-6/7-5 (RGB) false-color composite. Potential and actual chert source areas are highlighted in light green, and hydrothermally-altered zones are shown as black hatched polygons.

The band ratios generated improved the results obtained with band combinations. By accentuating differences of reflectance indicative of certain mineral groupings, the main geological formations of the Central Depression and the chert deposits that occur in this specific sector of Southern Atacama stand out. Ratio 4/2 (red) foregrounds continental volcanic sequences, which in the case of the Central Depression, are mainly represented by the Chile-Alemania Formation. Band 5 (blue) targets the calcareous and saline soils that form part of modern alluvial and colluvial deposits. The older alluvial/colluvial deposits of the Gravas de Atacama Formation appear in magenta, as they are mainly composed of detritus flows which carry clasts from the underlying Chile-Alemania Formation [80] and are mixed, when reaching lower grounds, with modern alluvial/colluvial deposits. Finally, ratio 6/7 highlights potential and actual chert-bearing deposits, which are clearly contrasted in a light green color against the predominantly magenta and blue background (further details under Section 7. Discussion).

### 6.2.3. PCA

The third, and final, processed image was obtained from a PCA. PC 1 comprises 99.99% of the variance, which suggests that most of the variability in the Landsat scene is common to all the bands. The other subsequent components, although they represent only the remaining 0.00006% of variance in the data, enhance subtle spectral features of the original scene, which are useful for the mapping of

chert-bearing formations. The selection of PCs was made by examining the eigenvector matrix (Table 1), which showed contrasting relations between original bands and PCs. In this case, the combination of PC 5, 4, and 2 in the RGB guns turned out to be the most suitable for differentiating the lithological units of interest, contrasting strongly in intense magenta the actual and potential chert source areas on a background dominated by green and light green tones (Figure 6).

**Table 1.** Eigenvector matrix of Landsat 8 VNIR bands PCA.

Eigenvector/PC	PC 1	PC 2	PC 3	PC 4	PC 5	PC 6
Eigenvector 1	0.170988	−0.451865	−0.62058	0.0738699	0.521468	0.322607
Eigenvector 2	0.277532	−0.446888	−0.314157	−0.111879	−0.43326	−0.651415
Eigenvector 3	0.374354	−0.396037	0.301608	−0.0688847	−0.478003	0.61548
Eigenvector 4	0.44429	−0.246103	0.60082	0.115229	0.526232	−0.301425
Eigenvector 5	0.574989	0.480726	−0.166831	−0.63249	0.0927344	0.0425876
Eigenvector 6	0.474966	0.384187	−0.190792	0.750972	−0.162328	0.00979504

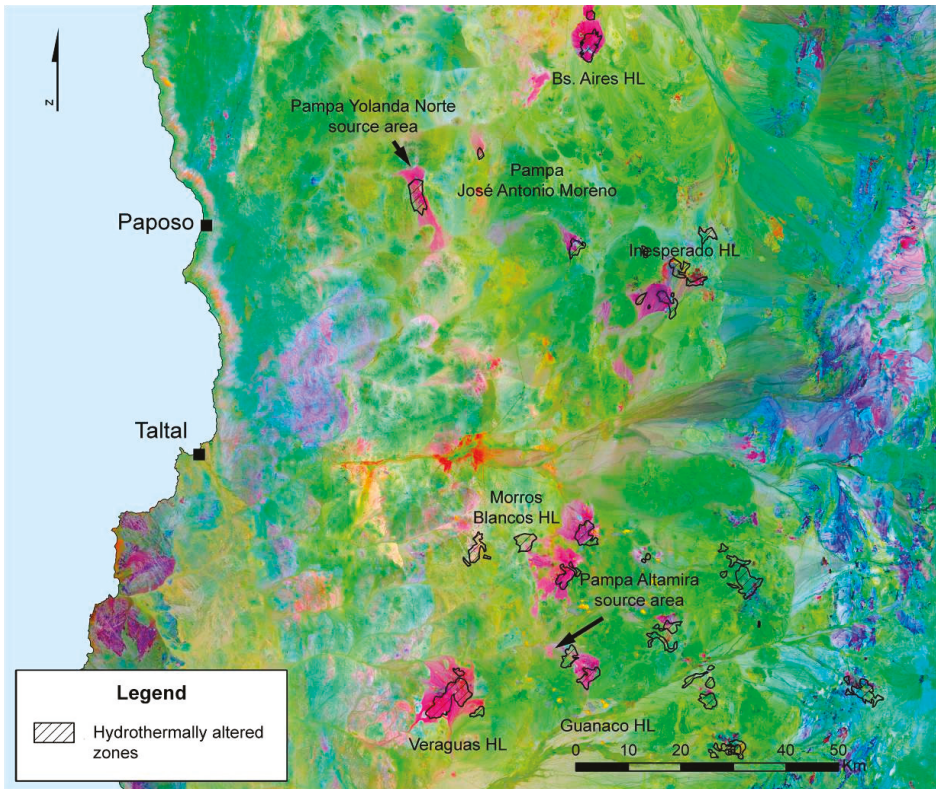


**Figure 6.** Landsat 8, PCs 5-4-2 (RGB) false-color composite. Potential and actual chert source areas are highlighted in magenta, and hydrothermally-altered zones are shown as black hatched polygons.

The PCA image yielded information which conforms with the band combination and band ratio RGB composites, in terms of the location of potential chert-bearing geological formations within the study area, a fact that is consistent with the archaeological and geological baseline data.

The integrated results of all these spectral analyses and the fieldwork detailed below, will be addressed in the Discussion section.

### 6.3. Stepping Inside the Core of the Atacama Desert

The pedestrian surveys covered 77 km<sup>2</sup> (39 km<sup>2</sup> in the Western Segment and 38 km<sup>2</sup> in the Central Segment) and resulted in the identification of a total of 1,517 points of archaeological interest. These correspond to locations with superficial lithic scatters, ranging from bounded and small low-density loci to large and diffuse areas composed of several lithic foci with a variable density. The lithic assemblages of these contexts reflect different stages of the reduction sequence of macroscopically diverse types of chert, the dominant raw material in 97.5% of the cases, and the only material documented in 85.5% of the cases. In turn, non-siliceous and coarse-grained silicified rocks (andesite, basalt, ignimbrite, sandstone, quartz, rhyolite, and tuff) comprise the only raw material in only 2.6% of the points.

In the Central Segment, with very few exceptions, only evidence of the primary processing of chert nodules was identified, including the production of bifacial cores and matrices (2.6% of the records). The intermediate and advanced stages of these raw material reduction sequences were predominantly documented in the Western Segment. This is consistent with the presence in the Central Segment of chert source areas and with the availability of a natural corridor (the Cascabeles and Portezuelo ravines) in the Western Segment, through which the reduction of chert pieces from the Central Depression sources to the coastal base and task camps took place (Figure 7).

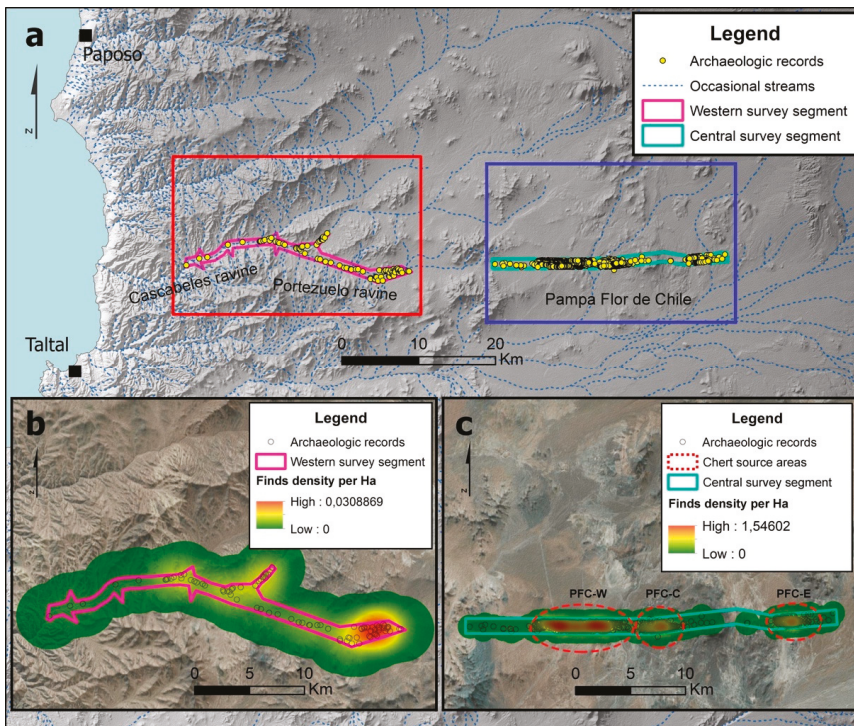


**Figure 7.** DEM of the study area showing the occasional streams (blue lines) and the locations with lithic scatters (yellow dots) recorded in the Western Segment (pink polygon) and Central Segment (light blue polygon) during systematic pedestrian surveys in the interior desert. Red box in (a) corresponds to a natural color composite (b) showing the Western Segment (pink polygon) and the archaeological finds (black circles) with their density per hectare. Blue box in (a) corresponds to a natural color composite (c) showing the Central Segment (light blue polygon); the archaeological finds (black circles) with their density per hectare; and the chert source areas Pampa Flor de Chile West, Center, and East (red circles).

In Pampa Flor de Chile (Central Segment), three new chert source areas were identified, which were named Pampa Flor de Chile West, Center, and East (PFC-W, PFC-C, and PFC-E). In the Western Segment, no source areas of this raw material were recorded, only low-density scatters of macrocrystalline quartz at the headwaters of the Portezuelo ravine.

The three chert sources in Pampa Flor de Chile can be added to those previously recorded in Pampa Yolanda Norte (PYN) and Pampa Altamira (PA), and to another chert source signalled by CRM reports and confirmed by the targeted field inspections (Arbiodo West or ARB-W), making a total of six main chert source areas. Focused archaeological and geological studies were conducted to characterize all these lithic sources and to collect “ground-truth” data for further studies, which are introduced as ongoing research lines in the following sections.

## 7. Discussion

The GIS integration of the data generated by the aforementioned analytical stages enabled us to obtain, with a low level of investment in terms of time and resources, an overview of the lithic landscape of this inland and little-studied portion of Southern Atacama. Although this is a preliminary and still coarse-grained approach, it has allowed us to corroborate certain aspects of interest, referred to in previous archaeological and geological studies, and to design strategies for systematic and focused fieldwork in a vast and harsh study area.

The different lines of evidence condensed in this investigation indicate that chert source areas are clearly clustered in the Central Depression, at linear distances between 40 and 80 km away from the modern coastline. None of these lithic procurement areas are found on the western flank of the study area (coastal platform and coastal range), with the exception of some of the deposits which comprise the large source of Pampa Yolanda Norte, a source located on the border between the coastal range and the Central Valley. On the eastern flank of the study area, which includes a portion of the western foothills of the Andes (Cordillera de Domeyko), chert only seems to be available in smaller and scattered deposits.

The absence of high-quality chert in the coastal platform and in the coastal range is consistent with the results of geological, petrographic, and geochemical studies, which report a predominance of intrusive rocks and, to a lesser extent, metasedimentary rocks in the coastal range between Taltal and Paposo [95]. This is a trend that characterizes the geology of this relief feature throughout the study area [80,81].

In the Andean foothills, as in the coastal range, hydrothermally-altered zones are scarce and widely scattered [80]. This is in line with the results of the remote sensing techniques deployed in this study, which show only faint traces of potential chert-bearing formations in both areas.

The spatial organization referred to above for the chert source areas is coherent with the archaeological record available for different sectors of the Southern Atacama, which points to a concentration in the Central Depression of the deposits of siliceous rocks accessed by local hunter-gatherer-fisher groups [46,48,50,53]. It has been suggested that this spatial configuration of the Southern Atacama lithic landscape was part of a broader regional pattern, within which the siliceous deposits, located at an average distance of 80 km from the coast, form an extensive system of approximately 800 km throughout northern Chile’s Central Valley [48]. Techno-functional and lithic reduction sequence analyses carried out in both coastal and interior prehistoric contexts support this idea, by signaling the presence of primary exploitations of chert nodules in the Central Depression and a marked predominance of small-sized flakes, mostly with no cortex, in the coastal assemblages [46–48,50,52,96].

Chert source areas in the Central Depression of the study area comprise primary and, especially, secondary, geological deposits. The outcrops are found, in most cases, in direct spatial association with (or close proximity to) hydrothermal alteration zones, mapped in the geological charts as part of the volcanic sequences of the Chile-Alemania Formation [80,81]. Nodules from these outcrops are carried by alluvial/colluvial deposits to distances of up to 15 km. [53,54]. It is in these large detritus

flows that locations of chert primary exploitation are most commonly recorded across the Southern Atacama [46,52–54].

The analysis of the multispectral Landsat images provides a significant advantage over the conventional 1:250,000 geological charts [80,81]: they do not only allow the main areas of hydrothermal alteration within the study area to be clearly highlighted, but they also bring about the possibility of distinguishing smaller areas with either primary or secondary deposits of this lithic raw material. This point will be demonstrated with three examples that compare the geological and geographical resolution of the 1:250,000 geological charts with the one obtained by remote sensing techniques. When available, the location of archaeological finds documented in CRM reports and by the preliminary inspections and systematic surveys conducted as part of this study, are included to show the aforementioned spatial relation of prehistoric lithic processing contexts and the chert deposits detected.

The first case (previously unknown primary deposits of chert) is illustrated by the Pampa Altamira source area, a single and relatively discrete primary outcrop (ca.  $2.7 \times 1.5$  km), the nuclear area of which covers lands assigned in the geological charts to the Gravas de Atacama Formation [82]. This deposit, despite being located not far from a hydrothermal alteration zone mapped in the geological charts, is not identified as such. Band combination 7-6-2, as well as the band ratio composite and PCA image, are able to clearly show it as a chert-bearing lithological deposit (Figure 8a,b).

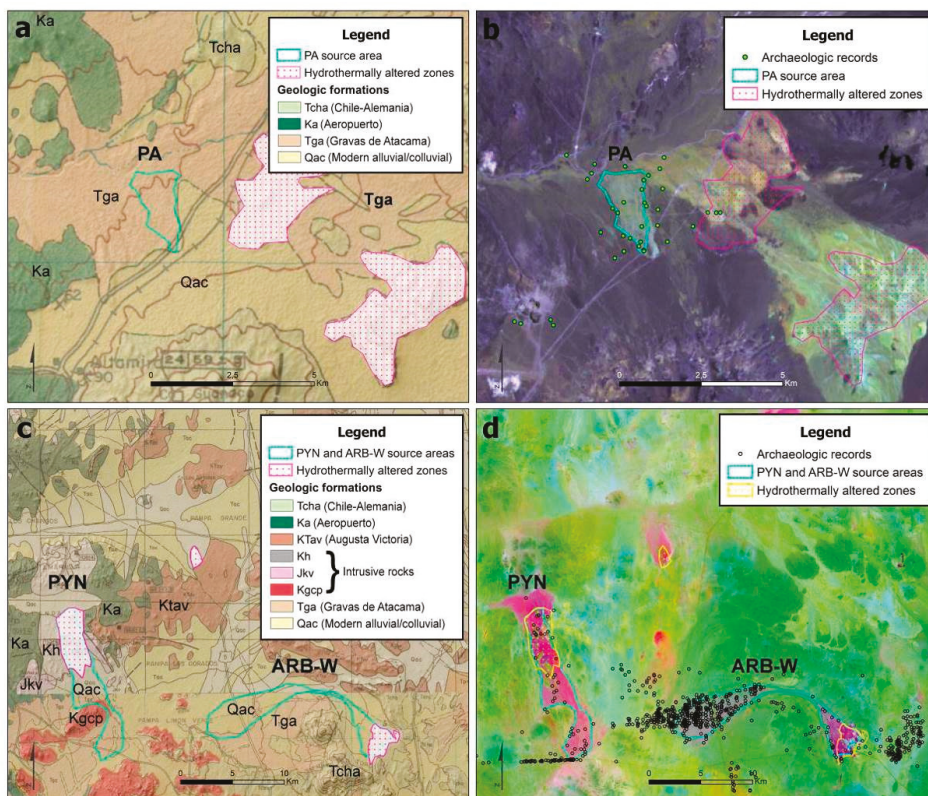


**Figure 8.** Comparison of 1:250,000 geological maps (a,c) [80,81] and processed satellite images: (b) 7-6-2 (RGB), and (d) PCs 5-4-2 (RGB), showing the geographical setting of chert source areas: (a,b) Pampa Altamira; (c,d) Pampa Yolanda Norte and Arbiado West.

A good example of the second case (previously unknown secondary deposits of chert) can be found in the sources of Pampa Yolanda Norte and Arbiado West, whose extensive secondary deposits are included in the geological charts as part of modern alluvial/colluvial deposits [80,81]. The spectral analysis of the Landsat scenes made it possible to detect both the primary and secondary deposits of these source areas, with Pampa Yolanda Norte standing out with a higher contrast (Figure 8c,d).

Another example worth mentioning is that of the Pampa Flor Chile East source areas, included in the geological charts within the Oligocene-Miocene detrital flows which constitute the Gravas de Atacama Formation [80]. The association of this chert-bearing secondary deposit to its primary source is not as direct, nor as clear, as in the previous cases. However, the analysis of the satellite images allows us not only to identify it as a secondary chert deposit, but also to infer a possible connection with the hydrothermal alteration zones registered 10 km to the northeast, in Cerro Inesperado (Figure 9a,b).

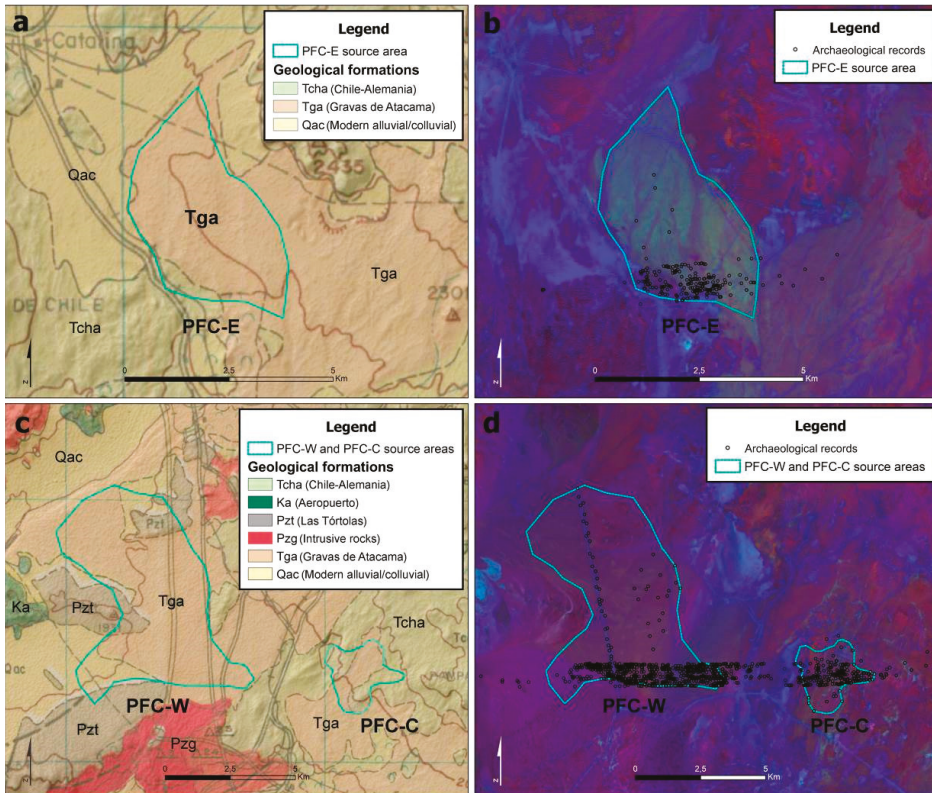


**Figure 9.** Comparison of 1:250,000 geologic map (a,c) [80] and band ratio 4/2-6/7-5 (RGB) false-color composite (c,d), showing the geographical setting of chert source areas: (a,b) Pampa Flor de Chile East; (c,d) Pampa Flor de Chile West and Pampa Flor de Chile Center.

Finally, the source areas of Pampa Flor de Chile West and Pampa Flor de Chile Centre present a more complex scenario for the interpretation of the processed satellite images. The spectral analysis only shows a very subtle sign of altered rocks in the secondary deposits of Pampa Flor de Chile West, assigned in the geological charts to the Gravas de Atacama Formation [80]. Meanwhile, in the area where the small outcrops of Pampa Flor de Chile Center are located, only traces of possible hydrothermal alteration zones are detected, which extend over land assigned to the Chile-Alemania and Gravas de Atacama formations. The low performance of remote sensing techniques to clearly map

these source areas may have to do with the brief lateral extension of the Pampa Flor de Chile Centre outcrops (averaging less than  $0.5 \times 0.3$  km) and their location on the boundary of two geological formations. Furthermore, Pampa Flor de Chile West chert deposits are presumed to be residual, meaning that the bedrock that originally housed them has been completely eroded [79]. This could explain the low spectral signal of these secondary deposits, which are thought to be relatively older and/or more heavily reworked than any others (Figure 9c,d).

The ability to map the chert carrier lithological units shown by the satellite remote sensing approach adopted in this study is derived from the presence of diagnostic spectral features of hydrous minerals in the VNIR range (0.3–2.5  $\mu\text{m}$ ), which can be used as an indicator of hydrothermal alteration zones [5,6,9]. These hydrous minerals have high reflectance in the 1.55–1.75  $\mu\text{m}$  range and high absorption at 2.08–2.35  $\mu\text{m}$ , a fact that explains the sharp contrast achieved by using the SWIR Landsat bands 6 and 7 in the RGB band ratio composite 4/2-6/7-5 (Figure 10).

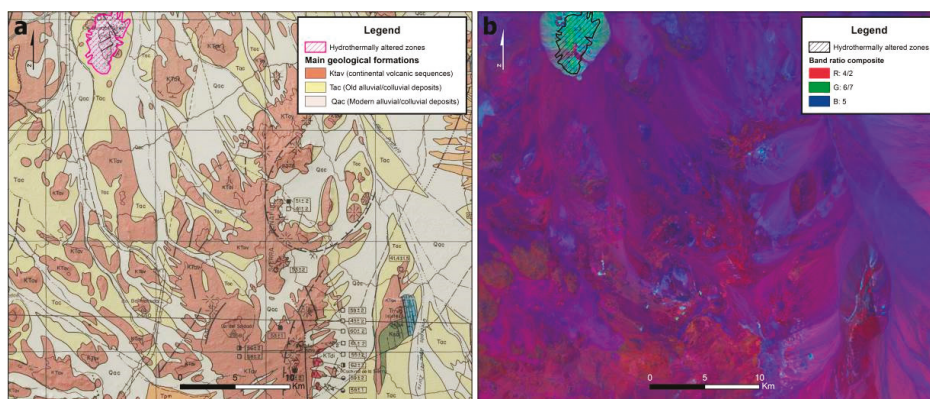


**Figure 10.** Comparison of: (a) 1:250,000 geologic map [83]; and (b) 4/2, 6/7, 5 Landsat 8 RGB band ratio composite for a section in the northeastern portion of the study area. The hydrothermally-altered zone (green area) corresponds to the Buenos Aires hill.

The near-infrared band 5 helped, in the absence of vegetation cover [97], to highlight the aforementioned contrast by showing the saline (nitrate-rich) and evaporitic soils, modern alluvial/colluvial deposits, and the more recently exposed calcareous soils of the hyper-arid Central Depression in blue. Meanwhile, the 4/2 ratio has the capacity to detect the presence of iron oxide-rich soils, which can be found in hydrothermal alteration zones [5,6,9], but which also have occurrences unrelated to them, such as in sedimentary red beds, volcanic rocks, and weathered alluvium [5].

The latter seems to be the case in our study area, where the 4/2 ratio highlights not only the hydrothermally-altered zones (due to the hydrothermal iron minerals), but also the iron oxide-rich volcanic sequences of the Central Depression (Chile-Alemania and Augusta Victoria Formations), which are shown in reddish shades in the band ratio composite. In correspondence to this, the magenta color in the processed image is presumed to be marking the erosive deposits that originated from those volcanic sequences, the mantling gravels of the Gravas de Atacama Formation, deposits that become progressively mixed with modern alluvial/colluvial detrital flows as they approach the flatlands of the Central Valley.

The inspection of the PCA eigenvector matrix supports the aforementioned results, since principal components 4 and 2, used in the PCA false color composite, account for differences between bands 6 and 7, and of these SWIR bands with bands 1 to 5, respectively (Table 1).

The capacity of Landsat VNIR bands to map prehistoric chert source areas is based on their ability to target alteration minerals which are spectrally active within this range due to the presence of water, carbonate, sulfate, and hydroxyl groups [6,9,58]. These alteration minerals can be found in the core

area of hydrothermally-altered zones, which are related to highly silicified chert outcrops in our study area. However, they can also be traced in the coarse-grained fraction represented by scattered lithic debris that remains on the surface surrounding ancient chert quarry areas [19]. Even in a low relative proportion, these freshly exposed rocks can provide a characteristic spectral signal which is useful for satellite remote sensing studies [19], making the mapping of extensive chert-bearing secondary deposits possible, as the results here presented show.

Although the visual and digital analysis of Landsat VNIR bands stands out as a great tool for the initial lithological mapping of a large and understudied area, its scope is limited to providing a broad-brush pattern of hydrothermal alteration, pointing out geological deposits of possible interest [7]. If a higher degree of geographical and geological resolution is desired, a combined use of VNIR and thermal (TIR) bands could provide a more detailed approach. This is suggested by recent studies using Landsat 8 TIR bands (10 and 11) along with VNIR bands to map alteration zones [98] and, especially, by research projects that take advantage of the SWIR and TIR bands of the ASTER sensor for this same purpose [99,100].

The greater number and narrower bandwidth of ASTER SWIR and TIR bands when compared to the ones captured by Landsat sensors offer the possibility of discriminating between minerals that are associated with phyllic, argillic, and propylitic alteration zones in the SWIR range [100,101], and to target chert and other siliceous and silicified rock types according to variations in terms of their content of SiO<sub>2</sub> and the crystal structure of silicate minerals, which are reflected in shifts in spectral features within the 7 to 14 μm TIR range [7,102]. These capacities of ASTER images allow researchers to move from mapping alteration indices (with Landsat), to the generation of mineral indices, which can be used in the study of alteration zones, differentiating them by their associated mineral assemblages and alteration intensity [9].

The procurement, processing, transport, and use of chert in the Southern Atacama configured a vast and complex lithic landscape. Multiple source areas bearing diverse chert types with overlapping macroscopic features were exploited across large extensions of land and over long time spans. To cope with this challenging scenario, the mapping of the potential source areas of the widest possible range of chert types and the study of the differential distribution of these toolstone varieties in the lithic assemblages of local base and task camps are considered critical steps [18]. In order to address this, the accumulated variation within and between the chert types present in the archaeological and geological contexts of the study area must be examined [79,103–105].

Accordingly, this project's ongoing research includes the systematic recovery and VNIR and FTIR reflective spectroscopic analysis [23] of geological chert samples collected in the six chert sources currently known for the study area, and of chert artefacts (unmodified flakes) selected from two types of locations: on the one hand, lithic assemblages of five coastal settlements with stratigraphic deposits dated between 11,500 and 1,500 cal. BP; and, on the other hand, assemblages from surface lithic scatters of six processing locations recorded during pedestrian surveys conducted by the research team in the interior desert [53,54]. This approach will enable us not only to confidently source those archaeological artefacts which fall within the range of variation documented in the six source areas already located, but also to explore the use of the detailed spectral "ground truth" data provided by the VNIR and FTIR analysis of these prehistoric chert samples in the remote detection of new potential chert sources via the digital processing of ASTER L1B images.

To address the interpretation of the Southern Atacama interior desert's archaeological record diachronically is a complex task. The very low deposition rates of the area normally prevent the burial and preservation of organic materials that could be dated with traditional methods. Thus, lithic surface assemblages are the main, and usually the only, evidence from which archaeological inferences about the human occupational history of this landscape can be grounded. This fact, together with a static conception of the paleoenvironmental conditions of this part of the Atacama Desert, has reinforced a monolithic vision of the area as a geographical barrier and or a territory exclusively used for inter-zonal mobility and the provisioning of high-quality lithic resources [54].

In order to challenge the aforementioned vision, the different paleoenvironmental and social scenarios that could have promoted or restricted more stable and/or intense human occupation in the core of the Atacama Desert, must be evaluated [54,75,76].

Consequently, the aforementioned approach via VNIR and FTIR reflective spectroscopic analysis selected artefacts of macroscopically diverse chert types from archaic coastal basecamps for provenance studies, targeting radiocarbon-dated deposits that represent the six main periods in which the prehistoric chrono-cultural sequence of the area has been analytically divided [50].

The coastal chert artefacts' spectral data are currently subject to statistical analysis in order to assess if their origin corresponds to one of the six source areas under study. Complementarily, their spectral signature will inform targeted remote sensing techniques to locate previously unknown potential chert source areas.

On the other hand, technological and morpho-functional analysis of chert artefacts recovered from the interior desert lithic assemblages will provide valuable information in terms of lithic reduction sequences and transport strategies to assess technological strategies and site function. Spectroscopic analysis of these artefacts will yield "ground truth" data to establish hypothetical connections between the coastal contexts and the interior desert's chert source areas, connections that will be further explored by the generation of GIS mobility models.

To complement the abovementioned lines of evidence, the geological and archaeological data systematically collected in the chert source areas under study, in terms of abundance, distribution, quality, and size of the "packages" available [18,106], will be incorporated. This final integration will grant the assessment of shifts in lithic procurement strategies, such as differential access to the sources, exploitation intensity, raw material selectivity, core reduction, and blank and or tool production techniques, which can be correlated with changes in the settlement pattern, subsistence, and technological organization documented along the archaic sequence for the hunter-gatherer communities of the Southern Atacama coast [45,47,50].

Preliminary results indicate that the archaeological record of the interior desert, in general terms, conforms to the lithic provisioning models proposed for Atacama [46,48]. A vast dominance of primary chert processing contexts is recorded in the Central Depression, located to a great extent in spatial correspondence with chert-bearing alluvial/colluvial deposits. Moving towards the coast, progressively advanced stages of the reduction of this raw material are found in ephemeral sites located along the dry valleys of the area, relief features used as natural corridors by local prehistoric groups. Nevertheless, evidence of other kinds of activities has also been detected in the area, such as hunting and processing gear (unifacial and bifacial lithic instruments), coastal cobbles with red pigment, and rock art in small rock panels along the Portezuelo ravine [54,107].

Although recorded in small frequency, this other evidence is added to differences in terms of architectural investment (e.g. number of circular structures) and artefactual and ecofactual content of the sites (sea shells and fish bones from the Pacific Ocean, terrestrial faunal remains, and vegetal fibers from higher Andean floors), to configure a more diverse and dynamic prehistoric setting that needs to be discussed considering social and ecological processes at a regional scale.

## 8. Conclusions

The purpose of our case study was to illustrate the capacity of a GIS-based remote sensing approach to delimit, in an informed and effective manner, the areas of higher potential interest in the analysis of lithic provisioning systems in extensive and understudied desert landscapes.

The systematization of georeferenced archaeological data contained in the "grey literature" of CRM projects and its GIS integration with basic, and easily accessible, thematic layers, can make it possible to gain a panoramic view of the archaeological record of a study area. Complementary, basic techniques of image manipulation applied to freely accessible multispectral satellite scenes of a moderate spatial and spectral resolution can contribute towards a rapid acquisition of a general

knowledge of the area in terms of the distribution of geological formations potentially carrying lithic resources of interest.

The large swath width of the Landsat sensors offers the possibility to cover vast extensions of land by handling only a small number of scenes. This greatly facilitates pre-processing and mosaicking of Landsat VNIR bands, which can be done with user-friendly tools and plugins in open source software, such as QGIS. This same software allows for the visualization and analysis of multispectral images, easily integrating satellite remote sensing data in a georeferenced database with different thematic layers. The coarse-grain pattern of lithic resource availability that this GIS-based approach provides helps to target spatially restricted areas of interest for archaeological fieldwork and, also, informs about the type and number of additional satellite images with a higher spatial and or spectral resolution that could be purchased, if the mapping of geological deposits bearing more specific types of lithic raw materials is a desired goal.

This case study illustrates the usefulness of satellite remote sensing analysis of Landsat images to complement the information available in basic geological charts with data of a finer and more appropriate spatial resolution. This can be used for the mapping of lithic resources, such as chert, which were of great relevance in the technological organization of prehistoric hunter-gatherer populations in different parts of the world.

The research strategy deployed provides new data regarding the availability and distribution of high-quality primary and secondary chert deposits in a large portion of the Southern Atacama. Such data offers a solid basis when facing the complex task of reconstructing the archaic lithic landscape of the area.

Other lines of research are currently being developed in order to access higher levels of geological and geographical resolution in the survey of the regional structure of lithic resources, and to link the data obtained in the different chert source areas studied with the large bulk of archaeological evidence gathered for the interior desert and the arctic coast of the Atacama in this, and previous, research.

Provenance studies using VNIR and FTIR reflective spectroscopic analysis will make it possible to trace the source areas of chert artefacts from archaic coastal deposits and superficial hinterland contexts. More sophisticated remote sensing techniques, applied to the higher spectral resolution ASTER satellite images, will assist in refining the lithological mapping of the study area and tracking new potential chert sources. Furthermore, GIS models will be explored to model the main mobility basins through which archaic coastal settlements were connected with the chert source areas of the Central Depression. Finally, the processing of geological and archaeological data systematically recovered from the six source areas studied up to now, will enable a more thorough evaluation of the socio-ecological factors which may have influenced differential access to the chert sources of the Southern Atacama in prehistoric times.

To sum up, the reconstruction of the lithic landscape requires the innovative integration of analytical techniques developed by different disciplines. This integration is fundamental in establishing solid grounds for the archaeological study of the material patterns of human behavior, the traces of which are accumulated in locations widely scattered in space, but recurrently occupied during extensive chronological sequences. This scenario is not exclusive to our area of study, but is transversal to different environmental and cultural contexts, as it is an inherent dimension of lithic production systems. Their study on a landscape scale and over broad time spans is a necessary task, and the methodological strategy presented here has the potential to significantly facilitate this endeavor, both in the desert lands of northern Chile and in arid and semi-arid environments of other latitudes.

**Supplementary Materials:** The following are available online at <http://www.mdpi.com/2072-4292/11/7/869/s1>, Table S1: Basic information of the datasets used in this study.

**Author Contributions:** Conceptualization, C.B. and C.P.; methodology, C.B. and Y.K.; formal analysis, C.B.; investigation, D.S., C.F., C.B., L.O., and P.A.; writing—original draft preparation, C.B. and C.P.; writing—review and editing, C.B., C.P., Y.K., D.S., C.F., L.O., and P.A.; visualization, C.B.; supervision, C.B.; project administration, D.S.; funding acquisition, D.S., P.A., L.O., C.F., and C.B.

**Funding:** This research was funded by Proyecto Fondecyt 1151203 and Beca CONICYT-PCHA/Doctorado Nacional/2015-21150953.

**Acknowledgments:** Luca Sitzia for his geological assistance; the team members involved in field work carried out in the interior desert of Taltal: Ximena Power, Sonia Parra, Ignacio Monroy, Patricio Galarce, Luca Sitzia Carlos Uribe, Valentina Hernández, Catalina Aliste, and Gabriela Marcelo; and Lautaro Núñez for his valuable guidance.

**Conflicts of Interest:** The authors declare no conflicts of interest.

## References

1. Dimitrios, A.; Agapiou, A.; Diofantos, H.; Sarris, A. Remote Sensing Applications in Archaeological Research. In *Remote Sensing—Applications*; Escalante, B., Ed.; InTech: London, UK, 2012.
2. Comer, D.C.; Harrower, M.J. *Mapping Archaeological Landscapes from Space*; Springer: New York, NY, USA, 2013.
3. Forte, M.; Campana, S. (Eds.) *Digital Methods and Remote Sensing in Archaeology. Archaeology in the Age of Sensing*; Springer: New York, NY, USA, 2016.
4. Rowan, L.C.; Wetlaufer, P.H.; Goetz, A.F.H.; Billingsley, F.C.; Stewart, J.H. *Discrimination of Rock Types and Detection of Hydrothermally Altered Areas in South-Central Nevada by the Use of Computer-Enhanced ERTS Images*; U.S. Govt. Print. Off.: Washington, DC, USA, 1974.
5. Abrams, M.J.; Brown, D.; Lepley, L.; Sadowski, R. Remote sensing for porphyry copper deposits in southern Arizona. *Econ. Geol.* **1983**, *78*, 591–604. [CrossRef]
6. Sultan, M.; Arvidson, R.E.; Sturchio, N.C.; Guinness, E.A. Lithologic mapping in arid regions with Landsat thematic mapper data: Meatiq dome, Egypt. *GSA Bull.* **1987**, *99*, 748–762. [CrossRef]
7. Sabins, F. Remote sensing for mineral exploration. *Ore Geol. Rev.* **1999**, *14*, 157–183. [CrossRef]
8. Gad, S.; Kusky, T. Lithological mapping in the Eastern Desert of Egypt, the Barramiya area, using Landsat thematic mapper (TM). *J. Afr. Earth Sci.* **2006**, *44*, 196–202. [CrossRef]
9. Van der Meer, F.D.; van der Werff, H.M.A.; van Ruitenbeek, F.J.A.; Hecker, C.A.; Bakker, W.H.; Noomen, M.F.; van der Meijde, M.; Carranza, E.J.M.; Smeth, J.B.D.; Woldai, T. Multi- and hyperspectral geologic remote sensing: A review. *Int. J. Appl. Earth Obs. Geoinf.* **2012**, *14*, 112–128. [CrossRef]
10. Goodyear, A. *A Hypothesis for the Use of Cryptocrystalline Raw Materials Among Paleo-Indian Groups of North America*; Research Manuscript Series; 1979; Available online: [https://scholarcommons.sc.edu/cgi/viewcontent.cgi?referer=https://scholar.google.com/hk/&httpsredir=1&article=1126&context=archanth\\_books](https://scholarcommons.sc.edu/cgi/viewcontent.cgi?referer=https://scholar.google.com/hk/&httpsredir=1&article=1126&context=archanth_books). (accessed on 10 April 2019).
11. Gardner, W.M. Stop me if you've Heard This one Before: The Flint Run Complex Revisited. *Archaeol. East. N. Am.* **1983**, *11*, 49–64.
12. Gould, R.A.; Saggars, S. Lithic Procurement in Central Australia: A Closer Look at Binford's Idea of Embeddedness in Archaeology. *Am. Antiq.* **1985**, *50*, 117–136. [CrossRef]
13. Bamforth, D.B. Technological Efficiency and Tool Curation. *Am. Antiq.* **1986**, *51*, 38–50. [CrossRef]
14. Andrefsky, W. Raw-material availability and the organization of technology. *Am. Antiq.* **1994**, *59*, 21–34. [CrossRef]
15. Bailey, G. Concepts, time-scales and explanations in economic prehistory. In *Economic Archaeology: Towards an Integration of Ecological and Social Approaches*; Sheridan, A., Bailey, G., Eds.; British Archaeological Reports: Oxford, UK, 1981; pp. 97–117.
16. Foley, R. A Model of Regional Archaeological Structure. *Proc. Prehist. Soc.* **1981**, *47*, 1–17. [CrossRef]
17. Dunnell, R.; Dancey, W. The siteless survey: A Regional scale data collection strategy. *Adv. Archaeol. Method Theory* **1983**, *6*, 267–287.
18. Barrientos, G.; Catella, L.; Oliva, F. The Spatial Structure of Lithic Landscapes: The Late Holocene Record of East-Central Argentina as a Case Study. *J. Archaeol. Method Theory* **2015**, *22*, 1151–1192. [CrossRef]
19. Carr, T.; Turner, M. Investigating regional lithic procurement using multi-spectral imagery and geophysical exploration. *Turner* **1996**, *3*, 109–127. [CrossRef]
20. Rosendahl, S. Lithic Procurement Strategies in Early Prehistoric Cyprus: A Predictive Model. Master's Thesis, University of Leicester, Leicester, UK, 2010.

21. Derooin, J.-P.; Téreygeol, F.; Heckes, J. Evaluation of very high to medium resolution multispectral satellite imagery for ge archaeology in arid regions—Case study from Jabali, Yemen. *J. Archaeol. Sci.* **2011**, *38*, 101–114. [[CrossRef](#)]
22. Vining, B. Reconstructions of local resource procurement networks at Cerro Baúl, Peru using multispectral ASTER satellite imagery and geospatial modeling. *J. Archaeol. Sci. Rep.* **2015**, *2*, 492–506. [[CrossRef](#)]
23. Parish, R.M. Reflectance Spectroscopy as a Chert Sourcing Method. *Archaeol. Pol.* **2016**, *54*, 115–128.
24. Thompson, V.D.; Arnold, P.J.; Pluckhahn, T.J.; Vanderwarker, A.M. Situating Remote Sensing in Anthropological Archaeology. *Archaeol. Prospect.* **2011**, *18*, 195–213. [[CrossRef](#)]
25. Banaszek, L.; Cowley, D.C.; Middleton, M. Towards National Archaeological Mapping. Assessing Source Data and Methodology—A Case Study from Scotland. *Geosciences* **2018**, *8*, 272. [[CrossRef](#)]
26. Agapiou, A.; Hadjimitsis, D.G.; Georgopoulos, A.; Sarris, A.; Alexakis, D.D. Towards an Archaeological Index: Identification of the Spectral Regions of Stress Vegetation due to Buried Archaeological Remains. In *Progress in Cultural Heritage Preservation*; Springer: Berlin/Heidelberg, Germany, 2012; pp. 129–138.
27. Cerra, D.; Agapiou, A.; Cavalli, R.M.; Sarris, A. An Objective Assessment of Hyperspectral Indicators for the Detection of Buried Archaeological Relics. *Remote Sens.* **2018**, *10*, 500. [[CrossRef](#)]
28. Fradley, M.; Sheldrick, N. Satellite imagery and heritage damage in Egypt: A response to Parcak et al. (2016). *Antiquity* **2017**, *91*, 784–792. [[CrossRef](#)]
29. Verhoeven, G. Are We There Yet? A Review and Assessment of Archaeological Passive Airborne Optical Imaging Approaches in the Light of Landscape Archaeology. *Geosciences* **2017**, *7*, 86. [[CrossRef](#)]
30. Harrower, M.; McCorrison, J.; Oches, E.A. Mapping the roots of agriculture in southern Arabia: The application of satellite remote sensing, global positioning system and geographic information system technologies. *Archaeol. Prospect.* **2002**, *9*, 35–42. [[CrossRef](#)]
31. Siart, C.; Eitel, B.; Panagiotopoulos, D. Investigation of past archaeological landscapes using remote sensing and GIS: A multi-method case study from Mount Ida, Crete. *J. Archaeol. Sci.* **2008**, *35*, 2918–2926. [[CrossRef](#)]
32. Salvi, M.C.; Salvini, R.; Cartocci, A.; Kozciak, S.; Gallotti, R.; Piperno, M. Multitemporal analysis for preservation of obsidian sources from Melka Kunture (Ethiopia): Integration of fieldwork activities, digital aerial photogrammetry and multispectral stereo-IKONOS II analysis. *J. Archaeol. Sci.* **2011**, *38*, 2017–2023. [[CrossRef](#)]
33. Parcero-Oubiña, C.; Fábrega-Álvarez, P.; Salazar, D.; Troncoso, A.; Hayashida, F.; Pino, M.; Borie, C.; Echenique, E. Ground to air and back again: Archaeological prospection to characterize prehispanic agricultural practices in the high-altitude Atacama (Chile). *Quat. Int.* **2017**, *435 Pt B*, 95–110. [[CrossRef](#)]
34. Smith, S.L.; Chambrade, M.-L. The Application of Freely-Available Satellite Imagery for Informing and Complementing Archaeological Fieldwork in the “Black Desert” of North-Eastern Jordan. *Geosciences* **2018**, *8*, 491. [[CrossRef](#)]
35. Lamenza, G. GIS and remote sensing in the archaeological research of the Argentine Chaco. *Arqueol. Iberoam.* **2015**, *27*, 40–54.
36. Dellepiane, J. Uso de imágenes satelitales para el reconocimiento de parapetos en el centro-oeste de Patagonia meridional. *Arqueología* **2018**, *24*, 259–269.
37. Bognanni, F. La teledetección aplicada al estudio del pasado a una escala inter-regional. *Rev. Española Antropol. Am.* **2010**, *40*, 77–93.
38. Binford, L.R. Organization and formation processes: Looking at curated technologies. *J. Anthropol. Res.* **1979**, *36*, 255–273. [[CrossRef](#)]
39. Kelly, R.L. The Three Sides of a Biface. *Am. Antiq.* **1988**, *53*, 717–734. [[CrossRef](#)]
40. Nelson, M. The study of technological organization. In *Archaeological Method and Theory*; Schiffer, M., Ed.; University of Arizona Press: Tucson, Arizona, 1991; pp. 57–100.
41. Roth, B.J. Mobility, Technology, and Archaic Lithic Procurement Strategies in the Tucson Basin. *Kiva* **1998**, *63*, 241–262. [[CrossRef](#)]
42. Binford, L.R. *An Archaeological Perspective*; Seminar Press: New York, NY, USA, 1972.
43. Odell, G. Economizing Behavior and the Concept of “Curation”. In *Stone Tools. Theoretical Insights into Human Prehistory*; Plenum Press: New York, NY, USA, 1996; pp. 51–80.
44. Beck, C.; Taylor, A.; Jones, G.; Fadem, C.; Cook, C.; Millward, S. Rocks are heavy: Transport costs and Paleoarchaic quarry behavior in the Great Basin. *J. Anthropol. Archaeol.* **2002**, *21*, 481–507. [[CrossRef](#)]

45. Núñez, L. Secuencia de asentamientos prehistóricos del área de Taltal. En Tres ensayos para una historia de Taltal y su zona. *Rev. Futuro* **1984**, *8*, 28–76.
46. Urrejola, C.; Orellana, M. *Explotación y Utilización de Recursos Líticos de la Zona Desértica al Interior de Tal-Tal*; Universidad de Chil: Santiago, Chile, 1999.
47. Castelleti, J. *Patrón de Asentamiento y uso de Recursos a Través de la Secuencia Ocupacional Prehispánica en la Costa de Taltal*; Universidad Católica del Norte-Universidad de Tarapacá: Arica, Chile, 2007.
48. Blanco, J.F.; de la Maza, M.; Rees, C. Cazadores Recolectores Costeros y el Aprovisionamiento de Recursos Líticos. Perspectivas Interpretativas de los Eventos de Talla en el Desierto Absoluto. *Rev. Werkén* **2010**, *13*, 45–68.
49. Pimentel, G.; Rees, C.; De Souza, P.; Arancibia, L. Viajeros costeros y caravaneros. Dos estrategias de movilidad en el Período Formativo del desierto de Atacama, Chile. In *En Ruta. Arqueología, Historia y Etnografía del tráfico Sur Andino*; Núñez, L., Nielsen, A., Eds.; Encuentro Grupo Editor: Córdoba, Argentina, 2011; pp. 43–81.
50. Salazar, D.; Figueroa, V.; Andrade, P.; Salinas, H.; Olguín, L.; Power, X.; Rebolledo, S.; Parra, S.; Orellana, H.; Urrea, J. Cronología y organización económica de las poblaciones arcaicas de la costa de Taltal. *Estud. Atacameños* **2015**, *50*, 7–46. [[CrossRef](#)]
51. Power, X.; Arenas, C.; Monroy, I.; Traverso, F.; Galarce, P.; Parra, S. *Informe Lítica Proyecto Fondecyt 1151203*, Unpublished manuscript, Santiago, Chile. 2019.
52. Ballester, B.; Crisóstomo, M. Percutores de la Pampa del Desierto de Atacama (Norte de Chile): Tecnología, Huellas de Uso, Decoración y Talladores. *Chungara* **2017**, *49*, 175–192. [[CrossRef](#)]
53. Borie, C.; Power, X.; Parra, S.; Salinas, H.; Rostan, P.; Galarce, P.; Peña, I.; Traverso, F. Tras la Huella del Sílice Pampino. Nuevas Metodologías para el Rastreo de las Áreas Fuente de Aprovisionamiento lítico en Taltal. *Estud. Atacameños* **2017**, *56*, 103–131. [[CrossRef](#)]
54. Borie, C.; Salazar, D.; Power, X.; Figueroa, M.J.; Orellana, H.; Parra, S.; Arenas, C.; Traverso, F.; Monroy, I. Cazadores-Recolectores Marítimos en la Pampa Desértica de Taltal. Conocimientos, Recursos, Prácticas Sociales y Territorialización. In *Estudios de Arqueología, Historia, Filosofía y Ciencias Sociales. En Homenaje a Mario Orellana Rodríguez (60 Años de Vida Académica y Científica)*; Orellana, F., Ed.; Ediciones del Desierto: San Pedro de Atacama, Antofagasta, Chile, 2017; pp. 205–242.
55. Dunai, T.J.; González López, G.A.; Juez-Larré, J. Oligocene–Miocene Age of Aridity in the Atacama Desert Revealed by Exposure Dating of Erosion-Sensitive Landforms. *Geology* **2005**, *33*, 321–324. [[CrossRef](#)]
56. Houston, J. Variability of Precipitation in the Atacama Desert: Its Causes and Hydrological Impact. *Int. J. Climatol.* **2006**, *26*, 2181–2198. [[CrossRef](#)]
57. Placzek, C.; Quade, J.; Betancourt, J.L.; Patchett, P.J.; Rech, J.A.; Latorre, C.; Matmon, A.; Holmgren, C.; English, N.B. Climate in the dry central andes over geologic, millennial, and interannual timescales. *Ann. Mo. Bot. Gard.* **2009**, *96*, 386–397. [[CrossRef](#)]
58. Amundson, R.; Dietrich, W.; Bellugi, D.; Ewing, S.; Nishiizumi, K.; Chong, G.; Owen, J.; Finkel, R.; Heimsath, A.; Stewart, B.; et al. Geomorphologic Evidence for the Late Pliocene Onset of Hyperaridity in the Atacama Desert. *Gsa Bull.* **2012**, *124*, 1048–1070. [[CrossRef](#)]
59. Chuvieco, E. *Teledetección Ambiental*; Ariel: Barcelona, Spain, 2006.
60. Hunt, G. Spectral Signatures of Particulate Minerals in the Visible and Near Infrared. *Geophysics* **1977**, *42*, 501–513. [[CrossRef](#)]
61. Clark, R.; King, T.; Klejwa, M.; Swayze, G.; Vergo, N. High spectral resolution reflectance spectroscopy of minerals. *J. Geophys. Res.* **1990**, *95*, 12653–12680. [[CrossRef](#)]
62. Carranza, E.J.M.; Hale, M. Mineral imaging with Landsat Thematic Mapper data for hydrothermal alteration mapping in heavily vegetated terrane. *Int. J. Remote Sens.* **2002**, *23*, 4827–4852. [[CrossRef](#)]
63. Cattáneo, R.; Di Lello, C.; Gómez, J.C. Cuantificación y análisis de la distribución de rocas útiles para la manufactura de instrumentos a través del uso de Sistemas de Información Geográfica (SIG) en el área de Piedra Museo, Santa Cruz, Argentina. In *El uso de Sistemas de Información Geográfica en Arqueología Sudamericana*; Figuerero, M.J., Izeta, A., Eds.; Archaeopress: Oxford, UK, 2013; pp. 43–60.
64. Goudie, A.S. *Arid and Semi-Arid Geomorphology*; Cambridge University Press: New York, NY, USA, 2013.
65. Ortlieb, L.; Vargas, G.; Saliéje, J. Marine radiocarbon reservoir effect along the northern Chile–southern Peru coast (14–24°S) throughout the Holocene. *Quat. Res.* **2011**, *75*, 91–103. [[CrossRef](#)]

66. Marquet, P.A.; Bozinovic, F.; Bradshaw, G.A.; Cornelius, C.; González, H.; Gutiérrez, J.R.; Hajek, E.R.; Lagos, J.A.; López-Cortés, F.; Núñez, L.; et al. Los Ecosistemas del Desierto de Atacama y Área Andina Adyacente en el Norte de Chile. *Rev. Chil. Hist. Nat.* **1998**, *71*, 593–617.
67. Vargas, G.; Rutllant, J.; Ortlieb, L. ENSO Tropical–Extratropical Climate Teleconnections and Mechanisms for Holocene Debris Flows Along the Hyperarid Coast of Western South America (17°–24°S). *Earth Planet. Sci. Lett.* **2006**, *249*, 467–483. [[CrossRef](#)]
68. Herrera, C.; Custodio, E. Origin of waters from small springs located at the northern coast of Chile, in the vicinity of Antofagasta. *Andean Geol.* **2014**, *41*, 314–341.
69. Placzek, C.; Matmon, A.; Granger, D.; Quade, J.; Niedermann, S. Evidence for active landscape evolution in the hyperarid Atacama from multiple terrestrial cosmogenic nuclides. *Earth Planet. Sci. Lett.* **2010**, *295*, 12–20. [[CrossRef](#)]
70. Gajardo, R. *La Vegetación Natural de Chile: Clasificación y Distribución Geográfica*; Editorial Universitaria: Santiago, Chile, 1994.
71. Clarke, J.D.A. Antiquity of Aridity in the Chilean Atacama Desert. *Geomorphology* **2006**, *73*, 101–114. [[CrossRef](#)]
72. Quade, J.; Rech, J.A.; Betancourt, J.; Latorre, C.; Quade, B.; Rylander, K.A.; Fisher, T. Paleowetlands and Regional Climate Change in the Central Atacama Desert, Northern Chile. *Quat. Res.* **2008**, *69*, 343–360. [[CrossRef](#)]
73. Gayó, E.M.; Latorre, C.; Jordán, T.; Nester, P.; Estay, S.; Ojeda, C.; Santoro, C. Late Quaternary Hydrological and Ecological Changes in the Hyperarid Core of the Northern Atacama Desert (~ 21°S). *Earth-Sci. Rev.* **2012**, *113*, 120–140.
74. Sáez, A.; Godfrey, L.V.; Herrera, C.; Chong, G.; Pueyo, J.J. Timing of Wet Episodes in Atacama Desert over the Last 15 ka. The Groundwater Discharge Deposits (GWD) from Domeyko Range at 25°S. *Quat. Sci. Rev.* **2016**, *145*, 82–93. [[CrossRef](#)]
75. Santoro, C.M.; Capriles, J.M.; Gayo, E.M.; de Porras, M.E.; Maldonado, A.; Standen, V.G.; Latorre, C.; Castro, V.; Angelo, D.; McRostie, V.; et al. Continuities and Discontinuities in the Socio-Environmental Systems of the Atacama Desert During the Last 13,000 years. *J. Anthropol. Archaeol.* **2017**, *46*, 28–39. [[CrossRef](#)]
76. Pfeiffer, M.; Latorre, C.; Santoro, C.M.; Gayo, E.M.; Rojas, R.; Carrevedo, M.L.; McRostie, V.B.; Finstad, K.M.; Heimsath, A.; Jungers, M.C.; et al. Chronology, Stratigraphy and Hydrological Modelling of Extensive Wetlands and Paleolakes in the Hyperarid Core of the Atacama Desert During the Late Quaternary. *Quat. Sci. Rev.* **2018**, *197*, 224–245. [[CrossRef](#)]
77. Llagostera, A. 9,700 Years of Maritime Subsistence on the Pacific: An Analysis by Means of Bioindicators in the North of Chile. *Am. Antiq.* **1979**, *44*, 309–324. [[CrossRef](#)]
78. Ballester, B.; Gallardo, F. Prehistoric and historic networks on the Atacama Desert coast (northern Chile). *Antiquity* **2011**, *85*, 875–889. [[CrossRef](#)]
79. Luedtke, B.E. *An Archaeologist's Guide to Chert and Flint*; Institute of Archaeology, University of California: Los Angeles, CA, USA, 1992.
80. Naranjo, J.; Puig, A. *Carta Geológica de Chile escala 1:250.000. Hojas Taltal y Chañaral N°62 y 63*; Servicio Nacional de Geología y Minería: Santiago, Chile, 1984.
81. Marinovic, N.; Smoje, I.; Makasev, V.; Hervé, M.; Mpodozis, C. *Carta Geológica de Chile Escala 1:250.000. Hoja Aguas Blancas, Región de Antofagasta*; Servicio Nacional de Geología y Minería: Santiago, Chile, 1995.
82. Sernageomin. *Mapa Geológico de Chile: Versión Digital*; Servicio Nacional de Geología y Minería: Santiago, Chile, 2003.
83. Rech, J.A.; Latorre, C. Climatic Controls on Fluvial Cut-and-Fill Cycles in Drainages with in-Stream Wetlands in the Central Andes. In Proceedings of the American Geophysical Union, Fall Meeting, San Francisco, CA, USA, 13–17 December 2004. Abstract-H51A-1103.
84. Kober, F.; Ivy-Ochs, S.D.; Schlunegger, F.; Baur, H.; Kubik, P.W.; Wieler, R. Denudation Rates and a Topography-Driven Rainfall Threshold in Northern Chile: Multiple Cosmogenic Nuclide Data and Sediment Yield Budgets. *Geomorphology* **2007**, *83*, 97–120. [[CrossRef](#)]
85. Xiong, Y.; Shuhab, K.; Khalid, M.; Sisson, V. Lithological mapping of Bela ophiolite with remote-sensing data: International. *J. Remote Sens.* **2011**, *32*, 4641–4658. [[CrossRef](#)]
86. Pour, A.B.; Hashim, M. Hydrothermal alteration mapping from Landsat-8 data, Sar Cheshmeh copper mining district, south-eastern Islamic Republic of Iran. *J. Taibah Univ. Sci.* **2015**, *9*, 155–166. [[CrossRef](#)]

87. Abrams, M.J.; Ashley, R.P.; Rowan, L.C.; Goetz, A.F.H.; Kahle, A.B. Mapping of hydrothermal alteration in the Cuprite mining district, Nevada, using aircraft scanner images for the spectral region 0.46 to 2.36 $\mu$ m. *Geology* **1977**, *5*, 713–718. [[CrossRef](#)]
88. Gad, S.; Kusky, T. ASTER spectral ratioing for lithological mapping in the Arabian–Nubian shield, the Neoproterozoic Wadi Kid area, Sinai, Egypt. *Gondwana Res.* **2007**, *11*, 326–335. [[CrossRef](#)]
89. Lillesand, T.; Kiefer, R.; Chipman, J. *Remote Sensing and Image Interpretation*, 6th ed.; John Wiley & Sons Ltd.: Hoboken, NJ, USA, 2008; p. 736.
90. Catella, L.; Barrientos, G.; Oliva, F. La identificación del uso de fuentes secundarias de materiales líticos asistida por SIG: El Arroyo Chasicó (Argentina) como caso de estudio. *Estud. Geol.* **2017**, *73*, 1–20. [[CrossRef](#)]
91. Magnin, L.A. Hunter–gatherer provisioning strategies in a landscape with abundant lithic resources (La Primavera, Santa Cruz, Argentina). *Quat. Int.* **2015**, *375*, 55–71. [[CrossRef](#)]
92. Skarbun, F. Estructura y explotación de los recursos líticos en el sector Meridional de la Meseta Central de Santa Cruz, Argentina. *Magallania (Punta Arenas)* **2015**, *43*, 191–209. [[CrossRef](#)]
93. Clarkson, C.; Bellas, A. Mapping stone: Using GIS spatial modelling to predict lithic source zones. *J. Archaeol. Sci.* **2014**, *46*, 324–333. [[CrossRef](#)]
94. Duke, C.; Steele, J. Geology and lithic procurement in Upper Palaeolithic Europe: A weights-of-evidence based GIS model of lithic resource potential. *J. Archaeol. Sci.* **2010**, *37*, 813–824. [[CrossRef](#)]
95. Clarke, K.D. *Geología, Petrografía y Geoquímica de las Rocas Intrusivas de la Cordillera de la Costa entre Paposo y Taltal. Memoria para Optar al Título de Geólogo*; Facultad de Ingeniería y Ciencias Geológicas, Departamento de Ciencias Geológicas, Universidad Católica del Norte: Antofagasta, Chile, 1998.
96. Galarce, P.; Santander, G. Contextos líticos de asentamientos arcaicos en la costa de Taltal (II Región, Chile). *Estud. Atacameños* **2013**, *46*, 5–26. [[CrossRef](#)]
97. Warner, T.A.; Campagna, D.J. *Remote Sensing with IDRISI Taiga: A Beginner's Guide*; Geocarto International Centre: Hong Kong, China, 2009.
98. Ali, A.; Pour, A.B. Lithological mapping and hydrothermal alteration using Landsat 8 data: A case study in ariab mining district, red sea hills, Sudan. *Int. J. Basic Appl. Sci.* **2014**, *3*, 199–208. [[CrossRef](#)]
99. Rowan, L.C.; Schmidt, R.G.; Mars, J.C. Distribution of hydrothermally altered rocks in the Reko Diq, Pakistan mineralized area based on spectral analysis of ASTER data. *Remote Sens. Environ.* **2006**, *104*, 74–87. [[CrossRef](#)]
100. Pour, A.B.; Hashim, M. The application of ASTER remote sensing data to porphyry copper and epithermal gold deposits. *Ore Geol. Rev.* **2012**, *44*, 1–9. [[CrossRef](#)]
101. Mars, J.C.; Rowan, L.C. Spectral assessment of new ASTER SWIR surface reflectance data products for spectroscopic mapping of rocks and minerals. *Remote Sens. Environ.* **2010**, *114*, 2011–2025. [[CrossRef](#)]
102. Watanabe, H.; Matsuo, K. Rock type classification by multi-band TIR of ASTER. *Geosci. J.* **2003**, *7*, 347–358. [[CrossRef](#)]
103. Shackley, M.S. Archaeological Petrology and the Archaeometry of Lithic Materials. *Archaeometry* **2008**, *50*, 194–215. [[CrossRef](#)]
104. Andrefsky, W. The Analysis of Stone Tool Procurement, Production, and Maintenance. *J. Archaeol. Res.* **2009**, *17*, 65–103. [[CrossRef](#)]
105. Parish, R.M. The Application of Visible/Near-Infrared Reflectance (VNIR) Spectroscopy to Chert: A Case Study from the Dover Quarry Sites, Tennessee. *Geoarchaeology* **2011**, *26*, 420–439. [[CrossRef](#)]
106. Wilson, L. Understanding prehistoric lithic raw material selection: Application of a gravity model. *J. Archaeol. Method Theory* **2007**, *14*, 388–411. [[CrossRef](#)]
107. Monroy, I.; Borie, C.; Troncoso, A.; Power, X.; Parra, S.; Galarce, P.; Pino, M. Navegantes del desierto. Un nuevo sitio con arte rupestre estilo El Médano en la Depresión Intermedia de Taltal. *Taltalia* **2016**, 27–48. [[CrossRef](#)]







Article

# Power and/or Penury of Visualizations: Some Thoughts on Remote Sensing Data and Products in Archaeology

Włodzimierz Rączkowski

Faculty of Archaeology, Adam Mickiewicz University in Poznań, 61-614 Poznań, Poland; wlodekra@amu.edu.pl; Tel.: +48-61-829-1421

Received: 27 July 2020; Accepted: 11 September 2020; Published: 15 September 2020

**Abstract:** Airborne and spaceborne remote sensing in archaeology generates at least two important issues for discussion: technology and visualization. Technology seems to open new cognitive perspectives for archaeology and keeps researchers increasingly fascinated in its capabilities (archaeological science being a case in point). Acquired data, especially via remote sensing methods, can be studied after processing and visualizing. The paper raises several issues related to the new cognitive situation of archaeologists facing the development of new technologies within remote sensing methods. These issues are discussed from ontological, epistemological, and discursive perspectives, supporting an exploration of the role of technology and visualization. The ontological perspective places the visualization of remote sensing data in the context of understanding Virtual Reality and Jean Baudrillard's simulacra. The epistemological perspective generates questions related to visualization as *mimesis*, the issue of cultural neutrality, and the use of sophisticated classifications and analytical techniques. The level of discursiveness of visualization includes categories such as persuasion, standardization, and aesthetics. This discussion is framed in relation to Martin Heidegger's understanding of technology and a dichotomy of naturalism versus antinaturalism.

**Keywords:** Martin Heidegger; technology; visualization; mimesis; remote sensing archaeology; cultural context

---

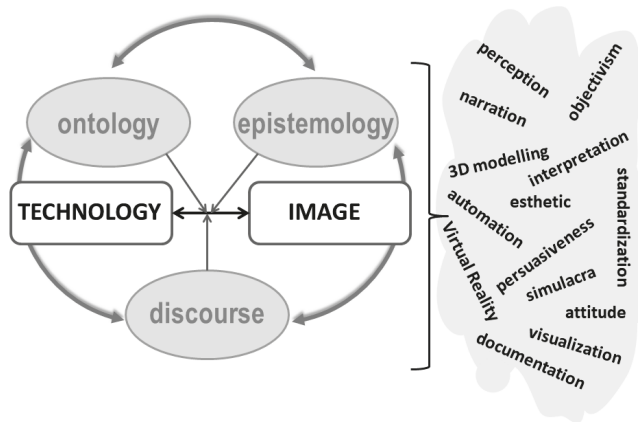
## 1. Introduction

Image is one of the most basic attributes of archaeology. Imagery has long been present in archaeology as a way of documenting/confirming the presence of relics of the past, thus serving to communicate about the past and creating visions of the past (e.g., [1]). Over time imagery became part of archaeological analysis. The emergence of photography in the mid-19th century created a new cognitive situation in the development of the understanding of the world. It was photography that had the ability to reproduce the world [2]. Photography and other techniques of visualization of data and imagery of the past have slowly entered archaeology, and in recent years this process has accelerated rapidly. Dave Cowley [3] (p. 18) noted that the application of new technologies in archaeology involves “[...] often expressions of shifting fashions in archaeological practice. There is thus a danger that changing fashion, rather than intellectual rigor, will heavily influence the application of particular methods, often with little of understanding of underlying principles.” I fully agree with this view because I have witnessed the phenomenon of almost universal introduction of new technologies (especially remote sensing methods) in archaeology without sufficient critical reflection. Cowley [3] (p. 18) constructs his deliberations within the framework of dichotomies: “believers vs. non-believers,” “traditional vs. progressive,” or “old vs. new.” I would like to approach the problem differently, without deciding what is better or worse, by focusing on the cognitive aspects associated with the introduction of new digital technologies to archaeology. The main axis of the

narrative that determines the place of technology in the cognitive process will be the dichotomy of naturalism and antinaturalism. During the past several decades in archaeological uses of photography (and other forms of imaging) several processes have significantly changed the cognitive position of different forms of visualizations (understood here as photographs, images, 3D models, animations etc.). These processes are: (1) opening archaeology to philosophical reflection and the role of archaeological theory (processual archaeology, Marxist archaeology, post-processual archaeologies, symmetrical archaeology etc.); (2) *linguistic turn* (understood as the shift in philosophy emphasizing the importance of the structure and usage of language in human meaning-making and communication) in relation to photography (Roland Barthes, Susan Sontag) and, consequently, the way the image is considered as text; and (3) technological changes (especially the rapid development of remote sensing methods) regarding data acquisition, analysis, and visualization.

The relationship between image/visualization and technology is crucial in these processes. It is technology that has significantly changed the ability to generate images related to the study of the past (cf. [4]). The question arises to what extent these changes have affected the understanding of the place and the cognitive status of image/visualization in archaeological research. How can the visualization of remote sensing data be treated in the context of contemporary philosophy and how does this translate into the cognitive process in archeology?

The technology–image relationship (in the context of the naturalism vs. antinaturalism dichotomy) is key in the analysis of these problems. I would like to look at this from ontological, epistemological, and discursive perspectives (Figure 1) using the example of remote sensing data application in archaeological research. On the one hand, these perspectives generate certain specific cognitive categories, and, on the other hand, permeate each other, which means that in the narrative below repetitions, shortcuts, or leaps of thought may appear.



**Figure 1.** The complexity of research structure and categories in the study of technology–image/ visualization relations.

## 2. Starting Point: Identification of Research Practice Area

Contemporary archeology is a broad spectrum of research practices referring on the one hand to the tradition of culture-historical archaeology, and on the other hand, reflecting trends in contemporary philosophy and social theories (e.g., ANT, agency, symmetrical archaeology etc.) [5,6]. Not all of these trends use remote sensing methods equally. The most common application is documenting traces of the past through various forms of visualization. The aim is to accurately describe the relics of the past so that they can be further examined. Visualizations created by remote sensing methods may also create the impression of an objective product. In a situation where documentation has a pictorial character, the principle of “what you see is what you get,” i.e., objectivity and “superculturality” of

seeing, applies. Such thinking and practice are part of Plato’s concept of *mimesis*, i.e., the belief that a perfect reproduction of a prototype is not a representation, but is identical with it, i.e., with the original (Figure 2). Contemporary data acquisition techniques (e.g., digital photography, airborne laser scanning (ALS), satellite imagery) enhance this view. It is therefore not surprising that visualizations meeting the criteria of photogrammetry or 3D models are treated as identical with the depicted objects, features, or landscapes.

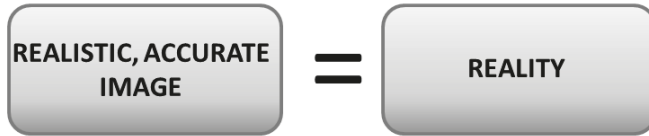


Figure 2. Plato’s concept of *mimesis*.

Remote sensing technologies were developed within formal sciences and were adopted by archaeologists to better and more effectively study the past. The use of data visualizations obtained with remote sensing methods as objective empirical data situates this approach in archaeologies that can be classified as naturalism. The philosophical turn of the mid-20th century questioned the possibility of objective cognition and thus the dominance of the existing model of formal and natural sciences. Science has been incorporated into the area of culture, and scientific activities are conditioned by the cultural context. Therefore, all research becomes culturally constituted, and the image of the world constructed by research gains an historical and discursive dimension. Thus, the division between culture and nature was removed, and natural sciences lost their ability to present the world objectively [7]. This is a certain simplification that I accept in this text, because the problem of the relationship between nature and culture has been approached differently within the framework of contemporary philosophy (e.g., [8–10]). However, it is from this perspective that I will examine archaeological research practices using remote sensing methods and the visualizations they generate, and try to consider the issues outlined above.

In the context of *mimesis*, the space between reality and its realistic image has been filled in contemporary philosophy with the presence of language, culture, and individual experience. Additionally, the author of the representation and its recipient (Figure 3) have also appeared in this space. The whole relation has been fundamentally changed, and even the existing ontological and epistemological sense of representation has been challenged. This creates a new cognitive perspective based on inspirations developed by philosophy after the *linguistic turn* in which both the language and cultural context of actors play a crucial role, fundamentally different from the previous one (naturalism).

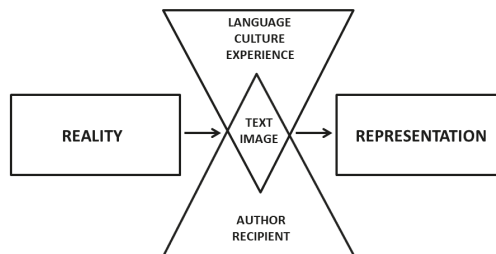


Figure 3. Diagram of the relationships between reality and its representation, accounting for the complexity of the space between them, inspired by postmodern philosophy.

These phenomena are also reflected in broadly understood aerial archaeology. The objectivity of aerial photography in the study of the past has been questioned and, as a result, there have been studies of the interaction of aerial photography (and its interpretation) with the cultural context [11–16]. This is particularly evident in the discussion of the cognitive status of aerial reconnaissance and taking oblique aerial photographs. The cultural entanglement of the aerial photographer and the randomness of the recorded relics of the past are the part of this discussion. This observed “bias” (understood as the impact of existing knowledge, cultural prejudice, and methods, for example) was challenged to become as limited as possible in the research procedure. To some extent, it is the new technological developments that are supposed to minimize the “bias” and increase the objectivity of the research approach [17]. Technology is meant to reduce subjectivity and restore, at least to some degree, the possibility of objective knowledge (description) of reality.

### 3. Technology and Data Visualization: An Ontological Perspective

The question of technology is important in view of the considerations discussed above because it is with the help of modern technology that we acquire, process, analyze and share data. It is also commonly believed that the more technologies we use, the more objectivity in the research procedure (including data acquisition, analysis and visualization) there is. Therefore, when considering the issues of technology and visualization as its result, we must ask ourselves two questions: What is technology? and What is visualization? Both questions have significant ontological foundations.

As far as modern philosophers are concerned, it was Martin Heidegger, among others, who dealt with the place of technology in the modern world. He proposed a specific approach to technology and an understanding of the risks it entails [18,19]. For Heidegger, the essence of technology is extremely complex and its technical dimension is not the most important. Technology in his view is both “a means to an end” (instrumental definition) and “a human activity” (anthropological definition). These two approaches are closely related, intertwined and inseparable. Technology allows beings to actualize and thus leads to the revealing of reality. Therefore, it is connected with the way the truth is revealed, not only with the instrumental attainment of specific results. This understanding of technology also indicates its role in cognition. Revealing the truth in this sense is reaching the truth by a being in its being-in-the-world, and not just discovery/ recognizing the presence of something by a being (as it is often understood in traditional archaeology and reduced to “identification” of relics on an aerial photograph or in other remote sensing data). And this element is particularly important: revealing the truth with the use of technology belongs to a being, it allows it to discover the truth as it understands it. Consequently, Heidegger views technology and its role in cognition as a cultural activity. Thus, technology is not culturally neutral, although it is often perceived and treated as such (this is how naturalism puts it, and in archaeology it is particularly strongly emphasized by processual archaeology and the so-called archaeological science). For Heidegger, this culturally neutral treatment of technology is the greatest threat because it leads to the concealment of the truth. Following this thought, Marcelo Vieta and Laureano Ralon propose the term “being-in-the-technologically-mediated-world” [20] (p. 38). This emphasizes the idea that the world, things, and truth are revealed to human beings when “encountered, manipulated, or generally engaged with.” Technology in these relationships becomes a “medium” that allows transmission and transforming human experience and activities [21] (pp. 56–61), [20] (p. 43). This perspective assigns a sense to the image production technology similar to the role of language in culture as it is understood after the *linguistic turn*, and it remains in contradiction with positivist/traditional thinking.

The way the image/visualization is presented in contemporary philosophy has also changed fundamentally. While in the 19th century images were still treated as representations of reality (e.g., still-life paintings), the introduction of photography exempted art from presenting the world as it is. This role was adopted by photography, and this new way of thinking about it became established. The technique of photography opened up new cognitive possibilities (e.g., the structure of movement imperceptible to the naked eye and identifiable in slow motion [22], and its neutrality was in no

way questioned (cf. [23] (pp. 27–29)). Critical reflection on photography and the role of language in its cultural presence (Roland Barthes, John Szarkowski, Susan Sontag) and other forms of visual representation led to the emergence of the terms *pictorial turn* (William J.T. Mitchell) or *iconic turn* (Gottfried Boehm) (e.g., [24,25]). This initiated the Visual Studies trend, which is a critical reaction to views emphasizing the dominance of language in culture and the study of reality as a consequence of the *linguistic turn* (e.g., [26]). In Visual Studies, culture is based on images as a primary and basic form of perception and understanding of the world. These images can be diverse and include optical or imaginative forms that present the world and its aspects in forms ranging from traditional paintings to any contemporary visualizations (including computer-generated imagery). Thus, to a large extent, these are now products of technology applications (from digital photography to computer visualizations), and their culture-forming role also applies to science (cf. [1]). Images as cultural constructs co-create reality. Therefore, the study of images and their cultural dimension should also consider the relationship between “the seen” and “the seer” [27] (references to Ferdinand de Saussure and his studies of language, and Barthes and his studies of photography).

The use of modern technology (mainly computer technology) in generating visualizations of data (including remote sensing data) related to objects to which we attribute a connection with the past, raises the question of what they are. I think we can treat them as images, i.e., created visions of objects, landscapes, and even events related to the past. If so then they constitute cultural entities, which we can put into textual categories and apply to them discourse terms introduced by Barthes with regard to photography [11,28,29]. However, such visualizations created by information technology can contain both real and fictional elements. And this significantly changes their cognitive status by opening up the possibilities of treating them as inscribed in the understanding of Virtual Reality (VR) [30–32] and by adding philosophical concepts formulated by Jean Baudrillard [33] to the cultural discourse.

VR is a technology that allows the user to create interactions with a computer-generated world regardless of its relationship with reality or imagination. Since the advent of VR technology in the 1980s, many different definitions have been formulated. Some emphasize technological aspects (computers, software, peripheral devices), while others focus on psychological issues (sensual experience, perception) (e.g., [30,34]). Among the characteristics of VR, in the ontological perspective the most important seem to be simulation, interaction, artificiality, and immersion (e.g., [30,31]). Simulation means a form of representing reality, but it cannot be treated as its copy. Interaction allows us to enter into specific relationships with virtual objects not always possible in the real world. Artificiality indicates that VR is a human creation, and thus it has nothing to do with natural processes. Finally, immersion means using solutions that raise the possibility of “sensual immersion” in this generated world.

The discussion of VR ontology is therefore an attempt to answer the question about the existence of objects in VR and their relation to reality (see also [35]). Features such as simulation and artificiality indicate that objects in VR are a form of emulation, imitation, and projection of what exists in reality. There is no doubt that such simulations are far from Plato’s *mimesis*: “One must remember what the object in the virtual world actually is: nothing more than a bunch of binary numbers stored in a computer memory” ([36]; see also [37]). So the reproduction is never complete (i.e., the same as the original). It is limited to certain physical elements, because in VR it is not possible to visualize all their complex properties (cf. [38,39]).

In the case of archaeology, visualizations that are part of a VR can have at least three characteristics: (1) They are “models” of real existing objects that have been assigned a link to the past, e.g., an axe, a fibula, an amphora; (2) they are images of space/landscape in which there are elements considered to have been created by humans in the past (e.g., Stonehenge area, Giza pyramid complex—see [40–42]); and (3) they are situations and fictional phenomena (e.g., images of events, people’s economic and social activities, or religious rituals) (e.g., [43] (pp. 94–96)). If (non-)real objects are simulations, forms of projection or imagining reality, this invites the conclusion that they are, in consequence, products of the

human mind. This means that they are not only the products of information technology, but also—and perhaps even, in particular—of human reflection on the world [30] (pp. 148–149).

Considering the reflection that objects in VR imitate or simulate real objects, it becomes obvious that references to Baudrillard's proposal [33] should be made. According to him, simulation means pretending, illusion, creating a world of imagination, and the products of this process, i.e., simulacra, pretend to be objects from reality, which are widely/commonly treated as real objects from the past. This means that visualization imitates objects but do not present them. Therefore, one can probably formulate a conclusion that visualizations of data (including remote sensing data) in archaeology constitute an imagined, modelled world, materialized by means of computer technologies. In this sequence of technological connections there are devices allowing for data acquisition (products of the human mind), computer software that processes them (a programmer's product), and processors (also constructed by humans). Visualizations may be revised, changed, or modified at each stage of this process and in consequence even create new visualizations of the same real objects (cf. [36]). From this perspective, visualizations of any form and any data are not ontologically significantly different from traditional photography, especially if we agree with Szarkowski's view that: "Photography is a system of visual editing. At bottom, it is a matter of surrounding with a frame a portion of one's cone of vision, while standing in the right place at the right time. Like chess, or writing, it is a matter of choosing from among given possibilities, but in the case of photography the number of possibilities is not finite but infinite" (quotation after [29] (p. 150)).

#### 4. Visualized Data and Cognitive Processes (Epistemological Perspective)

If ontological reflection gives us an idea of what visualizations in archaeology are (e.g., as a result of remote sensing methods application), then we should consider the connection between visualized data and the cognitive process. Again, recalling Heidegger [19], one may ask the following question: Does contemporary technology allow the world to reveal itself as it is? In terms of archaeology this question may be: Does technology allow the past to be revealed? In relation to ontological findings, the following question can be asked: What cognitive function does a simulation model/image/visualization play in the process of building knowledge about the past? Heidegger emphasized that technology was oriented toward revealing the truth as offered by natural sciences [44]. Thus, the reference to the role of technology in the cognitive processes in archaeology places the researcher in the naturalistic trend [45]. In the dominant archaeological research practices (cultural-historical archaeology, processual archaeology) there is no cognitive dissonance here, because they fit into this trend. This has far-reaching consequences in terms of formulating research questions and methods of solving problems. One of the traits of thinking in the spirit of naturalism is the recognition of the neutrality of the aforementioned technology (e.g., [46]). This means that in the process of revealing, it is possible to obtain and analyze data objectively, which only at the final stage of the research process is subjected to evaluation/interpretation (and even very often confined only to an objective description and presentation of results). In this understanding, technologies that allow visualization of data obtained in a culturally neutral way lead to learning about the past world. In this cognitive perspective, such an image/visualization, being a faithful representation of reality (e.g., documentation) in the Platonic understanding of *mimesis*, becomes the basis for building knowledge about the past (Figure 2), providing useful knowledge about the past. Thus, in this approach, the image/visualization constitutes an objective, empirical record allowing the formulation of valid conclusions and judgments about the past.

An anti-naturalistic perspective significantly changes the cognitive status of image/visualization. Barthes's reflections on photography questioned this way of thinking about images in whose creation an important role was played by technology (cf. also later reflections by Bruno Latour [47] (pp. 111–120)). The seeming absence of a human in the process of creating an image in no way guarantees the objectivity of reality representation. Barthes (e.g., [28,48,49]) reflected critically on photography (still analog then) in two respects: phenomenological and hermeneutical. Both significantly change the way of thinking about photography as a representation of reality, and entangle photography into complex

social relations, the cultural role of language, and perceptual abilities (e.g., [50,51]). Can this thinking be applied to the analysis of the role of visualizations produced by techniques other than the camera (e.g., ALS, Image Based Modelling, satellite imagery, geophysical methods) in the process of learning of the past?

In the application process of all remote sensing methods currently using new technologies, it is possible to distinguish the stages of planning and preparation of measurements, data acquisition, data processing, analysis, and final visualization. In a naturalistic, positivist approach, only the final visualization, as identical to the original, becomes the subject of research. However, the approach proposed by Barthes and other postmodernist thinkers indicates that at each of the mentioned stages of research procedure we are dealing with individual decisions, whether of an expert in data acquisition and processing, or of an archaeologist formulating his or her expectations and evaluating the final product (e.g., [52–54]).

## 5. Data Acquisition

Technology has opened up new possibilities of data acquisition, the purpose of which is to provide information about reality. This is relevant to remote sensing methods and their applications in archaeology. It is commonly believed that these methods allow collecting information on terrain features associated with human activity in the past (aerial photographs, ALS, image-based modelling and rendering, satellite imagery, etc.) or relics under the surface of the earth (aerial photographs, optical satellite imagery, geophysical methods, etc.). Each method and each device records the specific characteristics of features and landscapes. It is also not the case that all data-collecting sensors possess identical characteristics that were apparent and within the sensing capacity of the device at the time of recording (e.g., [55]). This is illustrated by a comparison of spectral bands of selected optical satellite sensors (Table 1).

**Table 1.** Comparison of spectral bands of selected optical satellite sensors.

	Blue (µm)	Green (µm)	Red (µm)	NIR (µm)
<b>IKONOS</b>	0.45–0.52	0.52–0.60	0.63–0.69	0.69–0.90
<b>GeoEye-1</b>	0.45–0.51	0.51–0.58	0.655–0.69	0.78–0.92
<b>OrbView-3</b>	0.45–0.52	0.52–0.60	0.625–0.695	0.76–0.90
<b>QuickBird-2</b>	0.45–0.52	0.52–0.60	0.63–0.69	0.76–0.90
<b>WorldView-2, 3</b>	0.45–0.51	0.51–0.58	0.63–0.69	0.77–0.895
<b>Pleiades-1A, 1B</b>	0.43–0.55	0.49–0.61	0.60–0.72	0.75–0.95
<b>SPOT 7</b>	0.455–0.525	0.53–0.59	0.625–0.695	0.76–0.89

As a consequence, the data record different (even if only minimally) characteristics of objects that we later assign (or not) a connection with the past. The same applies to cameras (image sensors, lenses), recorders of different wavelengths (hyperspectral and multispectral sensors), devices used in geophysical methods, or airborne laser scanning. Device designers respond to the formulated needs, apply solutions according to their knowledge, and this means they are not culturally neutral in Martin Heidegger's understanding. As a consequence, the acquired data cannot be treated in a culturally neutral way either. In addition to the devices that represent the technological domain, there are also experts performing tasks assigned to them and/or archaeologists who formulate (precisely or not) their expectations. All this arrangement of relationships affects data retrieval and final format (Figure 4). Their relationship to reality is culturally shaped in many dimensions that are not entirely controllable and deconstructible. Evaluation of data conformity with reality (e.g., evaluation of measurement or scale precision), providing that it is possible at all, is affected by the views and in accordance with parameters and standards adopted by a given scientific community (e.g., [56]). Therefore, data gathered by means of various techniques are culturally oriented in their nature, due to the purpose, choice of devices, or method used.

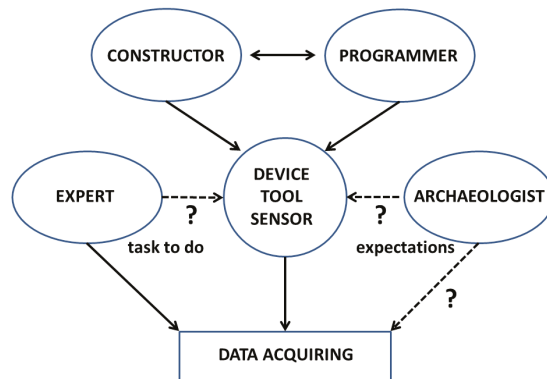


Figure 4. Cultural arrangement of relations within the process of data acquisition in archaeology.

### 6. Data Processing and Visualization

Culturally acquired digital data are subject to complex processing (nowadays almost exclusively computer-based). On the one hand, there are specially designed computer programs (the role of programmers) or existing software (also the work of programmers). On the other hand, data processing (evaluation of data quality, application of various algorithms, visualization of semi-finished products and products) relates to the formulated expectations of archaeologists. This process can be long-lasting, and various solutions can be applied until the image is generated in accordance with the imagination of the recipient (here most often the archaeologist). The inability to create such an image/visualization acceptable to the archaeologist often leads to rejection of data, discrediting the method/device, or even questioning the competence of the expert involved.

Is the archaeologist, as the first recipient of the final visualization, aware of the technical complexity of the data acquisition and processing processes (Figure 5) and, consequently, of the degree of reduction, manipulation and modification that occur throughout them? Between the formulation of the task and the final visualization there are at least two *black boxes* (in the understanding of Latour [57] (p. 304)) representing the areas of intensive use of technology, in which processes and manipulations usually take place uncontrolled by the archaeologist, but usually recognized by remote sensing methods experts. If the archaeologist is unaware of these processes, conditions arise for formulating an opinion about the cultural neutrality of technology and, consequently, visualizations. Hence, it is only one step to recognize that visualization is identical with reality (*mimesis*) and does not generate epistemological doubts.

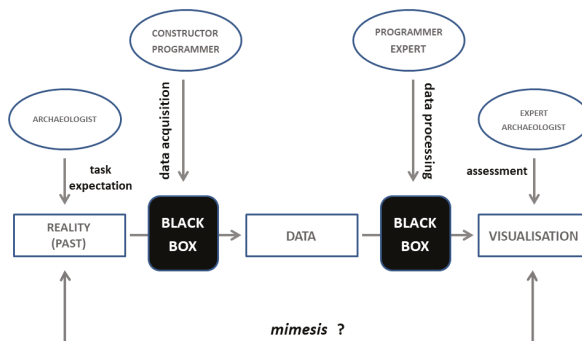


Figure 5. The place of technology in the process of creating visualization as a form of knowledge about the past.

Visualization is therefore a construct that is the result of many complex decision-making processes based on knowledge, technical capabilities, skills, goals, expectations, and awareness of research proceedings. Therefore, at each stage of the research process, signs, i.e., sets of things (including images), are generated, which according to the accepted cultural rules should evoke a specific thought or association in the recipient [58]. The data presented in the form of signs are subject to interpretation. Following Baudrillard, these are only imitations, not replications of reality. In this context, I can return to the question: Can these simulacra be the basis for (re-)constructing the past, playing some role in the process of learning about the world? In Baudrillard's view, visualization is not a presentation or an illustration of events (also past ones), because in the era of total simulation it is not possible (cf. [59]). Creating visualizations is, therefore, not a representation of an object from the past, but a cultural event in itself, here and now. An electronically generated visualization can be processed infinitely by creating new simulacra. Seemingly, such visualizations suggest realness, thus threatening the differences between the real and the imaginary, and between the true and the false [60].

By relating visualizations to the cognitive processes, a certain perspective begins to emerge, probably far from common thinking. In the research procedure, two levels on which the creation of meanings takes place become more and more clearly visible. Technology is connected with revealing, which is inevitably associated with assigning meanings to objects, even if only by linking them to the past. In data, these objects are often not readable directly, but only through data processing, and there is no doubt that this level is conditioned by the cultural experience of an archaeologist (or a data expert, not necessarily an expert archaeologist). The visualizations of these interpreted features/sites/landscapes, or rather their simulations, lead to the subsequent assignment of meanings (Roland Barthes, Jean Baudrillard). As a consequence, the simulacra archaeologists/ experts generate obscure reality, and they are not aware of it. This refers to the threats resulting from the use of technology that Heidegger wrote about. Archaeology becomes as virtual as the world around it. Archaeologists stop investigating the past and they only examine its images. Visualizations of data do not reflect reality (and even more so the past), but introduce a new system of signhood, which is subject to cultural interpretation.

As a result, visualizations (and the technology allowing their production) are part of the process of giving meaning. They are the Medium, and they become the Message [61] subject to hermeneutical interpretation (see [20] (p. 43)). This understanding opens up the possibility of looking at the hermeneutical potential of image technology from the perspective of Marshall McLuhan's tetradic analysis [62,63]. This analysis allows us to assess technology (McLuhan's laws of the tetrad) as a shared method. Marshall McLuhan's Heideggerian-inspired human–technology relation, on the one hand, expands certain forms of human activity and, on the other, reduces/obsolesces them [20] (p. 52). This means that tetradic analysis can be treated as a tool (probably not the only one) for a more in-depth understanding of the cultural functioning of the meanings given to visualizations, but also as building a conceptual bridge between the epistemological and discursive perspectives (visualization as a medium, message). The tetradic model of these relations involves: (1) intensification/enhancement of some aspects of individuals or social groups' activities within a given culture; (2) obsolescence of some capacities of people or social groups; (3) retrieval of something from a previous activity or capacity; and 4) reversal of something into its opposite, when taken to its limit (Figure 6).

Depending on the archaeologist's cultural context, experience, knowledge, and expectations, the same aspects of the archaeologist–technology relationship (and visualization) will be dealt with differently within the tetrad. Consequently, the cognitive value of visualization will be culturally constructed and will have a historical dimension. Archaeologists have dealt with such a phenomenon in the context of the use of aerial photographs in archaeology. The perception of their cognitive value (but also the way of taking photos) changed depending on the needs of archaeologists, resulting from the emergence of new theoretical concepts and research questions [12,15,51] and this phenomenon was relatively well recognized recently. The emergence of new trends did not necessarily replace the earlier

approaches, which meant that, to varying degrees, there existed and do exist simultaneously various practices assigning different cognitive value to aerial photographs.

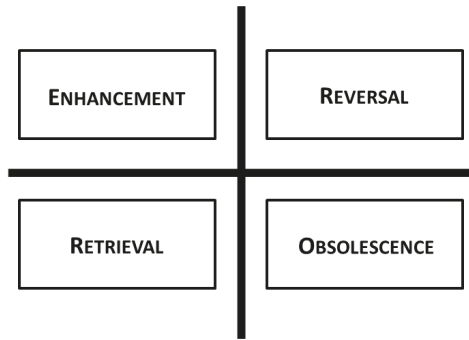


**Figure 6.** Diagram of Marshall McLuhan's tetradic model.

The historical dimension of the cognitive value of aerial photographs/remote sensing data relates not only to the methods of obtaining them, but to their processing leading to the culturally expected results. This is what archaeology is facing now in connection with new methods of obtaining mass data. Currently, this factor encourages an emphasis on technical solutions with limited critical reflection on the cognitive value of remote sensing data and generated visualizations, as was the case with aerial photography in archaeology.

In the context of the cognitive value of data, it is worthwhile to take up the subject of the significant change resulting from the introduction of new methods of data acquisition. Methods such as ALS and satellite imagery provide so much data that traditional, manual, and visual methods of data processing, analysis, and interpretation are no longer effective [3]. In archaeological studies of small areas or sites, this is not a serious problem, but in landscape studies or in building strategies for managing archaeological heritage over large areas it has already been a challenge. It is therefore not surprising that since the 2010s discussion on the use of (semi-)automatic feature recognition or (semi-)automatic detection in remote sensing archaeology (see [64,65]) has begun. This is probably an unavoidable process and archaeologists should face it conceptually [66,67].

In current archaeological practices, three basic strategies are being developed, which are, in fact, procedures of data classification: pixel-based classification, object-based image analysis (OBIA), and machine learning (ML) implemented with the use of modern tools such as neural networks (e.g., [65,67–70]). In the first strategy, pixels are the basic classification units. Different algorithms are used to classify data, and the strategy is optimal if it operates with well-defined and well-separated classes of pixels corresponding to unique archaeological/landscape features. This is not always possible and can lead to an incorrect classification of a pixel. The second strategy is an attempt to circumvent these limitations. OBIA methods use image segmentation into identified homogeneous objects using multiple variables (pixel value, shape, texture, geographic components, etc.) [65,67,69]. Both strategies are supervised methods of classification. The third strategy, i.e., ML, has recently been added to the range of strategies for classifying archaeological objects. ML is a set of algorithms for recognizing patterns (e.g., support vector machines—SVM, artificial neural networks—ANNs, Random Forests—RFs,  $k$ -nearest neighbor— $k$ -NN, etc.) that allows (1) modelling complex class signatures, (2) accepting a variety of input predictor data, and (3) not making assumptions about data distribution [71]. Currently, ML also includes deep learning (DL) strategies, which are techniques permitting the construction of a multi-level analysis and classification architecture. In particular, this concerns the improvement of relations between false-negative and false-positive results owing to the introduction of several levels between the input layer and the output layer (e.g., [72,73]). Within DL

different methods can be used as needed, e.g., recurrent neural networks—RNNs, or convolutional neural networks—CNNs.

Regardless of the differences arising from the nature of data and the classification algorithms used in (semi-)automatic detection procedures, a number of essential stages can be distinguished in these strategies. The first is data acquisition and pre-processing. At present this strategy most often involves ALS data, allowing preparation of DTM and its multiple visualizations (often trend removal techniques such as LRM), and satellite imagery (optical and/or SAR). All pre-trained datasets expect input images to be normalized. The next step is the development of a dataset as a reference for the classification process. This dataset, depending on the strategy adopted, can take the form of defined groups of pixels or a set of object images as templates (based on image segmentation). In practice, existing resources are often used (e.g., ResNet, GoogLeNet, ImageNet), or a custom set of images is introduced which can be used as a training set (extraction of training images, augmentation and cropping). This is often applied in archaeological projects [70,72,74]. Based on the reference data prepared in this way, an automatic classification process is launched, which leads to the identification of objects that meet the adopted criteria. The output is subject to an accuracy assessment in terms of compliance with archaeologists' expectations/knowledge. If OBIA or ML is used the output is not subject to further classification procedures. For DL this process may be repeated by indicating false-negatives and false-positives. In this way, the algorithm "learns" to recognize the expected objects. One training round (epoch) is included in the subsequent cycles. The end of the process depends on the decision of the archaeologist/expert [74]. The final stage is validation of the results, which may involve a desktop survey and/or fieldwork (different versions of ground truthing) [65,70,72]. From a purely technological perspective this seems to be a process that eliminates the weaknesses of a traditional interpreter-based approach. In practice, from an epistemological perspective, it is not very different from the latter. In both approaches the interpreter's knowledge, expectations and experience are decisive.

Many authors emphasize "expert knowledge-driven" decisions, which relate to all the aforementioned stages. The quality of the prepared output data significantly affects all subsequent stages [67] (p. 487), including image segmentation (OBIA) and creation of training datasets [69] (p. 2). In DL the possibility of the cycle repetition is left to the expert (archaeologist?) to decide on the completion of the process. This decision, and the evaluation of results in this classification model (also in others), depends on the archaeologist's expectations. The question is if the network can overlearn, and how this may affect the information obtained. Is it possible to identify such a problem? What could be the consequences for the archaeologist's expected outcome? Is the archaeologist aware of the consequences or possible need for data modification?

I have no doubt that all these stages are consecutive steps in data work comprising certain communicative arrangements that involve making cultural decisions, creating signs, and assigning meanings. Logical consistency, which is to guarantee the construction of algorithms allowing for a quick and "objectivized" data search, is based on our expectations, knowledge, and previous experience.

The assignment of meanings is involved at the all stages of these classification strategies. The attempts made so far have concerned selected categories/classes of archaeological sites (mounds, barrows, roundhouses, charcoal kilns, Celtic fields etc.—[72,74,75], i.e., they are based on existing knowledge, experience, and expectations. The question can be posed whether these methods allow for the qualitative identification of other/new types of relics of the past. In this context, Rodney Brooks's opinion that "[...] deep learning does not help in giving a machine 'intent' or any overarching goals or 'wants'" may be relevant [76] (p. 280).

This question indicates the need to look at the algorithms used in ML and DL. Does repetition of the process lead to such a type of "self-learning" in which objects that are radically different from those included in training data sets can be identified, i.e., beyond existing knowledge? Do archaeologists fully understand how the algorithms operate? Do they have an insight into what the network knows? If they are not able to answer these questions positively, by definition they are dealing with *black box(es)* (for both experts and archaeologists) (e.g., [77]). It also means that archaeologists are unable to answer

the question about the relationship between the obtained result and what is commonly called reality. Archaeologists can therefore assume that even despite the process of “self-learning,” there is a reduction in the potential and resources of past relics contained in the data. Such are the limitations resulting from the use of a specific algorithm (problem-oriented algorithm) and its positive result. In this sense an algorithm used in detection can be treated in the same way as previous classifications in archaeology conditioned by theories, trends, and research questions (cf. [78]). In every situation archaeologists lose the diversity of the world as it is etic approach (instead of emic). And, it should be noted, using traditional methods suffers from the same problems.

A number of researchers [3,70,72,79] have expressed the opinion that the results of (semi-)automatic detection methods should be verified. It is difficult to argue with this view. But what does it mean in a cognitive perspective? In my opinion it means that the result of the algorithm(s) used is not to be considered a final determination. The final determining authority is the archaeologist, and (very often) involves some form of ground truthing (see [80] (pp. 518–521), such as field survey, digging test trenches etc., (e.g., [70,72,75]) which is an essential element of the whole cognitive procedure. I have no doubt that the perceptive and interpretative capabilities of an archaeologist are significantly different from what can be stored in the algorithm(s). Moreover, I believe that it is probably impossible to capture in mathematical equations the entire cultural complexity of the world in the past, formation processes, and the interpretative experiences and expectations of archaeologists.

The need to verify (semi-)automatic detection results accounts for only one side of this complex process. (Semi-)automatic detection places the objects selected by the archaeologist (and thus already known to us) and learned by the algorithm in our area of interest. Verification allows us to accept or reject what the archaeological/non-archaeological algorithm suggests. In this respect, the process of reduction and modification of information by the archaeologist takes place twice: first, at the stage of preparation of the input dataset, and then at the stage of verification, i.e., output assessment. Both stages lead to the rejection and reduction of world complexity. In this sense, technology in Heidegger’s sense obscures some aspects of the world (including the past world) and, consequently, it (this past world) disappears in its complexity from the cognitive process. At the first stage, it is due to the fact that the input is prepared according to the archaeologist’s knowledge and expectations. This stage is consequently burdened with the archaeologist’s bias. As a consequence, the algorithm(s) can at best identify the objects archaeologists expect. An algorithm will magnify any patterns in the input data. It means that if bias is present at the stage of data input preparation (let alone the archaeologist’s bias at the pre-processing stage) the algorithm will also magnify that bias [81]. Consequently, algorithms reflect the biases of both programmers and datasets prepared by archaeologists. It should also be noted, however, that the algorithm may point to a potential object that the archaeologist might omit in their interpretation (e.g., the question of noticing minimal alternations).

Our knowledge and experience play a role in the data assessment and verification stages leading to the acceptance or rejection of selected objects. The Archaeologist’s judgment is necessary to assess the accuracy of algorithmic output [81], though the processes by which that may happen can be opaque. It is definitely a reduction of the potential and stock of past relics present in the data. Such are the limitations resulting from the use of a specific algorithm (problem-oriented algorithm) and its positive result. There is also a question about the possibility of validating its (their) functioning. At these stages of automatic detection (including DL) archaeologists focus on what the algorithm offers (even if it is finally rejected). In the “cognitive non-existence” there remain all those objects that do not meet the criteria of the algorithm and fall out of the field of the archaeologist’s perception. Although they are still in the raw data, the question remains, will there be new data search algorithms, and will the new algorithms allow for a significantly similar or a different result?

At one point, archaeologists became aware of the presence of bias in their work (e.g., [14,82–84]) and almost simultaneously, initiatives were undertaken to eliminate this phenomenon (e.g., discussion on bias of oblique and vertical aerial photographs). The need to reduce bias in archaeological research procedures is often an argument for the application of high-tech methods and devices in remote sensing

(e.g., [17,85,86]). In particular, this occurs in the context of working with remote sensing data. The above considerations of automatic detection probably sufficiently demonstrate that such solutions do not lead to bias reduction. Bias permeates the whole complex classification procedure and perhaps because of that it is so difficult to grasp. However, there is also a growing awareness of its presence and inevitability (e.g., [72]), even when using sophisticated technologies.

My primary objective in considering (semi-)automatic detection in archaeology is not to assess its effectiveness in comparison with traditional methods of identifying archaeological objects. Rather, I would like to ask the following question: Does this new technology change anything in archaeologists' cognitive process, or does it modify the current thinking about the past? The existing applications of (semi-)automatic detection in remote sensing archaeology clearly demonstrate the risks mentioned by Heidegger.

For many authors, the main goal is to identify archaeological resources in areas that have so far been poorly explored. The effectiveness of the method is assessed on the basis of the extent to which it generates an increase in the number of database records (e.g., more round barrows, charcoal kilns or round houses). Archaeologists frequently are driven by their desire to find/reveal new (although already known types) sites. The question arises whether increasing the amount of empirical data (records in the database) can transform archaeology and the archaeologist's ability to explore the past? In archaeology, technology only serves to increase the number of discoveries. Conceptually, archaeologists remain at the same stage when aerial archaeology was criticized of a "stamp collection" approach (e.g., [87–89]). The fetish of empirical data (efficiency of identifying new objects) leads to a focus on discovery in the common sense (see above). And in this sense, technology is a threat to science (as understood by Heidegger). The effectiveness of technology obscures the complexity of the world, including the past world (and not only because archaeologists discover what they know), but also the complexity of research practices. This leads to impoverished reflection on what archaeologists do and how they do it.

## 7. Archaeologist as User: From Perception to Interpretation

Image technology (and the image itself) is a medium that allows the transmission, translation, storage, and transformation of a message. But it is not created without prior perception and interpretation. While hermeneutical interpretation has been present for quite a long time in humanistic discourse (Edmund Husserl, Paul Ricoeur), the reflection on perception and its cultural entanglement is not at all obvious. The process of perception is related to the inflow of external stimuli (here usually visual), which are subject to various further transformations leading to the recognition of the object (e.g., [90] (p. 6), [91]). Perception and its role in cognitive processes is now largely a subject of cognitive psychology ([92–94]), but philosophical reflection on the relationship between perception and cognition goes back to Immanuel Kant's considerations. Among many studies dealing with this issue from an epistemological perspective, it is worth recalling the works of Ludwik Fleck from the 1930s [95], which appear more and more frequently in contemporary discussions (e.g., [96,97]). In the discourse on the development of science and technology, Fleck's views place him conceptually (not chronologically) between Thomas Kuhn and Bruno Latour [97,98]. While the former, for example, emphasizes the commitment to the paradigm in science, Fleck places scientific activity in the cultural context of the researcher, i.e., in line with the anti-naturalistic approach proposed in this paper. Considering the questions raised, Fleck's assertion that "To see is to know" seems fundamental. Certainly, such a statement does not raise any fundamental doubts today, but in the period when it was formulated it must have had a very controversial resonance. With this assertion Fleck questioned perception as a means of objective learning about the world, and thus the foundations of science built on Enlightenment concepts [99]. According to him, it is impossible to see without anticipating knowledge, and consequently we see what is mental and not physical (!). It is not stimuli that decide what we see, but the processes taking place in our minds. Such assertions contradict the common opinion that physical vision is objective. Ludwig Wittgenstein (late Wittgenstein) [100] expressed himself in a

similar spirit, claiming that we see only an insignificant tangle of shapes and colors, which we give meaning to, but which can change. This is related to targeted or directed perception (attention, attitude, aspect) (e.g., [101]) and, in consequence, to interpretation. The way of perceiving is nothing more than a certain interest in the surroundings, but also an image/visualization. In the case of remote sensing data, the problem is even more complex and multilevel, because we observe a mediated reality in the data. In our interpretation, we usually ignore the whole process of data acquisition, processing, and generation of various forms of visualization and focus on the final product (final visualization). The perception processes are present in the data workflow much earlier. The way we see is the social arrangements (contracts) of what we see. They are so mentally close to us that we do not even notice that we are learning to see [99]. This social creation of ways of seeing illustrates very well the difference in the presentation and reading of topography in the tradition of British archaeology and other countries (e.g., [102–104]). This social dimension of knowledge-based perception was also stressed by Fleck. His concepts of “thought style” and “thought collectives” have been widely discussed in literature [96–98,105,106]. An independent (socially excluded) researcher does not exist. Everyone is entangled in certain communities, including groups of scientists with their exchanges of ideas or intellectual interactions. Directed perception, with corresponding mental and objective assimilation of what has been so perceived. It is characterized by common features in the problems of interest to a tht. The “thought collective” is “[ . . . ] a community of persons mutually exchanging or maintaining intellectual interaction, we will find by implication that it also provides the special “carrier” for the historical development of any field of thought, as well as for the given stock of knowledge and level of culture” [95] (p. 39). The opportunity to be part of such a community is given to those who, in the course of their education, have mastered and accepted the rules in force [107] (p. 198). The “thought style” is understood by Fleck [95] (p. 99) as “[the readiness for] directed perception, with corresponding mental and objective assimilation of what has been so perceived. It is characterized by common features in the problems of interest to a thought collective, by the judgment which the thought collective considers evident, and by the methods which it applies as a means of cognition. The thought style may also be accompanied by a technical and literary style characteristic of the given system of knowledge.”

In science, the consequences of “thought styles” and “thought collectives” are far-reaching. Of course, they also concern archaeology and the use of visualization in the study of the past. Belonging to “thought collectives” perpetuates the belief in the rightness of the adopted views and research conduct. As a consequence, scientists have identical or very similar views in a given field. They do not realize the nature of their own thinking, conditioned by the socio-historical context. The conviction is formed that since everyone thinks the same, it is the only possible culture-independent way of seeing the world [107]. The dissemination of certain views in society (outside the research community) co-creates common-sense knowledge that is not even subject to verification. This is in line with Heidegger’s concept of concealing the world by formulated and accepted views, and with the lack of critical reflection on such views resulting in “idle talk.” In the context of archaeological development, such deeply rooted and unconscious convictions are “belief in experience/observation,” “objectivity of facts,” “pure description and classification,” and the possibility of “knowing the past.” They originate from the 18th- and 19th-century concepts influencing science (empiricism, positivism, evolutionism) and are particularly strongly rooted in cultural-historical archaeology.

According to Fleck, two elements in the most popular views, in particular, affect the consolidation of our beliefs about the objectivity of our findings on the (past) world. These are “technical terms” and “scientific device.” The specific power of scientific terms consists, to a large extent, in detaching their significance from the subject of cognition, hence in establishing the “objective” meaning. In this way the object being defined becomes independent, as if possessing absolute existence [108] (p. 108). Even more so, the cultural dimension of data acquisition for visualizing the (past) world resounds in the context of the “scientific device.” “The analysis of epistemological significance of a scientific device would also require a separate study. It can be mentioned briefly that a scientific appliance, which is realization of

some result of a definite thought-style, directs our thinking automatically on to the tracks of that style. Measuring instruments force one to apply the notion of unit for which they were constructed; even more so, they force one to apply the notion from which they originated [...]” [108] (p. 109). From this perspective, there is no gap between the process of cognition in Fleck’s viewpoint and the views of contemporary philosophers significant in the context of the use of images/visualizations (e.g., Roland Barthes, Jean Baudrillard).

Both “thought styles” and “thought collectives” affect the perception and interpretation of the world, and their alterations modify ways of thinking about it. There is no single “thought style” or “thought collective,” which means that particular groups of scientists compete against each other, as if participating in specific social games [109] within the space between the legitimate and the illegitimate image of the world. “Pure facts” do not play a decisive role in these games because facts do not exist independently of cognition, and this cognition refers only to what is useful to the “learner” [110] (p. 267). The emphasis is therefore placed on language games, because it is through language that we communicate our views, ideas, and manipulate the image of the world. Therefore, it is important to construct a narrative in such a way that it becomes more persuasive and, as a result, it can become established and, relatively, universally accepted. This invites reflection on the discursive dimension of visualizations produced from remote sensing data.

## 8. Discursive Dimension of Visualization

In contemporary humanistic reflection, the concept of truth is far from the common understanding of it going back to ancient Greek philosophy (e.g., [111]). This also applies to the role of empirical data in knowing about the world and the determinants of knowledge legitimacy (e.g., [112]). In a fundamental way, the understanding of truth has been shifted from the external world, as a point of reference, to the knowledgeable subject entangled in culture. This means that seemingly mimetic visualizations of data are in practice involved in a variety of discourses and cultural games that include dialogue, communication, and power experience. Discursive practices permeate all spheres of culture and are part of the processes of producing images of the world (including archaeological construction of knowledge about the past). Thus two aspects that are increasingly being raised in the context of images/visualizations and their presence in the scientific/political.

Research on image persuasion is conducted, in particular, in psychology and cognitive science. Does archaeology use such knowledge and, consequently, consciously manipulate the image to achieve the intended effect in the recipient? It is difficult to find examples in literature that could support such an unequivocal assertion (although, for example, the analytical uses of DEM visualization algorithms may prove otherwise, see [113]). I think that rather a common-sense approach to the image, i.e., what is the object/site/landscape everyone sees, is the dominant one. To a greater extent, one can count on complying to certain standards and established customs in the archaeological community. This means that in terms of the persuasive power of the image, we use categories that fit into Fleck’s concept of “thought style.” It is this “thought style” that makes images/visualizations more comprehensible (and thus persuasive), if they are consistent with the knowledge and expectations of the audience [114,115]. John Casey [116] (p. 172–173), in his discussion of Wittgenstein’s views, even formulates a claim that the unity of perception implies identical judgements. In archaeological practice, this persuasiveness seems to be multilevel and concerns at least two relations: data processing expert → archaeologist, and archaeologist → other archaeologists and the public.

Not every archaeologist using remote sensing data has the ability to work with it. Archaeologists are often unaware of the complexity of data acquisition processes and data processing (*black boxes*). As a consequence, in order for the data to be used in research, visualizations should be in line with an archaeologist’s expectations. It is often an expert who prepares a visualization in such a way that it satisfies the archaeologist (regardless of whether it is to be used only as an illustration or for analytical and/or interpretative procedures—though simple visualization toolboxes are changing this dynamic).

Persuasion as a form of communication can influence the recipient in various ways. It is not only a matter of conveying a message, but also of exerting influence (even pressure) on the recipient (cf. [117]). In their reflections on the role of persuasion in advertising, Gerald Miller [118] and Richard Perloff [119] (pp. 19–20) stress that it can take on various functions: shaping, reinforcing, and changing. Shaping is a tendency to use persuasive messages to influence the actions and attitudes of the recipients; reinforcing is rather directed toward strengthening and deepening existing attitudes and actions; and changing is aimed at causing a significant change and establishing new, expected actions or attitudes [119]. Can archaeologists directly apply the reflection present in the discourse concerning the role of advertising in trade or persuasion in politics? Persuasion is addressed to the recipient; thus it is the broadcaster (expert, archaeologist) who formulates objectives related to the form of persuasive visualization. A question can be asked: is the role of persuasion (in the sender–recipient relationship) in scientific archaeological discourse discussed? Is the sender (archaeologist) aware of the significance of this message, or do they operate in the knowledge of how it is received? If we look at this problem from the perspective of the “thought collective,” it may turn out that what is persuasive to me is also persuasive for the recipient as a representative of the same “thought collective” (no matter if it is a different archaeologist or the public). Visualization is persuasive if it convinces me, and reinforces my views. The viewer might be less important, or is treated as a representative of the same “thought collective.” Then, if something is persuasive for me, it will also be persuasive for the recipient, because it represents the same learned way of thinking. In consequence, we continue to function using the same cognitive models and remain exclusively in the area of persuasion as “reinforcement.” There is no chance for a “changing” or “shaping” effect to take place because it requires critical reflection and attention to the way the viewer thinks. Such thinking appears in studies and practices related to the inclusion of children, youth, and local communities in the understanding of the past (e.g., [120]).

The power of persuasion is inseparably connected with aesthetics. It is assumed that aesthetics plays an important role in cognition, because it influences, among other things, the perception and understanding of described phenomena. In the traditional understanding, aesthetics is considered a philosophy of beauty and art, and stands in opposition to reason, knowledge, and science. At present, the approach to aesthetics has been re-evaluated toward the study of the aesthetic process which includes the creator (artist), the creative process, the work, the recipient, perception, and aesthetic values (e.g., [121,122]). It is clear that this contemporary approach to aesthetics is linked to the linguistic turn and the philosophy of postmodernity. Aesthetics has become a general trend that also encompasses science (including archaeology). As a result, the boundary between traditional science and truth and persuasive narratives is blurred. The problem is that in the persuasive, discursive sphere, the boundaries between reproduction, creation, and simulation are fading. There is a loss of attributes of the real world, and the phenomenon of “vanishing reality” can be observed. As a consequence, aestheticism is one of the processes that leads to the concealment of the sense of a visualized object [60]. This automatically evokes Heidegger’s view that the sense of the phenomenon under investigation is concealed by the initial interpretation. If it is enhanced with aesthetic visualization, this effect is much stronger. Walter Benjamin [22] went even further, claiming that aesthetics can be used in politics to strengthen demagogic messages that mold the ideas of broad social groups. But, is this only in politics? Or, does it also apply to archaeology or messages about the past? Is it at the level of critical reflection on the past or methods of researching it and creating new models of narration, or is it at the level of inscribing oneself into existing research questions, which have been repeated for decades, and ways of solving them?

In traditional discourse visualization is a tool of power and domination. An archaeologist uses visualization to impose a vision of reality that they accept, but does not know how it is constructed (a *black box* product). In this way archaeologists value themselves and their research (e.g., [123]). It is in such an approach that the aesthetics of visualization plays a decisive role. The data itself becomes less important. The visual attractiveness of generated images or 3D models brings a fascination with the potential of technology and becomes a part of technological fetishism in archaeology [124]. Such an approach to

technology (including remote sensing and visualization methods) is consistent with Heidegger's view that the greatest threat of technology is the formation of attitudes in which we treat a given technology as a provider of ready-made solutions. The applied technology, however, obscures our reality and consequently, we ignore other alternative solutions, interpretations, or possibilities [63] (p. 13).

Another important issue in these reflections on aesthetics relates to conventionalization. Contemporary technology moves toward standardization, repetition of patterns, comparability, and homogeneity. In the practiced discourses "The fact must be expressed in the style of thought collective" [95] (p. 102). Thus, the generated visualizations are adjusted to stylistic conventions, in which (aesthetic) visualization itself becomes a standard in the "research" procedure, and its aesthetics become inscribed in culturally fixed patterns (but not necessarily in postulated rules of standardization of visual representations, e.g., [53,125]). In further consequence, the aesthetics of visualization may replace the reflection on the meaning of an object in the past and in contemporary discourse. This state of affairs leads to the question: Why do archaeologists approach contemporary visualizations so exaggeratedly and uncritically? In a sense, Heidegger provides the answer to this question—that science has stopped thinking because it focuses on the technical approach.

In the contemporary debate on digital humanities, Heidegger's position is interesting because it allows us to gain a distance to the technical approach to the humanities, and reveals the necessity of turning to the original thinking that underlies all thinking, including thinking about the humanities [126] (p. 137). This seems to be the essence of the matter. Thinking should be the basis for all activities of archaeologists. These activities cannot be limited to collecting and describing (also visualizing) data. Critical reflection and understanding cannot be limited only to *black boxes*, but to all components of the research procedure. Referring again to Heidegger, the lack of critical reflection on the created and used visualizations may lead to obscuring (past) reality and perpetuating the ideas proposed by archaeologists themselves and/or even by experts cooperating with them. And the use of once fixed images, additionally subject to cultural standardization, contributes to the spread of Heidegger's "idle talk" in the context of visual assertions (and through visualization) about reality (also past reality). According to Heidegger, "idle talk" is a superficial statement that only roughly refers to beings. Speech or text (or visualization in archaeology) does not touch beings as it is, but communicates through repetition. Such a statement quickly becomes popular, "authoritative," and inscribes itself in power relations losing its reference in being [18] (pp. 157–159). Additionally, the excessive pursuit of efficiency, resulting in the loss of the essence, contributes to the formation of an intellectual desert [126] (p. 144).

## 9. Final Remarks

In trying to answer the questions posed about the extent to which changes in technology (including remote-sensing methods) influence the understanding of the place of image/visualization in archaeological research and the cognitive status of images, it is worth remembering that it is not only the cultural environment that shapes archaeology, but also what archaeologists themselves think about archaeology and its cognitive capabilities (obviously affected by their own cultural contexts).

In 1973 David Clarke published an article *Archaeology: The Loss of Innocence* in which he summarized the changes in archaeology and its setting from the 1950s to the 1970s. Clarke wrote that "The loss of disciplinary innocence is the price of expanding consciousness; certainly the price is high but the loss is irreversible and the prize substantial. Although the loss of disciplinary innocence is a continuous process we can nevertheless distinguish significant thresholds in the transitions from consciousness through self-consciousness to critical self-consciousness" [127] (p. 6). One may ask whether the "loss of innocence" has affected all archaeologists, and whether it has covered all the necessary areas of critical self-consciousness. I have no doubt that in practice a number of remote sensing archaeologists remain innocent in the way Clarke puts it [128–135]. The place of technology (including remote sensing methods) and forms of visualization is only one of the fields in which traditional innocence manifests itself. It is a consequence of what Fleck describes as "thought styles" and "thought collectives," which in themselves inhibit critical reflection and influence the rejection of

different views, perpetuating the innocence. Technology (especially remote sensing methods) itself does not constitute progress in archaeology. First of all, archaeologists need critical reflection on what they do, how they do it, and why they do it [136]. Only with such an attitude can we eliminate the threat to culture posed by technology as understood by Heidegger.

There are many different questions raised in the text above and the readers may not find simple answers to them. Rather, it is my intention to ask questions, not to provide answers, especially unequivocal ones. Gone are the days when one way specific of thinking could be imposed. If these questions have encouraged the readers to try to find their own answers, I will consider it a success.

**Funding:** This research received no external funding

**Acknowledgments:** I have found writing this paper a challenge, as it has demanded that I address some unfamiliar topics—for this reason I would like to thank all those who supported me in this struggle. I have consulted philosophical and theoretical archaeology issues with Danuta Minta-Tworzowska, Anna Pałubicka and Henryk Mamzer as well as automatic detection topics with Jacek Marciniak. Their comments were very valuable and made me believe that I have not made any glaring mistakes in these fields. I would like to thank the editors of SI (Arianna Traviglia, Dave Cowley, and Geert Verhoeven) for their openness to accept such an unusual text and their continued support, even if we differed on some issues. I would also like to thank the anonymous peer reviewers for their insightful comments that allowed me to look at my text from a different angle. I did not accept all their comments, and this is certainly due to our different “thought style” and different scientific and cultural experiences. Of course, I am responsible for all narrative errors or inconsistencies.

**Conflicts of Interest:** The author declares no conflict of interest.

## References

1. Balm, R. *Archaeology's Visual Culture. Digging and Desire*; Routledge: London, UK, 2016; ISBN 978-036-787-427-8.
2. Bazin, A. The Ontology of the Photographic Image. *Film Q.* **1960**, *13*, 4–9. [[CrossRef](#)]
3. Cowley, D. In with the new, out with the old? Digital workflows and auto-extraction in remote sensing archaeology. In *Virtual Archaeology: Nondestructive Methods of Prospections, Modeling, Reconstructions: Proceedings of the First International Conference Held at the State Hermitage Museum, St. Petersburg, Russia, 4–6 June 2012*; Hookk, D., Ed.; The State Hermitage Publishers: St. Petersburg, Russia, 2013; pp. 18–30. ISBN 978-593-572-516-7.
4. Verhoeven, G. Methods of Visualisation. In *Analytical Archaeometry: Selected Topics*; Howell, E., Vandenebeele, P., Eds.; Royal Society of Chemistry: Cambridge, UK; London, UK, 2012; pp. 3–48. ISBN 978-184-973-162-1.
5. Trigger, B.G. *A History of Archaeological Thought*, 2nd ed.; Cambridge University Press: Cambridge, UK, 2006; ISBN 978-052-160-049-1.
6. Johnson, M. *Archaeological Theory: An Introduction*; Blackwell: Oxford, UK, 1999; ISBN 978-063-120-295-0.
7. Feyerabend, P. *Against Method. Outline of an Anarchistic Theory of Knowledge*; Verso: London, UK, 1975; ISBN 978-039-100-381-1.
8. Latour, B. *Science in Action: How to Follow Scientists and Engineers through Society*; Harvard University Press: Cambridge, MA, USA, 1987; ISBN 067-479-291-2.
9. Latour, B. *We Have Never Been Modern*; Harvard University Press: Cambridge, MA, USA, 1993; ISBN 978-067-494-839-6.
10. Nettle, D. Beyond nature versus culture: Cultural variation as an evolved characteristic. *J. R. Anthr. Inst.* **2009**, *15*, 223–240. [[CrossRef](#)]
11. Rączkowski, W. Power of image: Some ideas on post-processual aerial archaeology. *AARGnews* **1999**, *19*, 10–14.
12. Rączkowski, W. Beyond the technology: Do we need ‘meta-aerial archaeology’? In *Aerial Archaeology: Developing Future Practice*; Bewley, R.H., Rączkowski, W., Eds.; IOS Press: Amsterdam, The Netherlands, 2002; pp. 311–327. ISBN 978-158-603-184-8.
13. Rączkowski, W. Why interpretation?: Chairman’s Piece. *AARGnews* **2009**, *39*, 5–8.
14. Cowley, D. A case study in the analysis of patterns of aerial reconnaissance in a Lowland area of Southwest Scotland. *Archaeol. Prospect.* **2002**, *9*, 255–265. [[CrossRef](#)]

15. Brophy, K.; Cowley, D. *From the Air. Understanding Aerial Archaeology*; Tempus: Stroud, UK, 2005; ISBN 978-075-243-130-7.
16. Hanson, W.S. The Future of Aerial Archaeology (or Are Algorithms the Answer?). In *Remote Sensing for Archaeology and Cultural Heritage Management, Proceedings of the 1st International EARSeL Workshop, CNR, Rome, 30 September–4 October 2008*; Lasaponara, R., Masini, N., Eds.; Arracne: Rome, Italy, 2008; pp. 47–50. ISBN 978-885-482-030-2.
17. Verhoeven, G. Are We There Yet? A Review and Assessment of Archaeological Passive Airborne Optical Imaging Approaches in the Light of Landscape Archaeology. *Geosciences* **2017**, *7*, 86. [[CrossRef](#)]
18. Heidegger, M. *Being and Time*; State University of New York Press: Albany, NY, USA, 1996; ISBN 079-142-678-5.
19. Heidegger, M. *The Question Concerning Technology and Other Essays*; Harper and Row: New York, NY, USA, 1977; ISBN 978-006-090-419-7.
20. Vieta, M.; Ralon, L. Being-in-the-Technologically-Mediated-World: The Existential Philosophy of Marshall McLuhan. *Pop. Cult. Stud. J.* **2013**, *1*, 36–59.
21. McLuhan, M. *Understanding Media: The Extensions of Man*; The MIT Press: Cambridge, MA, USA, 1994; ISBN 978-041-510-483-8.
22. Benjamin, W. The Work of Art in the Age of Mechanical Reproduction. In *Illuminations*; Arendt, H., Ed.; Schocken Books: New York, NY, USA, 1969; pp. 1–26. ISBN 978-080-520-241-0.
23. Moholy-Nagy, L. *Painting, Photography, Film*; Lund Humphries: London, UK, 1967.
24. Paić, Ž.; Purgar, K. (Eds.) Introduction. In *Theorizing Images*; Cambridge Scholars Publishing: Cambridge, UK, 2016; pp. 1–21. ISBN 978-144-388-800-4.
25. Bertolini, M. The “Pictorial Turn” as Crisis and the Necessity of a Critique of Visual Culture. *Philos. Study* **2015**, *5*, 121–130.
26. Zeidler-Janiszewska, A. The anthropology of image and knowledge of the image (*Bildwissenschaft*) as transdisciplinary project. Archaeology in the transdisciplinary network. *Archaeol. Pol.* **2006**, *22*, 53–64.
27. Bal, M. Visual essentialism and the object of visual culture. *J. Vis. Cult.* **2003**, *2*, 5–32. [[CrossRef](#)]
28. Barthes, R. *Camera Lucida: Reflections on Photography*; Farrar, Straus & Giroux: New York, NY, USA, 1982; ISBN 978-080-901-398-2.
29. Sontag, S. *On Photography*; Farrar, Straus & Giroux: New York, NY, USA, 1977; ISBN 978-038-528-757-9.
30. Bondecka-Krzykowska, I. Uwagi na temat ontologii wirtualnej rzeczywistości. *Filoz. Nauk.* **2012**, *20*, 139–153.
31. Brey, P. Virtual Reality and Computer Simulation. In *Handbook of Information and Computer Ethics*; Himma, K., Tavani, H., Eds.; John Wiley & Sons: Hoboken, NJ, USA, 2008; pp. 361–384. ISBN 978-047-179-959-7.
32. Mandal, S. Brief Introduction of Virtual Reality & its Challenges. *IJSER* **2013**, *4*, 304–309.
33. Baudrillard, J. *Simulacra and Simulation*; University of Michigan Press: Ann Arbor, MI, USA, 1994; ISBN 978-047-206-521-9.
34. Barker, P. Virtual reality: Theoretical basis, practical applications. *Res. Learn. Technol.* **1993**, *1*, 15–25. [[CrossRef](#)]
35. Forte, M. Cyberarchaeology: A Post-Virtual Perspective. In *Between Humanities and the Digital*; Svensson, P., Goldberg, D.T., Eds.; The MIT Press: Cambridge, MA, USA, 2015; pp. 295–310. ISBN 978-026-202-868-4.
36. Tylman, W. Computer Science and Philosophy: Did Plato Foresee Object-Oriented Programming? *Found. Sci.* **2018**, *23*, 59–172. [[CrossRef](#)]
37. Forte, M. Cyber-archaeology: An eco-approach to the virtual reconstruction of the past. In *Digital Heritage: Proceedings of the 14th International Conference on Virtual Systems and Multimedia, Full Papers, Limassol, Cyprus, 20–25 October 2008*; Ioannides, M., Addison, A., Georgopoulos, A., Kalisperis, L., Eds.; Archaeolingua: Budapest, Hungary, 2008; pp. 261–268. ISBN 978-963-804-699-4.
38. Reilly, P. Additive Archaeology: An Alternative Framework for Recontextualising Archaeological Entities. *Open Archaeol.* **2015**, *1*, 225–235. [[CrossRef](#)]
39. Forte, M. Virtual Reality, Cyberarchaeology, Teleimmersive Archaeology. In *3D Recording and Modelling in Archaeology and Cultural Heritage. Theory and Best Practices*; Remondino, F., Campana, S., Eds.; Archaeopress: Oxford, UK, 2014; pp. 113–127. ISBN 978-140-731-230-9.
40. Cummings, V. Virtual Reality, Visual Envelopes, and Characterizing Landscape. In *Handbook of Landscape Archaeology*; David, D., Thomas, J., Eds.; Left Coast Press: Walnut Creek, CA, USA, 2008; pp. 285–290. ISBN 978-159-874-294-7.

41. Gaugne, R.; Gouranton, V.; Dumont, G.; Chauffaut, A.; Arnaldi, B. Immersia, an open immersive infrastructure: Doing archaeology in virtual reality. *Archeol. E Calc.* **2014**, *5*, 180–189.
42. Cassidy, B.; Sim, G.; Robinson, D.W.; Gandy, D. A Virtual Platform for Analyzing Remote Archaeological Sites. *Interact. Comput.* **2019**, *31*, 167–176. [[CrossRef](#)]
43. Crandall, R.; Levich, M. *A Network Orange. Logic and Responsibility in the Computer Age*; Springer: New York, NY, USA, 1998; ISBN 978-038-794-647-4.
44. Blitz, M. Understanding Heidegger on Technology. *New Atlantis* **2014**, *41*, 63–80.
45. Rączkowski, W. Theory, empiricism and practice: Archaeological discourses in a network of dependency and opposition. *Analecta Archaeol. Ressorv.* **2011**, *4*, 7–34.
46. Huggett, J. What lies beneath: Lifting the lid on archaeological computing. In *Thinking beyond the Tool: Archaeological Computing and the Interpretive Process*; Crysanthi, A., Murietta Flores, P., Papadopoulos, C., Eds.; Archaeopress: Oxford, UK, 2012; pp. 204–214. ISBN 978-140-730-927-9.
47. Latour, B. Technology is society made durable. In *A Sociology of Monsters Essays on Power, Technology and Domination*; Law, J., Ed.; Routledge: London, UK, 1991; pp. 103–131. ISBN 978-041-507-139-0.
48. Barthes, R. *Elements of Semiology*; Hill & Wang: New York, NY, USA, 1977; ISBN 978-037-452-146-2.
49. Barthes, R. *Image–Music–Text*; Hill & Wang: New York, NY, USA, 1978; ISBN 978-037-452-136-3.
50. Jenks, C. *Visual Culture*; Routledge: London, UK, 1995; ISBN 978-041-510-623-8.
51. Rączkowski, W. *Archeologia Lotnicza—Metoda Wobec Teorii*; Wydawnictwo Naukowe UAM: Poznań, Poland, 2002; ISBN 978-832-321-194-5.
52. Doneus, M.; Briese, C. Airborne Laser Scanning in forested areas—Potential and limitations of an archaeological prospection technique. In *Remote Sensing for Archaeological Heritage Management*; Cowley, D., Ed.; Europae Archaeologia Consilium: Brussels, Belgium, 2011; pp. 59–76. ISBN 978-963-991-120-8.
53. Opitz, R.; Cowley, D. *Interpreting Archaeological Topography. 3D Data, Visualisation and Observation*; Oxbow Books: Oxford, UK, 2013; ISBN 978-184-217-516-3.
54. Banaszek, Ł. *The Past amidst the Woods. The Post-Medieval Landscape of Polanów*; Wydawnictwo ad rem: Poznań, Poland, 2019; ISBN 978-839-163-426-4.
55. Agapiou, A.; Alexakis, D.D.; Hadjimitsis, D.G. Potentials of Virtual Earth Observation Constellations in Archaeological Research. *Sensors* **2019**, *19*, 4066. [[CrossRef](#)]
56. Forte, M. Virtual archaeology: Communication in 3D and ecological thinking. In *Beyond Illustration: 2D and 3D digital Technologies as Tools for Discovery in Archaeology*; Frischer, B., Dakouri-Hild, A., Eds.; Archaeopress: Oxford, UK, 2008; pp. 75–119. ISBN 978-140-730-292-8.
57. Latour, B. *Pandora's Hope: Essays on the Reality of Science Studies*; Harvard University Press: Cambridge, MA, USA, 1999; ISBN 978-067-465-336-8.
58. Peirce, C.S. *Peirce on Signs: Writings on Semiotic by Charles Sanders Peirce*; University of North Carolina Press: Chapel Hill, NC, USA, 1991; ISBN 978-080-784-342-0.
59. Zawojski, P. Jean Baudrillard i fotografia. *Kult. Współczesna* **2008**, *1*, 190–213.
60. Barański, J. Estetyzacja epistemologiczna a modele symulacyjne—W kontekście modelu anatomicznego Visual Human Project. *Acta Univ. Lodz. Folia Philos.* **2006**, *17*, 153–169.
61. Ihde, D. *Existential Technics*; State University of New York Press: Albany, NY, USA, 1983; ISBN 978-087-395-687-1.
62. McLuhan, M.; McLuhan, E. *Laws of Media: The New Science*; University of Toronto Press: Toronto, CA, USA, 1988; ISBN 978-080-205-782-2.
63. Sui, D.; Goodchild, M. A tetradic analysis of GIS and society using McLuhan's law of the media. *Can. Geogr.* **2003**, *47*, 5–17. [[CrossRef](#)]
64. Lambers, K.; Traviglia, A. Automated detection in remote sensing archaeology: A reading list. *AARGnews* **2016**, *53*, 25–29.
65. Davis, D. Object-based image analysis: A review of developments and future directions of automated feature detection in landscape archeology. *Archeol. Prospect.* **2018**, *26*, 155–163. [[CrossRef](#)]
66. Traviglia, A.; Cowley, D.C.; Lambers, K. Finding common ground: Human and computer vision in archaeological prospection. *AARGnews* **2016**, *53*, 11–24.
67. Sevara, C.; Pregebauer, M.; Doneus, M.; Verhoeven, G.; Trinks, I. Pixel versus object—A comparison of strategies for semi-automated mapping of archaeological features using airborne laser scanning data. *J. Archaeol. Sci. Rep.* **2016**, *5*, 485–498. [[CrossRef](#)]

68. Blaschke, T.; Strobl, J. What's wrong with pixels? Some recent developments interfacing remote sensing and GIS. *Geobit/Gis* **2001**, *6*, 12–17.
69. Guirado, E.; Tabik, S.; Alcaraz-Segura, D.; Cabello, J.; Herrera, F. Deep-learning *Versus* OBIA for Scattered Shrub Detection with Google Earth Imagery: *Ziziphus lotus* as Case Study. *Remote Sens.* **2017**, *9*, 1220. [[CrossRef](#)]
70. Lambers, K.; Verschoof-van der Vaart, W.B.; Bourgeois, Q.P.J. Integrating Remote Sensing, Machine Learning, and Citizen Science in Dutch Archaeological Prospection. *Remote Sens.* **2019**, *11*, 794. [[CrossRef](#)]
71. Maxwell, A.E.; Warner, T.A.; Fang, F. Implementation of machine-learning classification in remote sensing: An applied review. *IJRSE* **2018**, *39*, 2784–2817. [[CrossRef](#)]
72. Trier, Ø.T.; Cowley, D.C.; Waldeland, A.U. Using deep neural networks on airborne laser scanning data: Results from a case study of semi-automatic mapping of archaeological topography on Arran, Scotland. *Archaeol. Prospect.* **2018**, *26*, 1–11. [[CrossRef](#)]
73. Kazimi, B.; Thiemann, F.; Malek, K.; Sester, M.; Khoshelham, K. Deep Learning for Archaeological Object Detection in Airborne Laser Scanning Data. In Proceedings of the 2nd Workshop On Computing Techniques for Spatio-Temporal Data in Archaeology and Cultural Heritage, Melbourne, Australia, 25–28 August 2018; pp. 21–35. [[CrossRef](#)]
74. Verschoof-van der Vaart, W.B.; Lambers, K. Learning to Look at LiDAR: The Use of R-CNN in the Automated Detection of Archaeological Objects in LiDAR Data from the Netherlands. *JCAA* **2019**, *2*, 31–40. [[CrossRef](#)]
75. Davies, D.S.; Sanger, M.C.; Lipo, C.P. Automated mound detection using lidar and object-based image analysis in Beaufort County, South Carolina. *Southeast. Archaeol.* **2019**, *38*, 23–37. [[CrossRef](#)]
76. Barfield, W. *Cyber-Humans: Our Future with Machines*; Springer: Berlin/Heidelberg, Germany, 2015; ISBN 978-331-925-048-9.
77. Bathaee, Y. The Artificial Intelligence Black Box and the Failure of Intent and Causation. *Harv. J. Law Technol.* **2018**, *31*, 889–938.
78. Minta-Tworzowska, D. Continuity and change of classification in archaeology. In *Theory and Practice of Archaeological Research, Vol. III: Dialogue with the Data: The Archaeology of Complex Societies and Its Context in the '90*; Tabaczyński, S., Ed.; Institute of Archaeology and Ethnology Polish Academy of Sciences: Warszawa, Poland, 1998; pp. 191–223. ISBN 978-838-546-366-5.
79. Bennett, R.; Cowley, D.; De Laet, V. The data explosion: Tackling the taboo of automatic feature recognition in airborne survey data. *Antiquity* **2014**, *88*, 896–905. [[CrossRef](#)]
80. Johnson, M. Landscape studies: The future of the field. In *Landscape Archaeology between Art and Science. From a Multi- to an Interdisciplinary Approach*; Kluiving, S., Guttman-Bond, E., Eds.; Amsterdam University Press: Amsterdam, The Netherlands, 2012; pp. 515–525. ISBN 978-908-964-418-3.
81. Logg, J.M. Using Algorithms to Understand the Biases in Your Organization, Harvard Business Review. Decision Making. 2019. Available online: <https://hbr.org/2019/08/using-algorithms-to-understand-the-biases-in-your-organization#> (accessed on 17 March 2020).
82. Brophy, K. Subjectivity, bias and perception in aerial archaeology. In *From the Air: Understanding Aerial Archaeology*; Brophy, K., Cowley, D., Eds.; Tempus: Stroud, UK, 2005; pp. 33–49. ISBN 978-075-243-130-7.
83. Cowley, D.; Gilmour, S. Some observations on the nature of aerial survey. In *From the Air: Understanding Aerial Archaeology*; Brophy, K., Cowley, D., Eds.; Tempus: Stroud, UK, 2005; pp. 50–63. ISBN 978-075-243-130-7.
84. Wilson, D. Bias in aerial reconnaissance. In *From the Air: Understanding Aerial Archaeology*; Brophy, K., Cowley, D., Eds.; Tempus: Stroud, UK, 2005; pp. 64–72. ISBN 978-075-243-130-7.
85. Casana, J. Regional-Scale Archaeological Remote Sensing in the Age of Big Data. Automated Site Discovery vs. Brute Force Methods. *Adv. Archaeol. Prac.* **2014**, *2*, 222–233. [[CrossRef](#)]
86. Kokalj, Ž.; Somrak, M. Why Not a Single Image? Combining Visualizations to Facilitate Fieldwork and On-Screen Mapping. *Remote Sens.* **2019**, *11*, 747. [[CrossRef](#)]
87. Bewley, R.H.; Rączkowski, W. Past achievements and prospects for the future development of aerial archaeology: An introduction? In *Aerial Archaeology: Developing Future Practice*; Bewley, R.H., Rączkowski, W., Eds.; IOS Press: Amsterdam, The Netherlands, 2002; pp. 1–8. ISBN 978-158-603-184-8.
88. Brophy, K. The hermeneutic spiral: Aerial archaeology and subjectivity. *AARGnews* **2005**, *1*, 5–11.
89. Mills, J. Bias and the World of the Vertical Aerial Photograph. In *From the Air: Understanding Aerial Archaeology*; Brophy, K., Cowley, D., Eds.; Tempus: Stroud, UK, 2005; pp. 117–126. ISBN 978-075-243-130-7.

90. Goldstein, B. *Sensation and Perception*, 9th ed.; Wadsworth. Cengage Learning: Belmont, CA, USA, 2010; ISBN 978-113-395-849-9.
91. Michalik, T. Between eye and the mind. Technology, cognition and knowledge development—Eye-tracking study report. *AARGnews* **2014**, *48*, 24–34.
92. Quinlan, P.T.; Dyson, B. *Cognitive Psychology*; Pearson/Prentice Hall: Harlow, UK, 2008; ISBN 978-013-129-810-1.
93. Braisby, N.; Gellatly, A. *Cognitive Psychology*; Oxford University Press: Oxford, UK, 2012; ISBN 978-019-923-699-2.
94. Strenberg, R.J.; Sternberg, K. *Cognitive Psychology*, 6th ed.; Wadsworth. Cengage Learning: Belmont, CA, USA, 2012; ISBN 978-111-134-476-4.
95. Fleck, L. 1979. *Genesis and Origin of a Scientific Fact*; The University of Chicago Press: Chicago, IL, USA, 1979; ISBN 978-022-625-325-1.
96. Cohen, R.S.; Schnelle, T. *Cognition and Fact. Materials on Ludwik Fleck*; D. Reidel Publishing Company: Boston, MA, USA, 1986; ISBN 978-902-771-902-7.
97. Jasanoff, S. Genealogies of STS. *Soc. Stud. Sci.* **2012**, *42*, 435–441. [[CrossRef](#)]
98. Peine, A. Challenging Incommensurability: What We Can Learn from Ludwik Fleck for the Analysis of Configurational Innovation. *Minerva* **2011**, *49*, 489–508. [[CrossRef](#)] [[PubMed](#)]
99. Rydlewski, M. *Żeby Widzieć, Trzeba Wiedzieć. Kulturowy Wymiar Percepcji Wzrokowej*; Oficyna Wydawnicza Epigram: Bydgoszcz, Poland, 2016; ISBN 978-836-123-169-1.
100. Wittgenstein, L. *Philosophical Investigations*; Basil Blackwell: Oxford, UK, 1986; ISBN 0-631-11900-0.
101. Fish, S. *Is There a Text in Their Class? The Authority of Interpretive Communities*; Harvard University Press: Cambridge, MA, USA, 1980; ISBN 978-067-446-725-5.
102. Poller, T. The craft of earthwork survey. In *Re-mapping Archaeology: Critical Perspectives, Alternative Mappings*; Gilling, M., Hacıgüzeller, P., Lock, G., Eds.; Routledge: London, UK, 2018; pp. 117–139. ISBN 978-113-857-713-8. [[CrossRef](#)]
103. Torge, W. Müfflings geodätisches Wirken in der Umbruchepoche vom 18. zum 19. Jahrhundert. *ZfV* **2002**, *127*, 97–108.
104. Opondo, S.O.; Shapiro, M.J. *The New Violent Cartography. Geo-Analysis after the Aesthetic Turn*; Routledge: London, UK, 2012; ISBN 978-041-578-284-5.
105. Babich, B. From Fleck’s Denkstil to Kuhn’s paradigm: Conceptual schemes and incommensurability. *Int. Stud. Philos. Sci.* **2003**, *17*, 75–92. [[CrossRef](#)]
106. Sady, W. Ludwik Fleck. In *Stanford Encyclopedia of Philosophy*; 2016; Available online: <https://plato.stanford.edu/entries/fleck/#3> (accessed on 2 May 2020).
107. Sady, W. Ludwik Fleck—Thought collectives and thought styles. *Poznań Stud. Philos. Sci. Humanit.* **2001**, *74*, 197–205.
108. Fleck, L. The problem of epistemology. In *Cognition and Fact. Materials on Ludwik Fleck*; Cohen, R.S., Schnelle, T., Eds.; D. Reidel Publishing Company: Boston, MA, USA, 1986; pp. 79–112. ISBN 978-902-771-902-7.
109. Bourdieu, P. *Outline of a Theory of Practice*; Cambridge University Press: Cambridge, UK, 1977; ISBN 978-052-129-164-4.
110. Nietzsche, F. *The Will to Power*; Random House: New York, NY, USA, 1968; ISBN 978-039-470-437-1.
111. Lynch, M.P. *The Nature of Truth. Classic and Contemporary Perspectives*; A Bradford Book, MIT Press: Cambridge, MA, USA, 2001; ISBN 978-026-262-145-8.
112. Lyotard, J.F. *The Postmodern Condition: A Report on Knowledge*; University of Minnesota Press: Chicago, IL, USA, 1984; ISBN 978-081-661-166-9.
113. Kokalj, Ž.; Hesse, R. *Airborne Laser Scanning Raster Data Visualization: A Guide to Good Practice*; Založba ZR: Ljubljana, Slovenia, 2017; ISBN 978-961-254-984-8.
114. Guzowska, B. Estetyzacja—Nowa matryca kultury. *Człowiek I Społeczeństwo* **2015**, *39*, 57–67. [[CrossRef](#)]
115. Perkowska, H. *Postmodernizm a Metafizyka*; Scholar: Warszawa, Poland, 2003; ISBN 978-837-383-009-7.
116. Casey, J. *The Language of Criticism*; Barnes & Noble: London, UK, 1966.
117. Austin, J.L. *How to Do Things with Words: The William James Lectures Delivered at Harvard University in 1955*; Clarendon Press: Oxford, UK, 1962; ISBN 978-067-441-150-0.
118. Miller, G.R. On being persuaded: Some basic distinctions. In *Persuasion: New Directions in Theory and Research*; Roloff, M.E., Miller, G.R., Eds.; Sage Publications: Beverly Hills, CA, USA, 1980; pp. 11–28. ISBN 978-080-391-213-7.

119. Perloff, R.M. *The Dynamics of Persuasion. Communication and Attitudes in the 21st Century*; Lawrence Erlbaum Associates Publishers: Mahwah, NJ, USA, 2003; ISBN 978-080-584-087-2.
120. Hooper-Greenhill, E. *Museums and Education. Purpose, Pedagogy, Performance*; Routledge: London, UK, 2007; ISBN 978-041-537-936-6.
121. Welsch, W. *Undoing Aesthetics*; Sage Publications: London, UK, 1997; ISBN 978-076-195-594-8.
122. Shusterman, R. Aesthetic Argument and Perceptual Persuasion. *Critica* **1983**, *15*, 51–74. [[CrossRef](#)]
123. Mitchell, W.J.T. Showing seeing: A critique of visual culture. *J. Vis. Cult.* **2002**, *1/2*, 165–181. [[CrossRef](#)]
124. Huggett, J. A manifesto for an introspective digital archaeology. *Open Archaeol.* **2015**, *1*, 86–95. [[CrossRef](#)]
125. Cowley, D.; Opitz, R. Topografia archeologiczna: Dane 3D, obserwacja, wizualizacja i interpretacja. In *Lotnicze Skanowanie Laserowe Jako Narzędzie Archeologii*; Gojda, M., Kobyliński, Z., Eds.; Fundacja Res Publica Multiethnica: Warszawa, Poland, 2018; pp. 45–55. ISBN 978-839-483-523-1.
126. Rebes, M. Filozoficzny protest Heideggera wobec współczesnej nauki i techniki. *Rocz. Kult.* **2016**, *7/1*, 131–145. [[CrossRef](#)]
127. Clarke, D. Archaeology: The loss of innocence. *Antiquity* **1973**, *47*, 6–18. [[CrossRef](#)]
128. Reuter, R. *Remote Sensing of Science, Education, and Natural and Cultural Heritage*; IOS Press: Amsterdam, The Netherlands, 2010; ISBN 978-300-033-435-1.
129. Hanson, W.; Oltean, I. *Archaeology from Historical Aerial and Satellite Archives*; Springer: Heidelberg/Berlin, Germany, 2012; ISBN 978-146-144-504-3.
130. Lasaponara, R.; Masini, N. *Advances on Remote Sensing for Archaeology and Cultural Heritage Management*; Aracne Editrice: Rome, Italy, 2008; ISBN 978-885-482-030-2.
131. Tapete, D. *Remote Sensing and Geosciences for Archaeology*; MDPI AG: Basel, Switzerland, 2019; ISBN 978-303-842-763-6.
132. Lasaponara, R.; Masini, N. *Satellite Remote Sensing: A New Tool for Archaeology*; Springer: Heidelberg/Berlin, Germany, 2012; ISBN 978-904-818-800-0.
133. Czajlik, Z.; Bödőcs, A. *Aerial Archaeology and Remote Sensing from the Baltic to the Adriatic*; Eötvös Loránd University: Budapest, Hungary, 2013; ISBN 978-963-734-395-7.
134. Hadjimitsis, D.; Themistocleous, K.; Cuca, B.; Agapiou, A.; Lysandrou, V.; Lasaponara, R.; Masini, N.; Schreier, G. *Remote Sensing for Archaeology and Cultural Landscapes. Best Practices and Perspectives Across Europe and the Middle East*; Springer: Heidelberg/Berlin, Germany, 2020; ISBN 978-303-010-978-3.
135. Campana, S.; Forte, M.; Liuzza, C. (Eds.) Space, Time, Place. In Proceedings of the Third International Conference on Remote Sensing in Archaeology, Tiruchirappalli, India, 17–21 August 2009; Archaeopress: Oxford, UK, 2010. ISBN 978-140-730-659-9.
136. Opitz, R. Three Dimensional Field Recording in Archaeology: An Example from Gabii. In *Visions of Substance: 3D Imaging in Mediterranean Archaeology*; Olson, B.R., Caraher, W.R., Eds.; The Digital Press at the University of North Dakota: Grand Forks, ND, USA, 2015; pp. 73–86. ISBN 978-069-236-839-8.



© 2020 by the author. Licensee MDPI, Basel, Switzerland. This article is an open access article distributed under the terms and conditions of the Creative Commons Attribution (CC BY) license (<http://creativecommons.org/licenses/by/4.0/>).



Article

# Bringing Lunar LiDAR Back Down to Earth: Mapping Our Industrial Heritage through Deep Transfer Learning

Jane Gallwey \*, Matthew Eyre, Matthew Tonkins and John Coggan

Camborne School of Mines, University of Exeter, Tremough Campus, Penryn TR10 9EZ, UK

\* Correspondence: j.gallwey@exeter.ac.uk

Received: 31 July 2019; Accepted: 21 August 2019; Published: 28 August 2019

**Abstract:** This article presents a novel deep learning method for semi-automated detection of historic mining pits using aerial LiDAR data. The recent emergence of national scale remotely sensed datasets has created the potential to greatly increase the rate of analysis and recording of cultural heritage sites. However, the time and resources required to process these datasets in traditional desktop surveys presents a near insurmountable challenge. The use of artificial intelligence to carry out preliminary processing of vast areas could enable experts to prioritize their prospection focus; however, success so far has been hindered by the lack of large training datasets in this field. This study develops an innovative transfer learning approach, utilizing a deep convolutional neural network initially trained on Lunar LiDAR datasets and reapplied here in an archaeological context. Recall rates of 80% and 83% were obtained on the 0.5 m and 0.25 m resolution datasets respectively, with false positive rates maintained below 20%. These results are state of the art and demonstrate that this model is an efficient, effective tool for semi-automated object detection for this type of archaeological objects. Further tests indicated strong potential for detection of other types of archaeological objects when trained accordingly.

**Keywords:** deep learning; transfer learning; historic mining; heritage management; LiDAR

## 1. Introduction

Airborne LiDAR systems are an increasingly valuable tool for locating, visualizing and understanding cultural heritage sites. The ability to perceive subtle depressions and patterns in the landscape uncoupled from photometric representations has led to discoveries ranging from additional monuments at Stonehenge [1] to Mayan cave dwelling entrances in Belize [2]. These are examples of the more traditional uses of LiDAR in archaeology, where data over a small area is visually analyzed through an experience and knowledge based process to obtain a detailed understanding of a landscape, usually by displaying the LiDAR data as a hillshaded image [3]. This approach is effective for discrete areas, especially where high resolution datasets have been gathered, but does not fully leverage the advantages of newly available large scale general purpose LiDAR datasets [4]. Whilst analysis by experts will always produce the best results, the increasing availability of these new datasets now requires a paradigm change towards the integration of computer aided detection to take advantage of these greatly increased volumes of data [5].

In England alone, the Environment Agency has pledged nationwide coverage at 1 m resolution or higher by 2020, totaling over 130,000 km<sup>2</sup> of coverage [6]. Scotland has currently been partially covered by a two phase campaign, with more coverage planned for the future [4]. Analyzing these volumes of data efficiently by human operators is extremely challenging. For example, the English Heritage National Mapping Program (primarily aerial image interpretation) achieves a coverage rate of approximately 1 km<sup>2</sup> per person per day; this project has been running for over 20 years employing on average 15–20 staff

and had covered an area of 52,000 km<sup>2</sup> by 2012, in contrast, the Baden-Württemberg study, whilst still a primarily manual approach, took advantage of automated processing where possible, allowing an estimated coverage rate of over 35,000 km<sup>2</sup> by a single operator in six years [7]. These two projects are not directly comparable, as the quality and accuracy of their results varies greatly along with the data types analyzed [3], but it is an indication of the speed advantages gained from integrating automated processes into an analysis workflow. Despite the differing data types, the English Heritage study provides an indication of the timescales required to put human eyes over nationwide remotely sensed data tiles at a high resolution scale. With current advances in computing power the potential to pre-process entire national datasets in weeks rather than decades is now a distinct possibility.

This approach would be particularly valuable for countries which do not have many existing historic site records; a rapid Artificial Intelligence (AI) scan would provide a preliminary database which could be developed further as more resources become available. Due to the very low time and cost overheads required for automated processing there can be complementarity between achieving the quantity of the automated results versus the quality of traditionally generated databases, which can proceed to be created as normal in tandem to the automated processing. Even if imprecise, these machine learning tools would be capable of identifying the greater trends in the data [3], allowing human resources to be prioritized to the areas with a large number of potential sites for detailed precision mapping. Especially when sites are under threat from development, rapid identification and mapping would give cultural heritage managers more time to act.

In the UK, sites such as those defined by English Heritage as National Importance sites would also benefit from a semi-automated approach. These are sites that are deemed to have national importance but are not currently or cannot be designated as heritage assets and scheduled monuments [8]. Many of these sites have a landscape scale, consisting of ‘a coherent and contiguous group of monuments, the group value of which augments the significance or importance of each, though the importance of the whole landscape can also be defined in its own terms’ [8]. Identification and delineation of sites such as these remains a challenge due to limited mapping resources and the large extent of these sites. Large-scale monument counting tools, especially if cheap and efficient to run, would underpin more informed management of these types of sites, provided the sites present above ground topographical representations visible to an aerial LiDAR sensor. The results from such a preliminary survey could be stored in a geospatial database such as that described in [9].

Alongside the vast speed improvements possible from semi-automated detection, computer-based methods have other strengths compared to human observers. Humans are inherently unable to process height data in its native state; therefore, it must be processed to create visualizations that are interpretable by the human eye. This can lead to a loss of information, image artefacts [10] or a bias stemming from the visualization techniques used [11]. As a computer can process the single channel numeric gridded height data directly, this removes some of these issues. Conversely, multi-channel or hyperspectral data containing more than three channels is also not easily representable in a human readable form [12], whereas a computer can stack as many channels as necessary to process hyperspectral or multiple data source imagery. Artificial intelligence based solutions can also make their own generalizations and assumptions; often different to those that a human would make. Whilst this in itself will create biases, discussed later in this work, the addition of a very alien ‘brain’ to the problem will go some way to alleviate human biases. Humans see what they are expecting to see [13], and a trained neural network will also see what it is expecting to see; using both allows for potentially unexpected objects to be discovered.

However, despite all the advantages discussed above, computer aided methods are still inferior to human interpretation in terms of accuracy, inference and knowledge [3]. To benefit from the power of automation whilst maintaining the experience and insight gained from human experts a twofold approach is needed. The challenge lies in both improving the algorithms to a point where they are ‘fit for purpose’ and integrating the semi-automated detections into the archaeological prospection workflow in an appropriate manner [3]. It is envisioned that once applicable tools have been designed, they would

be run as a pre-processing step over entire datasets, narrowing the areas to be inspected manually. Another integration possibility is the combined citizen science and automation workflow proposed in [14]. The integration of citizen science is already a powerful and well developed methodology for both conventional and semi-automated LiDAR projects addressing the need for more manpower than is available from experts in the field, alongside leveraging the intimate knowledge of a local area provided by the people who live, work and recreate there [15,16]. However, a major building block of any large-scale site detection system is the algorithm itself; accurate, generalizable and repeatable methods are required to create confidence in such a system and much research has been focused on this problem.

Early methods for semi-automated archaeological site identification used template matching (where a predefined template is passed over the scene) or rule-based methods (where rules are applied to determine an object's category). Successful applications of template matching are described by Trier in [17,18]. Other proposed methods utilize Geographic Object-Based Image Analysis (GEOBIA), examples of these are described in Sevara et al. [19] and Freeland et al. [20]. These types of techniques require prior knowledge of the shape and size of the object to be identified and perform well on relatively simple geometries but are less effective at generalizing to unseen or partially occluded examples [21]. This is because these methods are responding to preprogrammed definitions of the object to be detected rather than 'taught' about the object features.

Machine learning is where a computer model is developed that can recognize features. The model is developed by 'training'—a process by which known examples are fed into the model and it is adjusted until it can predict the correct answer. The model is then evaluated with a second set of known examples (to ensure that the model does not simply memorize the data) before being used in a real situation. There are many types of machine learning algorithms from simple statistical models to deep neural networks. Recently, some results with very high accuracy have been obtained by combining an advanced visualization technique based on topographic deviation at multiple scales with a random forest machine learning classifier to identify Neolithic burial mounds [22].

In the field of computer vision, a particular type of neural network called a convolutional neural network (CNN) has been shown to be capable of solving diverse and complex problems such as visual image question answering [23] and real time object detection for over 9000 categories [24]. Considerable research has been carried out in the broader remote sensing community as to how to design and modify similar systems for aerial remote sensing tasks. Primarily this work has involved Very High Resolution (VHR) images as the input to the CNN, either building their own network architecture [25] or modifying and fine tuning existing computer vision models [26,27]. Nogueira et al. [28] give an overview of the advantages and disadvantages of these approaches, concluding that fine tuning an existing trained model provides the best results, however, the lack of an appropriate training datasets makes it very difficult to develop a model. Borrowing a similar model and transferring it to the problem at hand is one possible solution [29].

The primary balance that must be addressed when choosing an approach is the applicability of the model versus the availability of training data. If training data and computing power allow, the ideal scenario is to design and train a model from scratch for the required task using the specific data that is required. However, available training datasets for remote sensing data are small and usually not representative of a wide range of environments. Conversely, labelled training datasets in the computer vision community are vast: ImageNet has over 14 million labelled images in 20,000 object categories [30] and models trained on these large datasets tend to be less prone to overfitting and can generalize well compared to ones trained on small datasets [28]. However, there are differences in the type of objects they have been trained to detect. For example, in computer vision the objects tend to take up more of the frame and can appear at very different scales, but generally not in many different rotations, whereas for aerial data the scale is relatively constant, but the object can have many rotations [27]. When using a pretrained model to generalize to images created from a LiDAR DEM the problem is exacerbated, as most existing models have been trained on three channel RGB images and

not one channel depth images. This, along with the differing ways that objects appear in a LiDAR DEM versus imagery, can make transfer learning with LiDAR data challenging [31].

Two published studies have used CNNs with LiDAR data to identify archaeological objects, with promising results. Trier et al. [32] found strong positive identifications on one dataset but on their second dataset, which contained more varied objects, their results were less conclusive. Verschoof-van der Vaart and Lambers [33] employed a similar methodology using variously trained versions of the same pretrained deep learning model to detect multiple classes of archaeological objects, achieving accuracy scores comparable or surpassing those obtained by the other machine learning methods. In both studies a transfer learning technique was used, with the essential methodology involving the generation of a local relief model [34] from the LiDAR data and then either converting this generated single channel image into a conventional three channel image stack by triplicating the greyscale channel [32] or by modifying the input layer of the CNN [33]. Both studies used models that had been trained on RGB images of terrestrial scenes such as ImageNet. A recommendation from both studies was to use a model pretrained on data more similar to LiDAR data in the future; however, obtaining such models was determined to be challenging.

A possible solution can be found in the planetary remote sensing field. Large planet scale digital DEM datasets exist from sources such as the Lunar Reconnaissance Orbiter [35] and the Mars Global Surveyor [36]. Several studies have built and trained CNNs to detect craters from these datasets [37–39]. These models are designed to be highly receptive to elevation changes and to roughly circular patterns observed in single channel DEM images. This makes them a good fit for the problem of archaeological object detection. An example of this type of model was built by Silburt et al. [37], based on the U-net semantic segmentation model, itself originally designed for medical image segmentation [40]. This model, named DeepMoon (Available at <https://github.com/silburt/DeepMoon.git>) was trained on 30,000 labelled images randomly extracted over the entire surface of the moon combined with the existing catalogues of moon craters. This is a larger and more robust training data set than those available for archaeological remote sensing, solving the problem of applicable transfer learning datasets.

In this paper we propose a highly effective transfer learning strategy to detect historic mining pits utilizing the DeepMoon base model fine-tuned with local LiDAR data. Several different resolutions and representations of LiDAR data are tested, and the final model predictions are verified with a full ground inspection. Mining remains were chosen as the class of interest as there is a rich mining cultural history in South West England, and the evidence of these historic extractive industries is both numerous and well recorded. These mining areas are also suitably covered by freely available high-resolution LiDAR data. Whilst this model has been trained and tested specifically to detect historic mining pits, it is hypothesized that the principals will remain true for any archaeological feature that presents with a circular height change in aerial LiDAR data, such as: Charcoal kilns [41], pitfall traps [42], shell rings [43], conical mounds [18,20,43] and roundhouses [32] Thus, our method has potential applicability across many archaeological prospection challenges when furnished with appropriate training data.

## 2. Materials and Methods

### 2.1. Study Area

The primary study area for this research is Dartmoor National Park, an upland area of moorland studded with exposed granite hilltops known as tors. The ground cover is primarily low vegetation, including heather, bracken, gorse, fern and marsh grasses. Tin and copper mining on Dartmoor has taken place almost continuously from the 12th to the 20th centuries and the remains are pervasive and visually striking throughout the landscape [44]. Three areas of concentrated historic mining activity were used to develop this deep learning model; these are shown in Figure 1. The different colors in Figure 1 refer to the distribution of training, validation and testing data. The training and validation areas include in the north the old Birch Tor Mine (1726–1928) [45] and in the south the

former Whiteworks Mine. It is believed that the Whiteworks area was being mined as early as 1180 although the mine was expanded substantially around 1790 towards the beginning of the industrial revolution when the demand for tin increased [45]. The mine was owned by the wealthy Tavistock mining entrepreneur Moses Bawden and operated for just under 100 years until 1880, briefly reopening in early 1900 before finally closing for good by 1914 [46]. The test area for Dartmoor is the site of Hexworthy Mine (1891–1912). This is an interesting site as it displays remains from multiple eras of mining; from the early unrecorded open workings, through traditional 19th century mining to semi-modern 20<sup>th</sup> century workings [47]. The mine operated productively until the call up for men in 1914, during the war it was placed in care and maintenance before a large storm in 1920 destroyed the waterwheel flume, causing the underground workings to flood [46].

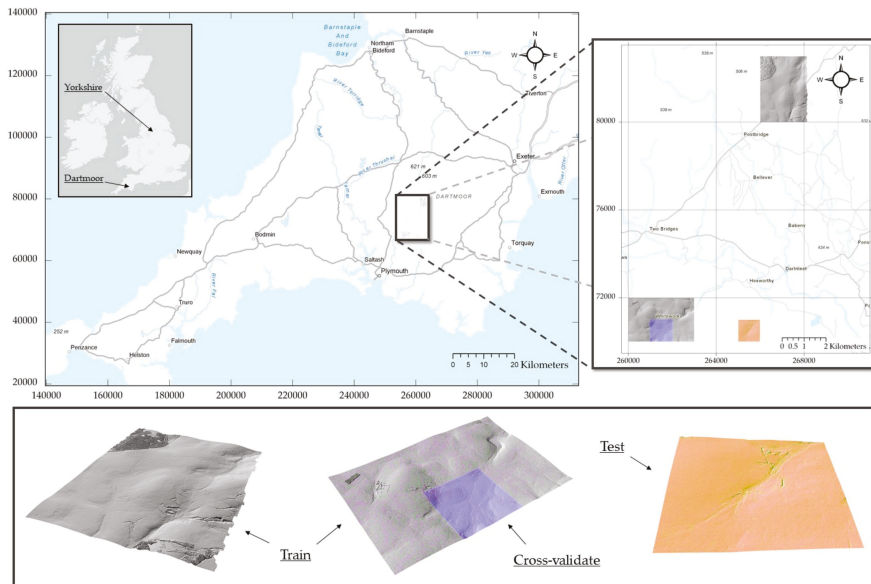


**Figure 1.** Overview of the Dartmoor dataset. Grey areas represent training data (14 tiles), the purple tile shows the cross validation area and the orange tile shows the test area. Coordinate system British National Grid, image data © Environment Agency 2015 & Getmapping Plc. Basemap © ESRI 2019.

A further testing area was selected in the Yorkshire Dales National Park more than 500 km from Dartmoor to examine the model’s ability to generalize to new locations, mine types and data resolutions. This test area is part of the site of the former Grassington Moor lead mine. The first known exploitation of lead at Grassington was by the 4th Earl of Cumberland in the early 17th century, although it is thought that some primitive extraction and smelting had taken place earlier. The early exploitation involved the digging of shallow shafts along the vein. The first mill to process the Grassington lead ore was the Low Mill built in 1605. The test area covers the western part of the Yarnbury mine, including Tomkins, Barretts and Good Hope shafts [48].

In all cases, the objects to be detected are trial pits, shallow pit workings and shaft heads. Examples of these are shown in Figure 2. Trial pits are dug whilst prospecting for tin lodes. They are usually 2–3 m in diameter, of limited depth (up to 1 m) and are often silted, water filled and reedy [44]. Shallow pit workings are comprised of alignments of deeper pits which are dug to below the soil overburden and mined downwards from there; however, these are not underground mines and there is no lateral development between the pits. The depth of these types of workings would be limited by the ability of the surrounding side-walls to remain intact before collapsing, which is usually less than 3 m. These

workings present as conical depressions often accompanied by a ring of spoil material, crescentic on the downhill side in sloping ground [44]. The final category are shafts for true underground mines. These have mainly been capped or backfilled in Dartmoor for public safety; however, evidence may remain in the form of large conical pits or straight openings. Site inspections may reveal a collar of finished material lining the inside of the shaft, but this is generally not visible from aerial surveys.

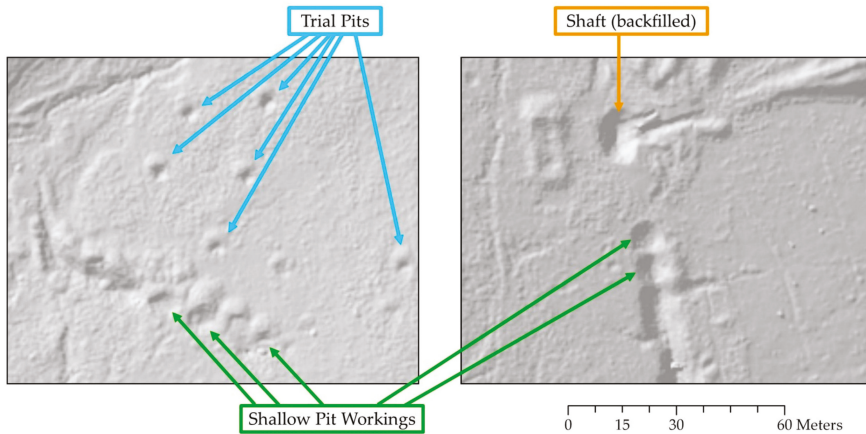


**Figure 2.** Examples of the historic mining objects found in this study displayed on a 315° azimuth 35° sun elevation hillshaded visualization created in ArcGIS. Base DSM © Environment Agency 2015.

## 2.2. Data Pre-Processing

The LiDAR datasets used for this project was obtained from the Environment Agency under their Open Government License and are available at <https://environment.data.gov.uk/> [49]. The Dartmoor data was flown in 2009 at a resolution of 0.5 m and the Yorkshire data in 2012 at a resolution of 0.25 m. In total twelve 1km × 1km tiles were processed for this study. Both datasets are available in either Digital Surface Model (DSM) or Digital Terrain Model (DTM) formats produced by the Environment Agency. The DSM was chosen in preference to the filtered DTM due to concerns that the filtering algorithms used to produce the DTM can excessively smooth small features [50].

The data was imported into ArcGIS Pro [51] along with several other interpretive layers such as historical maps [52] and aerial images [53] to create a GIS of the study area. Other GIS software could be used for this step, but ArcGIS Pro was chosen as it has a function for automatic exporting of image tiles and training labels, crucial for the later steps of the workflow. The additional GIS layers were only used to add context to the dataset to aid the human operator. To generate training and validation datasets, a desktop survey was carried out to identify features resembling mining pits. From this survey over 1,500 samples were identified and marked as point features. The test area dataset was created in the same way, but in order to validate the performance of the model every feature in the test set was also confirmed with a ground survey. This survey involved visiting the test sites with two reference maps, one containing the predictions and one containing the human generated pit locations from the desktop survey. Using these maps in conjunction with a handheld GPS for site orientation the true existence of pits shown on the maps was confirmed or rejected. The pits were not recorded with the GPS as in many cases it is not safe to access the ground directly above suspected shafts. A schematic of the project process is shown in Figure 3 and full details of the processing steps are provided in Supplementary Document S1.

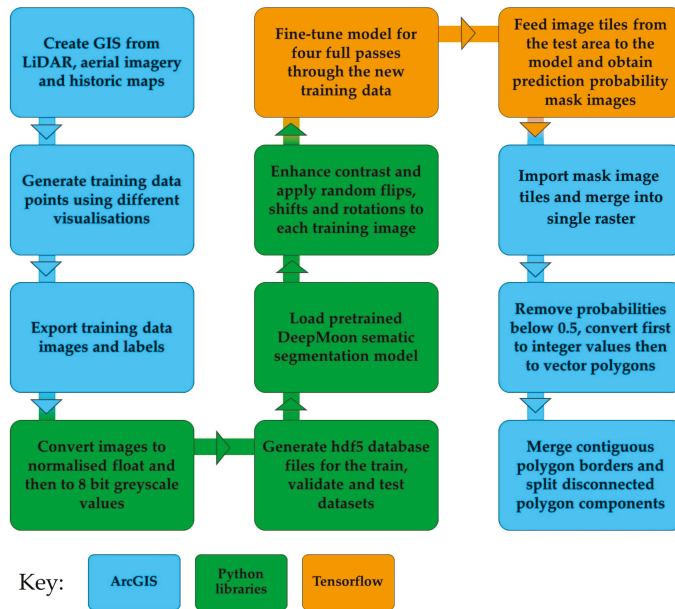


**Figure 3.** Methodology process diagram. Full details of the processing steps are provided in Supplementary Document S1.

For the model inputs, image tiles of  $256 \times 256$  pixels were exported along with the pit locations as xml labels to create image segmentation masks. The overlap between tiles was set to 52%. To preserve the fine detail in the DSM image, the image tiles first were exported as 16-bit float images with the values corresponding to the actual ground elevation of the data within that tile. Each tile was then individually rescaled to greyscale values between 0–1 maintaining its original distribution before finally being converted to an 8-bit integer format. To enhance contrast the image tiles were further rescaled linearly prior to model input. The image tile preparation process is shown in Figure 4. For the training and validation datasets, only image tiles which contain mining pits were exported. The training dataset contains 520 images and the test and validation datasets contain 70 images each. These datasets are stored in hdf5 format with the image names used as the database key. Table 1 shows the dataset split, number of pits and pit instances per dataset, along with the minimum, mean and maximum pits per image tile. The pit instances are greater than the number of pits as some pits are present on more than one image tile due to the >50% overlap between tiles.

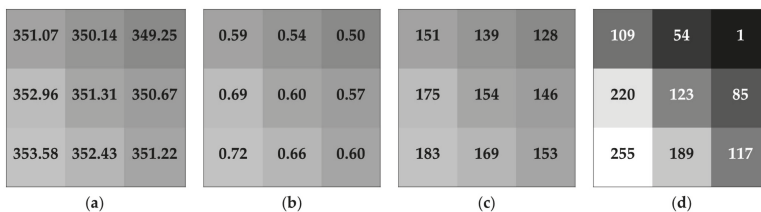


**Figure 4.** Overview of image preprocessing pipeline. (a) shows a selection of original individual pixel values, (b) shows the same pixels rescales between 0 and 1. (c) shows the conversion to greyscale. For subimages (a–c) the actual greyscale value does not change as the range is still determined by the elevation range across the original  $1 \text{ km} \times 1 \text{ km}$  DSM tile, in this simple example this is set as 20 m. (d) shows the pixel values after linearly rescaling by tile range.

Table 1. Dataset statistics.

Dataset	Image Tiles	Pit Ground	Pit Instances	Minimum	Mean	Maximum
Train	542	1568	3649	1	5.96	59
Cross-validate	71	254	423	1	5.96	33
Test Dartmoor	196	193	654	1	5.74	24
Test Yorkshire	900	172 <sup>1</sup>	n/a <sup>2</sup>	n/a <sup>2</sup>	n/a <sup>2</sup>	n/a <sup>2</sup>

<sup>1</sup> Only pits within a section of the dataset were ground truthed as shown in Figure 10c. <sup>2</sup> The Yorkshire dataset was exported for testing without human generated labels.

Other visualization of LiDAR data have been shown to aid in identification of archaeological features. Using the Relief Visualization Toolbox [10,54] several other representations of the data were generated from the original exported tiles. A simplified local relief model (SLRM) is a representation where the major features of the landscape have been removed. This process is known as detrending. These models are created first by smoothing a DEM so that small features are removed. The smoothed DEM is then compared to the original DEM and areas that are the same in both models are extracted to build the new smoothed DEM. This is finally subtracted from the original to produce the SLRM [34]. The SLRM is a very clear way to depict small relative changes in the landscape such as those from archaeological or mining features, and is the visualization method chosen by both [32,33] for their models.

Alongside the SLRM another visualization type known as openness was created. Openness is a geographical visualization technique that is calculated by measuring the angular size of a sphere either looking up or down from each pixel. It is described as either positive or negative openness. Negative openness is not the inverse of positive openness and highlights deep features instead of protruding features. As openness is calculated in relation to terrain rather than the sky, features on slopes appear the same as features on horizontal ground [55]. This is a valuable property for the Dartmoor data as most of the features are situated in rolling moorland terrain. Figure 5 illustrates the different visualization types generated for this study.

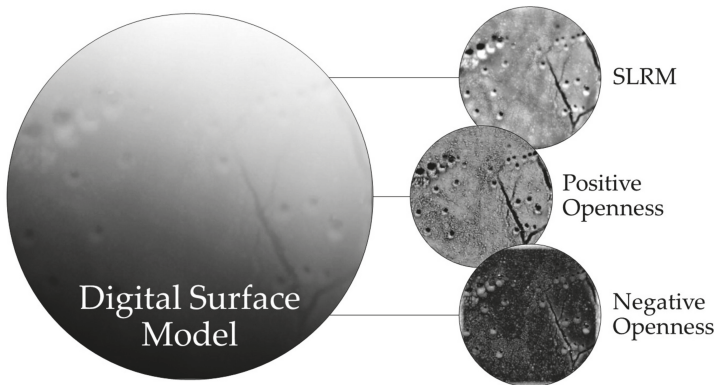


Figure 5. Illustration of the different advanced visualizations created from the original LiDAR DSM. Base DSM © Environment Agency 2015, visualizations created using the Relief Visualization Toolbox [54].

### 2.3. Deep Learning Model

The type of model used in this research is a variant of an Artificial Neural Network (ANN) known as a Convolutional Neural Network (CNN). A simple ANN contains one or more hidden layers, with every node in a hidden layer directly connected to every node in the layers before and after it. Each node has a weight associated with it which determines the final output result. When first initialized, the weights are randomly assigned and the first result from the network most likely will be incorrect.

The direction in which to change the weights to approach the correct answer is then determined using gradient descent and the weights are updated; this process is known as backpropagation. The network continues to feedforward and backpropagate until it has converged on a satisfactory result. Each input is treated individually, therefore a  $256 \times 256$  pixel image would have 65,536 inputs; as input images get larger the process becomes untenable.

The original Convolutional Neural Network was proposed by Lecun et al. [56], however the power of CNNs to solve complex image processing problems was not capable of being fully realized until the advent of powerful graphical processing units since 2010, with the first highly successful implementation [57] winning the 2012 Large-Scale Visual Recognition Challenge (ILSVRC) by a significant margin. CNNs improve upon the ANN design by allowing the sharing of weights across nodes, thus greatly decreasing the number of weights to optimize whilst also introducing spatial connectivity across the image. This is achieved by convolving a filter across the image which activates different underlying structures. The result of this convolution is a feature map. A single convolutional layer can have many filters, producing a multidimensional feature map of activations. To reduce the dimensionality of the image and increase the field of view of the filter, downsampling via max pooling is carried out on the layers to reduce the spatial dimensions. For a detailed description of the theory and mathematics of CNNs, see [58] Chapter 9.

In general, the lower layers of a CNN have high spatial resolution and describe the low level features which make up an image, and the upper layers have low spatial resolution and describe more complex patterns such as objects. For the task of image classification this is the final convolutional stage, as the question being asked is whether a certain object is present in the image. The next step, object detection is popularly achieved using R-CNNs, which use a region proposal network to identify areas of the image which may contain objects, these regions are then extracted and classified [59]. Finally, semantic segmentation, where every pixel in the image is assigned a class can be achieved by either extending the R-CNN approach [60] or by adding a deconvolutional network which up-samples the high level, low resolution feature layers by up-convolution to return to the resolution of the input image; this architecture is known as an encoder-decoder model [40].

Initially in this research an object detection pipeline using the Inception model [61] pretrained on the Common Objects in Context dataset [62] was trialed. The preliminary results from this method were reasonable but there appeared to be many mining pits not detected by the model even after 100,000 training epochs. Images from this initial method are shown in Figure 6. It is suspected that the mining pits detection task is simply too different from the original task to achieve optimum results. These initial tests showed a detection rate of less than 40%, this result, along with the recommendations from Trier et al. [32] motivated a search for a transfer learning candidate model that resembles more closely the task at hand instead of continuing to refine the Inception model.

After exploring several alternatives, the exact model chosen for this study is a version of the U-net model designed by Ronneberger et al. [40] and modified by Silburt et al. [37]. The U-net model is an encoder-decoder (see [63]) model with a near symmetrical architecture, designed for biomedical image segmentation. It has no final fully connected layer, replacing it with a  $1 \times 1$  convolutional layer with a sigmoidal activation function to output pixelwise class probabilities, thus reducing the number of hyperparameters to tune and making it more suitable for small numbers of training data. The original U-net achieved significant accuracy improvements over the next best architecture in the ISBI cell tracking challenge despite the training set only containing 35 images [40]. Biomedical image analysis shares many challenges with remote sensing LiDAR analysis such as small training sample sizes, single channel images and high resolution data. Therefore, it is more applicable to use a model such as U-net rather than one of the models designed for large datasets of natural images, as shown in Figure 6.

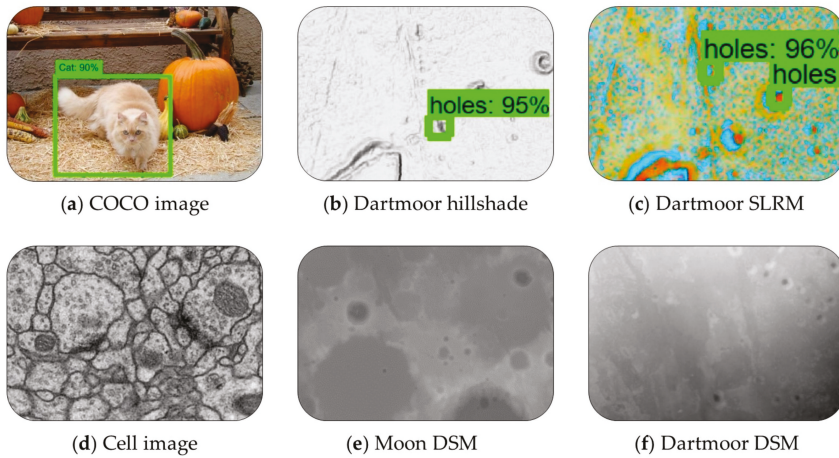


**Figure 6.** Examples of the input data to different pretrained models. (a) is an example from the Common Objects in Context (COCO) [62] dataset which many existing models are trained with and is similar to the image type found in ImageNet [30] and other natural photography datasets. (b) and (c) show the results from an object detector pre-trained using the COCO dataset. It can be seen that whilst it makes many correct detections there are also many missed pits. (d) shows the type of microscopy data which the U-net architecture was designed to segment [40] and (e) shows data from the lunar DSM which was used to pre-train the model used in this research [37]. (f) shows the DSM data used in this project. Base DSM in (b,c,f) © Environment Agency 2015.

#### 2.4. Transfer Learning

Nogueira et al. [28] found that for remote sensing problems with limited training data, a transfer learning strategy achieved the most accurate results across all tested datasets. In transfer learning, instead of initializing the model weights from scratch, the weights from another model trained for many epochs on a larger dataset are used. One transfer learning strategy involves removing the last layer of the network and replacing it with a layer to classify the objects of interest, this is required if the final classification categories are different. Another approach is to fine tune a model by adding new training examples whilst keeping the final output layer the same. All the model weights can be updated, or the lower layers can be frozen and only the weights in the upper layers are updated. For this research, as the classification is the same geometrically if ‘crater’ is substituted for ‘pit’ a fine-tuning strategy was employed with all weights unfrozen and the learning rate set to  $10^{-4}$ . As this study utilizes a pre-existing model, the same software (Python [64], TensorFlow [65] and Keras [66]) used by the creators of the original DeepMoon model [37] are used throughout. All of these packages are industry standard and available free from their respective websites.

#### 2.5. Training

In a neural network the hyperparameters can be used to control overfitting; for the DeepMoon model, the hyperparameters include weight regularization for the convolutional layers, dropout layers, filter size, model depth, and learning rate. Full details on these hyperparameters and complete model design can be found in [37]. These hyperparameters were chosen after a cross validation check using 60 models, where the hyperparameters were chosen randomly from across their standard ranges. To avoid overfitting on the small project dataset used in this research the hyperparameters chosen in [37] have been maintained here, with only minimal fine tuning training. Silbert’s base model was trained for 4 epochs (where one epoch equals a full pass through the entire training set). As the lunar dataset contained 30,000 images this training totaled 120,000 training examples. A standard learning

rate of  $10^{-4}$  was found to deliver the best results [37]. The additional training for transferring the model to its terrestrial archaeological context involved 4 more epochs of 520 images, totaling 2080 new training examples. The number of fine-tuning epochs was varied to determine the most effective fine-tuning strategy, this is discussed further in Section 3.1. To further control overfitting between epochs data augmentation is carried out, where all input images are randomly flipped, rotated and shifted prior to model input.

## 2.6. Post-Processing

Once the model is trained and verified against the cross validation dataset, individual image tiles to be tested are inputted to the model and probability masks are outputted as tif files. Using the same naming convention for both input and output files results in correct translation into the original coordinate system. Using ArcGIS, all output probability masks are then mosaiced into one continuous raster covering the entire test area.

For qualitative visual analysis and map creation, a graduated stretch symbology where solid color depicts probabilities of 1 and fully transparent depicts probabilities of 0 is used for maximum readability. This visualization scheme maintains information on the confidence of the prediction and allows for the more subtle workings of the model to remain visible. This enhances the model's readability in comparison to a yes/no response as it symbolizes uncertainty in the model, allowing an archaeological prospector more freedom to interpret the results using superior human reasoning. To quantitatively determine the rate of true positives, false negatives and false positives in order to report accuracy metrics, a new binary mask layer was created containing only pixels with prediction probabilities above 0.5. These pixels were then vectorized, merged and filled to create a vector layer of predicted pits to use in spatial queries. A comparison of these post processing methods is shown in Figure 7. It can be seen in Figure 7c that there are some incomplete rings, this is because some detections are made up of a mixture of pixels above and below 0.4 probability. This further supports the decision to use the full masks rather than the instances for interpretation where possible.

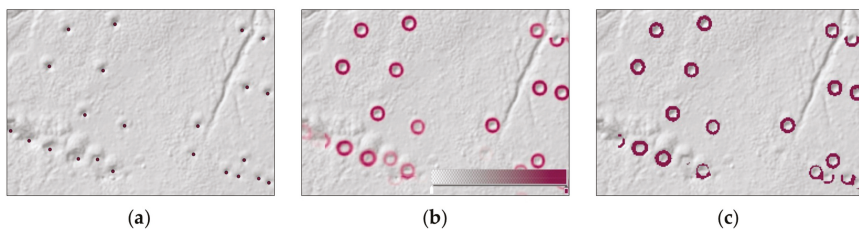


**Figure 7.** Comparison of qualitative and quantitative results representations. (a) shows the ground truth locations of a section of very shallow (30–50 cm depth) mining pits in the Hexworthy test area. (b) shows the model's predicted results depicted with a graduated transparency color scale representing model confidence and (c) shows a binary mask where all prediction pixels above 0.4 are assigned as 'pit' and all others are discarded. DSM © Environment Agency 2015.

## 3. Results

### 3.1. Cross Validation Results

During training binary cross-entropy was used as the loss metric; the training loss began at approximately 0.02 for the DSM and between 0.03–0.04 for the other visualization types, reducing to an average of 0.0146 for all data types after four epochs. There was negligible variation in the loss by visualization type. The cross validation loss remained within 0.005 of the training loss for each epoch with the average cross validation loss 0.0145 after four epochs. However, during human examination of the output masks it was observed that because the model is attempting to lower the global loss over

every pixel, the numeric values output from the TensorFlow console did not fully describe the real effectiveness of the model for detecting pit objects. This is suspected to be due to the fact that the model loss is a pixel based loss function rather than an object based one. Figure 8a displays the losses per epoch; showing that whilst the cross validation loss continues to decrease after four epochs, when compared to the F1 score shown in Figure 8b it can be seen that the real detection accuracy degrades after four epochs.

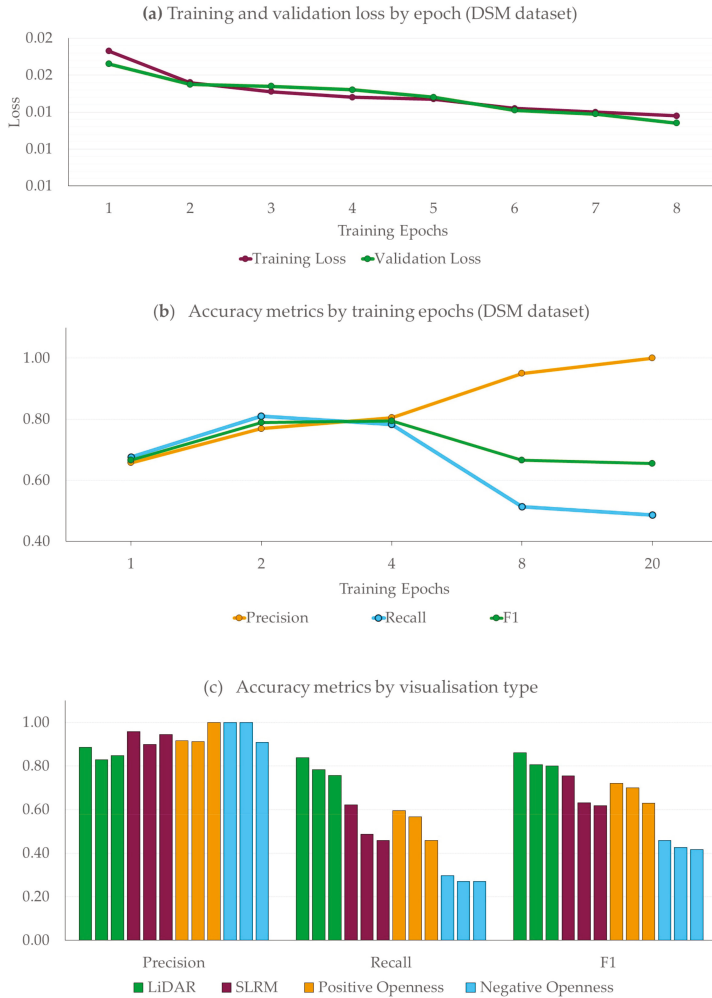


**Figure 8.** Training and validation loss by epoch across the entire validation dataset (a). Accuracy metrics by training epochs (b) and accuracy metrics by visualization type (c), both evaluated on sample tiles from the validation dataset. Note: (b) and (c) show accuracy metrics over only 5 tiles from the validation dataset chosen for their difficulty to evaluate model generalization ability. Therefore, they do not represent the accuracy obtained by the model on the test datasets.

In light of this, a much smaller human cross validation was carried out on five sample tiles from the cross validation dataset. These tiles were visually chosen after inspecting all tiles in the validation dataset to assess each model’s performance at both ends of the difficulty spectrum, from simple cases

with several well defined pits to complex cases with multiple ill-defined and overlapping pits or pits within larger trenches. To determine the optimal fine-tuning strategy, the number of epochs for which the model was retrained was varied and the results were examined by counting the detection instances over these tiles.

For each model and each tile, the number of true positives (correctly detected pits), false negatives (undetected pits) and false positives (detections which do not correspond to true pits) were counted. From these numbers the precision (the proportion of the model's pit predictions that were correct) and the recall (the proportion of actual pits that were detected) were calculated. The F1 score (harmonic mean of precision and recall) was also calculated, as it is a useful single valued accuracy metric for a detection problem of this kind (formulas defined in Table 2). Due to the variability of deep learning model convergence, training will not produce identical results every time, to account for this each test was run three times and averaged. Figure 8b shows how the precision, recall and F1 scores vary as the number of fine-tuning epochs is increased. It should be noted that this figure shows accuracy metrics over only 5 tiles from the validation dataset, chosen for their difficulty to evaluate model generalization ability. Therefore, it does not represent the accuracy obtained by the model on the test datasets. It can be seen that the best results are found after three to four epochs of training. The degradation of accuracy after four epochs could correspond to overfitting; because each epoch trains the model using the same 520 test images, albeit augmented differently each time. As another test, the DeepMoon model was also run directly on the Dartmoor data without any fine-tuning training, this gave detection rates of approximately 40% with a bias towards large pits more similar in appearance to impact craters.

**Table 2.** Full results from test datasets.

Test Area	True Positives	False Positives	False Negatives	Precision <sup>1</sup>	Recall <sup>2</sup>	F1 <sup>3</sup>
Dartmoor	155	37	38	0.81	0.80	0.81
Yorkshire	142	13	30	0.92	0.83	0.87

<sup>1</sup> Precision = True Positives/(True Positives + False Positives), <sup>2</sup> Recall = True Positives/(True Positives + False Negatives), <sup>3</sup> F1 = 2 × ((Precision × Recall)/(Precision + Recall)).

Once the optimal amount of fine tuning was determined, the four advanced visualization types were tested against the same five sample images. Each of the visualization types depicted previously in Figure 5 were used as the training data input for fine tuning the model. Using the knowledge from the previous validation test, the models were trained for four epochs, as before, each test was run three times and averaged. Longer training runs of eight epochs were also tested. This is to account for the possibility that due to the greater difference between some of the visualization styles and the model's original lunar DSM training data more epochs might be required to obtain strong results. However, these tests displayed the same behavior as that shown in Figure 8b. It can be seen from Figure 8c that whilst the precision is high for all four data representations, the recall and therefore the F1 score is poorer for the advanced visualizations.

### 3.2. Test Area Results

The cross-validation results informed the development of the final model, which was then evaluated on the final unseen test datasets. The model was evaluated on a 1km<sup>2</sup> tile of LiDAR data in Dartmoor approximately 20 km away from the training area. An additional test was carried out on a 0.2 km<sup>2</sup> of Yorkshire more than 500 km away from the training data. The results obtained are summarized in Table 2. For both sets of results the highest performing model from the validation dataset was used for the predictions. It must be noted that these results have been calculated from the binary results mask. Of the missed detections 23 out of the 38 in Dartmoor and 17 out of 30 in Yorkshire are still visibly predicted in the full transparency results layer. This is because they fall below the 0.5 probability threshold used in the binary masking operation, thereby removing them from the count.

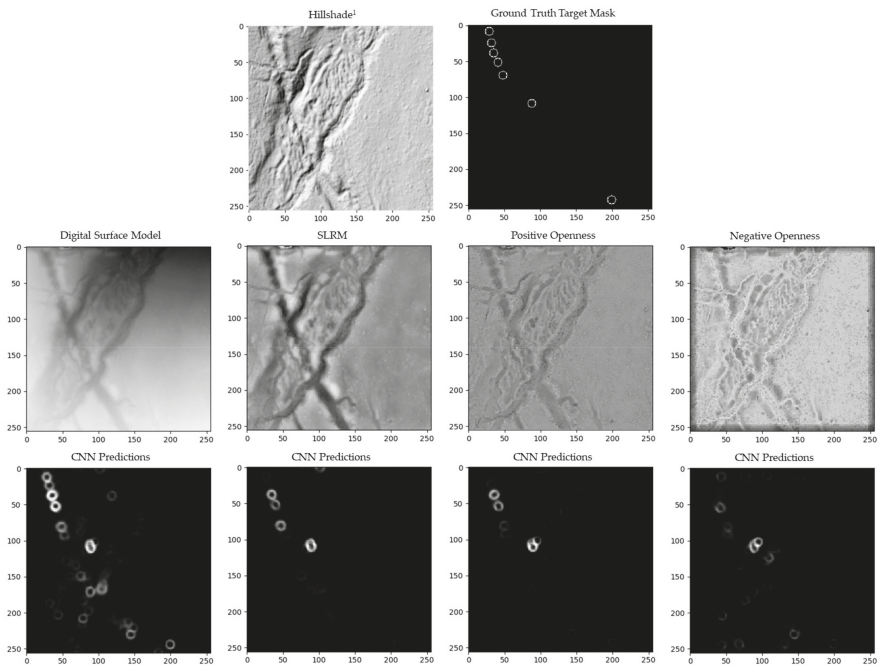
To further investigate the model's generalization capabilities for additional archaeological object detection, a final experiment was carried out. For this, the model was run directly on 1m resolution LiDAR from the same section of Machie Moor (Arran, Scotland) as that tested by Trier et al. [32]. To validate, the true roundhouse locations were taken from [32]. In this experiment no additional training was carried out and the Dartmoor model was applied in its naive state. The results show the model generalized well considering the lack of training, with a precision rate of 0.55 and a recall rate of 0.45. This suggests real potential if trained for this type of feature detection. These results are consistent with how the original DeepMoon naive model performed on the Dartmoor data before fine tuning training was undertaken. From these results it is hoped that by introducing limited amounts of training data for other features of interest, this model is capable of being applied to a wide range of archaeological prospection problems.

#### 4. Discussion

The cross-validation results from the different types of LiDAR visualizations indicated that the model performed better when trained on the raw 8-bit DSM height values rather than any of the advanced visualizations. It is suspected that whilst these visualizations are effective for human interpretation of archaeological data [11] and also effective for more traditional machine learning techniques [22], because deep CNNs learn their own feature representations during training, it is not desirable to artificially alter the data representation prior to input. However, it also must be taken into account that the CNN chosen in this study was pretrained on 8-bit DSM height values, thereby introducing a bias towards this representation. To fully test which LiDAR visualization is best suited for CNNs in future, would require a robust CNN trained from scratch on multiple differently visualized representations of the same data; however, such a model has not been made publicly available from any known sources at this time. To attempt to test this theory with the existing datasets experiments were carried out to create a model from scratch using the DeepMoon architecture and the Dartmoor training data with different visualizations. However, no meaningful results were obtained from any visualization, presumably due to the limited size of the training data. The SLRM and openness visualizations are included in this study as discussion points, to observe how the predictions vary and to provide stimulation for future work. An example of the predictions on a single challenging tile for each visualization type is shown in Figure 9. It can be seen that the predictions from the raw DSM are the most sensitive, resulting in the least amount of missed detections, and is the only one that picks up the isolated pit in the lower right corner. The confusion areas of low probability are easily filtered out by setting a probability threshold of 0.5 in the post-processing steps, as discussed in Section 2.6.

The final test area results demonstrate that the model is highly effective with the correct detections greatly outnumbering the missed and false detections, displaying strong precision and recall simultaneously. Precision and recall figures concurrently above 0.8 has not been achieved to date by any other deep learning tool for archaeological prospection [33], however, as there is no standard archaeological test dataset different approaches are not directly comparable, though the results obtained here clearly indicate this model has achieved state of the art results.

Figure 10 shows the full transparency results overlaid on the Dartmoor and Yorkshire test datasets. This figure shows that the model is highly capable of discerning mining pits and is not overwhelmed by false positives. It also demonstrates that even if individual detections might not always be correct the greater trends in the landscape are very clearly reproduced by the model. This is in line with the recommendations from Cowley for 'a key conceptual shift from a widely held fixation in archaeology on individual identifications being correct to overall patterns being descriptive' [3]. From a management perspective, these automatically generated maps clearly delineate the extents and key structures of these historic mining sites, with limited confusion areas due to model assumptions and landscape morphology.



<sup>1</sup>Hillshade used for display purposes only and not processed by CNN model

**Figure 9.** Results from a single image tile for each of the different visualization predictions. <sup>1</sup>Hillshade used for display purposes only and not processed by the CNN model. Coordinate system arbitrary pixel based.

In Figure 10a,b small confusion areas can be seen around the ends of larger openworked trenches. This is due to the fact that the model is making predictions on cropped image tiles; if only the end of the trench is visible in the tile, the model’s strong generalization ability works against it and it will predict a semi-circular occluded hole. As the tiles have 52% overlap these false positives are typically removed by the raster mosaic post processing step, however, due to anomalies in position and tile overlap, some remain.

The Yorkshire test as shown in Figure 10c,d was carried out to examine the model’s ability to generalize to different types of mines and different resolution data. The model surpassed its previous performance on this dataset, as shown in Table 2. The Yorkshire LiDAR DSM is twice the resolution of the Dartmoor data at 0.25 m but contains more confusion objects such as building remains, stone lined trenches and drainage culverts. The model was capable of discriminating between building foundation remains and excavated platforms from mining pits and made only two false positive detections in these areas. This is an extremely positive result and indicated the model is doing more than just looking for unnatural changes in ground elevation and is searching instead for areas that contain the features which it was trained on.

Of the mistakes, one drainage culvert was mistaken for a hole, but the geometry was such that it was only discernible as a culvert from a side view under the road unafforded to the LiDAR data. This is a limitation of all overhead remotely sensed data and is not specific to a deep learning model. Two trenches were misidentified as pits but only where dense vegetation masked their linearity causing them to appear as circular depressions on the LiDAR.

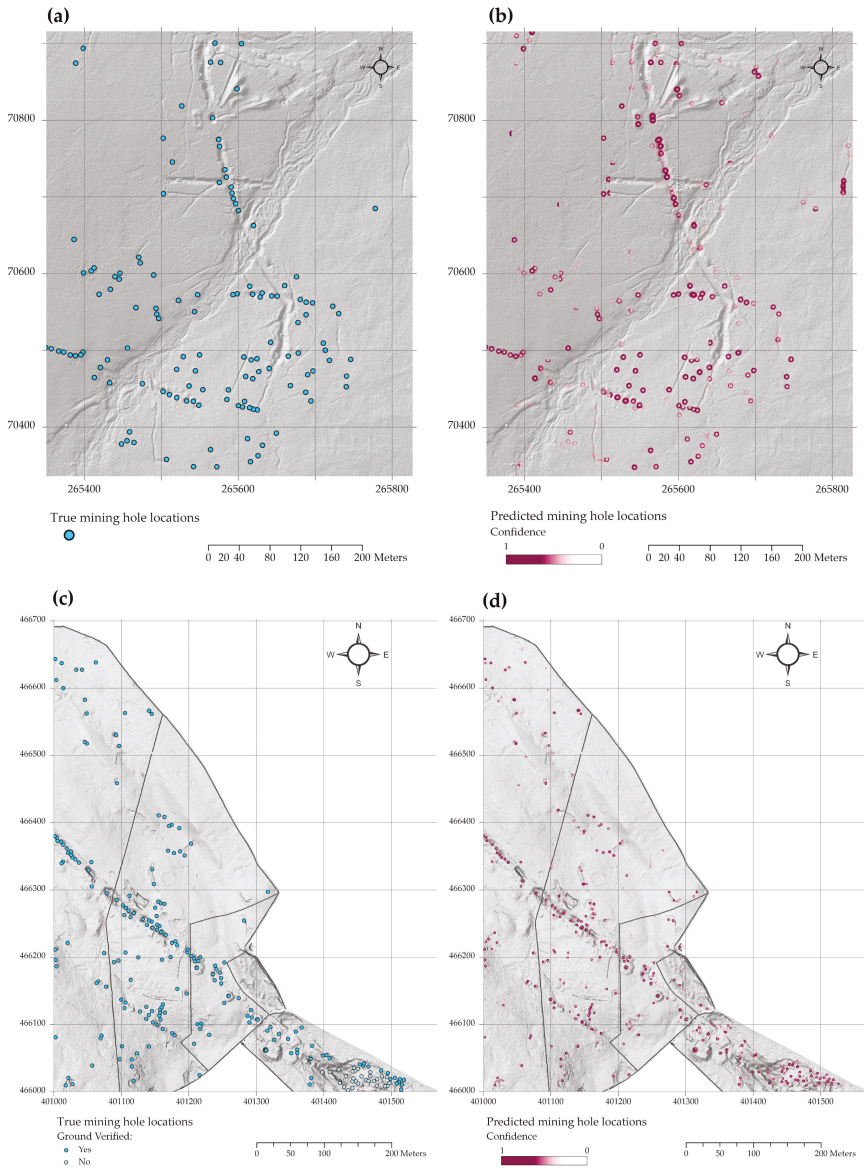


**Figure 10.** Results overlaid on hillshaded LiDAR. (a,b) are from the Dartmoor Hexworthy mine test area, Ordnance Survey grid tile SX6570. (a) shows the true mining hole locations in blue and (b) shows the model’s predicted mining hole locations in magenta. (c) and (d) show the results from the Yorkshire Yarnbury mine test area, Ordnance Survey grid tile SE0166. (c) shows the true mining hole locations in blue and (d) shows the model’s predicted mining hole locations in magenta. In the extensively mined area to the southeast it was not possible to ground verify precise locations as it was fenced off as a hazardous area, however, a visual inspection confirmed many pits and shafts present thereabouts. Their locations were determined from a desktop search and are marked accordingly in (c). Coordinate system British National Grid, DSM © Environment Agency 2015.

The site verification visits revealed that many of the detected pits would be difficult to locate either on foot or from aerial photography as they are faint, shallow and reed-filled. Whilst ground truthing many pits were near-invisible until the surveyor was within a few meters of the model's predicted location; as well, whilst traversing the sites to verify the predictions, no isolated pits were seen that were missed by the model, all missed detections were within larger excavations that had caused confusion. Figure 11 shows a photograph taken looking north from the Hexworthy site, aligned with the same view from the LiDAR model overlaid with aerial imagery and predicted hole locations.

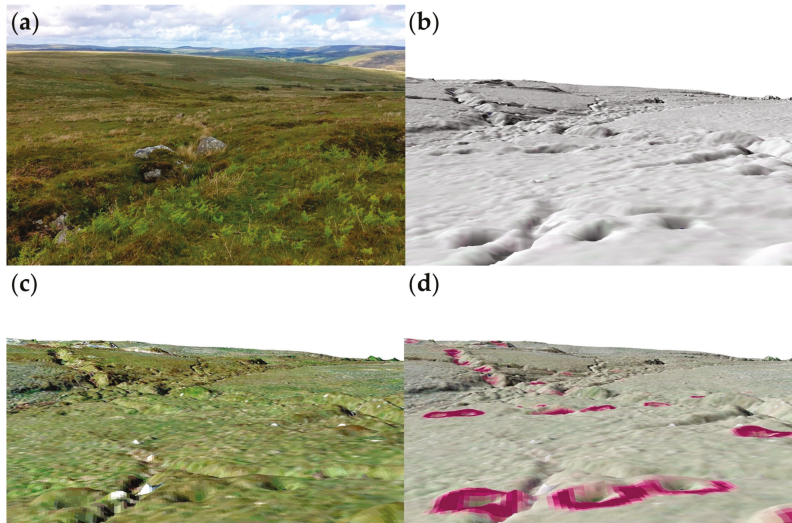


**Figure 11.** Ground level view of the Hexworthy historic mine site. (a) is a photograph taken during the verification survey, (b) shows the same scene in a hillshaded DSM, (c) includes OSGB 2010 aerial imagery and (d) includes the model's predictions. DSM and aerial imagery © Environment Agency 2015 & Digimap Getmapping Plc.

The results from the two tests indicate that this model is able to generalize to new sites and that higher resolution LiDAR improves classification accuracy. These tests also show that despite being trained on one resolution of data the model is capable of being applied at a different resolution without the need for additional training, greatly increasing its applicability for varying quality and resolution general purpose LiDAR datasets. This is crucial as most LiDAR is not flown specifically for archaeological site detection purposes; therefore, site detection algorithms must be capable of working with varying accuracy and resolution datasets gathered by many agencies for diverse reasons.

This model is a single class segmenter; therefore, to extend the model to more general archaeological prospection tasks multiple models must be trained for different classes. Whilst this could be considered a weakness of this approach, no other work to date has managed to fully optimize models for multiple classes simultaneously, despite architectures which permit multiclass outputs. Verschoof-van der Vaart and Lambers [33] successfully trained a multi-class detector and achieved high F1 scores in both classes, however, the highest F1 scores per class did not occur simultaneously. Multi-class learning is more difficult than single class learning, and the problem of automated archaeological site detection is also more difficult than general image classification, due to the small amount of training data and the subtlety of the detections required. It is proposed that at this early stage, development of accurate single class detectors which can be stacked into multi-layer images will produce the most effective, repeatable and easily usable results. These detectors do not have to be trained for every type of potential feature, an approach which would be neither achievable nor desirable, but rather trained to

detect general areas of suspicious topology in several broad categories, flagging it for further inspection, leaving the interpretation to humans for now. The results shown in this study prove that as a first part of a multi-stage phased landscape analysis this model is capable and effective. Delineation and quantification of sites using an approach such as this would add to the body of knowledge about such sites, provide impetus for further surveys and underpin protection of these sites from future threats.

The mining pit detection model created here can be rapidly run on any LiDAR DSM suspected of containing remains of historic mining activity; the approximate time to process a 1km tile including manual ArcGIS post-processing is 5 min. This pipeline could be easily automated further, as this research has been concerned with the ultimate performance of the deep learning model the periphery workflow has not yet been streamlined. As an output, simple GIS point layers (with their accuracy specifications of  $\pm 20\%$ ) can be supplied to the land managers such as Dartmoor National Park and Yorkshire Dales National Park. These results are usable directly by the land managers to rapidly inform future decisions about preservation and management.

A model trained for a different type of site detection could be applied similarly, provided the appropriate training and testing had been carried out. Development of these new models is an exciting direction for further research. The logical next step would be to trial this model on a well-researched study area such as Arran [4], with the aim of developing accurate general purpose, large scale semi-automated site detection tools in the near future.

## 5. Conclusions

The transfer learning model developed in this research shows strong, repeatable results for the task of detecting historic mining pits, alongside promising generalization abilities for other similar tasks. It is a novel application of knowledge from the disparate but related field of planetary remote sensing, achieving state of the art results on its allocated task. It is capable of differentiating between natural depressions and manmade ones, even in areas of occlusion and erosion. This is due to the close resemblance between the data on which the base model was pretrained and the data for the problem at hand. Other strengths of this model are its ability to output full pixelwise segmented confidence masks for any size and resolution data, alongside this workflow's integration with existing ArcGIS tools where possible to ensure ease of use and repeatability.

This research builds on the work of Trier et al. [32] and Verschoof-van der Vaart and Lambers [33] by following their recommendations to seek closely applicable transfer learning models for deep learning on archaeological LiDAR data. It is hoped that this model will prove suitable for other archaeological prospection tasks when furnished with applicable training data. The initial naive applicability test using the Arran data showed promising results for future work in this direction.

This model can run on large swathes of LiDAR data extremely quickly and produces meaningful results which will aid interpretation of large scale historic mining landscapes. The model is also valuable for detecting outlying smaller pits away from the main shafts and mineral veins. These are often unrecorded remains of earlier prospecting and information on their location can add to understanding of a site's exploitation history. It is envisaged that this model would be run as a first step in the prospection process, vastly reducing the areas to be analyzed in fine detail in a desktop search or fieldwork survey by a mining historian. With a false positive rate of less than 20% it does not overwhelm the analyst with incorrect predictions, providing an effective tool for preliminary site investigation and allowing confidence in the use of the model. The workflow and model presented here will allow the scale and magnitude of sites to be rapidly analyzed, underpinning better cultural heritage management decisions for these valuable records of our industrial past.

**Supplementary Materials:** The following are available online at <http://www.mdpi.com/2072-4292/11/17/1994/s1>, Workflow document: S1, Model S2: Deep learning model.

**Author Contributions:** Conceptualization, M.E. and J.G.; investigation, J.G.; methodology, J.G.; software, J.G. and M.T.; validation, J.G.; writing—original draft preparation, J.G.; writing—review and editing, M.E. and J.C.; supervision, M.E. and J.C.

**Funding:** This research received no external funding.

**Conflicts of Interest:** The authors declare no conflict of interest.

## References

1. Bewley, R.H.; Crutchley, S.P.; Shell, C.A. New light on an ancient landscape: Lidar survey in the Stonehenge World Heritage Site. *Antiquity* **2005**, *79*, 636–647. [CrossRef]
2. Moyes, H.; Montgomery, S. Locating Cave Entrances Using Lidar-Derived Local Relief Modeling. *Geosciences* **2019**, *9*, 98. [CrossRef]
3. Cowley, D.C. In with the new, out with the old? Auto-extraction for remote sensing archaeology. *Remote Sens. Ocean Sea Ice Coast Waters Large Water Reg.* **2012**, *8532*, 853206. [CrossRef]
4. Banaszek, L.; Cowley, D.; Middleton, M. Towards National Archaeological Mapping. Assessing Source Data and Methodology—A Case Study from Scotland. *Geosciences* **2018**, *8*, 272. [CrossRef]
5. Bennett, R.; Cowley, D.; De Laet, V. The data explosion: Tackling the taboo of automatic feature recognition in airborne survey data. *Antiquity* **2014**, *88*, 896–905. [CrossRef]
6. Winter, S. Uncovering England's Landscape by 2020. Available online: <https://environmentagency.blog.gov.uk/2017/12/30/uncovering-englands-landscape-by-2020/> (accessed on 9 June 2019).
7. Hesse, R. The changing picture of archaeological landscapes: Lidar prospection over very large areas as part of a cultural heritage strategy. In *Interpreting Archaeological Topography: 3D Data, Visualisation and Observation*; Opitz, R.S., Cowley, D.C., Eds.; Oxbow: Oxford, UK, 2013; pp. 171–183.
8. Brightman, J.; White, R.; Johnson, M. Landscape-Scale Assessment: A Pilot Study Using the Yorkshire Dales Historic Environment. 2015; Unpublished Historic England report number 7049, available upon request from Historic England.
9. Loren-Méndez, M.; Pinzón-Ayala, D.; Ruiz, R.; Alonso-Jiménez, R. Mapping Heritage: Geospatial Online Databases of Historic Roads. The Case of the N-340 Roadway Corridor on the Spanish Mediterranean. *ISPRS Int. J. Geo-Inf.* **2018**, *7*, 134. [CrossRef]
10. Kokalj, Ž.; Hesse, R. *Airborne Laser Scanning Raster Data Visualization. A Guide to Good Practice*; Prostor, K.C., Ed.; Založba ZRC: Ljubljana, Slovenia, 2017; Volume 14, ISBN 12549848.
11. Kokalj, Ž.; Somrak, M. Why Not a Single Image? Combining Visualizations to Facilitate Fieldwork and On-Screen Mapping. *Remote Sens.* **2019**, *11*, 747. [CrossRef]
12. Jacobson, N.P.; Gupta, M.R. Design Goals and Solutions for Display of Hyperspectral Images. *IEEE Trans. Geosci. Remote Sens.* **2005**, *43*, 2684–2692. [CrossRef]
13. Cowley, D.C. What do the patterns mean? Archaeological distributions and bias in survey data. In *Digital Methods and Remote Sensing in Archaeology*; Springer: Cham, Switzerland, 2016; pp. 147–170.
14. Lambers, K.; Verschoof-van der Vaart, W.B.; Bourgeois, Q.P.J. Integrating remote sensing, machine learning, and citizen science in dutch archaeological prospection. *Remote Sens.* **2019**, *11*, 1–20. [CrossRef]
15. Duckers, G.L. Bridging the 'geospatial divide' in archaeology: Community based interpretation of LIDAR data. *Internet Archaeol.* **2013**, *35*. [CrossRef]
16. Morrison, W.; Peveler, E. *Beacons of the Past Visualising LiDAR on a Large Scale*; Chilterns Conservation Board: Chinnor, UK, 2016.
17. Trier, Ø.D.; Larsen, S.Ø.; Solberg, R. Automatic Detection of Circular Structures in High-resolution Satellite Images of Agricultural Land. *Archaeol. Prospect.* **2009**, *16*, 1–15. [CrossRef]
18. Trier, Ø.D.; Zortea, M.; Tonning, C. Automatic detection of mound structures in airborne laser scanning data. *J. Archaeol. Sci. Rep.* **2015**, *2*, 69–79. [CrossRef]
19. Sevara, C.; Pregesbauer, M.; Doneus, M.; Verhoeven, G.; Trinks, I. Pixel versus object—A comparison of strategies for the semi-automated mapping of archaeological features using airborne laser scanning data. *J. Archaeol. Sci. Rep.* **2016**, *5*, 485–498. [CrossRef]
20. Freeland, T.; Heung, B.; Burley, D.V.; Clark, G.; Knudby, A. Automated feature extraction for prospection and analysis of monumental earthworks from aerial LiDAR in the Kingdom of Tonga. *J. Archaeol. Sci.* **2016**, *69*, 64–74. [CrossRef]

21. Trier, Ø.D.; Salberg, A.-B.; Pilø, L.H. Semi-automatic mapping of charcoal kilns from airborne laser scanning data using deep learning. In Proceedings of the 44th Conference on Computer Applications and Quantitative Methods in Archaeology, Oslo, Norway, 29 March–2 April 2016; Matsumoto, M., Uleberg, E., Eds.; Archaeopress: Oxford, UK, 2018; pp. 219–231.
22. Guyot, A.; Hubert-Moy, L.; Lorho, T. Detecting Neolithic burial mounds from LiDAR-derived elevation data using a multi-scale approach and machine learning techniques. *Remote Sens.* **2018**, *10*, 225. [[CrossRef](#)]
23. Gao, H.; Mao, J.; Zhou, J.; Huang, Z.; Wang, L.; Xu, W. Are you talking to a machine? Dataset and methods for multilingual image question answering. In Proceedings of the Advances in Neural Information Processing Systems, Motreal, QC, Canada, 7–12 December 2015; pp. 1–10.
24. Redmon, J.; Farhadi, A. YOLO9000 Better, stronger, faster. In Proceedings of the IEEE Conference on Computer Vision and Pattern Recognition, Las Vegas, NV, USA, 26 June–1 July 2016; pp. 7263–7271.
25. Sun, Y.; Zhang, X.; Xin, Q.; Huang, J. Developing a multi-filter convolutional neural network for semantic segmentation using high-resolution aerial imagery and LiDAR data. *ISPRS J. Photogramm. Remote Sens.* **2018**, *143*, 3–14. [[CrossRef](#)]
26. Cheng, G.; Zhou, P.; Han, J. Learning Rotation-Invariant Convolutional Neural Networks for Object Detection in VHR Optical Remote Sensing Images. *IEEE Trans. Geosci. Remote Sens.* **2016**, *54*, 7405–7415. [[CrossRef](#)]
27. Ren, Y.; Zhu, C.; Xiao, S. Small Object Detection in Optical Remote Sensing Images via Modified Faster R-CNN. *Appl. Sci.* **2018**, *8*, 813. [[CrossRef](#)]
28. Nogueira, K.; Penatti, O.A.B.; dos Santos, J.A. Towards better exploiting convolutional neural networks for remote sensing scene classification. *Pattern Recognit.* **2017**, *61*, 539–556. [[CrossRef](#)]
29. Razavian, A.S.; Azizpour, H.; Sullivan, J.; Carlsson, S. CNN features off-the-shelf: An astounding baseline for recognition. In Proceedings of the IEEE CVPR Workshop, Columbus, OH, USA, 23–28 June 2014; pp. 512–519. [[CrossRef](#)]
30. Deng, J.; Dong, W.; Socher, R.; Li, L.-J.; Li, K.; Fei-Fei, L. ImageNet: A Large-Scale Hierarchical Image Database. In Proceedings of the CVPR09, Miami, FL, USA, 22–24 June 2009.
31. Ball, J.E.; Anderson, D.T.; Chan, C.S. Comprehensive Survey of Deep Learning in Remote Sensing: Theories, Tools and Challenges for the Community. *J. Appl. Remote Sens.* **2017**, *11*. [[CrossRef](#)]
32. Trier, Ø.D.; Cowley, D.C.; Waldeland, A.U. Using deep neural networks on airborne laser scanning data: Results from a case study of semi-automatic mapping of archaeological topography on Arran, Scotland. *Archaeol. Prospect.* **2019**, *26*, 165–175. [[CrossRef](#)]
33. Verschoof-van der Vaart, W.B.; Lambers, K. Learning to Look at LiDAR: The use of R-CNN in the automated detection of archaeological objects in LiDAR data from the Netherlands. *J. Comput. Appl. Archaeol.* **2019**, *2*, 31–40. [[CrossRef](#)]
34. Hesse, R. LiDAR-derived Local Relief Models—A new tool for archaeological prospection. *Archaeol. Prospect.* **2010**, *17*, 67–72. [[CrossRef](#)]
35. Zuber, M.T.; Smith, D.E.; Zellar, R.S.; Neumann, G.A.; Sun, X.; Katz, R.B.; Kleyner, I.; Matuszeski, A.; McGarry, J.F.; Ott, M.N.; et al. The Lunar Reconnaissance Orbiter Laser Ranging Investigation. *Space Sci. Rev.* **2009**, *150*, 63–80. [[CrossRef](#)]
36. Albee, A.L.; Arvidson, R.E.; Palluconi, F.; Thorpe, T. Overview of the Mars Global Surveyor mission. *J. Geophys. Res. E Planets* **2001**, *106*, 23291–23316. [[CrossRef](#)]
37. Silburt, A.; Ali-Dib, M.; Zhu, C.; Jackson, A.; Valencia, D.; Kissin, Y.; Tamayo, D.; Menou, K. Lunar crater identification via deep learning. *Icarus* **2019**, *317*, 27–38. [[CrossRef](#)]
38. Wang, H.; Jiang, J.; Zhang, G. CraterIDNet: An end-to-end fully convolutional neural network for crater detection and identification in remotely sensed planetary images. *Remote Sens.* **2018**, *10*, 67. [[CrossRef](#)]
39. Palafox, L.F.; Hamilton, C.W.; Scheidt, S.P.; Alvarez, A.M. Automated detection of geological landforms on Mars using Convolutional Neural Networks. *Comput. Geosci.* **2017**, *101*, 48–56. [[CrossRef](#)]
40. Ronneberger, O.; Fischer, P.; Brox, T. U-net: Convolutional networks for biomedical image segmentation. In *Lecture Notes in Computer Science*; Springer: Berlin, Germany, 2015; Volume 9351, pp. 234–241.
41. Žutautas, V. Charcoal Kiln Detection from LiDAR-derived Digital Elevation Models Combining Morphometric Classification and Image Processing Techniques. Master's Thesis, University of Gävle, Gävle, Sweden, 2017.

42. Trier, Ø.; Zortea, M. Semi-automatic detection of cultural heritage in lidar data. In Proceedings of the 4th International Conference GEOBIA, Rio de Janeiro, Brazil, 7–9 May 2012; pp. 123–128.
43. Davis, D.S.; Sanger, M.C.; Lipo, C.P. Automated mound detection using lidar and object-based image analysis in Beaufort County, South Carolina. *J. Archaeol. Sci.* **2018**. [CrossRef]
44. Newman, P. Environment, Antecedent and Adventure: Tin and Copper Mining on Dartmoor, Devon. Ph.D. Thesis, University of Leicester, Leicester, UK, 2010.
45. Dines, H.G. *The Metalliferous Mining Region of South West England*, 3rd ed.; British Geological Survey: Nottingham, UK, 1988.
46. Hamilton Jenkin, A.K. *Mines of Devon Volume 1: The Southern Area*; David and Charles (Holdings) Limited: Newton Abbot, UK, 1974.
47. Richardson, P.H.G. *British Mining Vol. 44: Mines of Dartmoor and the Tamar Valley*; Northern Mine Research Society: Sheffield, UK, 1992.
48. Northern Mine Research Society. *British Mining No 13: The Mines of Grassington Moor*; Northern Mine Research Society: Sheffield, UK, 1980.
49. Lidar Composite Digital Surface Model England 50cm and 25 cm [ASC Geospatial Data], Scale 1:2000 and 1:1000, Tiles: sx6780, sx6781, sx6782, sx6880, sx6680, sx6681, sx6070, sx6071, sx6170, sx6171, sx6270, sx6570 and se0166. Available online: <https://digimap.edina.ac.uk> (accessed on 7 March 2019).
50. Yeomans, C.M. Tellus South West data usage: A review (2014–2016). In Proceedings of the Open University Geological Society, Exeter, UK, April 2017; Hobbs the Printers Ltd.: Hampshire, UK, 2017; Volume 3, pp. 51–61.
51. ESRI ArcGIS Pro 2.3.1. Available online: <https://www.esri.com/en-us/arcgis/products/arcgis-pro/overview> (accessed on 1 January 2019).
52. 1:2500 County Series 1st Edition. [TIFF Geospatial Data], Scale 1:2500, Tiles: Devo-sx6780-1, devo-sx6781-1, devo-sx6782-1, devo-sx680-1, devo-sx6681-1, devo-sx6070-1, devo-sx6071-1, devo-sx6170-1, devo-sx6171-1, devo-sx6270-1 and devo-sx6570-1. Available online: <https://digimap.edina.ac.uk> (accessed on 7 March 2019).
53. High Resolution (25cm) Vertical Aerial Imagery. (2011, 2015) Scale 1:500, Tiles: sx6780, sx6781, sx6782, sx6680, sx6681, sx6070, sx6071, sx6170, sx6171, sx6270, sx6570 and se0166, Updated: 25 October 2015, Getmapping, Using: EDINA Aerial Digimap Service. Available online: <https://digimap.edina.ac.uk> (accessed on 09 March 2019).
54. Relief Visualisation Toolbox (RVT). Available online: <https://iaps.zrc-sazu.si/en/rvt#v> (accessed on 26 March 2019).
55. Doneus, M. Openness as visualization technique for interpretative mapping of airborne lidar derived digital terrain models. *Remote Sens.* **2013**, *5*, 6427–6442. [CrossRef]
56. Lecun, Y.; Bottou, L.; Bengio, Y.; Haffner, P. Gradient-based learning applied to document recognition. *Proc. IEEE* **1998**, *86*, 2278–2324. [CrossRef]
57. Krizhevsky, A.; Sutskever, I.; Hinton, G.E. ImageNet Classification with Deep Convolutional Neural Networks Alex. *Adv. Neural Inf. Process. Syst.* **2012**, *25*, 1106–1114. [CrossRef]
58. Goodfellow, I.; Bengio, Y.; Courville, A. *Deep Learning*; MIT Press: Cambridge, MA, USA, 2016.
59. Girshick, R.; Donahue, J.; Darrell, T.; Malik, J. Rich feature hierarchies for accurate object detection and semantic segmentation. In Proceedings of the IEEE Conference on Computer Vision and Pattern Recognition, Columbus, OH, USA, 23–28 June 2014; pp. 580–587. [CrossRef]
60. He, K.; Gkioxari, G.; Dollár, P.; Girshick, R. Mask R-CNN. In Proceedings of the IEEE International Conference on Computer Vision, Venice, Italy, 22–29 October 2017; IEEE: Piscataway, NJ, USA, 2017; pp. 2980–2988. [CrossRef]
61. Szegedy, C.; Vanhoucke, V.; Ioffe, S.; Shlens, J.; Wojna, Z. Rethinking the Inception Architecture for Computer Vision. In Proceedings of the IEEE Conference on Computer Vision and Pattern Recognition, Las Vegas, NV, USA, 27–30 June 2016; pp. 2818–2826. [CrossRef]
62. Lin, T.Y.; Maire, M.; Belongie, S.; Hays, J.; Perona, P.; Ramanan, D.; Dollár, P.; Zitnick, C.L. Microsoft COCO: Common objects in context. In *Lecture Notes in Computer Science*; Springer: Berlin, Germany, 2014; Volume 8693, pp. 740–755.
63. Badrinarayanan, V.; Kendall, A.; Cipolla, R. Segnet: A deep convolutional encoder-decoder architecture for image segmentation. *IEEE Trans. Pattern Anal. Mach. Intell.* **2017**, *39*, 2481–2495. [CrossRef] [PubMed]

64. Python 3.6.7. Available online: <https://www.python.org> (accessed on 14 August 2019).
65. Abadi, M.; Agarwal, A.; Barham, P.; Brevdo, E.; Chen, Z.; Citro, C.; Corrado, G.S.; Davis, A.; Dean, J.; Devin, M.; et al. TensorFlow: Large-scale machine learning on heterogeneous systems. *arXiv* **2015**, arXiv:1603.04467.
66. Chollet, F. Keras 2015. Available online: <https://keras.io> (accessed on 14 August 2019).



© 2019 by the authors. Licensee MDPI, Basel, Switzerland. This article is an open access article distributed under the terms and conditions of the Creative Commons Attribution (CC BY) license (<http://creativecommons.org/licenses/by/4.0/>).



Article

# Airborne Hyperspectral Imaging for Submerged Archaeological Mapping in Shallow Water Environments

Alexandre Guyot <sup>1,2,\*</sup>, Marc Lennon <sup>2</sup>, Nicolas Thomas <sup>2</sup>, Simon Gueguen <sup>2</sup>, Tristan Petit <sup>2</sup>, Thierry Lorho <sup>3</sup>, Serge Cassen <sup>4</sup> and Laurence Hubert-Moy <sup>1</sup>

<sup>1</sup> Laboratoire LETG—UMR 6554, Université Rennes 2, Place du recteur Henri Le Moal, 35043 Rennes, France

<sup>2</sup> Hytech-Imaging, 115 Rue Claude Chappe, 29280 Plouzané, France

<sup>3</sup> DRAC Bretagne, Service régional de l'archéologie, Avenue Charles Foulon, 35700 Rennes, France

<sup>4</sup> Laboratoire LARA—UMR6566, Université de Nantes, Chemin la Censive du Tertre, 44312 Nantes, France

\* Correspondence: alexandre.guyot@univ-rennes2.fr

Received: 23 August 2019; Accepted: 23 September 2019; Published: 25 September 2019

**Abstract:** Nearshore areas around the world contain a wide variety of archeological structures, including prehistoric remains submerged by sea level rise during the Holocene glacial retreat. While natural processes, such as erosion, rising sea level, and exceptional climatic events have always threatened the integrity of this submerged cultural heritage, the importance of protecting them is becoming increasingly critical with the expanding effects of global climate change and human activities. Aerial archaeology, as a non-invasive technique, contributes greatly to documentation of archaeological remains. In an underwater context, the difficulty of crossing the water column to reach the bottom and its potential archaeological information usually requires active remote-sensing technologies such as airborne LiDAR bathymetry or ship-borne acoustic soundings. More recently, airborne hyperspectral passive sensors have shown potential for accessing water-bottom information in shallow water environments. While hyperspectral imagery has been assessed in terrestrial continental archaeological contexts, this study brings new perspectives for documenting submerged archaeological structures using airborne hyperspectral remote sensing. Airborne hyperspectral data were recorded in the Visible Near Infra-Red (VNIR) spectral range (400–1000 nm) over the submerged megalithic site of Er Lannic (Morbihan, France). The method used to process these data included (i) visualization of submerged anomalous features using a minimum noise fraction transform, (ii) automatic detection of these features using Isolation Forest and the Reed–Xiaoli detector and (iii) morphological and spectral analysis of archaeological structures from water-depth and water-bottom reflectance derived from the inversion of a radiative transfer model of the water column. The results, compared to archaeological reference data collected from in-situ archaeological surveys, showed for the first time the potential of airborne hyperspectral imagery for archaeological mapping in complex shallow water environments.

**Keywords:** hyperspectral data; submerged areas; cultural heritage monitoring; anomaly detection; MNF; radiative transfer model

## 1. Introduction

Whether of natural (e.g., erosion, rising sea level and exceptional climatic events) or human (e.g., urbanization, agriculture, and pollution) origin, threats to archaeological heritage are increasingly significant [1,2]. Documenting and monitoring archaeological sites is consequently increasingly becoming a crucial aspect of conserving cultural heritage. In an underwater context, documenting archaeological remains requires mapping seabed details to interpret various forms of past human

traces [3–5]. While much underwater archaeological research has been oriented to shipwrecks [5–7], nearshore areas contain a wide variety of ancient structures, including prehistoric remains submerged by the sea rise initiated 15,000 years ago by the Holocene glacial retreat. On a global scale, the now-submerged landscapes that were once attractive terrestrial habitats for prehistoric human occupation are estimated to cover ca. 20 million km<sup>2</sup> [8].

In the last few decades, active remote-sensing methods have successfully detected and recorded submerged archaeological sites in deep and shallow water. From the water surface, multibeam echo sounders (MBES) installed on hydrographic vessels or USV (unmanned surface vehicles) are used for archaeological applications. Despite high costs of operation and relatively low spatial coverage per time unit, MBES remain the preferred solution for seabed prospection, especially in deep water [9]. In coastal shallow waters, however, rock outcrops and rough sea conditions can reduce the potential area of operation due to safety issues, and multipath acoustic propagation interference also decreases the quality of acoustic measurements [10]. More recently, underwater hyperspectral imagers have also shown considerable potential for underwater archaeological surveys [11]; however, their use is limited to in-situ observations and low spatial coverage. Airborne LiDAR bathymetry (ALB) has gained great interest for underwater archaeological mapping [12–14]. When operated in topo-bathy mode, it can cover the intertidal zone and provide seamless representation of terrestrial and submerged topography. ALB has drawbacks, however, including relatively high deployment costs and difficulty in retrieving reliable depth measurements in very shallow water [15,16].

In comparison, passive remote-sensing data, such as multispectral or hyperspectral airborne and spatial imagery, have so far focused almost exclusively on terrestrial archaeological contexts. Airborne hyperspectral instruments measure, for a large number of pixels (millions) and wavelengths (tens to hundreds), the radiation (spectral radiance) received at the sensor. The data they collect are generally presented in the form of a data cube (2 spatial dimensions × 1 spectral dimension). Depending on sensor characteristics, the spectral dimension covers specific wavelength ranges, such as the Visible Near Infra-Red (VNIR) range, corresponding to wavelengths of 400–1000 nm. Due to its ability to acquire highly detailed spectral information, airborne hyperspectral imagery (AHI) has been used for various types of earth observation: land-cover/land-use mapping [17,18], target detection [19], geology [20] and coastal mapping [21]. For archaeological applications, airborne hyperspectral data have been greatly valuable for terrestrial mapping [22–31], but to our knowledge, no studies have yet assessed AHI in a submerged context. Using it for underwater mapping requires addressing challenges related to the complexity of (i) the data (including high dimensionality and signal-to-noise ratio), (ii) the object of study (degraded and partially documented structures) and (iii) the environment, especially the complex light-matter interactions in water, affected by multiple environmental factors such as water constituents, surface conditions and benthic composition.

Thus, the aim of this study was to evaluate the potential of AHI for detecting and documenting submerged sites in coastal archeology. The questions addressed are (a) can submerged archaeological structures be visible using AHI? (b) Can they be detected automatically? (c) Can they be characterized spatially and spectrally?

## 2. Materials and Methods

### 2.1. Study Area

The Gulf of Morbihan (France) has one of the most important architectural heritages of megaliths in the world. Due to their density and exceptional character, these Neolithic monuments, built from the 5th to 3rd millennia BC, are candidates for the UNESCO World Heritage List. One of the most emblematic sites in this region is the islet of Er Lannic and its two semicircular stone monuments.

The islet of Er Lannic, 80 ha in size, lies between the island of Gavrinis (with an imposing tumulus and abundant Neolithic engravings), 300 m to the north, and the Point of Penbert, on the Rhuy

peninsula, 500 m to the south (Figure 1a). The islet borders the main channel of the Gulf of Morbihan, which has one of the strongest tidal currents in Europe.

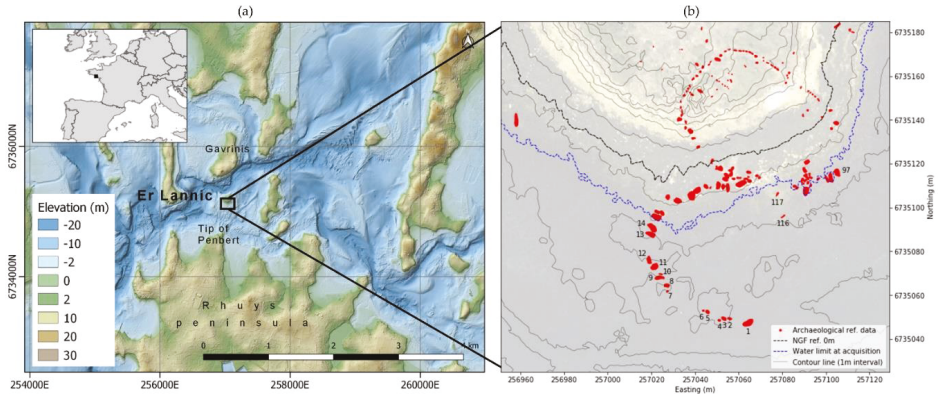


**Figure 1.** (a) Location of the study area (Er Lannic islet, Morbihan, France), (b) the archaeological reference data (submerged stiles are numbered).

The two semicircular stone monuments, each 50–60 m wide, are located on the southern end of Er Lannic. After its construction by Neolithic humans, the site was submerged due to the rise in sea level during the post-glacial marine transgression [32]. The coastline of the Gulf of Morbihan is estimated to have been ca. 5 m below the current sea level during the Neolithic period [32]. The megalithic site of Er Lannic (Figure 2) was first mentioned in 1866 by archaeologist G. de Closmadec [33]. Initially, only the terrestrial part of the monument was discovered and identified as a complete stone circle. The submerged structures were then revealed to archaeologists several years later by an extremely low tide. The first site map, depicting two adjacent stone circles, was drawn in 1882 [34]. Since then, several archaeological operations have been performed on site to complement and improve the site map. However, the strong tidal current and rock outcrops at the sea surface complicate surveys of the subtidal rocky platform, preventing any MBES surveys by boat. Despite the scientific interest of the site, few underwater measurements have been taken. The most recent documented underwater surveys were performed in the early 1990s [35] using traditional topographic techniques with a theodolite and a leveling rod, the latter being held in shallow water by divers during each measurement.



**Figure 2.** Megalithic monument of Er Lannic.

## 2.2. Airborne Hyperspectral Data

The study was based on AHI acquired by Hytech Imaging (Plouzané, France) with a NEO HySpex VNIR-1600 push broom sensor (Table 1). The sensor was coupled with an IMAR iTrace-RT-F200 system and an OmniSTAR L1/L2 GNSS antenna to measure position and orientation.

**Table 1.** Characteristics of the HySpex Visible Near Infra-Red (VNIR)-1600 sensor.

Spectral Range	Spatial Pixels	Spectral Resolution	Spectral Sampling	Number of Bands	FOV across Track	Pixel FOV across/Along Track	Coding
0.4–1.0 $\mu\text{m}$	1600	4.5 FWHM	3.7 nm	160	17°	0.18 mrad/0.36 mrad	12 bits

The aerial survey was performed on 14 September 2018 at an altitude of ca. 1200 m to obtain a ground sampling distance of 50 cm (Table 2).

**Table 2.** Parameters of the aerial survey.

Flight Altitude	Ground Sampling Distance	Swath	Integration Time	Viewing Angle	Solar Zenith Angle
1200 m	50 cm	176 m	10.1 ms	16.75°	16.75°

During the survey, images were collected in clear sky and calm sea conditions (preconditions to reduce sun-glint effects and solar irradiance variation). Er Lannic was overflown at 13:00 UTC, corresponding to low-tide conditions (tide coefficient of 85).

## 2.3. Bathymetric Reference Data

The reference bathymetric data used for this study are based on the Litto3D project [36,37] of the French Naval Hydrographic and Oceanographic Office (Shom) and the French National Geographic Institute (IGN). This project produced a seamless, high-resolution topographic and bathymetric model of French coastal areas using multiple survey techniques (Topographic LiDAR, ALB, MBES). For the Gulf of Morbihan, the Litto3D data consist of three complementary, locally overlapping surveys:

- ALB (SHOALS-1000T) by Shom (2005):
  - Topographic and bathymetric modes: spot spacing 2 and 5 m, altitude 900 and 400 m, absolute planimetric accuracy < 1.5 and < 2.8 m, and absolute vertical accuracy < 0.3 and < 0.5 m, respectively
- MBES by Shom (2003) and IFREMER (2013)

Shom/IGN provided the data as a merged 3D point cloud with source identifiers (Figure 3a). Each point is defined as XYZ coordinates in Lambert93 system using the RGF93 geodetic system (EPSG: 2154) and NGF/IGN69 height reference for elevation. The merged point cloud was converted to a raster of 1 m resolution using Triangulated Irregular Networks interpolation (Figure 3b).

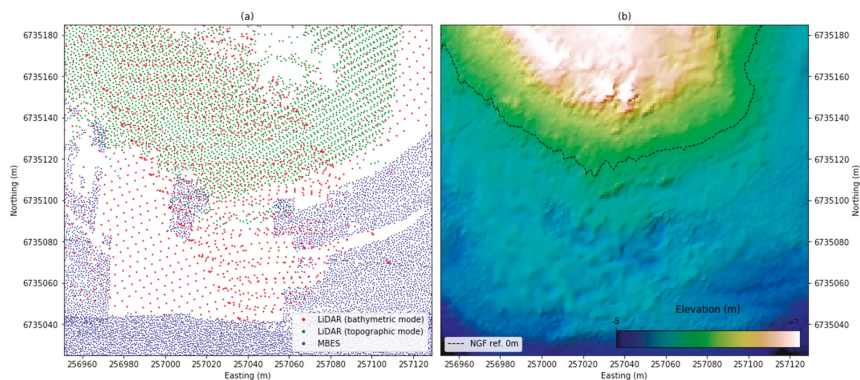


**Figure 3.** Litto3D bathymetric reference data (a) point cloud and (b) 1 m resolution raster.

#### 2.4. Archaeological Reference Data

Archaeological reference data for this study came from a georeferenced 2D map (Figure 1b) of each stone (or stele) of the site recorded by archaeologists from 1990–2018 [38–40]. The Regional Archaeological Service of Brittany (DRAC/SRA) currently uses this map. The map is projected in the Lambert93 system using the RGF93 geodetic system (EPSG: 2154).

Spatially, the northernmost semicircular stone monument, composed of ca. 60 steles—collapsed or erect—is entirely visible at lowest astronomical tide. The second semicircular stone monument, composed of 29 steles, is submerged and sits on the shore platform 2–3 m below mean sea level. Additional steles are also present at the junction of the semicircles, near a granite outcrop north of the second semicircle, and at isolated points away from the semicircles. The steles, most of them metamorphic orthogneiss, vary in projected horizontal area from <math>0.5\text{--}11\text{ m}^2</math>.

For identification purposes, steles are numbered from 1–201 [38] (i.e.,  $Stl_{\#1}$  to  $Stl_{\#201}$ ). Based on the tide and sea conditions when the images were acquired, 17 steles ( $Stl_{\#1}$  to  $Stl_{\#14}$ ,  $Stl_{\#97}$ ,  $Stl_{\#116}$  and  $Stl_{\#117}$ ) were located beyond the shoreline, of which 15 were completely submerged and 2 ( $Stl_{\#1}$  and  $Stl_{\#14}$ ) were partially submerged.

#### 2.5. Dimensionality Reduction and Visualization

Dimensionality reduction techniques concentrate information by projecting the original data, with high dimensionality, into a lower dimensional space. Its objective is to decrease computational burden (i.e., reduce the number of bands), remove spectrally redundant information or noise and highlight informative spectral variation in the imagery. For remote-sensing hyperspectral data, for which interband correlation is high and noise omnipresent, dimensionality reduction algorithms are used to enhance visual interpretation or as pre-processing before other procedures, such as classification [30]. These algorithms include Principal Component Analysis (PCA) and Minimum Noise Fraction (MNF) [41]. PCA projects data into a new subspace where the projected components maximize the variance of the data under the constraint that each component is orthogonal to its preceding component. PCA can thus reduce dimensionality of the data while conserving the maximum amount of information. When applied to hyperspectral imagery, however, PCA is not the most suitable method, notably because of its limitation with noisy observations. MNF is a linear transformation based on two sequential PCA rotations. The first rotation decorrelates and scales the noise using a noise covariance matrix calculated by estimating local noise using the difference between adjacent pixels. The result is a hyperspectral data cube in which noise has unit variance and no band-to-band correlation (white noise). The second rotation performs a PCA on the noise-whitened data cube to separate noise from data and thus maximize the signal-to-noise ratio (SNR).

## 2.6. Unsupervised Anomaly Detection

In the machine learning field, unsupervised learning is the task of identifying structures or relationships in the input data without prior knowledge by mean of reference or labelled data. Since submerged archaeological structures might be undescribed in nature, degraded or covered (with sediments, vegetation or biofilm), archaeological prospection using remote-sensing data usually seeks anomalies rather than looking for known signatures [24,31]. Unsupervised anomaly-detection techniques are adapted to these conditions, since they require no predefined target characteristics and try to separate common observations from unusual observations. Doing the latter requires two main assumptions: anomalies are (i) spectrally different from the surrounding background and (2) represent a minority of pixels in an image (low occurrence). Existing unsupervised anomaly-detection algorithms include the Reed–Xiaoli detector (RXD) and associated variants, and the Isolation Forest (IF) algorithm.

RXD, developed by [42], is based on a statistical distance (Mahalanobis distance) calculated between the observation (a pixel) and the image background. Global RXD relies on a pre-calculated background at the image level, while local RXD (LRXD) is based on a local background estimated using a sliding window that can have inner and outer sizes to adapt to specific anomaly sizes.

IF, developed by [43], is based on the widely used Random Forest classification algorithm. IF combines multiple weak decision trees to calculate an anomaly score that reflects how much an observation differs from other observations. Each tree is created recursively by randomly selecting a feature and an associated random threshold value. Each observation is passed through the tree and compared to each node (feature and threshold) until it can be isolated from other observations (reaching an external node). The shorter an observation's path in the tree, the higher is its anomaly score. The final anomaly score equals the mean score of all trees.

## 2.7. Radiative Transfer Model over Shallow Water

Over optically shallow water (inland or coastal waters whose bottom is visible from the surface), total radiance measured by the remote sensor includes contributions from the atmosphere, the water surface, the water column and the water bottom. Hyperspectral remote sensing uses this radiative relationship to characterize the water column and water bottom physically. The radiative transfer model of Lee [44] calculates subsurface remote-sensing reflectance  $R_{rs}^-$  as:

$$R_{rs}^- = R_{rs}^\infty \left( 1 - A_1 e^{-(K_d + k_{uW})Z} \right) + A_2 R_{rs}^B e^{-(K_d + k_{uB})Z} \quad (1)$$

where  $R_{rs}^\infty$  is the remote-sensing reflectance for optically deep water;  $K_d$ ,  $k_{uW}$ ,  $k_{uB}$  are diffuse coefficients related to downwelling irradiance, upwelling radiance of the water column, and upwelling radiance from bottom reflection, respectively;  $A_1$  and  $A_2$  are constants;  $R_{rs}^B$  is the bottom reflectance and  $Z$  is the bottom depth.

Equation (1) verifies that for  $Z \rightarrow \infty$ ,  $R_{rs}^- \rightarrow R_{rs}^\infty$ , and for  $Z \rightarrow 0$ ,  $R_{rs}^- \rightarrow R_{rs}^B$ . This semi-analytical model is then inverted to retrieve the parameters (including  $R_{rs}^B$  and  $Z$ ) that minimize the difference between the observed and modeled spectra [45].

This radiative-transfer-based method, unlike empirical approaches, has the advantage of not requiring prior bathymetric data (existing elevation model or in-situ measurements) for the inversion process and derivation of bottom depth [21].

## 3. Methodology

### 3.1. Workflow

The methodology developed and the associated workflow (Figure 4) were organized in subsections corresponding to the research questions of this study.

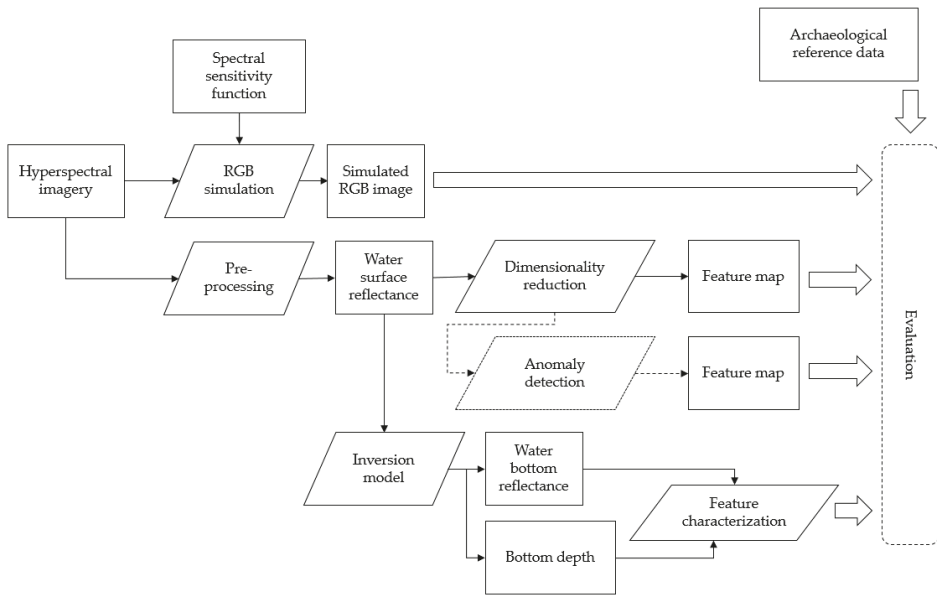


Figure 4. Diagram of the method developed.

### 3.2. Pre-processing

The hyperspectral images were processed from level 0 (raw) to level1b (radiometrically and geometrically calibrated) using the HYPIP (HYPPerspectral Image Preprocessing) chain of Hytech-imaging that includes ATCOR/PARGE software applications (ReSe Applications, Wil, Switzerland) to obtain georeferenced images in spectral radiance ( $W.m^{-2}.sr^{-1}.\mu m^{-1}$ ). Surface reflectance was then obtained by performing atmospheric corrections in a two-step process: (i) atmospheric corrections using ATCOR-4 software and (ii) empirical adjustment of each spectrum by applying coefficients (gain and bias) calculated per spectral band by linear regression between surface reflectance data and the reflectance signature of pre-calibrated targets (tarps) positioned near the area of interest and overflow during the survey. The resulting hyperspectral products (at-sensor radiance, surface reflectance) were then spatially subset to a 2048 px × 2048 px tile (representing an area of ca. 1 km<sup>2</sup>), encompassing the area of interest of Er Lannic islet.

### 3.3. Simulation of True-color Image

The initial hypothesis of the study was that VNIR AHI carries information valuable for visualizing submerged archaeological structures. To evaluate the contribution of hyperspectral data compared to that of traditional true-color photography, a red-green-blue (RGB) image was simulated using the spectra sensitivity response (Figure 5) of a digital single-lens reflex camera (DSLR Canon EOS 10D) and the hyperspectral cube.

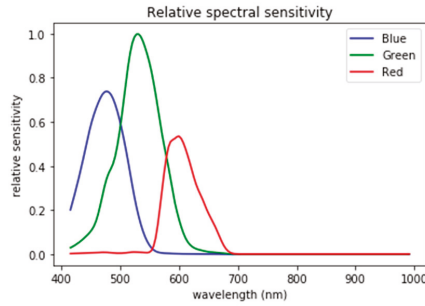


**Figure 5.** Relative spectral sensitivity function of a Canon 10D digital single-lens reflex camera used to simulate a true-color red-green-blue (RGB) image from the hyperspectral imagery.

Red, green and blue bands of the simulated image were produced by convolution products (Equations (2), (3) and (4), respectively):

$$Red_{sim} = \sum_{\lambda=400}^{\lambda=700} RSS_r(\lambda) * L(\lambda)_{tot}^s \quad (2)$$

$$Green_{sim} = \sum_{\lambda=400}^{\lambda=700} RSS_g(\lambda) * L(\lambda)_{tot}^s \quad (3)$$

$$Blue_{sim} = \sum_{\lambda=400}^{\lambda=700} RSS_b(\lambda) * L(\lambda)_{tot}^s \quad (4)$$

where  $L(\lambda)_{tot}^s$  is the at-sensor radiance from hyperspectral imagery, and  $RSS_r(\lambda)$ ,  $RSS_g(\lambda)$ , and  $RSS_b(\lambda)$  are relative spectral sensitivity functions of the red, green and blue channel, respectively, of the DSLR ([46] citing [47]).

The contrast/brightness of the simulated RGB image was then adjusted using gamma correction ( $\gamma = 0.4$ ) to improve visualization [48].

### 3.4. Dimensionality Reduction Using MNF Minimum Noise Fraction Transform

MNF transform was then applied to the reflectance hyperspectral images. Full spectral information from 400–1000 nm wavelengths was kept for the MNF decomposition. Noise was estimated by (i) selecting a homogeneously dark area of the image and (ii) extracting the noise covariance matrix from it using the shift difference method (i.e., the processed pixel minus its top-right neighbor). This procedure respectively exploits the facts that (i) signal variation in a homogeneously dark area of an image is due primarily to environmental and instrumental noise and (ii) the signal at any point in the image is strongly correlated with the signal at neighboring pixels, while noise is not or only weakly spatially correlated [41].

Given the site context and to allow for continuous visual interpretation of terrestrial and submerged structures (including rock outcrops or emerging steles), the MNF transform was applied to the entire subset of the imagery, including terrestrial and submerged areas. Only MNF components with a  $SNR \geq 5$  were conserved. The resulting components were visualized individually and in multiple pseudo-colored images (combining three components selected to highlight spectral and spatial variation in the data) to enhance visualization of submerged features. The results were compared to (i) the synthetically created true-color image and (ii) the georeferenced archaeological reference data identifying each stele.

### 3.5. Automatic Anomaly Detection

LRXD and IF unsupervised anomaly-detection algorithms were used to identify submerged anomalies automatically and compare them to the known archaeological reference data. The algorithms were applied to the MNF results calculated from the surface reflectance image. LRXD was applied to the MNF subset within a sliding window of 30 px × 30 px (outer window) and 15 px × 15 px (inner window). The IF model was trained with 100 decision trees, 100 randomly drawn observations and 10 randomly drawn features to train each tree.

For both algorithms, results were evaluated visually and statistically. Visually, the anomaly score map was compared to the georeferenced archaeological reference data. Statistically, the receiver operating characteristic (ROC) curve was calculated to illustrate the trade-off between the true positive rate and false positive rate at different score thresholds. Accuracy was assessed by calculating a normalized confusion matrix of the binary classification with a threshold defined from the ROC curve. Statistical evaluation was limited to the submerged area to focus on submerged anomalies.

### 3.6. Depth and Bottom Reflectance Estimation

Before inverting the radiative transfer model, a mask for the water was applied using the normalized difference water index (NDWI) [49]:

$$NDWI = \frac{R(\lambda_{550}) + R(\lambda_{850})}{R(\lambda_{550}) - R(\lambda_{850})} \quad (5)$$

where  $R(\lambda_{550})$  and  $R(\lambda_{850})$  are the pixel reflectance values in the green and near-infrared areas of the spectrum, respectively.

To reduce variability due to noise, reflectance was extracted using the median values within  $\pm 20$  nm of each central wavelength (550 or 850 nm).

The semi-analytical radiative-transfer model, as seen in Equation (1) was inverted using SWIM (Shallow Water mapping using optical reMote sensor(s)) [45,50] to estimate bottom reflectance ( $R_{rs}^b$ ), bottom depth ( $Z$ ) and water column parameters ( $C_{dom}$ ,  $C_{phy}$ ,  $C_{NAP}$ ) from the observed subsurface reflectance ( $R_{rs}^-$ ). The inversion problem is solved by minimizing a least square cost function representing distance between the observed subsurface reflectance and the modelled subsurface reflectance. Optimization was performed using the Levenberg-Marquardt. For each pixel, the algorithm converged to a solution for a vector of parameters ( $R_{rs}^b$ ,  $Z$ ,  $C_{dom}$ ,  $C_{phy}$ ,  $C_{NAP}$ ).  $R_{rs}^b$  and  $Z$  were used subsequently for further analysis. No external data (in-situ depth measurements or existing elevation model) was used for refining the bottom-depth estimation.

The bottom depth in raster format was post-processed using a median filter of  $5 \times 5$  px to reduce the salt-and-pepper noise that can decrease interpretability for archaeological purposes. The data were then corrected for the tidal effect using tide information available from Shom and converted from the hydrographic reference to the terrestrial height reference NGF/IGN69 using the RAM product (maritime altimetric reference values) provided by Shom. The results were compared to the archaeological reference data as well as to the Litto3D continuous topo-bathymetric reference dataset collected from MBES and ALB by Shom/IGN on the Gulf or Morbihan.

## 4. Results

### 4.1. Analysis of the Simulated Rgb Image

The northernmost and terrestrial semicircle of Er Lannic was visible on the RGB image, as were the locations of archaeological structures (individually for large steles and linear shapes for groups of smaller steles) (Figure 6b,c). Bright colors of on-shore steles and shadows projected by standing steles facilitated visualization and interpretation. On the submerged part of the site, large terrestrial steles on the upper intertidal platform were apparent, but the continuity of the submerged semicircle was

difficult to perceive without prior knowledge of the site or the reference archaeological data. Effects of the water surface were visible at the southern tip of the semicircle and corresponded to the presence of an emerging stele (*Stl#1*).

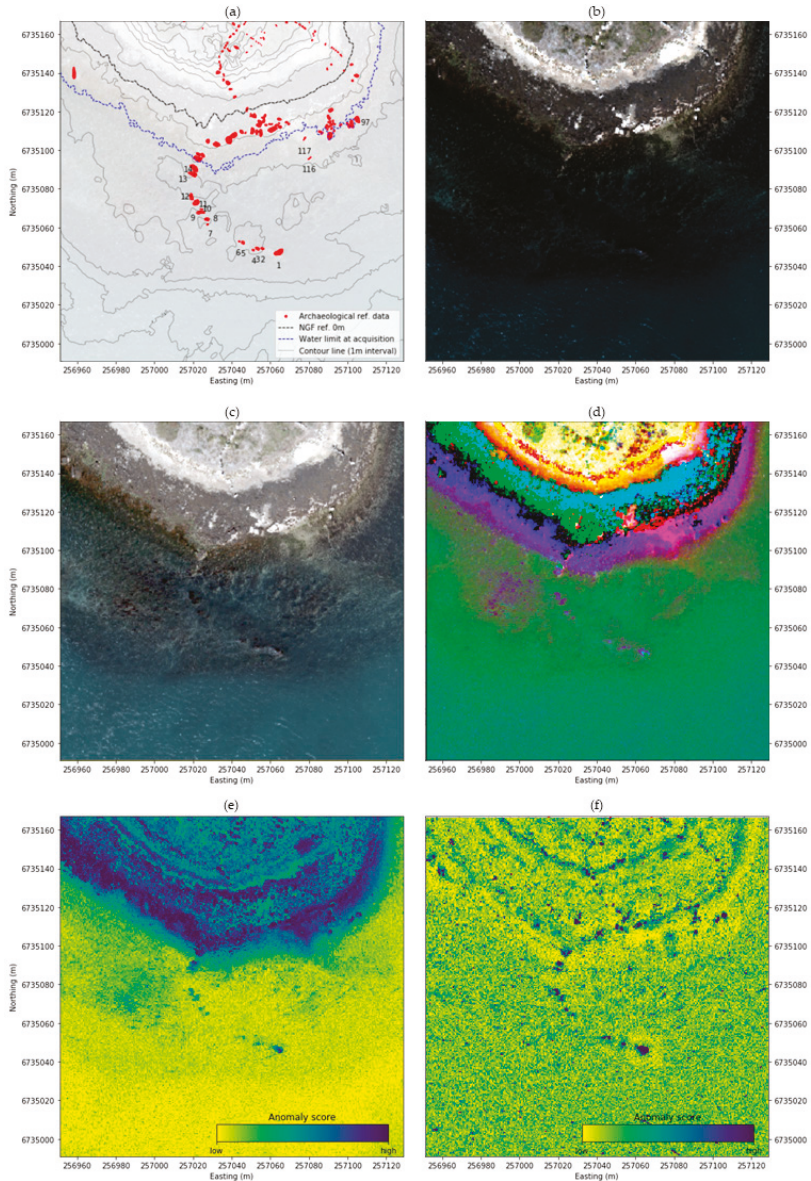


**Figure 6.** (a) Archaeological reference map of the study site (submerged steles are numbered). True-color (RGB) images simulated from hyperspectral data and spectral sensitivity functions (b) without and (c) with gamma correction ( $\gamma = 0.4$ ). (d) Minimum noise fraction pseudo-color image with bands Red = 9, Green = 3 and Blue = 4. (e) Anomaly score calculated using the Isolation Forest (IF) algorithm. (f) Anomaly score calculated using the local Reed–Xiaoli detector (LRXD) algorithm.

#### 4.2. Analysis of the Hyperspectral Imagery

According to the MNF components extracted from AHI, the hyperspectral data did not greatly improve visualization or description of the northernmost semicircle (Figure 7). However, the variability in the ground spectral signature near the steles highlighted many natural ground features (e.g., sands, granitic rocks, dry algae, grass). On intertidal and submerged platforms, the presence of features (local variations in MNF) through the water-column was visually confirmed, especially from MNF components 3, 4, 5, 8, 9, 12 and 13. Local variations were visually interpreted to identify the presence of the submerged semicircle.

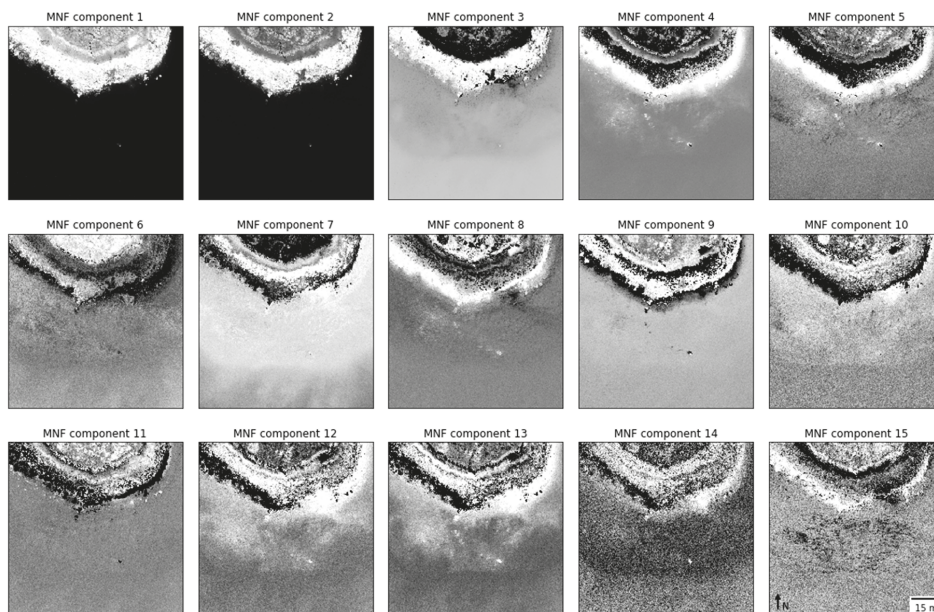


**Figure 7.** Minimum noise fraction (MNF) components 1–15 (signal-to-noise ratio  $\geq 5$ ) calculated from surface reflectance.

The pseudo-color image, created from visual selection of components 3 (green), 4 (blue) and 9 (red) of the MNF, confirmed the identification of submerged anomalies corresponding to the submerged steles ( $Stl_{\#1}$  to  $Stl_{\#14}$ ,  $Stl_{\#97}$ ,  $Stl_{\#116}$  and  $Stl_{\#117}$ ) (Figure 6d).

#### 4.3. Automatic Detection of Archeological Structures

According to IF, the most anomalous pixels were located mainly on-shore due to the high variability in spectral signatures (Figure 6e). Submerged archaeological structures had lower scores (i.e., less anomalous than on-shore structures) but were clearly visible and spatially defined due to their difference with the background (common observations). In contrast, structures at the land/water interface were not clearly defined due to little difference in the anomaly score.

Results obtained with the LRXD algorithm emphasized the location and shape of each submerged structure (Figure 6f). While LRXD is subject to impulse noise due to anomalous single-pixel observations, the spatial pattern of the submerged monuments was clearly distinguishable as a whole and as individual steles.

Comparing statistical results of the submerged area (at the time of acquisition) of the IF and LRXD methods, IF performed better than LRXD because LRXD (i) tended to enlarge anomalies spatially and

(ii) generated a higher false positive rate (0.16, vs. 0.08 for IF) because it detected more anomalies on the submerged area (Table 3, Figure 8).

**Table 3.** Normalized confusion matrix for Isolation Forest (IF) and local Reed–Xiaoli detector (LRXD) anomaly detection of submerged structures.

	Predicted Label "Standard"	Predicted Label "Anomaly"
True label "standard"	0.92 (IF) 0.84 (LRXD)	0.08 (IF) 0.16 (LRXD)
True label "anomaly"	0.12 (IF) 0.27 (LRXD)	0.88 (IF) 0.73 (LRXD)

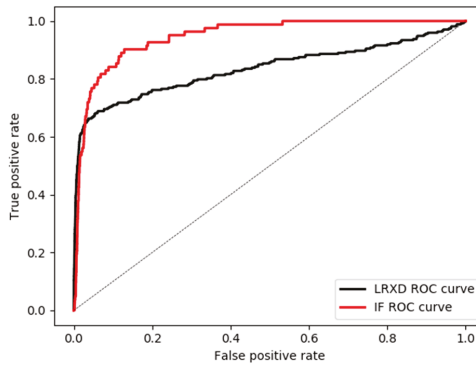


**Figure 8.** Receiver operating characteristic (ROC) curves for Isolation Forest (IF) and local Reed–Xiaoli detector (LRXD) anomaly detection calculated for the submerged structures.

#### 4.4. Characterization of Archeological Structures

##### 4.4.1. Morphological Characterization

The Bathymetric Digital Elevation Model (DEM) derived from AHI showed topographic variations corresponding to the submerged steles. An adapted view (using slope and colored-ramp overlay blending and 0.1 m contour lines) of the estimated water bottom highlighted the features (local maxima) and provided an initial morphological description (shape, area). On the submerged semicircle, 10 features on the DEM were interpreted as archaeological structures (Figure 9). Eight of these features (denoted *F#*) were associated with single steles (*F#1: Stl#1, F#3: Stl#5, F#4: Stl#6, F#5: Stl#8, F#6: Stl#9, F#7: Stl#11, F#8: Stl#12, F#10: Stl#116*), while the other two were associated with aggregations of multiple steles (*F#2: Stl#2, Stl#3, Stl#4; F#9: Stl#13, Stl#14*) since individual DEM signals for them were not apparent. Submerged steles *Stl#7, Stl#10* and *Stl#117* were not identified from the AHI-derived water-bottom morphology.

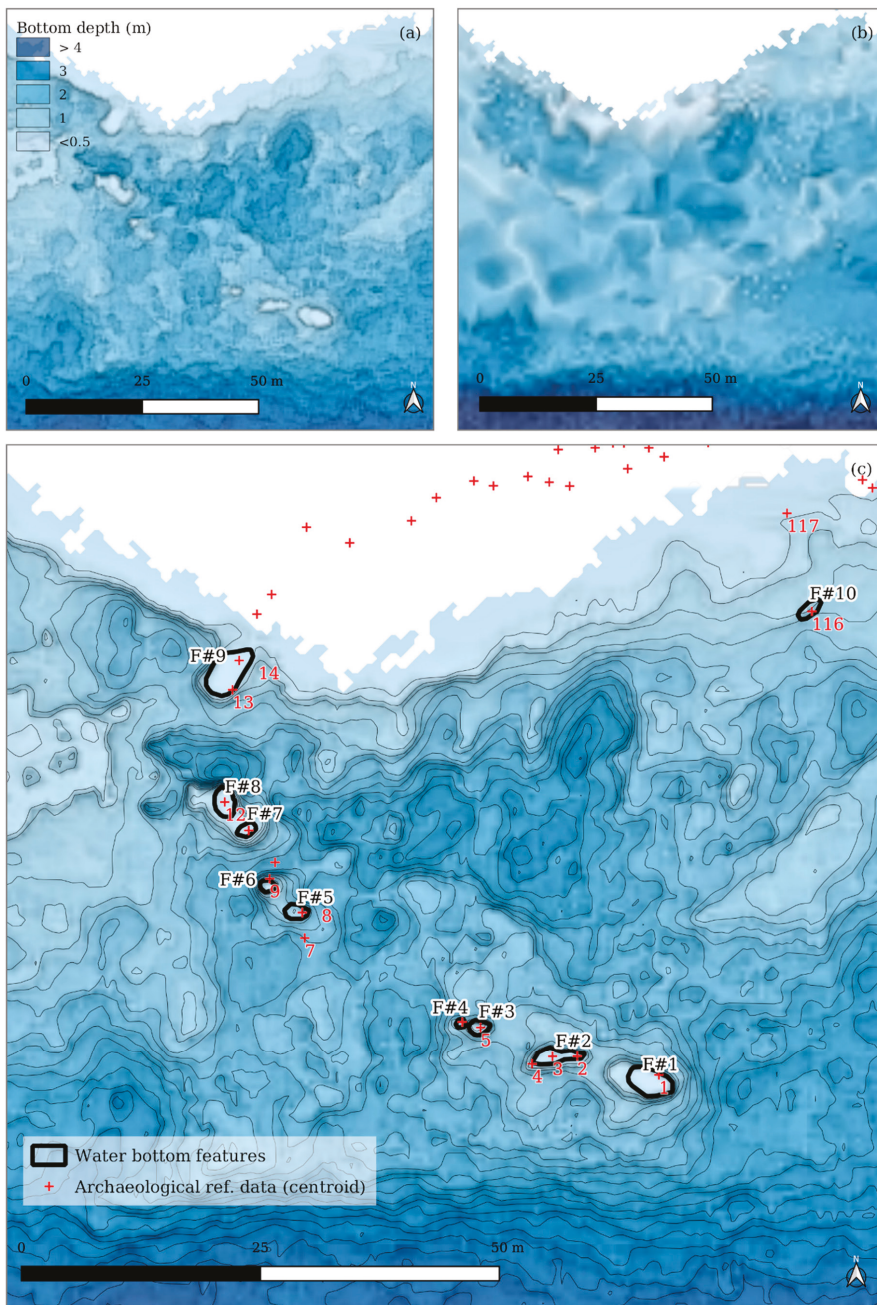


**Figure 9.** (a) Bottom depth estimated from airborne hyperspectral imagery (AHI), (b) Litto3D bathymetric data (Shom/IGN) and (c) Bottom depth estimated from AHI with extraction of visible water-bottom features (local maxima) from 0.1 m contour lines. Archaeological reference data (stele centroids) are shown in red.

The area of the features extracted (2D projected horizontal area) were then compared to those of the archaeological reference data (Table 4). Linear regression between the two indicated relatively good agreement ( $R^2 = 0.72$ ).

**Table 4.** Area of airborne hyperspectral imagery-derived water-bottom features compared those of steles from archaeological reference data. Coefficient of determination  $R^2 = 0.72$ .

Feature ID ( <i>Feat<sub>#n</sub></i> )	Feature Area (m <sup>2</sup> )	Stele IDs ( <i>Stl<sub>#n</sub></i> )	Stele Area (m <sup>2</sup> )
1	10.3	<i>Stl<sub>#1</sub></i>	9.8
2	5.8	<i>Stl<sub>#2</sub>, Stl<sub>#3</sub>, Stl<sub>#4</sub></i>	4.7 (1.4, 2.4, 0.9)
3	2.5	<i>Stl<sub>#5</sub></i>	2.1
4	0.7	<i>Stl<sub>#6</sub></i>	0.5
5	4.0	<i>Stl<sub>#8</sub></i>	9.0
6	1.5	<i>Stl<sub>#9</sub></i>	4.8
7	2.0	<i>Stl<sub>#11</sub></i>	6.9
8	5.1	<i>Stl<sub>#12</sub></i>	4.7
9	15.1	<i>Stl<sub>#13</sub>, Stl<sub>#14</sub></i>	16.1 (6.9, 9.2)
10	2.8	<i>Stl<sub>#116</sub></i>	0.7

Visualization of a path profile of bottom depth along the submerged semicircle (Figure 10) allowed AHI-derived bathymetry and Litto3D reference bathymetry to be compared. AHI-derived bathymetry described water-bottom morphology in more detail, and the presence of local maxima at the location of known archaeological structures confirmed its ability to visualize submerged structures and, to some extent, describe their morphological characteristics (i.e., shape, depth, and area).

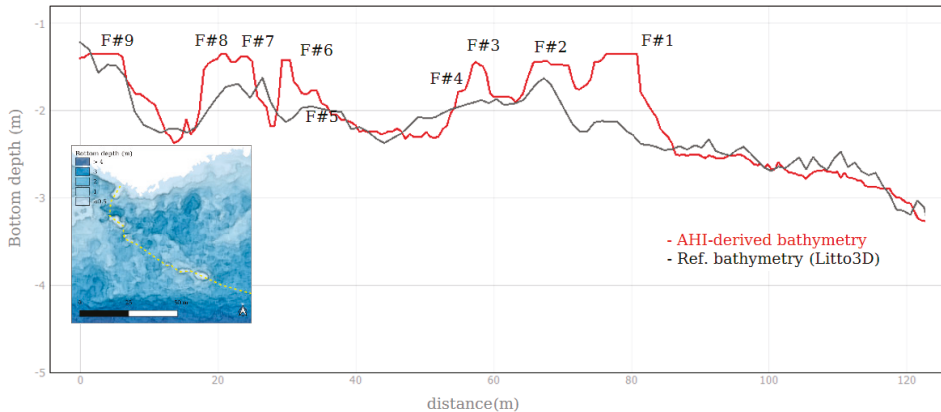


**Figure 10.** Path profile of bottom depth estimated from airborne hyperspectral imagery (AHI) and reference Litto3D (Shom/IGN) bathymetric data over the submerged structures.

#### 4.4.2. Spectral Characterization of the Archeological Structures

Spectral signatures (bottom reflectance) selected on the submerged semicircle (Figure 11a) had a low amplitude of estimated reflectance (< 1%) due to low reflectivity of the water bottom. It also revealed green (around 580nm) and red-edge (increase in spectral reflectance from 650–720 nm) peaks on the submerged features, which reflected the presence of vegetation in plant-based biofilm (i.e., micro-algae) or macro-algae on the steles. In-situ observations (Figure 11b) confirmed the presence and the diversity of macro-algae (green and brown) on the steles.

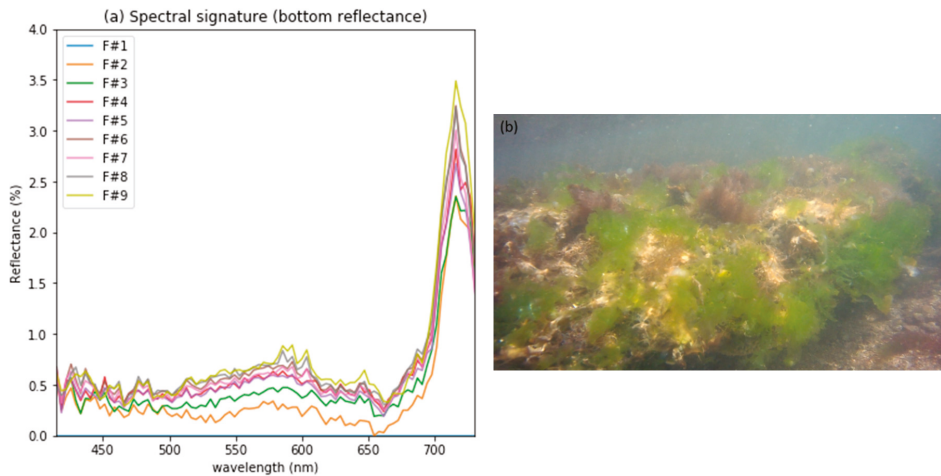


**Figure 11.** (a) Spectral signatures of bottom reflectance showing archaeological structures and (b) photograph of a permanently submerged stele of Er Lannic covered by green and brown algae.

## 5. Discussion and Perspectives

### 5.1. AHI: Potential for Application to Underwater Archaeology

Until recently, ALB was considered the only aerial remote-sensing technique that could collect high-resolution data in very shallow water [51]. Development of AHI for shallow water mapping, first in academic contexts and more recently towards operational usages, shows that passive remote sensing is becoming a potential alternative for estimating bathymetry and describing water-bottom morphology and benthic cover types at a fine scale (meter or sub-meter resolution) [21,52]. The present study opens new perspectives for underwater cultural heritage monitoring and archaeological prospection. Benefits of AHI for these applications include lower survey costs than those of ALB [53] and high spectral and spatial description. However, AHI also has drawbacks. As AHI is an optical remote sensing system (such as ALB), the efficiency of AHI for accessing water bottom information depends on environmental factors such as turbidity, water surface condition and sea state, bottom depth and bottom reflectance. Moreover, as a passive optical system, the quality of the data is also dependent on the illumination conditions and cloud cover [54]. While additional investigations are required to determine the dependency of the proposed approach on these environmental variables, the management of AHI surveys for archaeological mapping in a shallow water environment remains a sensitive aspect of the workflow.

### 5.2. Data Uncertainty and Statistical Results

The statistical results for unsupervised detection of anomalies were influenced by uncertainties in the context and input data. Since the target structures we sought had areas of 0.5–10 m<sup>2</sup>, they were represented by clusters of a few pixels in the image (spatial resolution: 50 cm). Given this resolution, the sensor's point spread function and the uncertainty in horizontal precision (usually 1–2 pixels), the probability of having local/spatial discrepancies between the collected data and the reference data was relatively high. Another source of uncertainty was the reference archaeological data. Like for other archaeological reference data, a "ground truth" map is limited by at least two factors. The first is the measurement itself: every spatial measurement is inaccurate (as it never exactly matches with the true value which remains undefined), especially for archaeological sites of limited accessibility (i.e., partially or entirely submerged), and the uncertainty in location can be high. The second is the exhaustiveness of the reference data, which is never guaranteed. Since the reference map of an archaeological site

evolves with methods and techniques, it should be considered a “current state of knowledge” rather than a “ground truth”. Since we did not consider any of these sources of uncertainty, the results must be analyzed with care. They should not be considered a baseline for similar approaches in different archaeological contexts, but rather a baseline for comparing novel anomaly-detection methods in the same experimental conditions.

### 5.3. From Anomaly to Archaeological Structure

As shown in this study, morphological and spectral characterization of submerged archaeological structures can be complex. The weak reflectance (and consequently low SNR) in water conditions, combined with the continuous presence of vegetation (micro- or macro-algae) on submerged mineral structures, limited the ability to distinguish between archaeological and natural structures spectrally. Thus, the use of the term “morphological or spectral characterization” could be an inappropriate description of hyperspectral remote sensing if it is assumed to provide information similar to that from in-situ archaeological analysis. Considering the information provided by remote sensing to be a faithful description of archaeological structures is premature. Instead, the information provided by AHI should be considered a proxy or surrogate description of archaeological structures. For example, archaeologists consider that algae covering steles are not part of the archaeological structures (in fact, algae are regularly removed from the steles of Er Lannic that are accessible at low tide). Therefore, the morphological or spectral descriptors of submerged features extracted from remote sensing data describe not only archaeological structures but the natural environment that surrounds them (their envelope). Nevertheless, a first characterization of the bottom spectral properties is a valuable information offered by AHI and an advantage over ALB for which the backscattering intensity of a single wavelength signal is less adapted for the description of benthic composition [55].

### 5.4. Perspectives and Future Research Directions

This study was an initial approach to demonstrate the potential of hyperspectral imagery for prospecting and monitoring submerged archaeological structures in shallow water environments. It opens new perspectives. First, from an archaeological perspective, the study focused on a known archaeological site built during the Neolithic period. The archaeological potential in coastal shallow water environment, for example in Brittany, is important and a major challenge from a scientific perspective and with regard to cultural heritage management. Our objective is to broaden this study to prospect or monitor archaeological sites of different chrono-typologies.

Second, from a remote-sensing and data-analysis perspective, we intend to continue research on unsupervised and supervised anomaly detection. For archaeological prospection, anomaly detection is a key challenge for identifying structures for which only partial knowledge usually exists. Indeed, the state of conservation and surface condition of archaeological structures, especially in water conditions, is *a priori* undefined, and the expected characteristics that reference typologies provide, although informative, can mislead prospections for predefined morphological structures that differ from the complex in-situ situation. To address this limitation, our future research will aim to go further in the use of unsupervised or self-supervised anomaly detection algorithms, including deep-learning techniques such as convolutional autoencoders in 2D (spatial) or 3D (spatial/spectral), to extract informative patterns from the hyperspectral cube for application to archaeology.

## 6. Conclusions

We demonstrated AHI’s potential for submerged archaeological prospection and monitoring in shallow water environments. While AHI is regularly used for terrestrial archaeology, its use has not yet been assessed for underwater archaeology. By taking advantage of the high-resolution spatial and spectral characteristics of AHI data, the study showed that AHI passive remote-sensing could be a valuable alternative to active remote-sensing techniques for mapping submerged archaeological structures. The study was performed on the megalithic site of Er Lannic in Morbihan (France),

composed of two semicircles of steles, one of which lay on the water bottom 2–3 m below the mean sea level. The method was divided into three steps: (i) visualize submerged structures, (ii) detect submerged anomalies automatically and (iii) characterize the features identified by estimating their morphological and spectral characteristics. The results showed that hyperspectral data can collect underwater information necessary for archaeological mapping. This information was extracted from AHI either by data-driven analysis (dimensionality reduction/anomaly detection) or by estimating physical parameters such as water depth and bottom reflectance by the inversion of a radiative transfer model. Comparing the information extracted to archaeological and bathymetric reference data confirmed AHI's potential for archaeological prospection and monitoring. Although this study focused on a single archaeological site (i.e., chrono-typology), the approach will be further explored to assess its application to a wider range of structures and archaeological and environmental contexts. Future research will also assess unsupervised or self-supervised machine-learning techniques to reduce dimensionality and detect submerged anomalies in hyperspectral images.

**Author Contributions:** Conceptualization, A.G., M.L. and L.H.-M.; methodology, A.G.; Resources, N.T., S.G., T.P. and S.C.; supervision, M.L. and L.H.-M.; writing—original draft, A.G.; writing—review & editing, M.L., T.L., S.C. and L.H.-M.

**Funding:** This research was co-funded by the Région Bretagne (project “Patrimoine - Mégalithes de Bretagne”) and DRAC Bretagne, Service régional de l’archéologie and Hytech-Imaging.

**Acknowledgments:** The authors would like to thank Yves Menez for sharing his views on the current challenges in cultural heritage management that led to this research. We are also grateful to Guillaume Sicot for the valuable technical discussions and guidance regarding hyperspectral analysis at the early stage of this study.

**Conflicts of Interest:** The co-funders DRAC Bretagne, Service régional de l’archéologie and Hytech-imaging had a role in the design of the study, processing the data, writing and publishing the results. Their objective was to evaluate the capabilities of AHI for submerged archeological mapping in shallow water environment. The authors declare no conflict of interest.

## References

1. Daire, M.-Y.; López-Romero, E.; Proust, J.-N.; Regnaud, H.; Pian, S.; Shi, B. Coastal Changes and Cultural Heritage (1): Assessment of the Vulnerability of the Coastal Heritage in Western France. *J. Isl. Coast. Archaeol.* **2012**, *7*, 168–182. [[CrossRef](#)]
2. Reeder-Myers, L.A. Cultural Heritage at Risk in the Twenty-First Century: A Vulnerability Assessment of Coastal Archaeological Sites in the United States. *J. Isl. Coast. Archaeol.* **2015**, *10*, 436–445. [[CrossRef](#)]
3. Singh, H.; Adams, J.; Mindell, D.; Foley, B. Imaging Underwater for Archaeology. *J. Field Archaeol.* **2000**, *27*, 319–328.
4. Guzinski, R.; Spondylis, E.; Michalis, M.; Tusa, S.; Brancato, G.; Minno, L.; Hansen, L.B. Exploring the Utility of Bathymetry Maps Derived with Multispectral Satellite Observations in the Field of Underwater Archaeology. *Open Archaeol.* **2016**, *2*. [[CrossRef](#)]
5. Costa, E. The progress of survey techniques in underwater sites: the case study of cape stoba shipwreck. *ISPRS Int. Arch. Photogramm. Remote Sens. Spat. Inf. Sci.* **2019**, *69–75*. [[CrossRef](#)]
6. Ruppe, C.V.; Barstad, J.F. *International Handbook of Underwater Archaeology*; Springer: New York, NY, USA, 2013; ISBN 978-1-4615-0535-8.
7. Westley, K.; Plets, R.; Quinn, R.; Mcgonigle, C.; Sacchetti, F.; Dale, M.; McNeary, R.; Clements, A. Correction to: Optimising protocols for high-definition imaging of historic shipwrecks using multibeam echosounder. *Archaeol. Anthr. Sci.* **2019**, *11*, 3647–3648. [[CrossRef](#)]
8. Harff, J.; Bailey, G.N.; Lüth, F. Geology and archaeology: Submerged landscapes of the continental shelf: An introduction. *Geol. Soc. Lond. Spec. Publ.* **2016**, *411*, 1–8. [[CrossRef](#)]
9. Plets, R.; Quinn, R.; Forsythe, W.; Westley, K.; Bell, T.; Benetti, S.; McGrath, F.; Robinson, R. Using Multibeam Echo-Sounder Data to Identify Shipwreck Sites: Archaeological assessment of the Joint Irish Bathymetric Survey data: Using multibeam echo-sounder data to identify shipwreck sites. *Int. J. Naut. Archaeol.* **2011**, *40*, 87–98. [[CrossRef](#)]
10. Xu, T.; Xu, L. *Digital Underwater Acoustic Communications*; Elsevier: Amsterdam, The Netherlands, 2017; ISBN 978-0-12-803009-7.

11. Ødegård, Ø.; Mogstad, A.A.; Johnsen, G.; Sørensen, A.J.; Ludvigsen, M. Underwater hyperspectral imaging: A new tool for marine archaeology. *Appl. Opt.* **2018**, *57*, 3214–3223. [[CrossRef](#)]
12. Doneus, M.; Doneus, N.; Briese, C.; Pregesbauer, M.; Mandlbürger, G.; Verhoeven, G. Airborne laser bathymetry—Detecting and recording submerged archaeological sites from the air. *J. Archaeol. Sci.* **2013**, *40*, 2136–2151. [[CrossRef](#)]
13. Shih, P.T.Y.; Chen, Y.H.; Chen, J.C. Historic Shipwreck Study in Dongsha Atoll with Bathymetric LiDAR. *Archaeol. Prospect.* **2014**, *21*, 139–146. [[CrossRef](#)]
14. Doneus, M.; Miholjek, I.; Mandlbürger, G.; Doneus, N.; Verhoeven, G.; Briese, C.; Pregesbauer, M. Airborne laser bathymetry for documentation of submerged archaeological sites in shallow water. *ISPRS Int. Arch. Photogramm. Remote Sens. Spat. Inf. Sci.* **2015**, *40*, 99–107. [[CrossRef](#)]
15. Bachmann, C.M.; Nichols, C.R.; Montes, M.J. Airborne Remote Sensing of Trafficability in the Coastal Zone. *NRL Rev.* **2009**, 223–228.
16. Yang, E.; LaRocque, P.; Guenther, G.; Reid, D.; Pan, W.; Francis, K. Shallow Water Depth Extraction—Progress and Challenges. In Proceedings of the US Hydrographic Conference, Norfolk, VA, USA, 14–17 May 2007; p. 13.
17. Adam, E.; Mutanga, O.; Rugege, D. Multispectral and hyperspectral remote sensing for identification and mapping of wetland vegetation: A review. *Wetl. Ecol. Manag.* **2010**, *18*, 281–296. [[CrossRef](#)]
18. Roessner, S.; Segl, K.; Heiden, U.; Kaufmann, H. Automated differentiation of urban surfaces based on airborne hyperspectral imagery. *IEEE Trans. Geosci. Remote Sens.* **2001**, *39*, 1525–1532. [[CrossRef](#)]
19. Manolakis, D.; Marden, D.; Shaw, G.A. Hyperspectral Image Processing for Automatic Target Detection Applications. *Linc. Lab. J.* **2003**, *14*, 79–116.
20. Van Der Meer, F.D.; Van Der Werff, H.M.; Van Ruitenbeek, F.J.; Hecker, C.A.; Bakker, W.H.; Noomen, M.F.; Van Der Meijde, M.; Carranza, E.J.M.; De Smeth, J.B.; Woldai, T.; et al. Multi- and hyperspectral geologic remote sensing: A review. *Int. J. Appl. Earth Obs. Geoinf.* **2012**, *14*, 112–128. [[CrossRef](#)]
21. Dekker, A.G.; Phinn, S.R.; Anstee, J.; Bissett, P.; Brando, V.E.; Casey, B.; Fearn, P.; Hedley, J.; Klonowski, W.; Lee, Z.P.; et al. Intercomparison of shallow water bathymetry, hydro-optics, and benthos mapping techniques in Australian and Caribbean coastal environments: Intercomparison of shallow water mapping methods. *Limnol. Oceanogr. Methods* **2011**, *9*, 396–425. [[CrossRef](#)]
22. Doneus, M.; Verhoeven, G.; Atzberger, C.; Wess, M.; Ruš, M. New ways to extract archaeological information from hyperspectral pixels. *J. Archaeol. Sci.* **2014**, *52*, 84–96. [[CrossRef](#)]
23. Savage, S.H.; Levy, T.E.; Jones, I.W. Prospects and problems in the use of hyperspectral imagery for archaeological remote sensing: A case study from the Faynan copper mining district, Jordan. *J. Archaeol. Sci.* **2012**, *39*, 407–420. [[CrossRef](#)]
24. Cavalli, R.M.; Licciardi, G.A.; Chanussot, J. Detection of Anomalies Produced by Buried Archaeological Structures Using Nonlinear Principal Component Analysis Applied to Airborne Hyperspectral Image. *IEEE J. Sel. Top. Appl. Earth Obs. Remote Sens.* **2013**, *6*, 659–669. [[CrossRef](#)]
25. Aqduş, S.A.; Hanson, W.S.; Drummond, J. The potential of hyperspectral and multi-spectral imagery to enhance archaeological cropmark detection: A comparative study. *J. Archaeol. Sci.* **2012**, *39*, 1915–1924. [[CrossRef](#)]
26. Cavalli, R.M.; Colosi, F.; Palombo, A.; Pignatti, S.; Poscolieri, M. Remote hyperspectral imagery as a support to archaeological prospection. *J. Cult. Herit.* **2007**, *8*, 272–283. [[CrossRef](#)]
27. Emmolo, D.; Franco, V.; Brutto, M.L.; Orlando, P.; Villa, B. Hyperspectral Techniques and GIS for Archaeological Investigation. In Proceedings of the ISPRS, Istanbul, Turkey, 12–23 July 2004.
28. Cerra, D.; Agapiou, A.; Cavalli, R.M.; Sarris, A. An Objective Assessment of Hyperspectral Indicators for the Detection of Buried Archaeological Relics. *Remote Sens.* **2018**, *10*, 500. [[CrossRef](#)]
29. Verhoeven, G.J. Are We There Yet? A Review and Assessment of Archaeological Passive Airborne Optical Imaging Approaches in the Light of Landscape Archaeology. *Geoscience* **2017**, *7*, 86. [[CrossRef](#)]
30. Traviglia, A. MIVIS Hyperspectral Sensors for the Detection and GIS Supported Interpretation of Subsoil Archaeological Sites. In Proceedings of the 34th Conference on Digital Discovery: Exploring New Frontiers in Human Heritage, CAA, Fargo, ND, USA, 18–22 April 2006.
31. Traviglia, A. Archaeological usability of hyperspectral images: Successes and failures of image processing techniques. *BAR Int. Ser.* **2006**, *1568*, 123.

32. Baltzer, A.; Cassen, S.; Walter-Simonnet, A.V.; Clouet, H.; Lorin, A.; Tessier, B. Variations du niveau marin Holocène en Baie de Quiberon (Bretagne sud): Marqueurs archéologiques et sédimentologiques. *Quaternaire* **2015**, *26*, 105–115. [CrossRef]
33. De Closmadeuc, G. Découverte d'un cromlec'h dans l'île d'El Lanic (Morbihan). *Bull. Société Polymath. Morbihan* **1867**, 28–30.
34. De Closmadeuc, G. Le cromlech d'Er Lanic et le Golfe du Morbihan à l'époque dite Celtique. *Bulletin et Mémoires de la Société Polymathique du Morbihan* **1882**, 8–24.
35. Gouezin, P. *Le Site Mégalithique d'Er Lannic*; Rapport Scientifique: Arzon, France, 1991.
36. Pastolt, Y. Use of Airborne LIDAR Bathymetry for Coastal Hydrographic Surveying: The French Experience. *J. Coast. Res.* **2011**, *62*, 6–18. [CrossRef]
37. Litto3D Terre Mer Altimétrie Bathymétrie Interface Terre-Mer Levé Lidar. Available online: <https://diffusion.shom.fr/pro/risques/l3d-mar-morbihan-2015.html> (accessed on 21 June 2019).
38. Cassen, S. *Corpus des Signes Gravés Néolithiques*; Programme Collectif de Recherche; Université de Nantes: Nantes, France, 2018.
39. Cassen, S.; Grimaud, V.; Boujot, C.; Chaigneau, C.; Collado, E.; De Jersey, P.; Querré, G.; Vigier, E.; Vourc'h, M. *Quelques résultats 2018 du PCR "Corpus des Signes Gravés Néolithiques en Bretagne"*; Journées du CREAAH: Rennes, France, 2019; pp. 16–17.
40. Cassen, S.; Grimaud, V.; Obeltz, C. Architectures monumentales néolithiques submergées en Morbihan. *Nouv. Archéologie* **2019**, *156*, 60–64.
41. Green, A.; Berman, M.; Switzer, P.; Craig, M. A transformation for ordering multispectral data in terms of image quality with implications for noise removal. *IEEE Trans. Geosci. Remote Sens.* **1988**, *26*, 65–74. [CrossRef]
42. Reed, I.; Yu, X. Adaptive multiple-band CFAR detection of an optical pattern with unknown spectral distribution. *IEEE Trans. Acoust. Speech Signal Process.* **1990**, *38*, 1760–1770. [CrossRef]
43. Liu, F.T.; Ting, K.M.; Zhou, Z.H. Isolation Forest. In Proceedings of the Eighth IEEE International Conference on Data Mining, Pisa, Italy, 15–19 December 2008; pp. 413–422.
44. Lee, Z.; Carder, K.L.; Mobley, C.D.; Steward, R.G.; Patch, J.S. Hyperspectral remote sensing for shallow waters. 2. Deriving bottom depths and water properties by optimization. *Appl. Opt.* **1999**, *38*, 3831–3843. [CrossRef] [PubMed]
45. Sicot, G.; Lennon, M.; Corman, D.; Gauthiez, F. Estimation of the Sea Bottom Spectral Reflectance in Shallow Water with Hyperspectral Data. In Proceedings of the International Geoscience and Remote Sensing Symposium, Milan, Italy, 26–31 July 2015; pp. 2311–2314.
46. Zhao, H. Spectral Sensitivity Database. Available online: <https://nae-lab.org/~rei/research/cs/zhao/database.html> (accessed on 19 June 2019).
47. Zhao, H.; Kawakami, R.; Tan, R.T.; Ikeuchi, K. Estimating Basis Functions for Spectral Sensitivity of Digital Cameras. In Proceedings of the Meeting on Image Recognition and Understanding, Miami, FL, USA, 20–25 June 2009; Volume 2009.
48. Maini, R.; Aggarwal, H. A Comprehensive Review of Image Enhancement Techniques. *arXiv* **2010**, arXiv:10034053.
49. McFeeters, S.K. The use of the Normalized Difference Water Index (NDWI) in the delineation of open water features. *Int. J. Remote Sens.* **1996**, *17*, 1425–1432. [CrossRef]
50. Lennon, M.; Sicot, G.; Thomas, N.; Smet, S.; Taillandier, C.; Corman, D.; Watremez, P.; Gauthiez, F. SWIM: Un Outil de Cartographie de la Zone de Petits Fonds à Partir de Données de Télédétection Optique Colloque Carhamb'ar, Cartographie des Habitats Marins Benthiques: De l'acquisition à la Restitution, Brest, 26–28 Mars 2013. In Proceedings of the Cartographie des Habitats Marins Benthiques: De L'acquisition à La Restitution, Brest, France, 26–28 March 2013; pp. 42–46.
51. Lecours, V.; Dolan, M.F.J.; Micallef, A.; Lucieer, V.L. A review of marine geomorphometry, the quantitative study of the seafloor. *Hydrol. Earth Syst. Sci.* **2016**, *20*, 3207–3244. [CrossRef]
52. Bajjouk, T.; Mouquet, P.; Ropert, M.; Quod, J.P.; Hoarau, L.; Bigot, L.; Le Dantec, N.; Delacourt, C.; Populus, J. Detection of changes in shallow coral reefs status: Towards a spatial approach using hyperspectral and multispectral data. *Ecol. Indic.* **2019**, *96*, 174–191. [CrossRef]
53. Gao, J. Bathymetric mapping by means of remote sensing: Methods, accuracy and limitations. *Prog. Phys. Geogr. Earth Environ.* **2009**, *33*, 103–116. [CrossRef]

54. Göritz, A.; Berger, S.A.; Gege, P.; Grossart, H.-P.; Nejtgaard, J.C.; Riedel, S.; Röttgers, R.; Utschig, C. Retrieval of Water Constituents from Hyperspectral In-Situ Measurements under Variable Cloud Cover—A Case Study at Lake Stechlin (Germany). *Remote Sens.* **2018**, *10*, 181. [[CrossRef](#)]
55. Pan, Z.; Glennie, C.; Fernandez-Diaz, J.C.; Starek, M. Comparison of bathymetry and seagrass mapping with hyperspectral imagery and airborne bathymetric lidar in a shallow estuarine environment. *Int. J. Remote Sens.* **2016**, *37*, 516–536. [[CrossRef](#)]



© 2019 by the authors. Licensee MDPI, Basel, Switzerland. This article is an open access article distributed under the terms and conditions of the Creative Commons Attribution (CC BY) license (<http://creativecommons.org/licenses/by/4.0/>).

Article

# Relative Radiometric Calibration of Airborne LiDAR Data for Archaeological Applications

Christopher Sevara <sup>1,\*</sup>, Martin Wieser <sup>2</sup>, Michael Doneus <sup>1,3</sup> and Norbert Pfeifer <sup>2</sup>

<sup>1</sup> Department of Prehistoric & Historical Archaeology, University of Vienna, Franz-Klein-Gasse 1-III, 1190 Vienna, Austria; michael.doneus@univie.ac.at

<sup>2</sup> Department of Geodesy and Geoinformation, Research Unit Photogrammetry, Technische Universität Wien, Gusshausstrasse 27-29, 1040 Vienna, Austria; martin.wieser@geo.tuwien.ac.at (M.W.); norbert.pfeifer@geo.tuwien.ac.at (N.P.)

<sup>3</sup> LBI for Archaeological Prospection and Virtual Archaeology, Hohe Warte 38, 1190 Vienna, Austria

\* Correspondence: christopher.sevara@univie.ac.at

Received: 19 March 2019; Accepted: 16 April 2019; Published: 19 April 2019

**Abstract:** Airborne laser scanning (ALS) data can provide more than just a topographic data set for archaeological research. During data collection, laser scanning systems also record radiometric information containing object properties, and thus information about archaeological features. Being aware of the physical model of ALS scanning, the radiometric information can be used to calculate material information of the scanned object. The reflectance of an object or material states the amount of energy it reflects for a specific electromagnetic wavelength. However, the collected radiometric data are affected by several factors that cause dissimilar values to be recorded for the same object. Radiometric calibration of such data minimizes these differences in calculated reflectance values of objects, improving their usability for feature detection and visualization purposes. Previous work dealing with calibration of radiometric data in archaeological research has relied on corresponding in-field measurements to acquire calibration values or has only corrected for a limited number of variables. In this paper, we apply a desk-based approach in which radiometric calibration is conducted through the selection of homogenous areas of interest, without the use of in-field measurements. Together with flight and scan parameters, radiometric calibration allows for the estimation of reflectance values for returns of a single full-waveform ALS data collection flight. The resulting data are then processed into a raster reflectance map that approximates a monochromatic illumination-independent true orthoimage at the wavelength of the laser scanner. We apply this approach to data collected for an archaeological research project in western Sicily and discuss the relative merits of the uses of radiometric data in such locations as well as its wider applicability for present and future archaeological and environmental research. In order to make the approach more accessible, we have developed a freely available tool that allows users to apply the calibration procedure to their own data.

**Keywords:** ALS; amplitude; radiometric calibration; reflectance; archaeology; Sicily

## 1. Introduction

Airborne laser scanning (ALS) data have become a common component of the archaeological prospection toolkit. The increasing availability of such data, along with the concomitant development of expertise in their collection, processing, and visualization for archaeological investigation continues to have a significant impact on the detection and interpretation of the present remains of human activity in landscapes around the world. Often, the main sources of such information are visualizations derived from digital terrain (DTM) or digital surface (DSM) models, which are geometric models that are calculated from the range data produced during a laser scan. However, there is other

information in laser pulses that, though often neglected, can be of great value to archaeological and paleoenvironmental research. In addition to range data, laser pulses reflected from a given surface also carry information about its physical properties. This information is included in the data in the form of radiometric values (e.g., the amplitude of the received laser pulse signal).

As these values are distinct from those of surface models, they can provide important additional information about the presence and composition of archaeological and environmental features. Radiometric values can be used to derive physical properties of surface objects related to the laser wavelength, independent of local lighting conditions [1] (p. 15). As they are collected, however, these radiometric values are distorted by many variables. These include factors related to the atmosphere, the instrument, its position in relation to the object being scanned, and the environmental context of the target. This makes it difficult to compare and quantify values as collected by the scanner. In order to make full use of the radiometric information, the received amplitude values collected for each laser pulse can be used to derive calibrated reflectance values so that radiometric differences of objects within and between strips are minimized [2] (p. 335), [3,4]. Once calibrated, these values can then be used for purposes such as visualization, interpretation, and detection of archaeological features.

Although a common component of ALS data capture, radiometric data sets have yet to become as integrated into the prospection toolkit as their geometric counterparts. Importantly, calibrated reflectance data in the infrared range have been shown to provide increased information regarding vegetation health, facilitating the appearance of vegetation marks associated with archaeological and paleoenvironmental features, when compared with other data sources [5–9]. Additionally, in cases where optical imagery is not concurrently recorded, reflectance-based imagery can be used as an approximation of simultaneously acquired monochromatic imagery for interpretation purposes [10] (p. 418), [11] (p. 50). While the usefulness of this information has been repeatedly demonstrated by such studies, its application in archaeological research continues to be explored in a very limited manner when compared to the uptake of other ALS-derived data products [7] (p. 161). This may be due to several factors, including the limited usability of amplitude data as acquired during flight, and difficulties involved in data processing.

While recent work has demonstrated the benefit of radiometrically calibrated full waveform (FWF) ALS data regarding increased archaeological feature detection, this work relies on the collection of simultaneous in-field radiometric measurements for calibration [5]. This may not always be a possibility (particularly when working with previously acquired data) or even a necessity for archaeological research that does not utilize and directly compare radiometric values between multiple ALS flights or to physical properties of objects. Often, single-flight ALS data sets are acquired ‘readymade’ by archaeologists from service providers who may have flown data collection sorties months in advance for other clients and are simply reselling the data. Moreover, whether looking for direct evidence of archaeological features or indirect indicators (e.g., vegetation marks) that may indicate buried archaeological or paleoenvironmental features, many archaeologists are usually only interested in the relative difference between the vegetation producing the marks and the surrounding environment (the contrast). Therefore, in many cases it may be sufficient for archaeologists to work with relatively calibrated reflectance values. However, even relative calibration of reflectance data requires metric information about the scan variables and target properties in order to be successfully applied.

In order to address this issue, the research presented in this paper outlines a desk-based methodology for relative radiometric calibration of FWF ALS data sets through the GIS-based selection and use of spectrally similar areas of interest (AOIs) across multiple ALS strips. This allows for the possibility of calculating reflectance values across strips without the need for simultaneously acquired in-field measurement. To make this approach more accessible to a wide variety of users, we have developed a freely available tool, based on the OPALS system [12], to assist with the calibration process. This approach can therefore be of particular use for single-flight ‘off the shelf’ FWF ALS data sets that contain radiometric information, may not have originally been acquired for archaeological purposes, and which lack contemporary optical imagery.

In this paper, we first outline the technical specifics of radiometric data as an element of ALS data capture, and its prior applications in archaeological research. Next, the desk-based methodology for relative calibration is presented and applied to FWF ALS data acquired from an archaeological case study area in western Sicily. Using the results, we evaluate the methodology, as well as the usability of such data as a component of archaeological research in western Sicily, which is a Mediterranean environment with considerably different environmental properties to that of previous archaeological studies dealing with the use of radiometric data. Considering this evaluation, we discuss the present and future potential of radiometrically calibrated data as a component of the archaeological prospection toolkit.

## 2. Radiometric Data from LiDAR: Theoretical Background and History in Archaeological Research

Radiometric calibration of amplitude data collected via ALS is a well-established process in the discipline of remote sensing and has also been explored in various capacities by the archaeological community. However, as can be seen in literature dealing with the subject (Section 2.3), the term ‘intensity’ is often used as a blanket term for diverse values, including uncalibrated values as collected by the scanner as well as subsequently calibrated data. Additionally, many authors have used the term ‘calibration’ for a wide range of attempts to compensate for distortions in uncalibrated data. The broad application of these terms can cause confusion, therefore in this paper uncalibrated values (as collected during a laser scan) are referred to as ‘amplitude’, and calibrated values as the ‘reflectance’ of materials or objects as a physical characteristic. The word ‘intensity’ is avoided, except when quoting the original authors of a study where the term was used. The following sections describe the background, properties, and terminology related to amplitude, reflectance, and calibration of reflectance data as well as its application in archaeological prospection.

### 2.1. LiDAR and Radiometric Data

ALS data capture is an optical 3D measurement technique that operates independently of local illumination, using a laser source for acquisition and measurement of a target surface [1] (p. 1). During an airborne laser scan, laser pulses of a certain wavelength are sent toward the ground surface and the backscattered radiation of each individual pulse is recorded. The scanning process results in two kinds of information:

1. The distance of the laser scanner to the reflecting object. This is the basic information gathered from the runtime of the laser pulse (therefore, the underlying principle is called “light detection and ranging”, i.e., LiDAR). With the addition of the exact location and orientation of the scanner and the laser pulse direction, coordinates can be assigned to the reflecting object.
2. Radiometric information and laser pulse characteristics. This information includes the strength of the received signal at the scanner, called amplitude. In FWF ALS systems, additional parameters such as the echo-width can be derived from the digitized waveform.

A laser scanner operates using electromagnetic (EM) radiation at a specific, well-defined wavelength (usually either 532 nm, 1064 nm or 1550 nm). As a function of the wavelength, EM radiation interacts in different ways when it hits object surfaces. Amplitude information, as a component of ALS data capture, represents the amount of energy reflected from an object that has been scanned with a focused pulse of laser radiation [1] (p. 15). Depending on the object’s material, a certain percentage of energy will be absorbed, transmitted, or reflected. The specific wavelength of the radiation being emitted by the scanner will also affect the transmission of the material being scanned. For example, the backscattered radiance from the 1550 nm short-wavelength infrared (SWIR) band has been shown to produce information about archaeological vegetation marks [5] (p. 170), which may be due to effects such as the greater absorption of SWIR radiance by water within plant materials [13]. Therefore, in theory, amplitude data contains wavelength-specific information about

the physical properties of the reflecting object. In practice, this information is distorted by several other factors that also affect the strength of the backscattered signal, such as the incidence angle or object size.

## 2.2. Radiometric Calibration

Material information within the received amplitude values from a laser scan can be very useful for identification of discrete objects, such as certain types of vegetation marks resulting from slightly higher levels of moisture retention or plant stress than their surrounding vegetation. Indications of plant stress may be more apparent in the near-infrared region of the electromagnetic spectrum, appearing earlier and more extensively than in the human visual range [14]. Thus, by extension, they may also appear in the amplitude values of a laser pulse in a similar wavelength. However, as it is collected the amplitude information is highly distorted. This is due to a number of variables, some of which are machine or workflow specific and thus relatively static, and some of which change with each new line or day of flight. Chief among these are the range and the influence of the laser pulse incidence angle on amplitude values, which is caused by changes in the position of the scanner relative to the surface being scanned. Figure 1 shows the influence of the incidence angle between two overlapping strips. On the border of a strip, the incidence angle is larger than in the middle, causing a visible decrease in the amplitude. Topographic variation (different range) and longer flight times (changing atmosphere) can also have a significant effect on amplitude values [3] (p. 416). Normalization of reflectance values of similar objects over an entire ALS data set (consisting of multiple parallel and cross strips) therefore requires calibration procedures that correct influences stated in the following sections [3].

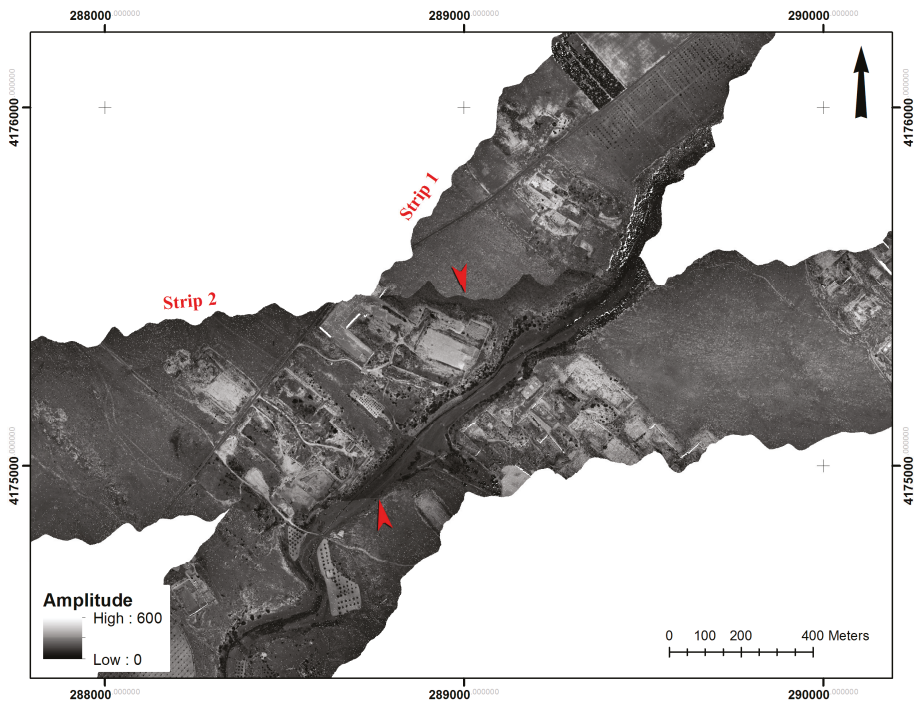


**Figure 1.** Uncalibrated amplitude map of two overlapping strips. Note the extreme differences between the edge of Strip 2 and Strip 1, as indicated by the red arrows. Visualization: 1 m spatial resolution raster using the median amplitude last echo point values for each cell. Coordinate System: WGS84 UTM Zone 33N.

### 2.2.1. Amplitude

The amplitude of the received signal is the remaining energy that is recorded by the system after the laser pulse is sent out, travels through the medium (e.g., air), is reflected by the object, and travels back (Figure 2). The amplitude, as described in Equation (1) [15,16], is therefore dependent on three types of parameters: (1) Scanner specific characteristics such as the emitted signal strength and the aperture size of the receiving optics, (2) signal loss due to the range, atmosphere and the incidence angle, and (3) target object characteristics (called the backscatter cross section).

Equation (1) Derivation of amplitude [15,16].

$$P_r = \frac{P_t D_r^2}{4 \pi R^4 \beta^2} \sigma \eta_{sys} \eta_{atm} \tag{1}$$

- $P_r$  Received signal
- $P_t$  Transmitted signal
- $D_r$  Diameter of the aperture
- $R$  Range
- $\beta$  Laser beam divergence
- $\sigma$  Backscatter cross section
- $\eta_{sys}$  System transmission
- $\eta_{atm}$  Atmospheric transmission

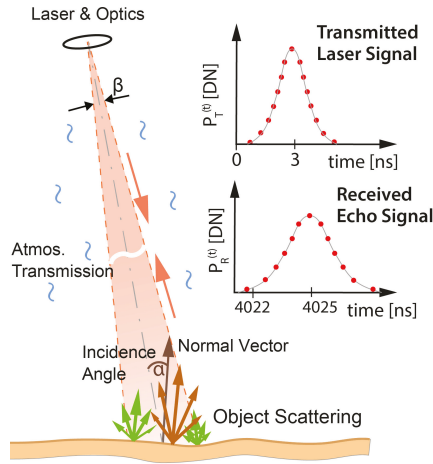


Figure 2. Airborne laser scanning (ALS), basic principle of transmission.

### 2.2.2. Reflectance

Reflectance is the physical property that denotes how much energy is reflected by an object’s material. Depending on the wavelength, EM radiation interacts in different ways when it hits object surfaces. As noted above, a certain percentage of energy will be absorbed, transmitted, or reflected. The backscatter cross section in Equation (2) [15], combines all target parameters, including the object’s material and its directionality of the scattering. It is a measure of the surface’s interaction with radiation. Within Equation (2), the reflectance is part of the backscatter cross section. For surfaces with uniformly bright, diffuse reflectance behavior (Lambertian surfaces, see [17] (p. 441)), the reflectance is therefore the physical property of how much energy is reflected by a material. For non-Lambertian surfaces, the value can be interpreted as a diffuse reflectance measure at the specific measurement geometry. Thus, this value only delivers the real reflectance for surfaces with Lambertian backscatter characteristics. In practice, these could be surfaces such as asphalt or unfinished wood. In order to calculate an

incidence angle corrected reflectance, Lambert's cosine law [18] is applied, as the reflected energy decreases with the incidence angle.

Equation (2) Derivation of reflectance [15].

$$\sigma = \frac{4\pi}{\Omega} \rho A_i \quad (2)$$

$\sigma$	Backscatter cross section
$\Omega$	Directionality of scattering
$\rho$	Reflectance
$A_i$	Area illuminated by the laser beam

### 2.2.3. Calibration to Derive Reflectance

The process of deriving material information in the form of the attribute reflectance from the received amplitude data is called radiometric calibration. Reflectance is derived by reformulation of Equations (1) and (2). Thus, the calibration process corrects the influences on the received amplitude and those from the object's geometry described above. Some of the parameters can be derived from laser echo information itself (e.g., range correction) or approximated using the incidence angle, which requires its neighboring points for estimation of the surface normal, scanner trajectory, and point of reflection information. All other parameters that are unknown but can be assumed to be invariant during one ALS campaign can be summarized in one constant, the calibration constant  $C_{cal}$  (The full derivation of the reflectance can be found in Appendix A.). Therefore,  $C_{cal}$  needs to be estimated during the calibration process. This is done by using areas whose reflectance values are known (either through separate measurement or estimation). Once  $C_{cal}$  is obtained, the reflectance data for each laser scan strip can be calculated.

### 2.2.4. Absolute and Relative Calibration

The derivation of the reflectance depends on the estimation of  $C_{cal}$  and therefore on areas with known reflectance values. Depending on the source of the known reflectance values, the calibration either results in absolute or relative calibration and reflectance values [2] (p. 335):

1. Absolute calibration uses in-situ measurements of the reflectance from ground targets that are measured in concert with the ALS acquisition.
2. Relative calibration uses approximate reflectance values from well-known surfaces that exhibit nearly Lambertian backscatter characteristics.

Absolute calibration can be used in order to compare values between multiple ALS data sets flown at different periods or wavelengths, or to relate radiometric data directly to physical properties of objects [2,5]. An absolute calibration approach is clearly necessary when comparing multiple data sets from different flights and/or wavelengths, or when the intent is to connect the physical properties of an object to the measurements (i.e., when calculating plant biomass or leaf-area indices). However, when using data from a single flight that has been previously acquired or purchased from a supplier after acquisition, it is not possible to obtain simultaneous in-field measurements. Furthermore, if the intent is simply to utilize the data to quantitatively or qualitatively look for relative differences in reflectance within a given data set, absolute calibration may be unnecessary. This includes the bulk of archaeologically relevant uses of radiometrically calibrated data, in which the user is only interested in examining the relative contrast between objects and where the real-world values of an object are not necessary.

## 2.3. Radiometric Data and Calibration in Archaeological Research

The technical specifics of FWF ALS data capture and its application in archaeological research for topography-based purposes (i.e., as described in point 1 of Section 2.1) have, by now, been widely

reported [19–23]. While the overview of various uses of LiDAR reflectance information presented by Höfle and Pfeifer [3] (p. 417–419) summarizes its use for the improvement of ALS data processing as well as its application in classification of land use/land cover, considerably less attention has been given to such characteristics of laser pulses in archaeological research. Coren [24] visualized ‘calibrated intensity’ data in the area of Roman Aquieia in Northern Italy, locating a number of “anomalies already seen in the digital orthophoto”. However, their archaeological significance was not discussed. Challis has used ‘intensity’ data in the interpretation of river valleys [6–9]. Challis’ work also discussed the wide range of factors contributing to its inherent distortion. Furthermore, attempts were made to compensate for surface variation [6,7] (p. 164). From the resulting normalized image, Challis could identify cropmarks suggesting a Romano-British villa site at Cromwell that was not visible in the DTM [6] (p. 7,11). At the river Trent, similar data revealed cropmarks of paleochannels and hinted at parched crop and “highly saturated ground” [7] (p. 163).

Although both Challis and Coren applied calibration procedures to their data sets, these only accounted for a limited number of parameters. Challis [6] (p. 6) corrected for topography using a range-based formula adapted from Luzum et al. [25]. The impact was, however, minimal [6] (p. 9). This may be due to the fact the calibration process applied in the study changed only one of many distorting factors. Based on this experience, Challis proposed further research into calibration, especially with regard to the use of FWF ALS, and to make further use of the results. This includes ALS acquisition flights during the vegetation season and combining the resulting data with other prospection data [7] (p. 168).

In 2014, Briese et al. [5] presented a workflow for absolute radiometric calibration of FWF ALS data that provides calibrated multi-wavelength reflectance images useful for archaeological prospection. In contrast to the findings of Challis and Howard [7] (p. 167), Briese et al. were able to show significant improvement in usability of calibrated reflectance data acquired from an ALS scan in low-relief areas of fairly uniform vegetation. It should be noted, though, that the scan parameters, scanner type, and flight conditions were very different to that of Challis and Howard’s study. The approach used in [5] is based on measurement of in-situ reference targets and recording of associated meteorological data, decomposition of the full-waveform to acquire echo parameters, and subsequent calculation of local variables and correspondence of ALS data with in-situ measurements in order to archive a calibration coefficient, which is applied to all strips [5] (p. 166). While the study showed a significant increase in the detection of vegetation marks indicating archaeological features of interest in the area of (formerly) Roman Carnuntum (Lower Austria) when compared with interpretations based on information from existing orthoimagery, the requirements of the absolute calibration process exceed the limits of data acquired ‘off the shelf’ or when simultaneous in-field measurements are not possible.

### 3. Methodology

Our workflow consists of a desk-based approach to derive the reflectance of a multi-strip ALS data set, ideally collected during a single flight period. Preferably, a geometric strip adjustment should be applied to the data set prior to application of the workflow, as was the case with our data set. The workflow used for the derivation of calibrated reflectance maps from FWF point clouds was implemented in the software package OPALS [12]. Instead of using in-field measurements, which were not available, estimated Lambertian reflectance values for given surfaces were used. However, the process for calibration is the same, regardless of the source of the reflectance values. Therefore, this approach may also be used for absolute calibration if the necessary measurements are available.

In addition to the point cloud (containing amplitude values) and estimated reflectance values for given locations, another key point attribute is the beam vector (Figure 3), which is needed to calculate the range and incidence angle. The beam vector is calculated using data from a trajectory file generated during the laser scan, which contains time, position and orientation information about the laser beam origin as acquired from the GNSS/IMU of the instrument. It is also possible, to some extent, to use

approximate estimations of such values. However, this may result in less accurate or unsatisfactory calibration results and more effort in pre-processing.

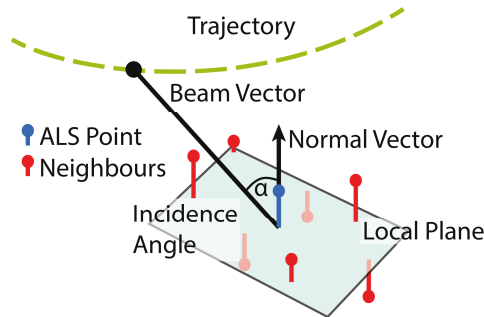


**Figure 3.** Illustration of the beam vector and normal vector of a laser pulse. The beam vector is calculated using absolute position and orientation information about the laser beam origin.

The calibration process is divided into three parts: (1) Pre-computation of the calibration attributes, (2) derivation of the calibration constant ( $C_{cal}$ ), and (3) reflectance calculation and generation of a reflectance map from the calibrated data in the point cloud (Figure 4):

1. **Pre-computation:** As described in Section 2.2, there are specific attributes that need to be calculated for each echo prior to derivation of the calibration constant. The principal attributes needed are the range of the laser beam and its incidence angle. The range is calculated by using the trajectory file generated during the laser scan, while the calculation of the incidence angle requires the beam vector and the local plane normal vector (Figure 5), using a robust plane interpolation of neighboring points based on the point cloud derived from the laser scan.
2. **Derivation of the Calibration Constant ( $C_{cal}$ ):** The calibration constant is derived by defining areas of similar, known reflectance (e.g., roofs, asphalt, or concrete), using the uncalibrated amplitude data in the form of a raster image as a guide. The areas are usually identified and chosen from on-site knowledge or, if available, from the orthoimages acquired simultaneously with the laser scan or satellite imagery. These AOIs are created as a shapefile containing the geometry of the AOI and an estimation of the surface reflectance. If the surface reflectance value is not known, values for individual material types can be acquired from online sources such as the USGS Spectral Library [26,27]. The calibration constant is calculated using the values defined in the AOI shapefile and the pre-computation data.  $C_{cal}$  is estimated for every point within each shape polygon, and the median value of the estimations is used for the reflectance calculation.
3. **Reflectance Calculation:** Once the radiometric calibration constant is obtained, the reflectance attribute is calculated for all echoes. A raster grid is calculated from the output using the median values of reflectance for each cell.

To apply the workflow, we began by creating a shapefile to digitize AOIs in a GIS environment, using a raster map created from the uncalibrated amplitude values in the point cloud as a reference. In our case, we used an asphalt road and assumed a standard reflectivity of 0.2, which has been shown to be the mean reflectivity for worn asphalt surfaces at the wavelength of the scanner used in our study [5] (p. 337), [28]. While such surfaces vary due to factors such as age, moisture, and material inclusion, assuming a mean value for calibration was valid enough, as we were only interested in relative values. What was more important was that the AOI areas chosen were similar in terms of wear and material. Each AOI was digitized as a separate shape with its own corresponding attributes in the attribute table. In addition to the unique identifier, the only other necessary field in the shapefile table was a numeric field in which the estimated Lambertian reflectance value for the material within the AOI was input. An initial pre-computation (1) was run to acquire the necessary attributes for

each echo. The OPALS module RadioCal [29] was then used to acquire the calibration constant in conjunction with the data from the AOI shapefile (2). RadioCal was then re-run in order to apply the reflectance calculation to all echoes in the data set (3). The resulting point cloud was used to generate the calibrated reflectance map in the OPALS module Cell [30], using the median reflectance values from the last return points in each cell of the raster grid. A batch file containing the necessary commands was used to automate all stages of the process subsequent to the generation of the AOI shapefile.

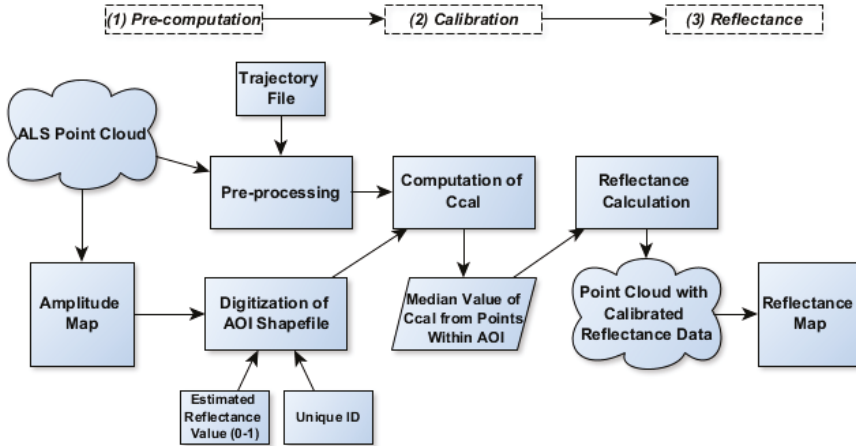


Figure 4. Workflow for relative calibration of reflectance data.

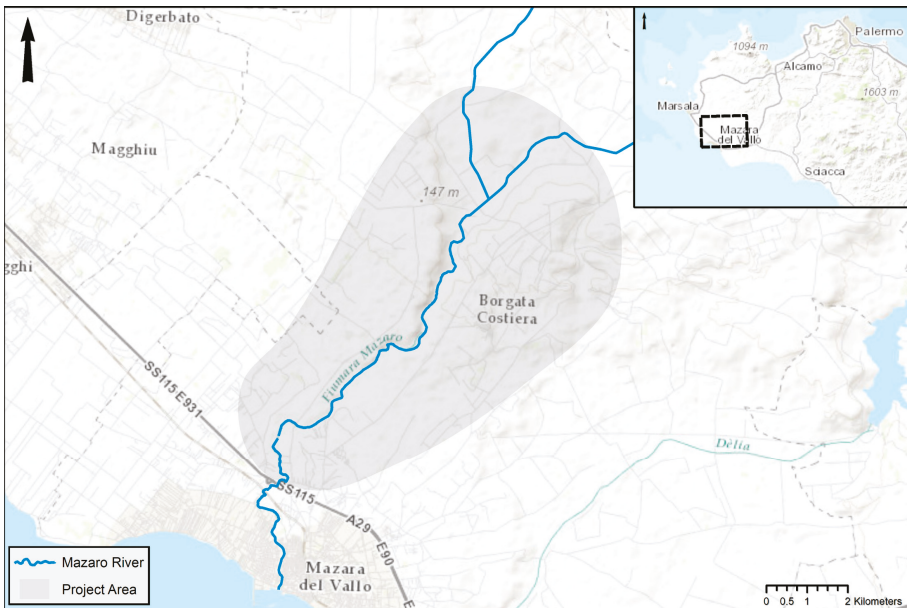


Figure 5. The Prospecting Boundaries project area, western Sicily. Background image © ESRI.

## 4. Case Study and Data Acquisition

### 4.1. The Mazaro River Corridor, Western Sicily

In order to evaluate the applicability of the relative calibration process for archaeological research, we applied the method to data collected during the Prospecting Boundaries project. The Prospecting Boundaries project [31], in cooperation with the Soprintendenza per i Beni Culturali ed Ambientali di Trapani, seeks to explore the diversity of land use in the region along the Mazaro river corridor using integrated archaeological prospection techniques to investigate the present remains of past activity in the landscape. These techniques include active and passive remote sensing data collection and interpretation, geophysical prospection, surface survey, and geoarchaeological evaluation. Centered on the Mazaro river, the project encompasses an area of roughly 70 km<sup>2</sup>, stretching inland from the river mouth at modern-day Mazara del Vallo (Figure 5). The project is concerned with human activity during all periods in the region, working backward from the present to document and deconstruct modern and historical land use in order to try to connect the relict fragments of prior human activity to continuity and change in the wider landscape. The hinterlands of Mazara del Vallo are a prime location in which to explore these topics, as they contain a rich matrix of known archaeological sites from the Upper Palaeolithic to the modern era [32–38]. However, while areas in the wider region of western Sicily have been the subjects of more systematic field surveys in recent years (e.g., [39,40]), the area around the Mazaro has received comparatively little systematic attention. This also makes it an ideal location to test the applicability of new integrated archaeological prospection techniques.

Modern land use in our project area has a variable impact on the surface visibility of the archaeological record. In the southern and northern parts of the project area, land use is largely given over to agricultural production. This includes the growing of cereal crops, vineyards, and olive and fruit trees. The central part of the project area with its rocky limestone outcrops, known locally as *sciara* (pl. *sciare*), is mainly used for pasturage and quarrying, which seem to be a common practice in the region from antiquity to modern times. A switch to more intensive agricultural and resource extraction practices since the 1950s, as evidenced by historical aerial imagery, has had a large impact on surface visibility in the region [41,42]. Furthermore, land fragmentation further reduces the visibility of manifesting vegetation marks between irregular fields containing discontinuous vegetation (Figure 6). Thus, the environmental conditions and land use in this study area are heterogeneous and noticeably different to those in the abovementioned studies.

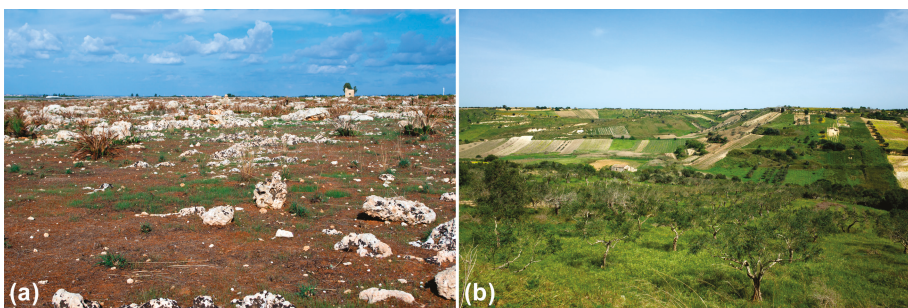


**Figure 6.** (a) The sciara di Mazara del Vallo; (b) land fragmentation resulting from the subdivision of parcels and agricultural diversity. Photographs: C. Sevara.

Due to the range of human activity and the physical properties of the modern landscape, archaeological sites tend to appear in a variety of direct and indirect ways in our study area. For instance, features of interest manifesting as rock-cut or rock-worn relief objects in ALS-derived digital elevation models (DEMs) generally tend to appear in the southern and central parts of our project area where the land use is more given over to pasturage and quarrying, and the Miocene/Pliocene rocks run closer to

the modern ground surface. In the northern part of the project area, topographic data is more indirectly useful, providing general information about the physiographic environment. This diversity also prompts us to look for new methodological solutions that can support our research goals. Therefore, one of the key goals of this research is to evaluate the applicability of radiometric data sets in extremely heterogeneous environments such as our case study area along the Mazaro.

#### 4.2. Data Sets

A single flight FWF ALS data set was acquired specifically for the project. Airborne Technologies GmbH (ABT), a commercial provider of ALS surveys with experience in data acquisition for archaeological research, conducted the survey on the morning of 21 February 2016 using a Riegl LMS-Q680i scanner [42] (p. 618), which operates at a wavelength of 1550 nm [43]. Laser data and corresponding orthoimagery were collected in 26 longitudinal strips with an overlap of 20%, and two cross strips, resulting in an average unfiltered point density of 16 points per square meter (Table 1). Initial postprocessing, including strip adjustment and calculation of the 3D point cloud, was carried out in Terrascan [44]. While amplitude data was recorded during the flight, no simultaneous ground acquisition of reflectance values was performed.

**Table 1.** ALS and orthoimage acquisition parameters. Acquisition date: 21 February 2016 0746-124. Source: Airborne Technologies, GmbH/Riegl Laser Measurement Systems.

Laser Scanner: Riegl LMS-Q680i Full Waveform		RGB Camera: IGI Digicam H-39	
Unfiltered Point-Density (per m <sup>2</sup> )	16	Array Size	39 MP
Strip Overlap	20%	Detector Pitch	6.8 µm
Scan angle (whole FOV)	60°	Image Size	7216 × 5412 px
Flying height (AGL)	511 m	Focal Length	50 mm
Speed of aircraft (TAS)	110 knots	Ground Sample Distance	8 cm
Laser Pulse Rate	400,000 Hz	Overlap (Side/Forward)	30/60%
Measurement Rate (max)	266,000 Hz	Exposure Time (s)	1/750
Scan Lines per second	169	Aperture	f/5
Laser Wavelength	1550 nm (SWIR)	Image Color Mode	RGB
Strip Adjustment/Error	Yes, 0.0128 m (std. deviation)		
Filtering	Robust interpolation (OPALS)		
Reflectance Image Resolution	50 cm		

## 5. Application and Results

### 5.1. Results of the Calibration Process

The calibration workflow was applied to our entire 60 km<sup>2</sup> dataset along the river Mazaro. A substantial minimization of per strip differences can be noted in the calibrated reflectance image as compared to one using the amplitude values as acquired from the scanner. When calibrated, the values for discrete objects become more uniform (Figure 7). While the differences between strips are not altogether eliminated, they are nevertheless greatly minimized.

This can be observed in the values for a highly reflective feature, such as the modern quarry illustrated in Figure 8. The area shown was used to calculate pixel wise differences of amplitude and reflectance maps from two overlapping strips, and a spot comparison was calculated for the two points illustrated in the figure. Point 1 was calculated from the surface of the modern quarry strip, while Point 2 was calculated from an asphalt road surface similar to that used as an AOI for the calibration process. The amplitude differences deviated significantly in comparison to the calibrated reflectance, as seen in the histogram displayed in Figure 9. The amplitude values were normalized by 600 (i.e., the maximum amplitude within the strips) for comparison purposes. The values for amplitude and calibrated reflectance for each point in three overlapping strips are provided in Table 2.

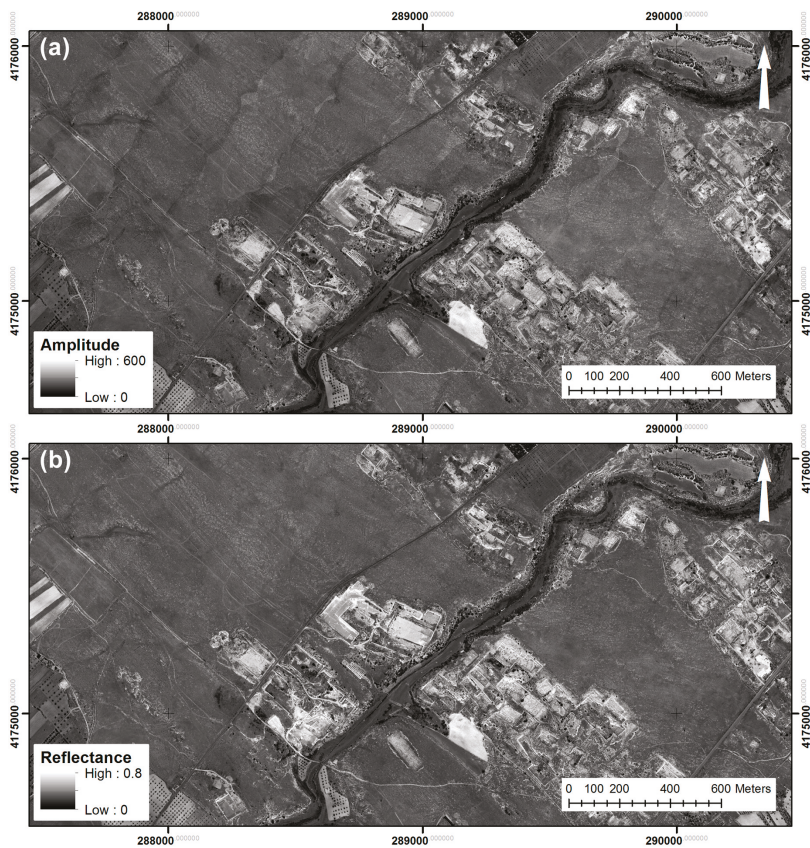


**Figure 7.** (a) Uncalibrated amplitude map of strips; (b) calibrated reflectance map of strips. Visualization: 1 m spatial resolution raster calculated using the median value of each cell. Coordinate system: WGS84 UTM Zone 33N.

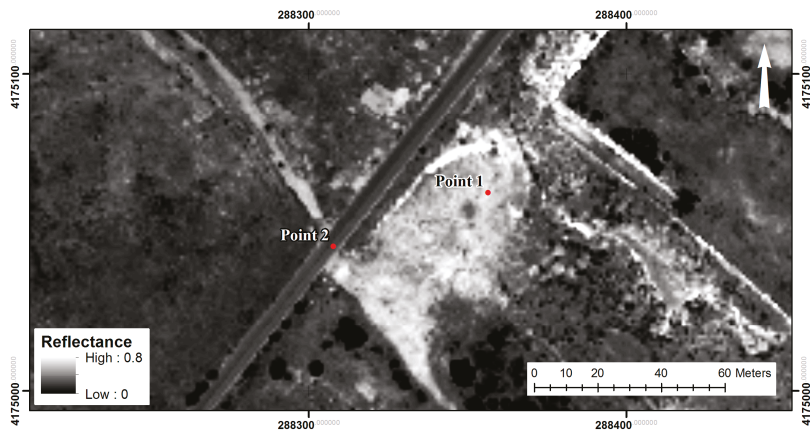


**Figure 8.** Calibrated reflectance map showing locations of spot comparisons. Point 1: Modern quarry strip. Point 2: Asphalt road. Visualization: 1 m spatial resolution raster calculated using the median value of each cell. Coordinate system: WGS84 UTM Zone 33N.

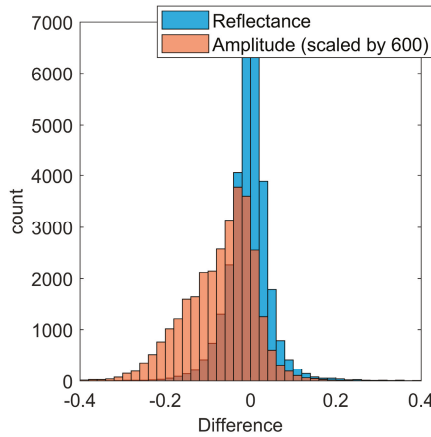


Figure 9. Histogram of differences of two strips. Red: Amplitude scaled by 600. Blue: Reflectance.

Table 2. Amplitude and calibrated reflectance values for points shown in Figure 8.

		Strip 1	Strip 2	Strip 3
Point 1	Amplitude	477.0	451.5	357.0
	Reflectance	0.51	0.49	0.54
	Range	Amplitude: 119.5/scaled by 600: 0.20 Reflectance: 0.06		
Point 2	Amplitude	215.0	190.0	179.5
	Reflectance	0.22	0.23	0.25
	Range	Amplitude: 35.5/scaled by 600: 0.06 Reflectance: 0.03		

### 5.2. Archaeological Applications

The calibrated reflectance data in the point cloud have provided useful information about archaeological features within our project area. A 50 cm spatial resolution raster calculated from the reflectance values in the last echoes of the calibrated ALS point cloud was used for the specific purpose of examining the viability of the data for feature detection via visual inspection of the data and comparison with RGB imagery and terrain-derived visualizations. From an archaeological standpoint, we find the reflectance data to be useful in our project area in two main ways: For direct detection of rock cut archaeological features, and for the indirect detection of features through the proxy of vegetation and soil marks.

Rock-cut and rock-worn features are some of the most prominent classes of features in our project area that are detectable in remote sensing data. In addition to the fairly prominent modern quarry sites mentioned above, other subtler rock-cut and rock-worn features could be delimited in the reflectance map. This included older quarries, foundations of habitation structures, and relict evidence of transport in the form of vehicle ruts worn into the exposed bedrock. This information has proven particularly helpful in differentiating between human made rock cut structures, such as the foundations of houses and other buildings, and the geological features visible in the area. The builders of these structures took advantage of the natural geological framework of the area, carving their dwellings into the softer components of the bedrock and following the rectilinear structure of the geological substrate. As the human-made structures often follow the geological pattern and are of similar sizes and shapes to the natural features, they can be difficult to delimit in remote sensing data. Unlike the quarries, many of these multi-room structures are also comparatively shallow, at as little as 20 cm below the surrounding

rock. However, like the modern quarries, the rock cut structures and their fill exhibit more uniform reflectance than their surrounding natural counterparts. This makes them easier to differentiate from the surrounding natural geology, as is the case with the structures in Figure 10, which depicts a group of rock-cut structures in the central part of the image (Figure 10a–c)

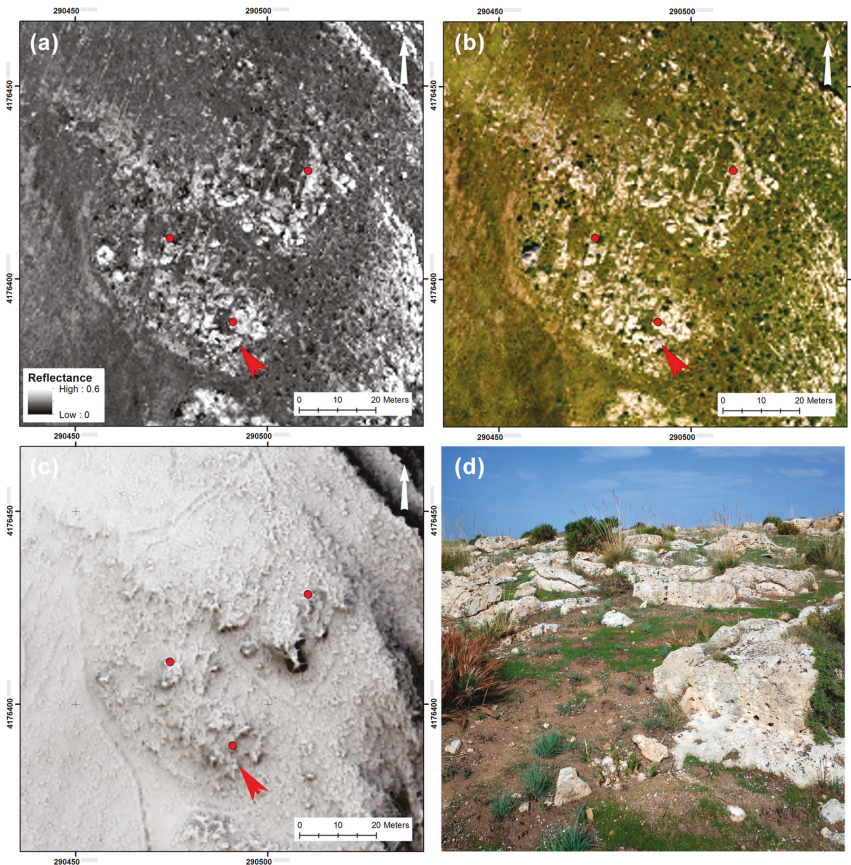


**Figure 10.** Rock-cut structure foundations (representative structures are to the left of red dots). (a) Contrast stretched calibrated reflectance image of rock cut structures, which can be identified as more homogenous rectangular objects amongst the bedrock outcrop; (b) contrast stretched RGB orthoimage; (c) multiple visualization (Multi hillshade, Slope, Sky-view factor, positive openness) of a 50 cm spatial resolution digital terrain model (DTM) specifically filtered to preserve archaeological structures; (d) ground image of one of the rock-cut structure foundations (position indicated by red arrows). Coordinate system (a–c): WGS84 UTM zone 33N. Photograph (d): C. Sevara.

Additionally, the reflectance values clearly delimit the extensive groups of animal-drawn vehicle ruts that crisscross the exposed bedrock in our project area (Figure 11). These anastomosing networks are relicts of the former landscape infrastructure in the region, and serve as important indicators of trade, transport, and other movement throughout the area. While such networks have been extensively studied in other areas, such as Malta and the Azores [45–47], their history has yet to be explored in western Sicily. Although the route relicts sometimes reach lengths of over 100 m, the individual tracks do not always manifest in terrain-derived visualizations of the ALS data, possibly due to a combination of effects that include their narrow feature dimensions (individual tracks have widths of approx. 50 cm

and depths of up to approx. 60 cm), filtering and interpolation of the elevation models. Some are shallow and appear to have been less frequently used, while others are set much deeper into the bedrock. Furthermore, they are often filled with soil and/or emergent vegetation, both of which could contribute to their low relief manifestation (Figure 11d). However, the terrain-based visualizations have other advantages, such as depicting the outlines of the more topographically prominent of the linear features, which may indicate that particular strands in the network were used more heavily than others. Figure 11 shows the complimentary nature of the terrain, orthoimage, and reflectance-based visualizations. While the terrain visualization indicates the direction, extent, cross-cutting, and depths of the more prominent parts of the network, the reflectance and RGB images detail individual tracks and allow for an estimation of the relative use-wear of tracks based on their color and reflectance. Therefore, we found it advantageous to use the reflectance map in conjunction with other data sets to delimit the properties of these features.

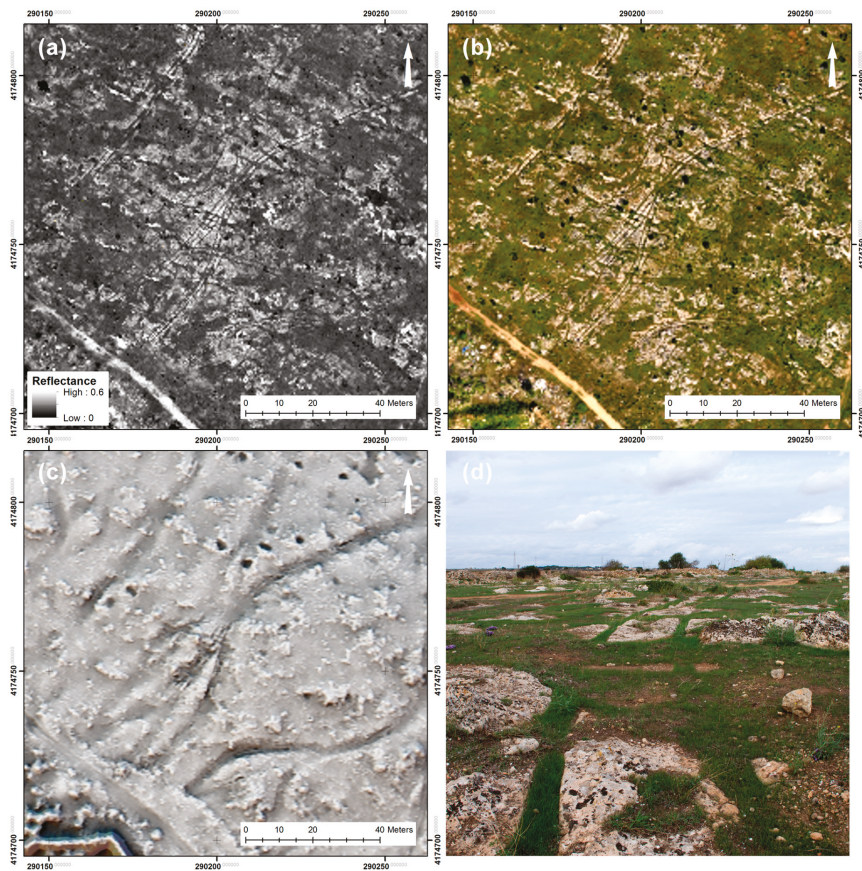


**Figure 11.** Cart tracks made by animal-drawn vehicles. (a) 50 cm spatial resolution contrast stretched calibrated reflectance image of track network; (b) 50 cm spatial resolution contrast stretched RGB image of track network; (c) multiple visualization (Multi hillshade, Simple Local Relief Model, Sky-view factor) of a 50 cm spatial resolution DTM specifically filtered to preserve archaeological structures; (d) ground image of one of the more ephemeral cart track pairs. Note that while the DTM visualization depicts the general outline of the deeper features in the network, the individual tracks for all but the deepest of the features are only visible in the reflectance and RGB images. Coordinate system (a–c): WGS84 UTM Zone 33N. Photograph (d): C. Sevara.

In some circumstances, radiometrically calibrated images are more informative than RGB orthoimagery for crop mark visibility [5]. However, this was not the case for the data acquired in our project area. This may be due in part to the time of year the ALS data were collected, but it was also due to the general environmental and agricultural conditions in the region. Although no new archaeological soil or vegetation marks were identified based solely on the reflectance data, we observed comparable marks in the reflectance map to those identified in the RGB imagery. At the site of Guletta, a key research site for our project, data from remote sensing, geophysical prospection, intensive surface survey, and artifact analysis indicate the presence of a multi-ditched archaeological structure occupied between the mid-2nd and 1st millennium BC [41,48]. Based on this information, we interpret the marks in the image as remnants of structures constructed during various phases of the site's occupation. Here, the calibrated reflectance data have helped to delimit soil and vegetation marks indicating the location of the prehistoric ditched enclosure, although the reflectance data alone did not provide a significant amount of new information about these features (Figure 12). Nevertheless, it can be seen from this example that, like the RGB image, the reflectance image contains information about the vegetation contrast that is indicative of archaeological features. This is, therefore, a good example of how reflectance data can also be used as a substitute for simultaneously acquired orthoimagery in cases where orthoimagery is not available.

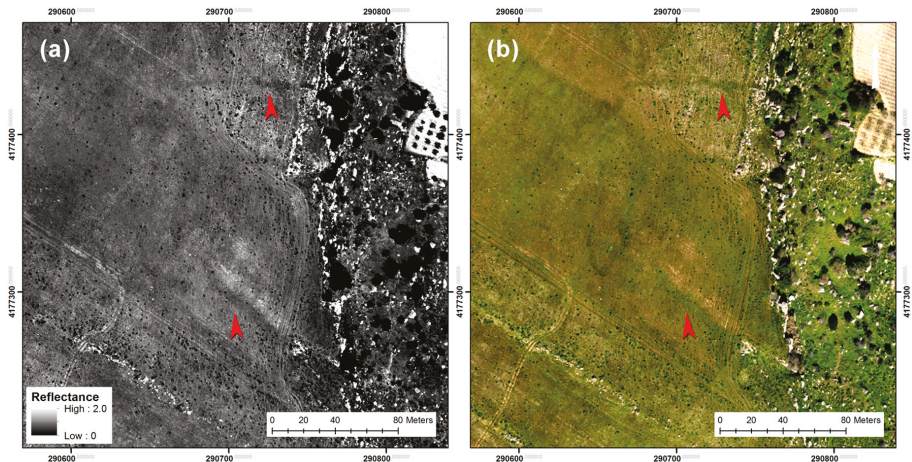


**Figure 12.** Vegetation marks indicating the presence of a ditched settlement structure. (a) 50 cm spatial resolution contrast stretched calibrated reflectance image of vegetation marks indicating ditched structure; (b) 50 cm spatial resolution contrast stretched RGB image of vegetation marks indicating ditched structure. Red arrows indicate location of vegetation marks. Coordinate system: WGS84 UTM Zone 33N.

### 5.3. Paleoenvironmental Applications

Reflectance data have also proven to be a useful source of paleoenvironmental information in the project area. Paleomeanders of the Mazaro are in evidence in the northern part of our project area, where the two spring-fed streams that form the Mazaro converge into the agricultural plain. Here, the calibrated reflectance image clearly indicated former channels of the Mazaro. While some could be attributed to the channelization of the river in the late 1960s and early 1970s as corroborated by historical aerial imagery from the time, others seem to predate this activity. While the presence of such paleochannel indicators in the *sciara* area, where the Mazaro runs deep in its river valley, was not highly evident, the reflectance map indicates further paleodrainage areas that may have once served as aggregation points in an area where access to water has long been a primary concern (Figure 13a,b).

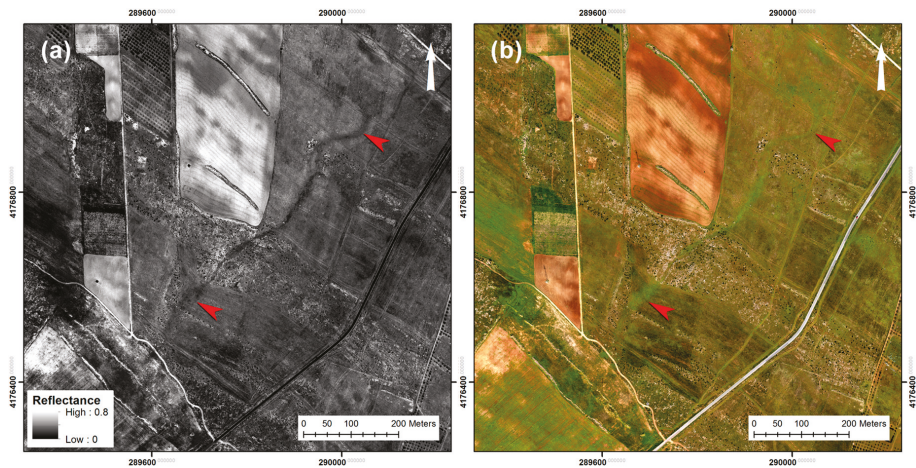


**Figure 13.** Paleoenvironmental features. (a) 50 cm spatial resolution contrast stretched calibrated reflectance image of the sciarra di Mazara del Vallo, in which a paleodrainage can be observed running through diverse land types; (b) 50 cm spatial resolution contrast stretched RGB image of the sciarra di Mazara del Vallo depicting the same location as (a). Red arrows indicate locations of paleochannel/paleodrainage. Coordinate system: WGS84 UTM Zone 33N.

## 6. Discussion and Future Research

### 6.1. Merits and Limits of the Calibration Approach

Relative radiometric calibration of amplitude information can increase the usability of LiDAR data by providing normalized reflectance values for similar features. This is useful for the delineation of human-made and natural features within an individual data set. As the resulting reflectance values are relative and based on estimation, they may not be able to be quantitatively compared to other reflectance data sets in the same area or directly to physical properties of the target objects themselves. However, this should not generally pose a problem for many applications. This includes those in which the user wants to qualitatively or visually assess the data in some way, generate true, shadow independent orthoimagery, manually or automatically detect and extract features within a single radiometric data set, perform statistical analyses, or calculate vegetation indices through a combination of the reflectance map with orthoimagery (since vegetation indices are generally relative calculations). Therefore, data generated using relative values can be applicable to a wide range of archaeological and environmental studies.

One thing that the approach we apply does not compensate for is significant change in the reflectance of an object due to changing environmental conditions such as moisture. If, for example, an archaeological feature is partially scanned while the ground surface is very dry, and partially scanned while the ground surface is very wet, there will naturally be a change in the reflective properties of the object. Furthermore, depending on the EM wavelength of the scanner, more radiation may be absorbed by the wet surface, meaning that less will be reflected. While this will generally not be an issue for data collected in a single flight, it may be problematic for data collected over an area when significant weather changes affect ground surface moisture levels during the day, or over multiple days (e.g., if the ground surface is very dry on one day that it is scanned, and very wet the next). This could be an issue for off-the-shelf datasets in which flights covering the project area are performed over multiple days. Scanner wavelength, acquisition times, and dates should be checked, and if no environmental data are present then historical weather records for the area in question should be consulted. In such cases, calibration could be performed separately for each epoch.

Currently, the calibration process requires access to proprietary ALS data processing software. Therefore, we have provided an interactive batch script and instructions for radiometric calibration in OPALS. Users who do not have access to a full version of OPALS can download the software and a key which unlocks the modules needed for radiometric calibration for a limited period. The batch file, test data, and information about how to download OPALS can be found at the University of Vienna Aerial Archive webpage [49,50]. In the future, we plan to release a freely available specialized tool with a graphical user interface that will streamline the calibration process. This application, currently in development, will be available for download in mid-2019 at the abovementioned website [49].

## 6.2. Archaeological and Environmental Potential

In addition to providing a workflow for calibration, our research provides further evidence that calibrated reflectance data can be of particular value in archaeological research. One of the chief merits of the approach outlined here is in its ability to unlock unique information about archaeological and environmental features that is stored within certain unexploited parameters of ALS data. In this way, ALS data sets can be seen as archives of not only vegetation and terrain, but also potential reflectance data indicating locations and properties of features that may no longer be extant. Therefore, the 'serendipity effect' [51] can also apply to archival ALS data.

In the context of our study area, archaeological features detectable using remote sensing techniques tend to manifest mainly as rock-cut and rock-worn structures and earthworks. Visualizations derived from the calibrated reflectance data have been very helpful in delimiting such features, providing clear differentiation between the texture of the structures, their fill and the surrounding areas compared to other data sets of similar spatial resolution. This is one way in which such data sets can be useful in environments such as ours, where it can be difficult to delimit visible features within the complex, noisy texture of exposed bedrock areas such as the *sciare*. As laser scanners are themselves a source of radiation, reflectance maps have the additional benefit of providing information similar to that of orthoimagery but without any shadows. This can be particularly advantageous for delimiting features that may be partially occluded by shadowing in orthoimagery. Thus, the calibrated reflectance maps provide complimentary information to terrain-based and orthoimage datasets.

The reflectance data in our study were less productive regarding detection of archaeological soil and vegetation marks in our project area. Although much of this may be due to the type of vegetation and terrain in our study area, it may also partly be due to the time of year in which the ALS data were collected. It would be worthwhile to investigate the usability of data collected at other times of the year and at different wavelengths to isolate the potential reasons for this. Nevertheless, we do see archaeological vegetation and soil mark manifestation on par with that seen in the corresponding orthoimagery, and a particular applicability for paleochannel/paleodrainage detection in both the *sciare* and the inland agricultural environments.

Regardless of the feature type, from a feature detection perspective, the ground sample distance (GSD) of a data set must be relatively high in order to clearly delineate small features and pick up subtle variations in reflectance value. The high density of returns in our ALS data set allowed us to generate a reflectance map at a GSD of 50 cm. This spatial resolution allows for the generation of data sets in which the resolution is high enough to identify fairly discrete features. Such resolution may not be possible for data collected at coarser ground spacing, although this should not limit the usability of reflectance information for the detection of features of larger size, including paleoenvironmental features.

## 6.3. Reflections on the Future of Radiometric Data in Archaeological Research

Through the development of a straightforward approach for relative calibration of amplitude values in LiDAR data, we hope to provide a wider range of users with access to an unexploited facet of information within their laser-based data sets. We see this parameter as being essential to a number of applications, yet chronically underused due to either the difficulty in processing it or an ignorance of its potential. While we have so far used our radiometrically calibrated data set for fairly

conventional purposes, we see further potential for such information as both direct and indirect aids to archaeological and environmental research. These uses include using reflectance values as parameters for the improvement of filtering routines for ALS data, where stone surfaces (representing surfaces devoid of vegetation containing archaeological features, such as incised cart ruts or stone walls) might be automatically excluded from filtering. Reflectance values can also be useful as parameters for automated feature detection applications [3] (p. 417), [52]. In our project area, we see particular potential for such applications with regard to automated detection and classification of modern and historic land use such as quarrying, which has significantly affected the modern ground surface. We envision this as part of a routine incorporating modern and historic data sets for continual monitoring of land use change, and as a way to inform our ongoing historic landscape characterization of the region.

There may also be potential in the combination of reflectance data with simultaneously acquired optical imagery to produce an approximation of false color infrared imagery [11] (p. 50), which could yield an increase in the detection of archaeological features, particularly vegetation marks. The success of such an approach would be dependent on several factors, including the laser wavelength and time of year of the flight. Image fusion techniques, such as those proposed by [53], may also be useful ways to combine reflectance map data with other remote sensing and geophysical prospection data sets. Additionally, reflectance data could be used for the calculation of vegetation indices [54] (p. 253), mitigating effects related to BRDF (bidirectional reflectance distribution function) [55]. Statistical calculations based on reflectance data could also be used for a number of other purposes, e.g., in order to calculate percentages of coverage of certain types of land cover over a given project area.

Calibrated reflectance maps may also be useful for terrestrial laser scanning applications in archaeology. For instance, as true orthoimages can be produced independent of local lighting conditions, reflectance data may be useful for generation of illumination-independent imagery for documentation and feature detection in low-light environments such as building interiors and caves. Thus, we see many applications for reflectance data, both as a standalone information source and in concert with other prospection information. These and numerous other applications for reflectance data could be very useful not only in the context of archaeological research in the Mediterranean, but for a wide range of disciplines working in a variety of physiographic environments.

## 7. Conclusions

In this paper, we have presented a desk-based methodology for relative radiometric calibration of amplitude information in ALS data sets and demonstrated its applicability for archaeological research. From our perspective, the lack of uptake in the use of radiometric data in archaeological research so far may be due to two issues: ignorance of its potential and difficulty in processing. We have addressed both of these issues, and have provided a workflow and freely available tools to help users to apply the approach to their own data sets. This approach provides an additional, accessible way to exploit often unused information already present in many LiDAR scans. Therefore, it is not only applicable to newly collected data, but also to the growing archive of LiDAR data sets that have a radiometric component. Furthermore, we see great potential for relative calibration of reflectance data not only in archaeological research, but in a wide array of disciplines that utilize LiDAR data for environmental analysis.

One of the chief merits of calibrated reflectance data lies in the potential to provide an illumination-independent true orthometric image that approximates an orthophotograph in the EM range of the scanner. We have investigated the use of such information in the context of western Sicily and found that reflectance data clearly provide us with important supplemental information in archaeological and paleoenvironmental contexts. This includes narrow linear features that are difficult to detect in corresponding terrain data, rock-cut habitation, and resource extraction features, paleodrainages, and paleomeanders indicative of the location of former water sources. What makes the reflectance data particularly useful as a comparative data set is that they are based on wholly different data values than visualizations derived from terrain values. While the terrain-derived visualizations highlight relief features in unique ways, they are all based on variations of the same core values.

Reflectance values, on the other hand, are based on different physical properties. Therefore, they can not only act as complimentary data sets to terrain-based visualizations, they can provide independent information about features whose reflectance may be uniform even if their relief displacement may be low. Furthermore, even when relatively calibrated, reflectance data have the potential to provide useful information for the improvement of LiDAR filtering, quantitative analyses, and automated feature detection. In light of this, we see reflectance data as being an important addition to the archaeological prospection toolbox in Mediterranean environments and beyond, providing additional ways to take even greater advantage of the information already present in LiDAR data.

**Author Contributions:** Paper Conceptualization C.S., M.D., M.W., N.P.; Writing—Original Draft C.S., M.W., M.D.; Methodology, M.W., C.S. Analysis, C.S, M.W., M.D. Visualization, C.S., M.W.; Writing—Review and Editing C.S., M.W., M.D., N.P.; Software M.W., C.S.; Funding Acquisition, M.D.

**Funding:** This research was funded by a grant from the Austrian Science Fund (Project ID: P-28410).

**Acknowledgments:** The Prospecting Boundaries project is carried out in cooperation with the Soprintendenza per I Beni Culturali ed Ambientali di Trapani. We would like to thank our project partner Sebastiano Tusa, Sicilian Regional Assessor of Cultural Heritage, and Dott.ssa Rossella Giglio, for their continued support of our research project. Programming of the software tool was carried out by the Vienna University of Technology Department of Geodesy and Geoinformation - Research Groups Photogrammetry and Remote Sensing. We would like to thank Dr. Geert Verhoeven, the anonymous reviewers and the special issue editors for their time and constructive comments on earlier drafts of this paper.

**Conflicts of Interest:** The authors declare no conflict of interest. The funders had no role in the design of the study; in the collection, analyses, or interpretation of data; in the writing of the manuscript, or in the decision to publish the results.

## Appendix A

The process of radiometric calibration is based on the following LiDAR adapted formulation of the radar equation, which describes the relation between the transmitted  $P_t$  and the received power  $P_r$  of an ALS system:

$$P_r = \frac{P_t D_r^2}{4 \pi R^4 \beta_t^2} \sigma \eta_{sys} \eta_{atm}$$

This formulation considers the following influencing factors: The receiver aperture diameter  $D_r$ , the range between the sensor and the target  $R$ , the laser beam divergence  $\beta_t^2$ , the backscatter cross section  $\sigma$  as well as losses occurring due to the atmosphere or in the laser scanner system itself, i.e., a system and atmospheric transmission factor  $\eta_{sys}$  and  $\eta_{atm}$  respectively. The backscatter cross section, which is given by the formula below, combines all target parameters such as the laser foot area  $A_i$  (i.e., the size of the area illuminated by the laser beam), the reflectivity  $\rho$ , and the directionality of the scattering of the surface  $\Omega$ .

$$\sigma = \frac{4 \pi}{\Omega} \rho A_i$$

All parameters which are unknown, but can be assumed to be invariant during one ALS campaign, can be summarized in one constant, the so-called calibration constant  $C_{cal}$ . This is eventually mathematically described as:

$$C_{cal} = \frac{\beta_t^2}{P_t D_r^2 \eta_{sys}}$$

Combining the first and third equation the formula for the backscatter cross section  $\sigma$  can be written as:

$$\sigma = \frac{C_{cal} 4 \pi R^4 \hat{P}_{iS_{p,i}}}{\eta_{atm}}$$

It is mentioned that in the above equation the actual received power  $P_r$  is replaced by the term  $\hat{P}_{iS_{p,i}}$ . This is due to the fact that received power  $P_r$  is proportional to the product of the amplitude  $\hat{P}_i$  and the echo width  $S_{p,i}$ .

Source: [15,16,29].

## References

1. Beraldin, J.; Blais, F.; Lohr, U. Laser Scanning Technology. In *Airborne and Terrestrial Laser Scanning*; Vosselman, G., Maas, H.-G., Eds.; Whittles Publishing: Dunbeath, Scotland, 2010; pp. 1–44.
2. Briese, C.; Pfennigbauer, M.; Lehner, H.; Ullrich, A.; Wagner, W.; Pfeifer, N. Radiometric Calibration of Multi-Wavelength Airborne Laser Scanning Data. In Proceedings of the XXII ISPRS Congress—ISPRS Annals of the Photogrammetry, Remote Sensing and Spatial Information Sciences, Melbourne, Australia, 25 August–1 September 2012; pp. 335–340. [CrossRef]
3. Höfle, B.; Pfeifer, N. Correction of laser scanning intensity data: Data and model-driven approaches. *ISPRS J. Photogramm. Remote Sens.* **2007**, *62*, 415–422. [CrossRef]
4. Wagner, W. Radiometric calibration of small-footprint full-waveform airborne laser scanner measurements: Basic physical concepts. *ISPRS J. Photogramm. Remote Sens.* **2010**, *65*, 505–513. [CrossRef]
5. Briese, C.; Pfennigbauer, M.; Ullrich, A.; Doneus, M. Radiometric Information from Airborne Laser Scanning for Archaeological Prospection. *Int. J. Herit. Digit. Era* **2014**, *3*, 159–178. [CrossRef]
6. Challis, K. Airborne Lidar Intensity and Georarchaeological Prospection in River Valley Floors. *Archaeol. Prospect.* **2011**, *18*, 1–13. [CrossRef]
7. Challis, K.; Howard, A.J. The role of lidar intensity data in interpreting environmental and cultural archaeological landscapes. In *Interpreting Archaeological Topography. Airborne Laser Scanning, 3D Data and Ground Observation*; Opitz, R., Cowley, D., Eds.; Oxbow Books: Oxford, UK, 2013; pp. 161–170.
8. Challis, K.; Howard, A.J.; Moscrop, D.; Gearey, B.; Smith, D.; Carey, C.; Thompson, A. Using airborne LiDAR intensity to predict the organic preservation of waterlogged deposits. In *From Space to Place: 2nd International Conference on Remote Sensing in Archaeology. Proceedings of the 2nd International Workshop, CNR, Rome, Italy, 4–7 December 2006*; Campana, S., Forte, M., Eds.; Archaeopress: Oxford, UK, 2006; pp. 93–98.
9. Challis, K.; Kinsey, M.; Carey, C.; Howard, A.J. Assessing the preservation potential of temperate, lowland alluvial sediments using airborne lidar intensity. *J. Archaeol. Sci.* **2011**, *38*, 301–311. [CrossRef]
10. Kraus, K. *Photogrammetry: Geometry from Images and Laser Scans*, 2nd ed.; De Gruyter: Berlin, Germany, 2007.
11. Vosselman, G.; Klein, R. Visualisation and Structuring of Point Clouds. In *Airborne and Terrestrial Laser Scanning*; Vosselman, G., Maas, H.-G., Eds.; Whittles Publishing: Dunbeath, Scotland, 2010; pp. 45–82.
12. OPALS: Orientation and Processing of Airborne Laser Scanning Data. Available online: <https://opals.geo.tuwien.ac.at/html/stable/index.html> (accessed on 7 April 2019).
13. Eitel, J.U.H.; Höfle, B.; Vierling, L.A.; Abellán, A.; Asner, G.P.; Deems, J.S.; Glennie, C.L.; Joerg, P.C.; LeWinter, A.; Magney, T.S.; et al. Beyond 3-D: The new spectrum of lidar applications for earth and ecological sciences. *Remote Sens. Environ.* **2016**, *186*, 372–392. [CrossRef]
14. Verhoeven, G. Near-Infrared Aerial Crop Mark Archaeology: From its Historical Use to Current Digital Implementations. *J. Archaeol. Method Theory* **2011**, *19*, 132–160. [CrossRef]
15. Wagner, W.; Ullrich, A.; Ducic, V.; Melzer, T.; Studnicka, N. Gaussian decomposition and calibration of a novel small-footprint full-waveform digitising airborne laser scanner. *ISPRS J. Photogramm. Remote Sens.* **2006**, *60*, 100–112. [CrossRef]
16. Jelalian, A.V. *Laser Radar Systems*; Artech House: Boston, MA, USA, 1992.
17. Koppal, S.J. Lambertian Reflectance. In *Computer Vision*; Ikeuchi, K., Ed.; Springer: Boston, MA, USA, 2014.
18. Lambert, J.H. *Photometria Sive de Mensura de Gratibus Luminis. Colorum et Umbræ. Sumpitibus Viduæ.*; E. Klett: Augsburg, Germany, 1760.
19. Doneus, M.; Briese, C.; Fera, M.; Fornwagner, U.; Griebel, M.; Janner, M.; Zingerle, M.-C. Documentation and Analysis of Archaeological Sites Using Aerial Reconnaissance and Airborne Laser Scanning. In Proceedings of the XXI International CIPA Symposium, Athens, Greece, 1–6 October 2007.

20. Doneus, M.; Briese, C.; Studnicka, N. Analysis of Full-Waveform ALS Data by Simultaneously Acquired TLS Data: Towards an Advanced DTM Generation in Wooded Areas. In Proceedings of the ISPRS TC VII Symposium, Vienna, Austria, 5–7 July 2010; Wagner, W., Székely, B., Eds.; Ernst Becvar Ges.mbH: Vienna, Austria, 2010.
21. Lasaponara, R.; Masini, N. Full-waveform Airborne Laser Scanning for the detection of medieval archaeological microtopographic relief. *J. Cult. Herit.* **2009**, *10*, 78–82. [CrossRef]
22. Lasaponara, R.; Coluzzi, R.; Masini, N. Flights into the past: Full-waveform airborne laser scanning data for archaeological investigation. *J. Archaeol. Sci.* **2011**, *38*, 2061–2070. [CrossRef]
23. Opitz, R.; Cowley, D.C. (Eds.) *Interpreting Archaeological Topography*; Oxbow Books: Oxford, UK, 2013.
24. Coren, F.; Visintini, D.; Prearo, G.; Sterzai, P. Integrating LiDAR intensity measures and hyperspectral data for extracting of cultural heritage. In Proceedings of the Italy–Canada 2005 Workshop on 3D Digital Imaging and Modeling: Applications of Heritage, Industry, Medicine and Land, Padova, Italy, 17–18 May 2005.
25. Luzum, B.; Starek, M.; Slatton, K.C. *2004 Normalizing ALSM Intensities*; Geosensing Engineering and Mapping (GEM) Center Report No. Rep\_2004-07-01; Civil and Coastal Engineering Department, University of Florida: Gainesville, FL, USA, 2004.
26. Kokaly, R.F.; Clark, R.N.; Swayze, G.A.; Livo, K.E.; Hoefen, T.M.; Pearson, N.C.; Wise, R.A.; Benzel, W.M.; Lowers, H.A.; Driscoll, R.L.; et al. *USGS Spectral Library Version 7: U.S. Geological Survey Data Series 1035*; United States Geological Survey: Reston, VA, USA, 2017. [CrossRef]
27. United States Geological Survey Spectral Library Version 7. Available online: <https://speclab.cr.usgs.gov/spectral-lib.html> (accessed on 27 February 2019).
28. United States Geological Survey Spectral Library Version 7: Asphalt GDS376 Black\_Road Old ASDFRa AREF. Available online: [https://crustal.usgs.gov/speclab/data/GIFplots/GIFplots\\_splib07a/ChapterA\\_ArtificialMaterials/splib07a\\_Aspphalt\\_GDS376\\_Blck\\_Road\\_old\\_ASDFRa\\_AREF.gif](https://crustal.usgs.gov/speclab/data/GIFplots/GIFplots_splib07a/ChapterA_ArtificialMaterials/splib07a_Aspphalt_GDS376_Blck_Road_old_ASDFRa_AREF.gif) (accessed on 27 February 2019).
29. OPALS: Orientation and Processing of Airborne Laser Scanning Data: Module RadioCal. Available online: <https://opals.geo.tuwien.ac.at/html/stable/ModuleRadioCal.html> (accessed on 7 April 2019).
30. OPALS: Orientation and Processing of Airborne Laser Scanning Data: Module Cell. Available online: <https://opals.geo.tuwien.ac.at/html/stable/ModuleCell.html> (accessed on 7 April 2019).
31. The Prospecting Boundaries Project. Available online: <http://mazara.univie.ac.at> (accessed on 27 February 2019).
32. Calafato, B.; Tusa, S.; Mammina, G. *Uomo e Ambiente Nella Storia di Mazara del Vallo—Indagine Topografica Nell'agro Mazarese*; Grafistampa Palermo: Palermo, Italy, 2001.
33. Di Stefano, C.A. Testimonianze archeologiche di età Arcaica e Classica da Mazara del Vallo. *Kokalos* **2016**, *LIII*, 35–52. [CrossRef]
34. Fentress, E.; Kennet, D.; Valenti, I. A Sicilian Villa and its Landscape. *Opus* **1986**, *5*, 75–95.
35. Leighton, R. *Sicily before History: An Archaeological Survey from the Palaeolithic to the Iron Age*; Duckworth: London, UK, 1999.
36. Mannino, G. Appunti di ricognizioni archeologiche. *Sicil. Archeol.* **1971**, *4*, 41–46.
37. Tusa, S. *La Sicilia Nella Preistoria*, 2nd ed.; Sellerio Editore: Palermo, Italy, 1999.
38. Tusa, S. Fenici, Indigeni ed Elimi alla luce delle nuove scoperte. In Proceedings of the Atti del V Congresso Internazionale di Studi Fenici e Punic, Marsala, Palermo, 2–8 October 2005; pp. 533–549.
39. Blake, E.; Schon, R. The Marsala Hinterland Survey: Preliminary Report. *Etruscan Stud.* **2010**, *13*, 49–66. [CrossRef]
40. Spanò Giammellaro, A.; Spatafora, F.; van Dommelen, P. Sicily and Malta: Between Sea and Countryside. In *Rural Landscapes of the Punic World*; van Dommelen, P., Gómez Bellard, C., Eds.; Equinox: Landon, UK, 2008; pp. 129–158.
41. Sevara, C.; Doneus, M.; Draganits, E.; Cusumano, R.; Frazzetta, C.; Palermo, B.; Pisciotta, F.; Stallone, R.; Totschnig, R.; Tusa, S.; et al. Testing Boundaries: Integrated Prospection from Site to Landscape in Western Sicily. In Proceedings of the AP2017: 12th International Conference of Archaeological Prospection, Bradford, UK, 12–16 September 2017; Jennings, B., Gaffney, C., Sparrow, T., Gaffney, S., Eds.; Archaeopress: Oxford, UK, 2017; pp. 230–232.

42. Sevara, C.; Verhoeven, G.; Doneus, M.; Draganits, E. Surfaces from the Visual Past: Recovering High-Resolution Terrain Data from Historic Aerial Imagery for Multitemporal Landscape Analysis. *J. Archaeol. Method Theory* **2018**, *25*, 611–642. [CrossRef] [PubMed]
43. Riegl LMS-Q680i: Long-Range Airborne Laser Scanner for Full Waveform Analysis. Available online: [http://www.riegl.com/uploads/tx\\_pxpriegldownloads/10\\_DataSheet\\_LMS-Q680i\\_28-09-2012\\_01.pdf](http://www.riegl.com/uploads/tx_pxpriegldownloads/10_DataSheet_LMS-Q680i_28-09-2012_01.pdf) (accessed on 27 February 2019).
44. Terrasolid Ltd. Terrascan—Software for LiDAR Data Processing and 3D Vector Data Creation. Available online: <http://www.terrasolid.com/products/terrascanpage.php> (accessed on 27 February 2019).
45. Mottershead, D.; Pearson, A.; Schaefer, M. The cart ruts of Malta: An applied geomorphology approach. *Antiquity* **2008**, *82*, 1065–1079. [CrossRef]
46. Trump, D.H.; Cilia, D. *Cart-Ruts and Their Impact on the Maltese Landscape*; Heritage Books: Sta. Venera, Malta, 2008.
47. Rodrigues, F.; Madruga, J.; Martins, N.; Cardoso, F. Dating the Cart-Ruts of Terceira Island, Azores, Portugal. *Archaeol. Discov.* **2018**, *6*, 279–299. [CrossRef]
48. Doneus, M. Aerial archaeology in the area of Mazara del Vallo, Sicily. Report of the reconnaissance seasons 2003–2004. *Archeol. AereaStudi Di Aerotopografia Aerea* **2007**, *2*, 269–284.
49. University of Vienna Aerial Archive, Resources Page. Available online: <https://luftbildarchiv.univie.ac.at/resources/> (accessed on 7 April 2019).
50. University of Vienna Aerial Archive, Radiometric Calibration of ALS Data. Available online: <https://luftbildarchiv.univie.ac.at/resources/software/radiometric-calibration-of-als-data/> (accessed on 12 April 2019).
51. Brugioni, D.A. The Serendipity Effect of Aerial Reconnaissance. *Interdiscip. Sci. Rev.* **1989**, *14*, 16–28. [CrossRef]
52. Hug, C.; Wehr, A. Detecting and identifying topographic objects in laser altimeter data. *Int. Arch. Photogramm. Remote Sens. Spat. Inf. Sci.* **1997**, *32*, 19–26.
53. Verhoeven, G.; Nowak, M.; Nowak, R. Pixel-level image fusion for archaeological interpretative mapping. In Proceedings of the 8th International Congress on Archaeology, Computer Graphics, Cultural Heritage and Innovation, Valencia, Spain, 5–7 September 2016; Lerma, J.L., Cabrelles, M., Eds.; Editorial Universitat Politècnica de València: València, Spain, 2016; pp. 404–407.
54. Rottensteiner, F.; Trinder, J.; Clode, S.; Kubik, K. Using the Dempster-Shafer method for the fusion of LIDAR data and multi-spectral images for building detection. *Inf. Fus.* **2005**, *6*, 283–300. [CrossRef]
55. Verhoeven, G. BRDF and its Impact on Aerial Archaeological Photography. *Archaeol. Prospect.* **2017**, *24*, 133–140. [CrossRef]



© 2019 by the authors. Licensee MDPI, Basel, Switzerland. This article is an open access article distributed under the terms and conditions of the Creative Commons Attribution (CC BY) license (<http://creativecommons.org/licenses/by/4.0/>).





Article

# Why Not a Single Image? Combining Visualizations to Facilitate Fieldwork and On-Screen Mapping

Žiga Kokalj <sup>1,2,\*</sup> and Maja Somrak <sup>1</sup>

<sup>1</sup> Research Centre of the Slovenian Academy of Sciences and Arts, Novi trg 2, 1000 Ljubljana, Slovenia; maja.somrak@zrc-sazu.si

<sup>2</sup> Centre of Excellence for Space Sciences and Technologies, Aškerčeva 12, 1000 Ljubljana, Slovenia

\* Correspondence: ziga.kokalj@zrc-sazu.si; Tel.: +386-1-4706-458

Received: 28 February 2019; Accepted: 20 March 2019; Published: 27 March 2019

**Abstract:** Visualization products computed from a raster elevation model still form the basis of most archaeological and geomorphological enquiries of lidar data. We believe there is a need to improve the existing visualizations and create meaningful image combinations that preserve positive characteristics of individual techniques. In this paper, we list the criteria a good visualization should meet, present five different blend modes (*normal*, *screen*, *multiply*, *overlay*, *luminosity*), which combine various images into one, discuss their characteristics, and examine how they can be used to improve the visibility (recognition) of small topographical features. Blending different relief visualization techniques allows for a simultaneous display of distinct topographical features in a single (enhanced) image. We provide a “recipe” and a tool for a mix of visualization techniques and blend modes, including all the settings, to compute a visualization for archaeological topography that meets all of the criteria of a good visualization.

**Keywords:** relief mapping; visualization; blend modes; digital elevation model; airborne laser scanning; lidar

## 1. Introduction

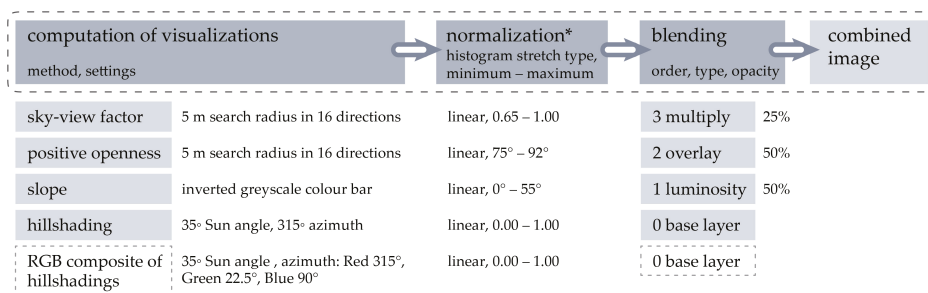
Many advanced visualization techniques for presenting high-resolution elevation data, such as airborne laser scanning (ALS)-derived elevation models, have been developed specifically for archaeological purposes or have been adapted from other scientific fields. Their usefulness for detection and interpretation of a variety of topographic forms has been demonstrated in several scientific papers and day-to-day practices, though the choices of visualizations are largely based on intuitive personal preferences.

Currently there is a lack of explicit workflows, conventions, and frameworks for visualizing remote sensing data for archaeological exploration. Some scientific fields have already experienced this requirement for optimization, transparency, and reproducibility of visualization methods. Medical diagnostics, for example, has been facing difficulties of integrating spatial information obtained from imaging data for many years, which finally led to the development of standardizations [1,2]. Hence, it makes sense to strive for unification of visualization methods also in archaeology and cultural heritage management, as well as other disciplines (e.g., geomorphology, geology, natural resource management, glaciology) that use visualized airborne laser scanning data. The need for common practice is becoming more pressing with increasing availability of national lidar datasets and resulting large-scale (national) mapping projects, where there is a need for homogeneous, reliable, and comparable results from multiple interpreters. This also raises the issue of effective training which benefits from clear objectives and standards, competent instructors, and supported by appropriate data, methods, and tools. We suggest that archaeological applications of ALS-derived visualizations often

suffer from a lack of rigor and explicitness in choices of visualization method, with little consideration of theoretical grounding, thorough review, or systematic testing on-screen and in the field. Indeed, there is a tendency to default to using ‘as many techniques as possible’, which is a difficulty as this is resource intensive and the cost/benefits for information return are not quantified. These issues are exacerbated by the proliferation of available methods, a sample of which is described in Section 2.2.

In this paper, we show that while different visualizations determine each information layer, image fusion with blend modes may maximize combined information. We also argue that different blend modes enhance the visibility (recognition) of small topographical features on the final combined visualization. We describe a method that uses blend mode techniques for combining visualizations into a single, enhanced image—a visualization for archaeological topography (Figure 1)—that preserves the positive characteristics of input images, while keeping information loss at a minimum. This is in line with the arguments of Borland and Russell [3], who reason that if the aim of a visualization is to effectively convey information to viewers, then we should also aim to ensure visualizations intended for scientific use are accurate, unbiased, and comparable.

The authors recognize the importance of exploration in research and are not arguing against the need to ‘see more than one image’—on the contrary, we support that premise but believe that the properties and utility of visualizations for tasks at hand should be properly understood. In support of this, we discuss the properties of a good visualization and propose a theoretical and practical framework for how such properties could be achieved. However, in setting out our proposed visualization for archaeological topography, we put it forward as a contribution to developing efficient and comparable outputs from archaeological mapping from ALS derivatives. Indeed, we do not believe that it should become the ‘go to’ choice before it has been more thoroughly discussed and compared with other similar ‘hybrid’ visualizations. The framework, however, provides a starting point for discussion. We believe that archaeological and historical management practices will benefit from a best-practice workflow that will ensure at least basic comparison of mapping results across different research groups, between regions, and internationally. This requires a set of guidelines on what works and what does not, and for conventions for visualizations that do not simply reflect ‘local’ personal or institutional preferences.



\*values between minimum and maximum are linearly transformed to the scale 0 – 1 before blending

**Figure 1.** A schematic workflow illustrating the steps, variables, and their settings in producing the visualization for archaeological topography. Either hillshading or an RGB composite of hillshadings from three directions can be used as a base layer. Figure 6 illustrates the results of the blending steps.

The paper first provides some background on why we have decided to use simple two-dimensional (2D) terrain representations, i.e., raster elevation models (Section 2.1). This is followed by information on how recognition of small-scale features can be enhanced with various visualization methods (Section 2.2), which provides the background to explaining why blend modes to combine information from different visualizations are useful (Section 2.3). In Section 3.1, we describe our case study areas, ALS data, and their processing procedures. We proceed with the description of

visualization methods (Section 3.2) and blend modes (Section 3.3). The effects of blend modes on ALS data visualizations are described in Section 4.1 and this knowledge is then used to construct the visualization for archaeological topography, explained in Section 4.2. We discuss the results in Section 5 and provide conclusions in Section 6.

## 2. Background

### 2.1. The Logic Behind Using Two-Dimensional Terrain Representations

It is beyond the scope of this paper to deeply explore the benefits and drawbacks of mapping in a two- or three-dimensional environment. We chose to focus on 2D terrain representations (i.e., raster elevation models), because the products computed from a raster elevation model, especially various visualizations, still form the basis of most archaeological and geomorphological inquiries of lidar data—even if they are later displayed in a seemingly 3D environment. Potree [4] and similar viewers now enable fast and reliable display of a lidar point cloud and the properties of single points, including, for example, RGB colors rendered from a photo camera, in a seemingly 3D environment. However, it is still beyond the average practitioner to successfully investigate or map from a large lidar dataset in 3D.

The preference for either 3D or 2D is neither obvious nor definite, but depends on the dataset, task, and context [5–7]. 3D visualization comes with increased complexity, where one of the most obvious issues is occlusion [5,8,9]; some parts of terrain (or structures) make it difficult to view others that are partially or completely hidden behind them. If the image is static rather than interactive, which does not make it possible to rotate the view point, the occluded data is effectively lost [8]. Even if people can move their viewpoint, there are issues of projection and perceptual ambiguity. Additionally, pseudocoloring in a 3D environment and simultaneous use of shading can interfere with each other [9,10], making visualizations harder to read or, worse, cause incorrect data analysis [8]. While 2D visualizations are simpler in certain regards, their main advantage is that they allow all the data to be seen at once. Numerous studies have confirmed that 2D visualizations are more comprehensible, accurate, and efficient to interpret than 3D representations for tasks involving spatial memory, spatial identification, and precision [5,11,12]. For these reasons, while we recognize the desirability of working in 3D environments, we believe that routine practice will remain heavily dependent on 2D representations for some time yet.

### 2.2. Enhancing Visibility of Small-Scale Features With Visualizations

Logical and arithmetical operations, classification, visibility analysis, overlaying procedures, and moving window operations can be used to enhance the edges of features or otherwise improve their recognition. Multiple studies compare the various visualization techniques (see e.g., References [13–17]), including the visualization guidelines by Kokalj and Hesse [18]. Some techniques are simple to compute, e.g., analytical hillshading and slope gradient, while others are more complex, e.g., sky-view factor [13], local relief model [19], red relief image map [20], multidirectional visibility index [21], or multiscale integral invariants [22]. While the first set of techniques focus on small-scale topographical forms, the latter consider topographic change of varying size and express it in a single image, similar to multiscale relief model [23]. An interesting approach uses a combination of a normalized digital surface model (nDSM) or a canopy height model (CHM) and shaded relief or a grayscale orthophoto image that help evaluate the immediate environment of archaeological features, especially when covered by forest. An approach that is especially effective in visualizing hydrological networks was proposed by Kennelly [24] who combined relief hillshading and curvature. In addition, a number of image processing local filters can be applied to the elevation model in order to detect high frequency variation (e.g., Laplacian, Sobel's, Robert's filters, unsharpen mask). The simplest is the Laplacian filter, specifically designed for local edge detection, i.e., emphasizing sharp anomalies [15]. Because edge detection filters emphasize noise, they are often applied to images that have been first smoothed to a

limited extent—e.g., Laplacian-of-Gaussian. Because so many methods exist, there are even studies that propose techniques to analytically assess the efficacy of various visualizations [25]. Among the dozens of techniques that can be applied to visually represent terrain characteristics, not all are easily interpretable, some introduce artifacts or give very different results in different areas. Some are intended to improve detection rates of new features and therefore visually exaggerate the small differences, while others strive for comparability between different areas and therefore for uniform representation of features with similar characteristics. We have to consider that the basic concepts of visualizations, their characteristics, advantages, and disadvantages must be understood by the user to successfully apply them. This is especially important because many processing methods are increasingly available as free tools or collections of tools [26,27] and a great variety of image manipulation functionality is likely to confuse or overwhelm the untrained or uncritical user. We believe there is a need to enhance the existing 2D visualizations and create meaningful image combinations that preserve relevant (positive) characteristics of individual techniques. Bennett et al. [14] have found that among the techniques they reviewed, no single one recorded more than 77% of features, whereas interpretation from a group of any three visualizations recorded more than 90%. Similarly, studies from various research fields showed images or visualizations are often easier to interpret if different visualizations of the same study subject are fused or layered one over another [28,29], combining their information.

### 2.3. Combining Information From Different Visualizations with Blend Modes

Image fusion is a process of combining information from multiple images into a single composite image [30]. Verhoeven et al. [31] report on the various pixel-based image fusion approaches, e.g., blend modes (methods), pan-sharpening, distribution fitting, and others, that are implemented in the Toolbox for Archaeological Image Fusion (TAIFU). Filzwieser et al. [32] describe their use for integrating images from various geophysical datasets for archaeological interpretation and especially for targeted examination of buried features. They report that interpretation of combined (fused) geophysical imagery enables more explicit observation of the extent of archaeological remains and is more revealing than any of the individual input datasets.

Blend modes are relatively simple to comprehend and implement, do not require a multitude of adjustable parameters, and may be efficient and reliable. They are, therefore, used to enhance images for visual interpretation in a variety of scientific applications, in archaeology [31–33], cartography [34], medicine [35], and mineralogy [36], where blending enhances images with subtle colors or increases the edge contrast, and thus improves visual interpretability. Extensive research has been done on fusion of medical images from different data sources—such as computed tomography (CT), positron emission tomography (PET), and magnetic resonance imaging (MRI). Image fusion algorithms used in medical imaging closely resemble the blending functionality available in image editing software (e.g., simple fusion algorithm with maximum method [37] is equivalent to the lighten blend mode in Photoshop software [38]). In medicine, fusion of images of different modalities has been thoroughly tested and shown to improve interpretability of results, reliability of localization (e.g., of tumor sites), and overall diagnostic accuracy [39–46].

Encouraged by these examples, we combine multiple elevation model visualizations of a historic landscape in order to improve visibility of diverse topographical forms and enhance the interpretability of ALS data.

## 3. Data and Methods

### 3.1. Study Areas, Data, and Data Processing

We present three distinct study areas. The main one is the area of Chactún, one of the largest Maya urban centers known so far in the central lowlands of the Yucatan peninsula (Figures 2 and 3). The area is characterized by low hills with constructions and surrounding seasonal wetlands (bajos). Two additional areas, selected to demonstrate very flat and very steep terrain, are, respectively,

Veluwe in the central Netherlands (Figure 4) and the Julian Alps in Slovenia (Figure 5). Figure 8 shows additional examples, illustrating various historical anthropogenic terrain modifications and natural landscape features on diverse terrain types.

Chactún is located in the northern sector of the depopulated Calakmul Biosphere Reserve in Campeche, Mexico, and is completely covered by tropical semi-deciduous forest. Its urban core, composed of three concentrations of monumental architecture, was discovered in 2013 by prof. Šprajc and his team [47]. It has a number of plazas surrounded by temple pyramids, massive palace-like buildings, and two ball-courts. A large rectangular water reservoir lies immediately to the west of the main groups of structures. Ceramics collected from the ground surface, the architectural characteristics, and dated monuments, indicate that the center started to thrive in the Preclassic period, reaching its climax during the Late Classic (c. A.D. 600–1000), and had an important role in the regional political hierarchy [47,48].

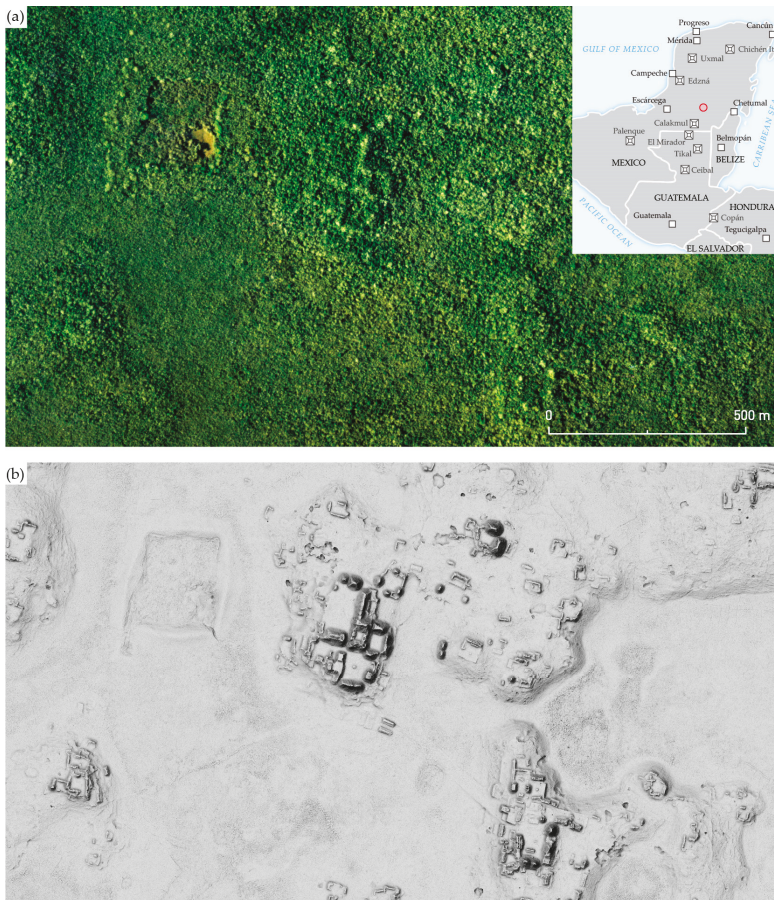


**Figure 2.** The Maya city of Chactún as seen on (a) an orthophoto image (CONABIO 1995–1996) and (b) a visualization for archaeological topography. As well as a number of plazas surrounded by temple pyramids, massive palace-like buildings, and two ball-courts, also visible on (b) are quarries, water reservoirs, and sacbeob (raised paved roads). The area is entirely covered by forest, the exploitation of which ceased when the Biosphere Reserve was declared in 1989.



**Figure 3.** A view of a palace with two turrets and an adjacent ball court, located in the Chactún's south-eastern group. Typical vegetation cover is broad-leaved, semi-deciduous tropical forest. For a sense of scale, note a hardly visible human figure (prof. Ivan Šprajc) in the lower left corner. Photo by Žiga Kokalj.

Airborne laser scanning data of an area covering 230 km<sup>2</sup> around Chactún was collected at the end (peak) of the dry season in May 2016. Mission planning, data acquisition, and data processing were done with clear archaeological purposes in mind. NCALM was commissioned for data acquisition and initial data processing (conversion from full-waveform to point cloud data; ground classification) [49,50], while the final processing (additional ground classification; visualization) was done by ZRC SAZU. The density of the final point cloud and the quality of derived elevation model proved excellent for detection and interpretation of archaeological features (Table S1) with very few processing artifacts discovered. Ground points were classified in Terrascan software and algorithm settings were optimized to remove only the vegetation cover but leave remains of past human activities as intact as possible (Table S2). Ground points, therefore, also include remains of buildings, walls, terracing, mounds, chultuns (cisterns), sacbeob (raised paved roads), and drainage channels. The average density of ground returns from a combined dataset comprising information from all flights and all three channels is 14.7 pts/m<sup>2</sup>—enough to provide a high-quality digital elevation model (DEM) with a 0.5 m spatial resolution. The rare areas with no ground returns include aguadas (artificial rainwater reservoirs) with water.

The second, much briefer, case study is of Veluwe in the Netherlands, an area that consists of ice-pushed sandy ridges formed in the Saale glacial period (circa 350,000 to 130,000 years ago), and subsequently blanketed with coversand deposits during the Weichselian glacial period (circa 115,000 to 10,000 years ago; [51]). We used the Dutch national lidar dataset (*Actueel Hoogtebestand Nederland - AHN2*), acquired in 2010 (Table S3) [52] of a flat terrain Section that contains a part of a large Celtic field system, preserved under forest in a relatively good condition, despite being crisscrossed by numerous tracks and marked by heather clearances (Figure 4) [53,54].

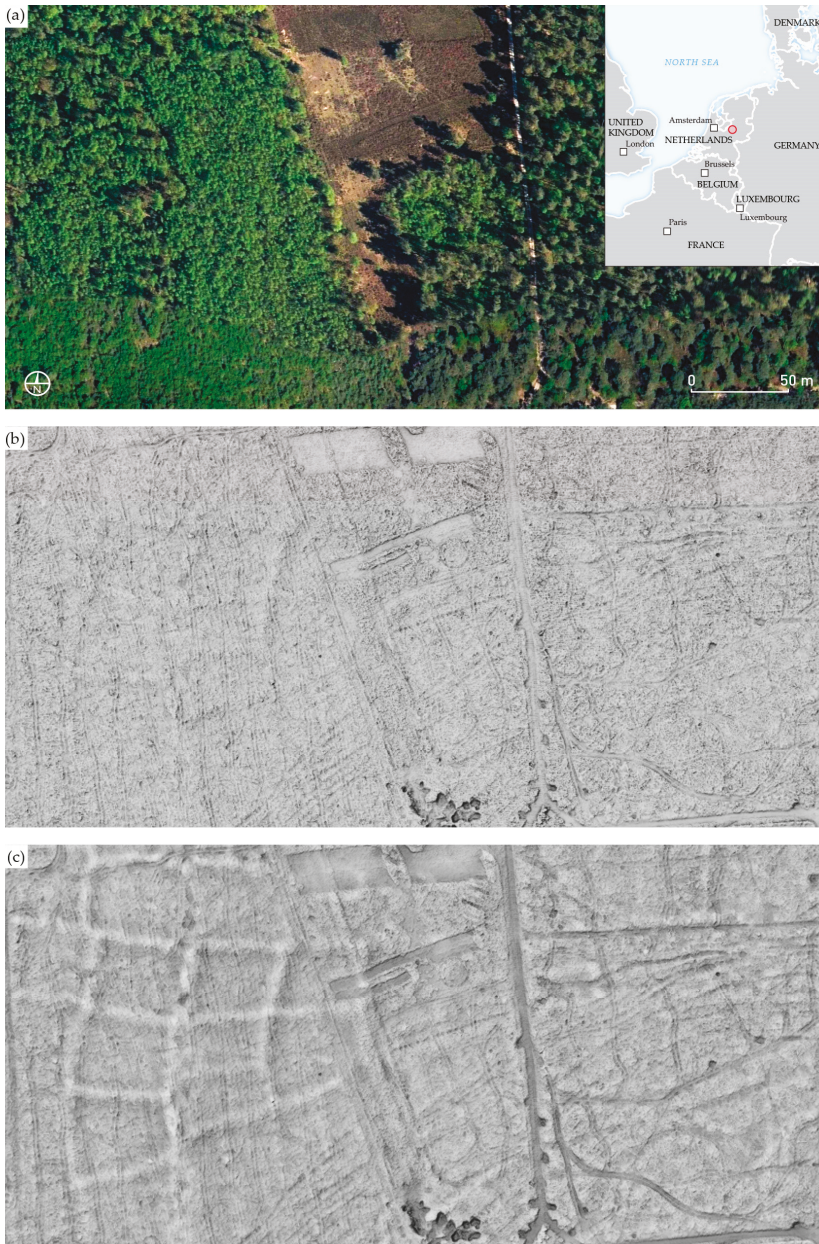


**Figure 4.** The Celtic fields on the Veluwe in central Netherlands as seen on (a) an orthophoto image (Landelijke Voorziening Beeldmateriaal 2018). (b) The combined visualization with default settings fails to portray the broader, very subtle features on flat terrain. (c) Changing the settings for sky-view factor and openness to include a wider area while disregarding the proximity (e.g., setting the search radius from 5 m to 10 m while disregarding the first 4 m) makes such structures very distinct. 0.5 m resolution ALS data © PDOK.

The third case study, also briefly presented, is in the Julian Alps, the biggest and highest Alpine mountain chain in Slovenia, rising to 2864 m at Mount Triglav. The ridge between the mountains of Planja (1964 m) and Bavški Grintavec (2333 m) are a testament to the powerful tectonic processes in the Cenozoic that have shifted the limestone strata almost vertically. These now lie almost 2 km above the valley floor and the underlying rock is still not exposed [55]. The location nearby Vrh Brda (1952 m) is known as Ribežni ('slicers') because of the exposed strata, which are beautifully shown on the visualization for archaeological topography despite the very steep and rugged terrain (Figure 5b). The Slovenian national ALS data has the lowest resolution in the mountains [56] (Table S4).

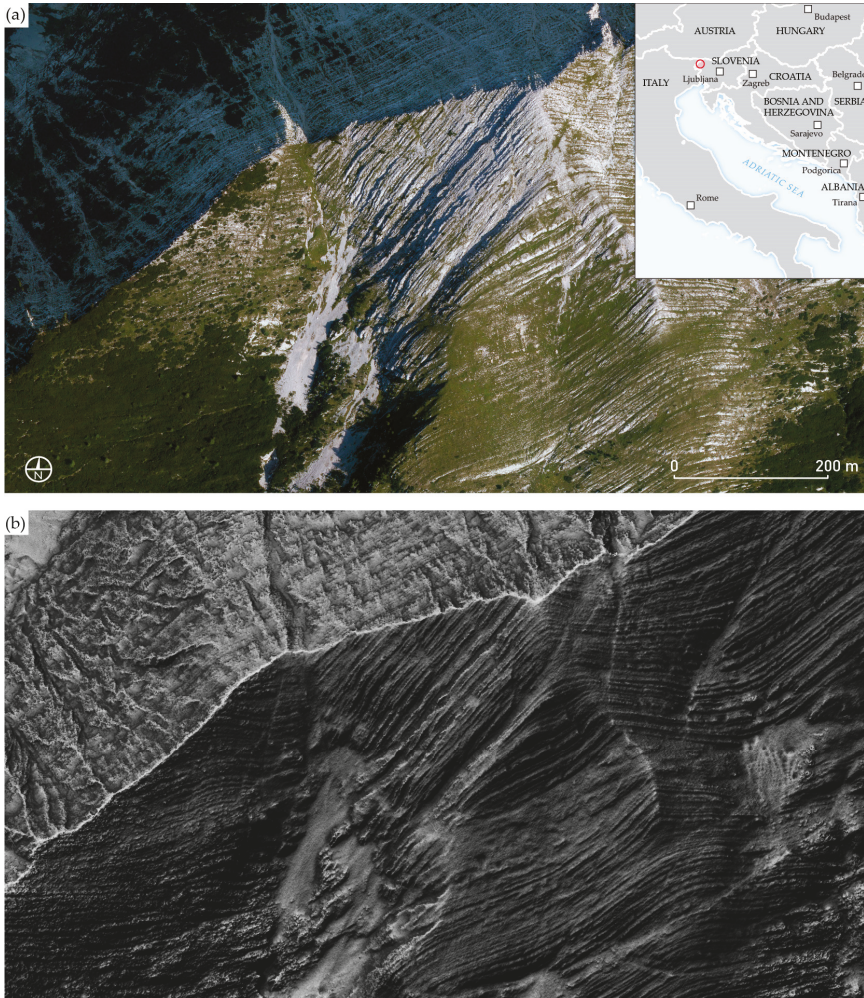


**Figure 5.** Dachstein limestone strata and scree fields exposed at Vrh Brda (1952 m) as seen on (a) an orthophoto image (GURS 2017) and (b) the visualization for archaeological topography. The top of the ridge is highlighted in white and the intricate geomorphological details are clearly visible. 1 m resolution ALS data © ARSO.

### 3.2. Visualization Methods

Because visual interpretation is based on contrast, the latter is very often enhanced by histogram manipulation and scale exaggeration, or otherwise artificially introduced; a good example is the well-known analytical shading. Consequently, the extent and shape of features being recorded can be, and usually is, altered. It is therefore necessary to know how different visualization techniques work and how to use them to best advantage according to the characteristics of data, the general morphology of the terrain, and the scale and preservation (i.e., surface expression) of features in question. When a certain technique is chosen for detection or interpretation, it is particularly important to know what the different settings do and how to manipulate them. Of course, the existing techniques are complementary to a great extent, but none is perfect. Because techniques show various objects in different ways, emphasizing edges, circular, or linear forms differently, a combination of methods is usually required. While there is no ideal visualization that would be effective in all situations, a good visualization should meet the following criteria:

- Small-scale features must be clearly visible;
- The visualization must be intuitive and easy to interpret, i.e., the users should have a clear understanding of what the visualization is showing them;
- The visualization must not depend on the orientation or shape of small topographic features;
- The visualization should ‘work well’ in all terrain types;
- Calculation of the visualization should not create artificial artifacts;
- It must be possible to calculate the visualization from a raster elevation model;
- It must be possible to study the result at the entire range of values (saturation of extreme values must be minimal even in extreme rugged terrain);
- Color or grayscale bar should be effective with a linear histogram stretch, manual saturation of extreme values is allowed; and
- Calculation should not slow down the interpretation process.

Producing a universal solution that incorporates these criteria is difficult and has not been tackled successfully yet, especially regarding the transferability of the method across regions and ease of understanding. We believe image fusion can provide an answer and blend modes are its most simple and comprehensible techniques. Below, we briefly present the techniques that we blended (combined, fused) into a combination—which we refer to as ‘a visualization for archaeological topography’—that we argue meets the criteria described above.

Relief shading (also known as hillshading or shaded relief) provides the most ‘natural’, i.e., intuitively readable, visual impression of all techniques (Figure 7b). The method developed by Yoëli [57] has become a standard feature in most GIS software. It is easy to compute and straightforward to interpret even by non-experts without training and is a wonderful exploratory technique. Direct illumination restricts the visualization in dark shades and brightly lit areas, where no or very little detail can be perceived. A single light beam also fails to reveal linear structures that lie along it, which can be problematic in some applications, especially in archaeology, or can completely change (inverse) the appearance of the landscape (i.e., false topographic perception).

An RGB composite image from hillshading in three directions overcomes these issues; because hillshadings from nearby angles are highly correlated, we advocate using consecutive angles of about 68° (e.g., azimuth 315° for red, 22.5° for green, and 90° for the blue band). The convexities and concavities, as well as orientations, are clearly and unambiguously depicted (Figures 6a and 7a).

Slope severity (gradient) is the first derivative of a DEM and is aspect independent. It represents the maximum rate of change between each cell and its neighbors. If presented in an inverted grayscale (steep slopes are darker), slope severity retains a very plastic representation of morphology (Figure 7c). However, additional information is needed to distinguish between positive/convex (e.g., banks) and negative/concave (e.g., ditches) features because slopes of the same gradient (regardless of rising or falling) are presented with the same color.

Sky-view factor (SVF) is a geophysical parameter that measures the portion of the sky visible from a certain point [13]. Locally flat terrain, ridges, and earthworks (e.g., building walls, cultivation ridges, burial mounds) which receive more illumination are highlighted and appear in light to white colors, while depressions (e.g., trenches, moats, plough furrows, mining pits) are dark because they receive less illumination (Figure 7g).

Positive openness is a proxy for diffuse relief illumination [58]. Because it considers the whole sphere for calculation, the result is an image devoid of general topography—a kind of trend-removed image (Figure 7e). It has the same valuable properties for visualization as sky-view factor with the added benefit of more pronounced local terrain features, although the visual impression of the general topography is lost.

All of the visualizations have proved their usefulness in archaeological interpretation in various environmental settings and at diverse scales, (see e.g., References [59–67]) and were computed using the relief visualization toolbox (RVT) created by ZRC SAZU [27]. Because we strive to preserve comparability between different geographical areas, the visualizations are presented with a minimum-maximum histogram stretch, usually with a saturation of minimum, maximum, or both. The displayed range of values is given in Figure 1.

### 3.3. Blend Modes

Blend modes (methods) in digital image editing and computer graphics determine how multiple image layers, one on top of another, are blended together (combined) into a single image. For blend modes to work, at least two layers (referred to as top and bottom or base layers) are needed, which can contain either two different images or the same image duplicated. Every blend mode is defined by an equation that takes values at coinciding pixels of top and bottom layer images as inputs to calculate the fused image. The blend mode is defined for the top layer. Finally, the opacity value controls translucency of the blended top image, allowing the bottom image to show through. The fundamental blend modes can be found in professional image editing software, but there is a lack of such functionality in GIS and remote sensing software. While QGIS supports some of the blend modes for display [34], ArcGIS provides only the normal blend mode, which only controls opacity.

Stacking more than two image layers in our implementation follows the convention used in Photoshop [68]. When multiple layers and blend modes are stacked, the effects are applied in order from the bottom layer of the stack upwards. Changes made to the lower layers propagate up through the stack, changing outputs all the way to the final blended image on the top most layer [69]. Using as many layers as possible is not always very efficient nor desired, because information can be lost if too many layers are used, and the user will not be able to comprehend it.

Blend modes are categorized into six groups, according to the type of effect they exert on the images:

- Normal: Only affects opacity;
- Lighten: Produces a lighter image;
- Darken: Produces a darker image;
- Contrast: Increases contrast, gray is less visible;
- Comparative: Calculates difference between images;
- Color: Calculations with different color qualities.

We describe five blend modes that we consider the most useful based on our experiences, one from each group (with the exception of the comparative group). We suggest pre-determined blend modes based on their theoretical performance with selected visualizations and our experiments. We hope that additional combinations will arise through the work of the research community following the publication of this article, as we recognize the need for critique and development in this field.

In equations that describe selected blend modes in following Sections, the letter *A* refers to the image on the top layer, while *B* refers to the image on the bottom layer. Before calculating blends with RGB images, the color values are normalized to fit onto the interval 0.0–1.0, where black corresponds to 0.0 and white to 1.0. We have implemented these blend modes in version 2.0 of relief visualization toolbox where they can be applied directly to the computed visualizations.

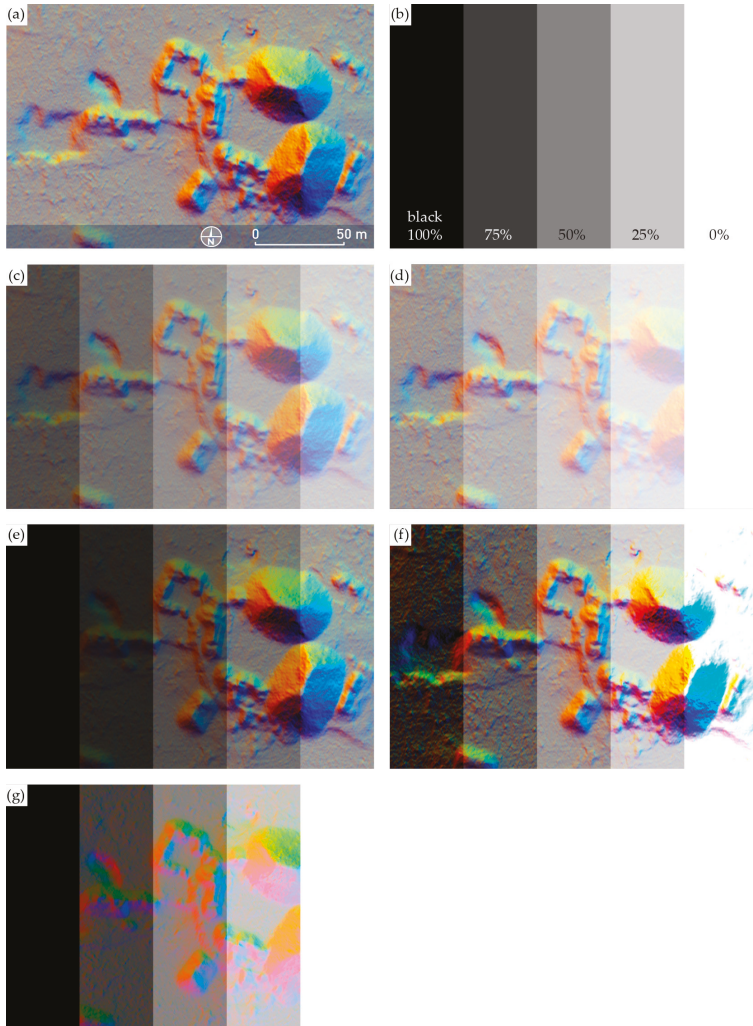


**Figure 6.** The effect of various blend modes. (a) The bottom (base) layer for blending shows the north-eastern complex in Chactún with two pyramidal structures. (b) The top layer is composed of rectangles with a varied degree of blackness. (c) *Normal* blend mode makes the foreground transparent (50% opacity). (d) *Screen* lightens the image. Black is neutral, white is opaque. (e) *Multiply* multiplies the luminance levels of the top layer’s pixels with the pixels in the layers below. Black is opaque, white is transparent. (f) *Overlay* enhances visibility of dark and bright areas. 50% gray is neutral. (g) *Luminosity* keeps the luminance of the top layer and blends it with the color of the combined view of the layers below. On a good grayscale printer, (b) and (g) should look the same.

*Normal* (normal group) is the default mode, where no special blending takes place—it keeps the top layer and hides the bottom layer (Figure 6c). The only effect achieved is by changing the opacity value of the top layer so that the bottom layer can be seen through (Equations (1) and (2)).

$$Normal(A, B) = A \tag{1}$$

$$Opacity(A, B) = A \cdot Opacity + B \cdot (1 - Opacity) \tag{2}$$

*Opacity* defines the “strength” of blending—to what degree the blend mode is considered. The lower the opacity, the more we allow the bottom layer to uniformly show through. When the top layer is fully opaque, the bottom layer is invisible (Figure 6b,c). It can be used in combination with any blend mode but is always applied after a blend result is calculated. Thus, when applying opacity there is already a blended image on the top layer while the bottom layer remains unchanged. The generalized opacity Equation (3), which we implemented for use with each of the blend modes described in this paper, is:

$$Opacity(Blend(A, B), B) = Blend(A, B) \cdot Opacity + B \cdot (1 - Opacity). \tag{3}$$

*Screen* (lighten group) treats every color channel separately, multiplies the inverse values of the top and bottom layer and, in a last step, inverts the product (Figure 6d). The result is always a lighter image. Screening with black leaves the color unchanged, while screening with white produces white. The Equation (4) is commutative, so switching the top and bottom layer order does not affect the result.

$$Screen(A, B) = 1 - (1 - A) \cdot (1 - B) \tag{4}$$

*Multiply* (darken group) is the opposite of screen. Multiply treats every color channel separately and multiplies the bottom layer with the top layer (Figure 6e). The result is always a darker image; the effect is similar to drawing on an image with marker pens. Multiplying any color with black produces black and multiplying any color with white keeps the color unchanged. The Equation (5) is commutative.

$$Multiply(A, B) = A \cdot B \tag{5}$$

*Overlay* (contrast group) combines multiply and screen blend modes to increase the contrast (Figure 6f). Overlay determines if the bottom layer color is brighter or darker than 50% gray, then applies multiply to darker colors and screen to lighter, thus preserving the highlights as well as shadows. The Equation (6) is non-commutative, meaning the layer order influences the result.

$$Overlay(A, B) = \begin{cases} (1 - (1 - 2 \cdot (B - 0.5)) \cdot (1 - A)) & \text{where } B > 0.5 \\ ((2 \cdot B) \cdot A) & \text{where } B \leq 0.5 \end{cases} \tag{6}$$

*Luminosity* blend mode (color group) keeps the luminance (the perceived brightness based on the spectral sensitivity of a human eye) of the top layer and blends it with hue and saturation components of the bottom layer [69]. This results in colors of the underlying layer replacing the colors on the top layer, while shadows and texture of the top layer stay the same (Figure 6g). Contrary to the blend modes we described so far, luminosity is not obtained by a straightforward pixel-wise calculation. The complete luminosity algorithm we implemented follows the methodology described in Adobe specification [70] (pp. 326–328) and is composed of several equations. Its core calculation is in the luminance Equation (7) where  $A_{red}$ ,  $A_{green}$ , and  $A_{blue}$  are the red, green, and blue channel in the RGB color space.

$$Luminance(A) = 0.3 \cdot A_{red} + 0.59 \cdot A_{green} + 0.11 \cdot A_{blue} \tag{7}$$

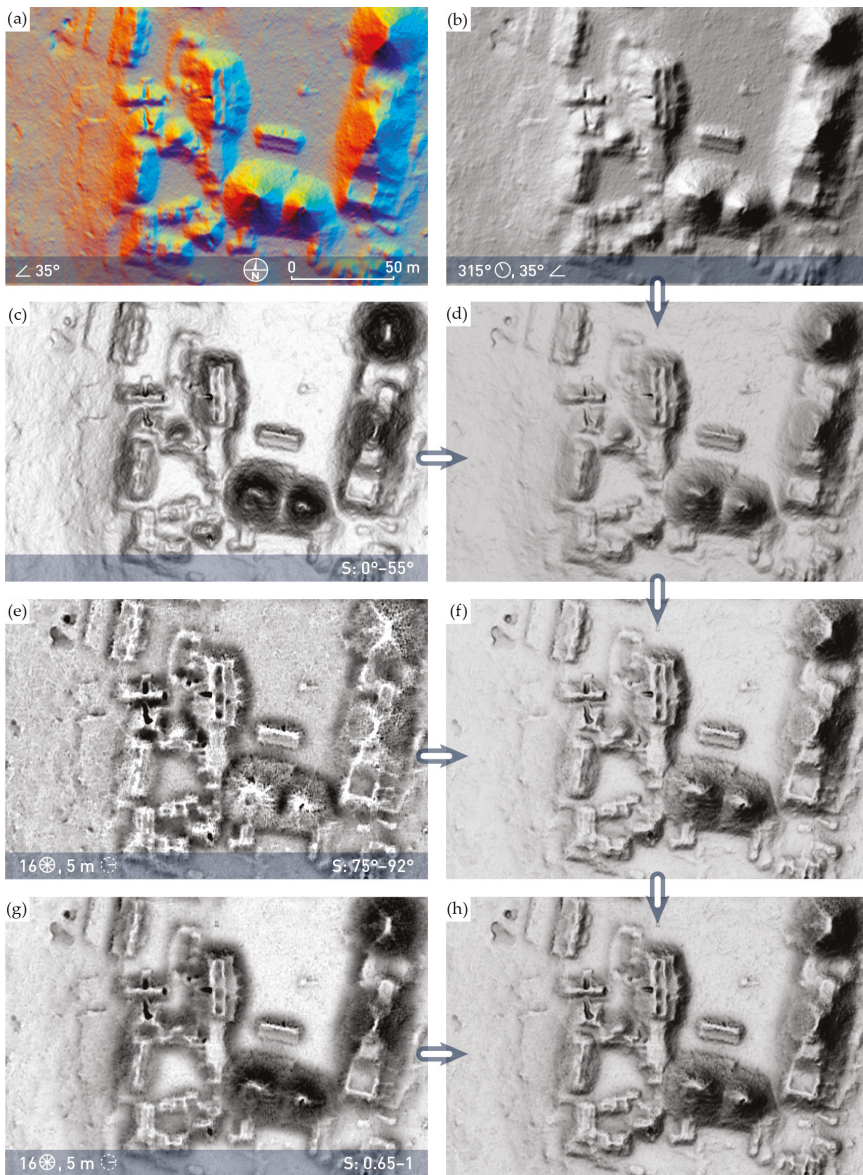


**Figure 7.** The results of individual steps of building the visualization for archaeological topography. A detail of Chactún south-eastern group is shown with (a) an RGB composite of hillshadings from three directions, (b) shaded relief, (c) slope, (e) positive openness, (g) sky-view factor. The latter three are consecutively added to (blended with) the (b), (d) and (f) in the right column to form the final combination (h). The (c) blends hillshading with slope using luminosity blend mode with 50% opacity, the (f) adds openness using overlay with 50% opacity, and the (h) adds sky-view factor using multiply with 25% opacity. The result of combining (a) as a base layer is shown in Figure 9d.

## 4. Results

### 4.1. Effect of Blend Modes on Visualizations

The aim of using blend modes with DEM visualizations is to visually enhance the existing images and to improve visibility of various topographic structures. Blending different visualizations together combines distinct topographical features emphasized on individual images. Depending on what visual features we want to enhance, we need to select relevant visualizations and appropriate blend modes to achieve the desired result. The ability of some of the most frequently used grayscale visualizations to capture small- and micro-relief, as well as the type of topographical features that are highlighted or shadowed on each particular visualization, is described in Table 1. It is important to keep highlighting and shadowing in mind when considering how different blend modes affect lighter and darker tones. The effect of blend modes on combining a color image (the RGB composite of hillshading from three directions) and a grayscale image of rectangles ranging from black to white is shown in Figure 6. The following descriptions in this subSection are based on theoretical knowledge of blend modes and visualizations.

**Table 1.** Display characteristics of grayscale visualizations.

Visualization	Visible Microrelief [18] (p. 35)	Highlighted Topography (Appears Bright)	Shadowed Topography (Appears Dark)
hillshading	o	non-level terrain facing towards illumination	non-level terrain facing away from illumination
slope (inverted grayscale color bar)	+	level terrain	steep terrain
simple local relief model	++	local high elevation	local depressions
positive openness	++	convexities	concavities
negative openness (inverted grayscale color bar)	++	convexities	lowest parts of concavities
sky-view factor	++	planes, ridges, peaks	concavities

o indistinct; + suitable; ++ very suitable

Normal blend mode is the most intuitive and straightforward because only uniform transparency takes effect with changing opacity. Screen renders black transparent, which means it is ideal to make darker colors disappear and to keep the whites. Multiply makes white transparent and is thus the most suitable choice to make lighter colors disappear while keeping the darker colors. Overlay makes 50% gray transparent, amplifying the contrast as a result. This is especially useful for improving the readability of images with subtle nuances. Luminosity works on color components of the images. It blends the luminance (a grayscale representation) of the top layer image, with the color (saturation and hue) from the bottom layer image. This is why luminosity only functions when a color image, e.g., hillshading from multiple directions or a composite of a principal components analysis, is used as a bottom layer, otherwise the result is the same as in blending with the normal blend mode. A color or monochromatic image can be used as the top layer. Because monochrome images do not have hue and saturation components, the luminance of a monochrome image is the monochrome image itself.

Opacity can be adjusted for any of the blend modes. The lower the opacity, the more transparent the result of blending will be. What shows through the transparent blend is the image from the bottom of the two layers. If blending multiple layers, merging is consecutive from the bottom layer to the top one. Therefore, the order of layers, not just the images and blend modes by themselves, greatly affects the final result of blending. This is because applying blend modes and opacity to a stack of layers propagate through the whole stack and because certain blend mode calculations are non-commutative (normal, overlay, luminosity).

Blending can also be used to enhance a single visualization, producing a so-called self-blend, but will have no effect when luminosity or normal blend mode is used. While screen, multiply, and overlay self-blends will either lighten or darken parts of the image, similar effects can be achieved with a histogram stretch applied to the original visualization.

The histogram stretch and saturation of minimum and maximum values (i.e., clipping) are useful to fine-tune individual visualizations. In this way, we can manipulate the visual effect to increase the visibility of the features we want to emphasize. For example, to improve the contrast we use a linear histogram stretch with clipping the minimum and maximum value of positive openness. The minimum cut-off was set at an angle of  $75^\circ$ , a value up to which all (smaller) values are represented with black. Similarly, the maximum cut-off was set at an angle of  $92^\circ$ , a point above which all values are represented with white (Figure 1). Angles between minimum and maximum cut-off values are assigned darker to lighter gray tones.

Histogram stretch methods, other than linear stretch, e.g., standard deviation, equalization, and Gaussian, distort relative relations among values. These can be used to enhance detectability of unknown features and further increase visibility of known ones, because they become more pronounced, but it ruins the comparability of features between different areas. A feature of the same physical characteristics can be displayed completely differently depending on the type of terrain, position, orientation etc. This is also true if clipping uses percentage rather than absolute minimum and maximum thresholds.

#### 4.2. Visualization for Archaeological Topography

We can now use the knowledge on how blend modes affect the color and tone of images to blend various visualizations described in Section 3.2 into a single combined visualization that retains the advantages of individual technique—the visualization for archaeological topography. The whole process of building the combined visualization is sketched in Figure 1, while Figure 7 shows the results of individual steps. Visualization for archaeological topography can have a hillshading or an RGB composite of hillshadings as a base layer, with preference for the former, while the other layers and blend modes are predetermined. We propose different calculation settings for ‘normal’ (complex) and very flat terrain (see discussion Section). We have selected the visualization methods based on their complementary positive characteristics, and the specific blending modes because they amplify these particular characteristics. They also work uniformly with varied data and the visualizations of different areas are therefore directly comparable.

Hillshading and the RGB composite of hillshading from three directions are a good base layer (bottom image) because they give a sense of general topography and are very intuitive to read. To provide a more plastic feel to the image, i.e., a more “three-dimensional” impression, we blend hillshading with slope, using luminosity with 50% opacity (Figure 7d). As described above, luminosity only has an effect if the bottom layer has colors (e.g., as in Figures 6g and 10), but is the same as normal blend mode if the bottom layer is monochromatic (e.g., as in Figures 7 and 9). The clipping of maximum values for slope depends on the type of terrain and structures of interest. For very flat terrain it should be lower (e.g., about  $15^\circ$ ) while it should be higher for steep or complex terrain (e.g., about  $60^\circ$ ). In our case, the terrain is neither very complex nor steep, but we had to set the maximum value to  $55^\circ$  nevertheless, because of high and steep pyramidal structures that would otherwise appear completely black. It is impossible to set strict general threshold values for minimum and maximum, because such diversities exist in almost every image (i.e., a larger study area). Kokalj and Hesse [18] (pp. 16–27) give guidelines for various visualization methods and terrain types. Similarly, the threshold values for opacity are arbitrary and depend on the terrain type, structures we want to highlight, and the overall desired effect. We defined the opacity thresholds for individual layers based on our own research and experience. We observed the effect of different opacity settings in increments of 25% and found that proposed numbers give good results.

In the next step, we focus on emphasizing the small-scale structures. Among the suitable visualization techniques are, for example, positive and negative openness, multiscale integral invariants, local dominance, local relief model, and Laplacian-of-Gaussian. We chose the first because it is easy to interpret and is complementary to sky-view factor in that it shows depressions as dark and exposed areas as bright. Another reason is that the most demanding part of the computation code for positive openness is the same as for sky-view factor; therefore, the calculation takes minimal additional time. Adding positive openness with 50% opaque overlay improves the contrast of the image by highlighting the small convexities (e.g., small ridges, edges, banks, peaks) and shadowing concavities (e.g., channels, ditches, holes), thus increasing the prominence of minute relief roughness (Figure 7f). Because openness is a trend removal method, the sense of general topography is completely lost and to some degree this effect is reflected in the combined image. Blending sky-view factor with 25% opaque multiply recovers some perception of the larger geomorphological forms as well as further enhancing the visibility of micro topography (Figure 7h).

Figure 8 shows applicability of the visualization for diverse archaeological and natural features and the environment they are a part of. The features are of varied scale, height, orientation, and form, they are convex and concave, and sit on terrain that ranges from extremely flat to very steep. The ALS data has been collected either intentionally to study these forms or as a part of a national (or regional) campaign, and therefore varies in scanning density and processing quality.

The calculation of the visualization for archaeological topography as well as blending of other visualization methods with the described blend modes is supported in the new version of Relief Visualization Toolbox [27].

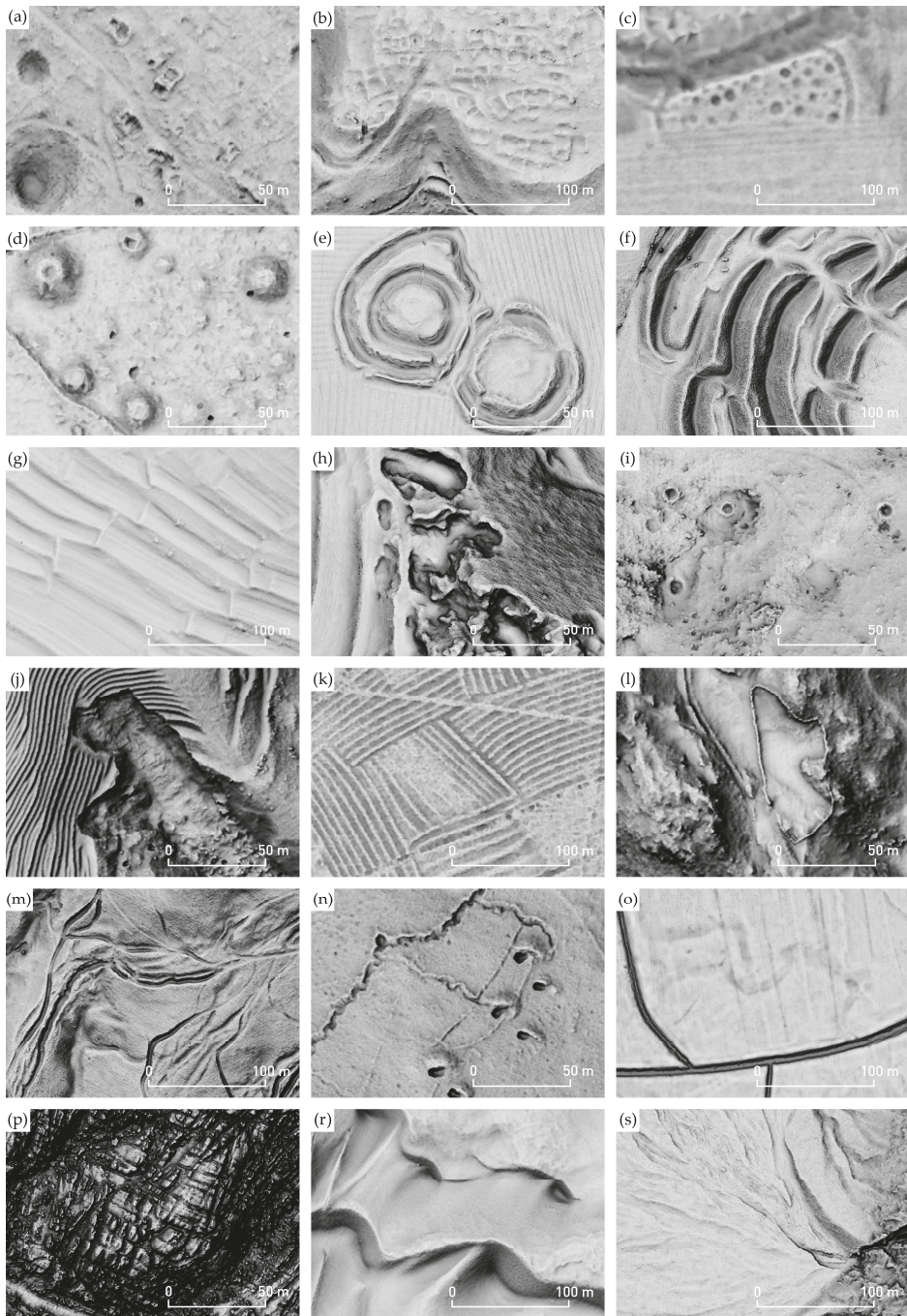


**Figure 8.** Various historical anthropogenic terrain modifications (a–o) and natural landscape features (j,m,o–s) on diverse terrain types as displayed by the visualization for archaeological topography. (a) Overgrown remains of the abandoned village of Novi Breg (Naubacher), Slovenia, surrounded by dolines. (b) Ajdovščina above Rodik hillfort in Slovenia is a prehistoric and Roman settlement, with visible massive ramparts, gates, and walls of individual houses. (c) A half-ploughed, 18th-century village of earth lodges at Biesterfeldt Site, North Dakota, USA. The unploughed part is under forest. (d) Early Iron Age barrow cemetery at Pivola, Slovenia. (e) A ring fort and a barrow on Hill of Tara, Ireland. (f) Entrance earthworks at Maiden Castle Iron Age hillfort, United Kingdom. (g) Alpine terraces at Rodine, Slovenia. (h) Small stone quarries at Vnanje Gorice, Slovenia. (i) Limekilns and dolines at Dečja vas, Slovenia. (j) Terraces and a landslide near Jeruzalem, Slovenia. (k) Ridge and furrow south of Harlaston, Staffordshire, United Kingdom. (l) A drywall enclosure north of Kobarič, Slovenia. (m) Hollow ways and headstreams near Rova, Slovenia. (n) Three different types of World War I trenches with shelters on the gentle NE slopes of Črni hribi, near Renče, Slovenia. (o) Remains of a palaeochannel and irrigation trenches in an agricultural landscape south of Staro selo, Slovenia. (p) Exposed bedrock and large granite boulders eroded into rounded bumpy and unusual shapes. Granite Dells geological feature north of Prescott, Arizona, USA. (r) Sand dunes at Guaiuba, Santa Catarina, Brazil. (s) The alluvial fan's apex and the upper part of the apron. Teakettle junction, California, USA. Data in (a), (c), (k), and (r) have 1 m spatial resolution, (e) has 0.2 m, (p) has 0.25 m, and others have 0.5 m spatial resolution. ALS data © (c) North Dakota State Water Commission, (e) Discovery Programme, (f, k) Environment Agency, (l, o) Walks of peace in the Soča river foundation, (m) Municipality Domžale, (p, s) NCALM [71,72], (r) FAPESP grant 2009/17675-5 [73], others ARSO.

## 5. Discussion

Slope, openness, and sky-view factor are all direction independent, which means they highlight structures irrespective of their orientation. This also means that, in contrast to shading techniques based on directional illumination such as hillshading, features visualized by slope, openness, and sky-view factor do not contain any horizontal displacements. The selected visualization techniques also do not introduce artificial artifacts (e.g., non-existent ditches).

Figure 9 shows that details, such as edges of the looting trenches in the buildings at the center and center left, are clearly recognizable on all four combinations. Whereas with normal blending more detail can be observed on the very steep, south-eastern slopes of pyramidal structures, the overall image appears flat (Figure 9, left column). Normal blending gives a big preference to the top layers over the lower ones (with the same opacity settings); therefore, because the effect of hillshading is almost lost, little perception of general topography remains. This is not desirable for interpretation; hence, the loss of detail on the sides of the largest and steepest pyramidal structures on the visualization for archaeological topography was intentional. The effect can be reduced by setting different saturation (clipping) thresholds. Blending with normal blend mode in an alternative order gives preference to other layers, but the key point here is that compromises have to be made on the visibility of certain layers (visualizations) and thus their useful characteristics. This is even more evident when we want to preserve colors, e.g., from hillshading from different directions. The normal blend mode does not preserve colors, because they are reduced to various extent regardless of the order and opacity setting (Figure 9c). The visualization for archaeological topography shows slopes with various orientations in distinct colors (Figure 9d). Figure 10a demonstrates the color of slopes of various orientation on a round, sharp-edged, shallow depression (top) and protrusion (bottom). The colors for slopes facing different directions are: N—green-yellow; NE—cyan; E—light blue; SE—dark blue, S—violet, SW—dark red; W—light red; NW—orange. It is important that the colors remain the same across different datasets and locations if comparability is required.

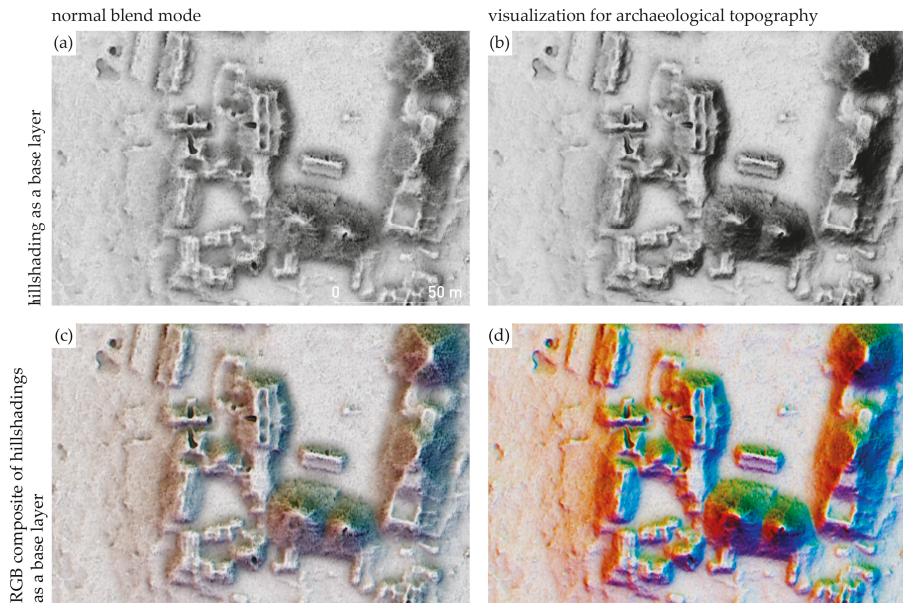


**Figure 9.** The left column, i.e., plates (a) and (c), shows two combinations of visualizations based on normal blend mode. The right column, i.e., images (b) and (d), shows two examples of the visualization for archaeological topography, which is based on blending with different blend modes. The opacity of the layers is the same for all plates. The layers that were combined are sky-view factor, positive openness, slope, and for (a) and (b) hillshading, while for (c) and (d) an RGB composite image of hillshading from three directions. Plates (b) and (d) use the same blend modes as used in Figure 7h.

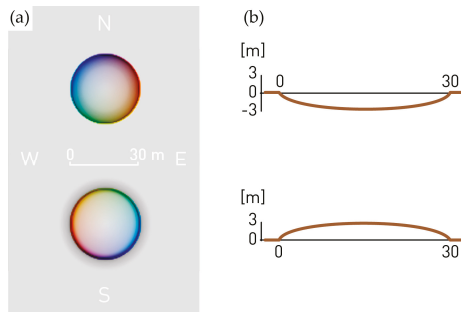


**Figure 10.** Different opacity settings and blend modes enable better representation of underlying colors. A combination of visualizations based on sky-view factor (25% opacity, multiply), positive openness (50% opacity, overlay), slope (50% opacity, luminosity), and an RGB composite image of hillshading from three directions. It is possible to see orientation of slopes from this image as demonstrated from the effect of the combination on a round, sharp-edged, shallow depression (top) and protrusion (bottom). The same combination is shown on Figure 9d.

Good representation of color is important because it provides a new visual dimension. Using color hue to display quantitative data is discouraged, because it can be misleading or difficult to discern (see e.g., Reference [16]). Using color lightness (luminance) is more appropriate to display such data [3,74]. Despite this, we argue that color hue can be used for detection when the interpretation is not dependent

on the exact quantitative value (e.g., azimuth of slope 85°; elevation 235 m a.m.s.l.), but rather provides a clue to the approximate value or difference (e.g., eastern slope; low elevation). Other base layers that provide color can be used in different combinations of visualizations. Examples include elevation, height of trees, water drainage, multiscale topographic position, [75,76] etc.

Even something as simple as the use of color can be an argument that supports the need for more generally accepted (and used) conventions for the sake of accuracy and comparability. What is often overlooked when visualizing any scientific data is that carefully selected, perceptually appropriate color maps lead to substantially fewer mistakes in analysis and interpretation [5]. Many color maps are inappropriate for scientific visualizations [77] due to confusing luminosity intensities (e.g., non-sequential luminosity for sequential data), introduction of false borders or artifacts in the data, or disregard for colorblind viewers. One of the biggest such offenders is the rainbow color map, which is still widely used, despite being perceptually unsuitable [3]. Scientists and professionals that are aware of its disadvantages still use it due to simplicity and inertia (the rainbow color map is often the default setting in software), as well as for aesthetic reasons [10,78]. A study by Borkin [5] revealed that even the scientists who claim to have adapted to reading the rainbow map still perform diagnostic tasks significantly worse when relying on the rainbow map instead of perceptually suitable color maps.

However, presuming a suitable color map is selected, there is no definitive answer to the question of whether a color scale necessarily performs better than grayscale for terrain visualizations. The utility of a map comes from its ability to display the ridges, valleys, cusps, and other relevant features [79] and this is similar in historic landscape visualizations. While color palettes perform better in some of the studies [12,28], others show that the human eye luminance channel (grayscale presentation) processes shape and stereoscopic depth more effectively than the chromatic channels (color presentation) [79]. Hence, a grayscale visualization can be just as effective as, and less biased than, a color one.

Additional benefits of the combined visualization are that a single visualization conserves disk space and displays faster. This is especially important in the field where data is accessed with tablets and smart phones or even as hard-copy sheets.

The visualization for archaeological topography meets all of the criteria for a good visualization set in Section 3.2. Because it is based on slope, openness, and sky-view factor, small-scale features are clearly visible and no artificial artifacts are introduced. For the same reason it shows small topographic features in the same way irrespective of their orientation or shape, and therefore we can judge their height and amplitude. The visualization can be calculated from a raster elevation model, which is the most frequent distribution format of ALS data. The calculation takes less than 20 seconds per km<sup>2</sup> of 0.5 m resolution lidar data (Table 2), depending on the size of the area to be calculated. This should not slow down the interpretation process, because it takes an individual longer to examine such an area. It is therefore suitable for small-scale studies as well as national deployment. For testing, we used a computer running Microsoft Windows 10 (64 bit) with 2.8 GHz Intel i7 processor and 20 GB of RAM. Not all RAM was used.

**Table 2.** Visualization for archaeological topography computation speed.

DEM Size [px] (0.5 m Resolution)	Size on Disk [MB]	Settings	Visualizations Time [mins]	Blending Time [mins]	Combined Time [mins]
1000 × 1000	4	same as in Figure 1	0:02	0:01	0:03
2000 × 2000	16	same as in Figure 1	0:09	0:03	0:12
10,000 × 10,000	390	same as in Figure 1	3:37	1:07	4:44

Saturation of extreme values is completely customizable with manual setting of the minimum and maximum threshold values for each individual input visualization and a linear stretch is used for all. It is therefore possible to study the result at the entire range of values. We advise some saturation if readability in important areas is not impeded, because contrast makes identification of features easier. The visualization has been tested by experts and beginners, in the field and for desktop analysis of various archaeological features in diverse landscapes. It has been found very intuitive to interpret.

Banaszek et al. [80] report that to produce coherent standardized mapping result on a national scale, beginners in interpretation of remote sensing data would need additional training in reading the ALS derived visualizations, which would be simpler with a single visualization to consider.

A good visualization depends on the dataset and context. Because distribution of data values is shifted for each terrain type, visualizing them in exactly the same way might obscure important relief features. The visualization for archaeological topography with default settings (Figure 1) works well on most terrain types (Figure 8), even on the extremely steep slopes of the Alps (Figure 5), but it fails to portray effectively some of the broader, very subtle features on very flat terrain (Figure 4b). This can be avoided by changing the settings for sky-view factor and openness to include a wider area while disregarding the proximity, e.g., setting the search radius from 5 m to 10 m while disregarding the first 4 m of the neighborhood from the calculation. The histogram stretch has to be amended accordingly, in our case to  $0^{\circ}$ – $35^{\circ}$  for slope,  $85^{\circ}$ – $92^{\circ}$  for openness, and 0.95–1.00 for sky-view factor. In this way, subtle structures in flat terrain become more easily recognizable (Figure 4c). A lower sun elevation angle for hillshading can further enhance visibility of such structures. This is an example of how a few different sets of visualization parameters could be used to fine-tune historic landscape visualization according to terrain type. We propose using a custom set of parameters at least for ‘normal’ (complex) and flat terrain. The extent to which these parameters can be fine-tuned and still constitute a standard custom set, remains to be investigated.

There is a question of the importance of using various visualization techniques and assessing their characteristics in view of ever more present computational approaches to detection of archaeological feature. The potential to find archaeological traces, and in future possibly classify them, with methods such as deep learning is increasingly accepted by the archaeological community (see e.g., References [81–85]). Despite this, or because of this, we believe there are still two fundamental benefits of having the best possible visualization for visual inspection:

- Deep learning requires a database of a large number of known and verified archaeological sites as learning samples—in the first instance these still have to come from visual interpretation and field observation;
- Large-scale results of deep learning have to be verified and the most straightforward ‘first check’ is visual inspection.

## 6. Conclusions

Combining results of various visualization techniques in a meaningful and deliberate way builds upon their strengths. Not only can we play with different histogram stretches and color tables, but also vary the degree of transparency and mathematical operations to combine layers. The word ‘play’ was deliberately left out of brackets in the sentence above, as we know that the process of creating an expressive visualization is indeed as much art as it is a technical outcome.

The process involves many decisions that all have an important effect on the final appearance of the visualization. The choice of visualizations, their individual computation settings, the type of histogram stretch, saturation of minimum and maximum values, blending methods, order of blending, and opacity settings have to be documented. Replicating the appearance is only possible if this information is stored in an accessible way or printed with the combined visualization. The archaeological mapping results equipped with such information can in future be assessed according to their confidence.

Having a single combined visualization to consider has advantages as well as potential pitfalls. The more important benefits are better representation of structures in a larger range of terrain types, conservation of disk space, and faster display. Using a single visualization that conserves the location of edges as well as relative perception of the height of archaeological structures can help with comparison of mapping results across environmental and archaeological areas. There is a risk that using a single visualization might miss potentially important traces in the landscape, as has been the case with other visualization techniques. However, combining specific positive characteristics of more methods into

a single image reduces this risk more than hoping time-pressed practitioners and scientists would consider using more than one or two visualizations in their quest to map larger areas. The visualization for archaeological topography that we constructed and presented in this paper has already been used for pedestrian surveys in various environments, from semi-deciduous tropical forests of Mexico to the largely open heather and scrub ground of western Scotland and the Mediterranean karstic rough terrain. It has been deemed practical and informative. Its benefits are:

- It highlights the small-scale structures and is intuitive to read,
- It does not introduce artificial artifacts,
- It preserves the colors of the base layer well,
- The visual extent and shape of recorded features are not altered,
- It shows small topographic features in the same way irrespective of their orientation or shape, allowing us to judge their height and amplitude
- Results from different areas are comparable,
- The calculation is fast and does not slow down the mapping process.

Thorough experimentation involving control tests with multiple observers, areas, and diverse visualizations, although much needed, has not been done in this study. Controlled testing of the different effectiveness of various visualizations in respect of time needed for interpretation and agreement between different observers' interpretations requires a huge experiment that has to be set up by the archaeological community involved in interpretation of ALS data. This issue has been evident more than a decade, but only a few experiments have been done so far, e.g., by Filzwieser et al. [32] and Banaszek et al. [80]. More generally, there is a notable lack of accountability and explicit documentation of processes in many projects and this lack of information about how archaeological interpretation and mapping are progressed is undesirable for wider comparability and reliable research outputs [86]. Therefore, there is a need to develop explicit protocols for more clarity about object identification/mapping process, including the categorization of the reliability of data and findings. In presenting our protocols for blended visualizations, and implementing them through our RVT toolkit, we recognize that we are not solving this problem in this paper but present our approach to open up debate.

**Supplementary Materials:** The following are available online at <http://www.mdpi.com/2072-4292/11/7/747/s1>: Airborne laser scanning data acquisition and processing parameters.

**Author Contributions:** Ž.K. conceived and designed the research. M.S. implemented the blend modes and analyzed the results. Both authors participated in the drafting and editing of the paper text, the review of the experimental results, and in creating the Figures.

**Funding:** This research was partly funded by the Slovenian Research Agency core funding No. P2-0406, and by research projects No. J6-7085 and No. J6-9395.

**Acknowledgments:** We are grateful for the technical support of Klemen Zakšek, Krištof Oštir, Peter Pehani, and Klemen Čotar, who helped with programming the first versions of RVT. We would like to acknowledge the work of prof. Ivan Šprajc, whose dedicated field verification and encouragement has helped us produce a better product. We appreciate the constructive comments and suggestions by editors and the anonymous reviewers.

**Conflicts of Interest:** The authors declare no conflict of interest. The funders had no role in the design of the study; in the collection, analyses, or interpretation of data; in the writing of the manuscript, and in the decision to publish the results.

## References

1. Zhuge, Y.; Udupa, J.K. Intensity standardization simplifies brain MR image segmentation. *Comput. Vis. Image Underst.* **2009**, *113*, 1095–1103. [CrossRef]
2. Fujiki, Y.; Yokota, S.; Okada, Y.; Oku, Y.; Tamura, Y.; Ishiguro, M.; Miwakeichi, F. Standardization of Size, Shape and Internal Structure of Spinal Cord Images: Comparison of Three Transformation Methods. *PLoS ONE* **2013**, *8*, e76415.

3. Borland, D.; Russell, M.T.I. Rainbow Color Map (Still) Considered Harmful. *IEEE Comput. Graph. Appl.* **2007**, *27*, 14–17. [[PubMed](#)]
4. Schuetz, M. Potree: Rendering Large Point Clouds in Web Browsers. Bachelor's Thesis, Vienna University of Technology, Vienna, Austria, 2016.
5. Borkin, M.; Gajos, K.; Peters, A.; Mitsouras, D.; Melchionna, S.; Rybicki, F.; Feldman, C.; Pfister, H. Evaluation of Artery Visualizations for Heart Disease Diagnosis. *IEEE Trans. Vis. Comput. Graph.* **2011**, *17*, 2479–2488. [[PubMed](#)]
6. Kjellin, A.; Pettersson, L.W.; Seipel, S.; Lind, M. Evaluating 2D and 3D Visualizations of Spatiotemporal Information. *ACM Trans. Appl. Percept.* **2008**, *7*, 19:1–19:23.
7. Kaya, E.; Eren, M.T.; Doger, C.; Balcisoy, S. Do 3D Visualizations Fail? An Empirical Discussion on 2D and 3D Representations of the Spatio-temporal Data. In *Proceedings of the EURASIA GRAPHICS 2014*; Paper 05; Hacettepe University Press: Ankara, Turkey, 2014; p. 12.
8. Szafir, D.A. The Good, the Bad, and the Biased: Five Ways Visualizations Can Mislead (and How to Fix Them). *Interactions* **2018**, *25*, 26–33. [[CrossRef](#)]
9. Gehlenborg, N.; Wong, B. Points of view: Into the third dimension. *Nat. Methods* **2012**, *9*, 851.
10. Moreland, K. Why We Use Bad Color Maps and What You Can Do About It. *Electron. Imaging* **2016**, *2016*, 1–6. [[CrossRef](#)]
11. Cockburn, A.; McKenzie, B. Evaluating the Effectiveness of Spatial Memory in 2D and 3D Physical and Virtual Environments. In *Proceedings of the SIGCHI Conference on Human Factors in Computing Systems*, Minneapolis, MN, USA, 20–25 April 2002; ACM: New York, NY, USA, 2002; pp. 203–210.
12. Tory, M.; Sprague, D.; Wu, F.; So, W.Y.; Munzner, T. Spatialization Design: Comparing Points and Landscapes. *IEEE Trans. Vis. Comput. Graph.* **2007**, *13*, 1262–1269. [[CrossRef](#)]
13. Zakšek, K.; Oštir, K.; Kokalj, Ž. Sky-view factor as a relief visualization technique. *Remote Sens.* **2011**, *3*, 398–415.
14. Bennett, R.; Welham, K.; Hill, R.A.; Ford, A. A Comparison of Visualization Techniques for Models Created from Airborne Laser Scanned Data. *Archaeol. Prospect.* **2012**, *19*, 41–48.
15. Štular, B.; Kokalj, Ž.; Oštir, K.; Nuninger, L. Visualization of lidar-derived relief models for detection of archaeological features. *J. Archaeol. Sci.* **2012**, *39*, 3354–3360. [[CrossRef](#)]
16. Kokalj, Ž.; Zakšek, K.; Oštir, K. Visualizations of lidar derived relief models. In *Interpreting Archaeological Topography—Airborne Laser Scanning, Aerial Photographs and Ground Observation*; Opitz, R., Cowley, C.D., Eds.; Oxbow Books: Oxford, UK, 2013; pp. 100–114. ISBN 978-1-84217-516-3.
17. Inomata, T.; Pinzón, F.; Ranchos, J.L.; Haraguchi, T.; Nasu, H.; Fernandez-Diaz, J.C.; Aoyama, K.; Yonenobu, H. Archaeological Application of Airborne LiDAR with Object-Based Vegetation Classification and Visualization Techniques at the Lowland Maya Site of Ceibal, Guatemala. *Remote Sens.* **2017**, *9*, 563.
18. Kokalj, Ž.; Hesse, R. *Airborne Laser Scanning Raster Data Visualization: A Guide to Good Practice*; Prostor, kraj, čas; Založba ZRC: Ljubljana, Slovenia, 2017; ISBN 978-961-254-984-8.
19. Hesse, R. LiDAR-derived Local Relief Models—A new tool for archaeological prospection. *Archaeol. Prospect.* **2010**, *17*, 67–72. [[CrossRef](#)]
20. Chiba, T.; Kaneta, S.; Suzuki, Y. Red Relief Image Map: New Visualization Method for Three Dimension Data. *Int. Arch. Photogramm. Remote Sens. Spat. Inf. Sci.* **2008**, *37*, 1071–1076.
21. Podobnikar, T. Multidirectional Visibility Index for Analytical Shading Enhancement. *Cartogr. J.* **2012**, *49*, 195–207. [[CrossRef](#)]
22. Mara, H.; Krömker, S.; Jakob, S.; Breuckmann, B. GigaMesh and gildamesh: 3D multiscale integral invariant cuneiform character extraction. In *Proceedings of the 11th International conference on Virtual Reality, Archaeology and Cultural Heritage*, Paris, France, 21–24 September 2010; Eurographics Association: Paris, France, 2010; pp. 131–138.
23. Orengo, H.A.; Petrie, C.A. Multi-scale relief model (MSRM): A new algorithm for the visualization of subtle topographic change of variable size in digital elevation models. *Earth Surf. Process. Landf.* **2018**, *43*, 1361–1369. [[CrossRef](#)] [[PubMed](#)]
24. Kennelly, P.J. Terrain maps displaying hill-shading with curvature. *Geomorphology* **2008**, *102*, 567–577.

25. Mayoral Pascual, A.; Toumazet, J.-P.; François-Xavier, S.; Vautier, F.; Peiry, J.-L. The Highest Gradient Model: A New Method for Analytical Assessment of the Efficiency of LiDAR-Derived Visualization Techniques for Landform Detection and Mapping. *Remote Sens.* **2017**, *9*, 120. [[CrossRef](#)]
26. Hesse, R. Visualisierung hochauflösender Digitaler Geländemodelle mit LiVT. In *Computeranwendungen und Quantitative Methoden in der Archäologie. 4. Workshop der AG CAA 2013*; Lieberwirth, U., Herzog, I., Eds.; Berlin Studies of the Ancient World; Topoi: Berlin, Germany, 2016; pp. 109–128.
27. Kokalj, Ž.; Zakšek, K.; Oštir, K.; Pehani, P.; Čotar, K.; Somrak, M. *Relief Visualization Toolbox*; ZRC SAZU: Ljubljana, Slovenia, 2018.
28. Alcalde, J.; Bond, C.; Randle, C.H. Framing bias: The effect of Figure presentation on seismic interpretation. *Interpretation* **2017**, *5*, 591–605.
29. Canuto, M.A.; Estrada-Belli, F.; Garrison, T.G.; Houston, S.D.; Acuña, M.J.; Kováč, M.; Marken, D.; Nondédéo, P.; Auld-Thomas, L.; Castanet, C.; et al. Ancient lowland Maya complexity as revealed by airborne laser scanning of northern Guatemala. *Science* **2018**, *361*, eaau0137.
30. Mitchell, H.B. *Image Fusion: Theories, Techniques and Applications*; Springer-Verlag: Berlin/Heidelberg, Germany, 2010; ISBN 978-3-642-11215-7.
31. Verhoeven, G.; Nowak, M.; Nowak, R. *Pixel-Level Image Fusion for Archaeological Interpretative Mapping*; Lerma, J.L., Cabrelles, M., Eds.; Editorial Universitat Politècnica de València: Valencia, Spain, 2016; pp. 404–407.
32. Filzwieser, R.; Olesen, L.H.; Verhoeven, G.; Mauritsen, E.S.; Neubauer, W.; Trinks, I.; Nowak, M.; Nowak, R.; Schneidhofer, P.; Nau, E.; et al. Integration of Complementary Archaeological Prospection Data from a Late Iron Age Settlement at Vesterager-Denmark. *J. Archaeol. Method Theory* **2018**, *25*, 313–333. [[CrossRef](#)]
33. Mark, R.; Billo, E. Application of Digital Image Enhancement in Rock Art Recording. *Am. Indian Rock Art* **2002**, *28*, 121–128.
34. Tzvetkov, J. Relief visualization techniques using free and open source GIS tools. *Pol. Cartogr. Rev.* **2018**, *50*, 61–71.
35. Wang, S.; Lee, W.; Provost, J.; Luo, J.; Konofagou, E.E. A composite high-frame-rate system for clinical cardiovascular imaging. *IEEE Trans. Ultrason. Ferroelectr. Freq. Control* **2008**, *55*, 2221–2233. [[CrossRef](#)]
36. Howell, G.; Owen, M.J.; Salazar, L.; Haberlah, D.; Goergen, E. Blend Modes for Mineralogy Images. U.S. Patent US9495786B2, 15 November 2016.
37. Krishnamoorthy, S.; Soman, K.P. Implementation and Comparative Study of Image Fusion Algorithms. *Int. J. Comput. Appl.* **2010**, *9*, 24–28. [[CrossRef](#)]
38. Ma, Y. The mathematic magic of Photoshop blend modes for image processing. In Proceedings of the 2011 International Conference on Multimedia Technology, Hangzhou, China, 26–28 July 2011; pp. 5159–5161.
39. Giesel, F.L.; Mehndiratta, A.; Locklin, J.; McAuliffe, M.J.; White, S.; Choyke, P.L.; Knopp, M.V.; Wood, B.J.; Haberkorn, U.; von Tengg-Kobligh, H. Image fusion using CT, MRI and PET for treatment planning, navigation and follow up in percutaneous RFA. *Exp. Oncol.* **2009**, *31*, 106–114.
40. Faulhaber, P.; Nelson, A.; Mehta, L.; O'Donnell, J. The Fusion of Anatomic and Physiologic Tomographic Images to Enhance Accurate Interpretation. *Clin. Positron Imaging Off. J. Inst. Clin. PET* **2000**, *3*, 178.
41. Förster, G.J.; Laumann, C.; Nickel, O.; Kann, P.; Rieker, O.; Bartenstein, P. SPET/CT image co-registration in the abdomen with a simple and cost-effective tool. *Eur. J. Nucl. Med. Mol. Imaging* **2003**, *30*, 32–39. [[CrossRef](#)]
42. Antoch, G.; Kanja, J.; Bauer, S.; Kuehl, H.; Renzing-Koehler, K.; Schuette, J.; Bockisch, A.; Debatin, J.F.; Freudenberg, L.S. Comparison of PET, CT, and dual-modality PET/CT imaging for monitoring of imatinib (STI571) therapy in patients with gastrointestinal stromal tumors. *J. Nucl. Med. Off. Publ. Soc. Nucl. Med.* **2004**, *45*, 357–365.
43. Sale, D.; Joshi, D.M.; Patil, V.; Sonare, P.; Jadhav, C. Image Fusion for Medical Image Retrieval. *Int. J. Comput. Eng. Res.* **2013**, *3*, 1–9.
44. Schöder, H.; Yeung, H.W.D.; Gonen, M.; Kraus, D.; Larson, S.M. Head and neck cancer: Clinical usefulness and accuracy of PET/CT image fusion. *Radiology* **2004**, *231*, 65–72. [[CrossRef](#)] [[PubMed](#)]
45. Keidar, Z.; Israel, O.; Krausz, Y. SPECT/CT in tumor imaging: Technical aspects and clinical applications. *Semin. Nucl. Med.* **2003**, *33*, 205–218. [[CrossRef](#)]
46. James, A.P.; Dasarathy, B.V. Medical image fusion: A survey of the state of the art. *Inf. Fusion* **2014**, *19*, 4–19. [[CrossRef](#)]

47. Šprajc, I. Introducción. In *Exploraciones arqueológicas en Chactún, Campeche, México*; Šprajc, I., Ed.; Prostor, kraj, čas; Založba ZRC: Ljubljana, Slovenia, 2015; pp. 1–3. ISBN 978-961-254-780-6.
48. Šprajc, I.; Flores Esquivel, A.; Marsetič, A. Descripción del sitio. In *Exploraciones Arqueológicas en Chactún, Campeche, México*; Šprajc, I., Ed.; Prostor, kraj, čas; Založba ZRC: Ljubljana, Slovenia, 2015; pp. 5–24. ISBN 978-961-254-780-6.
49. Fernandez-Diaz, J.C.; Carter, W.E.; Shrestha, R.L.; Glennie, C.L. Now You See It . . . Now You Don't: Understanding Airborne Mapping LiDAR Collection and Data Product Generation for Archaeological Research in Mesoamerica. *Remote Sens.* **2014**, *6*, 9951–10001. [[CrossRef](#)]
50. Fernandez-Diaz, J.; Carter, W.; Glennie, C.; Shrestha, R.; Pan, Z.; Ekhtari, N.; Singhanian, A.; Hauser, D.; Sartori, M.; Fernandez-Diaz, J.C.; et al. Capability Assessment and Performance Metrics for the Titan Multispectral Mapping Lidar. *Remote Sens.* **2016**, *8*, 936. [[CrossRef](#)]
51. Berendsen, H.J.A. *De Vorming van Het Land*; Van Gorcum: Assen, The Netherlands, 2004.
52. van der Sande, C.; Soudarissanane, S.; Khoshelham, K. Assessment of Relative Accuracy of AHN-2 Laser Scanning Data Using Planar Features. *Sensors* **2010**, *10*, 8198–8214. [[CrossRef](#)]
53. Kenzler, H.; Lambers, K. Challenges and perspectives of woodland archaeology across Europe. In *Proceedings of the 42nd Annual Conference on Computer Applications and Quantitative Methods in Archaeology*; Giligny, F., Djindjian, F., Costa, L., Moscati, P., Robert, S., Eds.; Archaeopress: Oxford, UK, 2015; pp. 73–80.
54. Arnoldussen, S. The Fields that Outlived the Celts: The Use-histories of Later Prehistoric Field Systems (Celtic Fields or Raatakkers) in the Netherlands. *Proc. Prehist. Soc.* **2018**, *84*, 303–327. [[CrossRef](#)]
55. Planina, J. Soča (Slovenia). A monograph of a village and its surroundings (in Slovenian). *Acta Geogr.* **1954**, *2*, 187–250.
56. Triglav-Čekada, M.; Bric, V. The project of laser scanning of Slovenia is completed. *Geodetski Vestn.* **2015**, *59*, 586–592.
57. Yoëli, P. Analytische Schattierung. Ein kartographischer Entwurf. *Kartographische Nachrichten* **1965**, *15*, 141–148.
58. Yokoyama, R.; Shlrasawa, M.; Pike, R.J. Visualizing topography by openness: A new application of image processing to digital elevation models. *Photogramm. Eng. Remote Sens.* **2002**, *68*, 251–266.
59. Doneus, M.; Briese, C. Full-waveform airborne laser scanning as a tool for archaeological reconnaissance. In *From Space to Place: 2nd International Conference on Remote Sensing in Archaeology: Proceedings of the 2nd International Workshop, Rome, Italy, 4–7 December 2006*; Campana, S., Forte, M., Eds.; Archaeopress: Oxford, UK, 2006; pp. 99–105.
60. Doneus, M. Openness as visualization technique for interpretative mapping of airborne LiDAR derived digital terrain models. *Remote Sens.* **2013**, *5*, 6427–6442. [[CrossRef](#)]
61. Moore, B. Lidar Visualisation of the Archaeological Landscape of Sand Point and Middle Hope, Kewstoke, North Somerset. Master's Thesis, University of Oxford, Oxford, UK, 2015.
62. Schneider, A.; Takla, M.; Nicolay, A.; Raab, A.; Raab, T. A Template-matching Approach Combining Morphometric Variables for Automated Mapping of Charcoal Kiln Sites. *Archaeol. Prospect.* **2015**, *22*, 45–62. [[CrossRef](#)]
63. de Matos Machado, R.; Amat, J.-P.; Arnaud-Fassetta, G.; Bétard, F. Potentialités de l'outil LiDAR pour cartographier les vestiges de la Grande Guerre en milieu intra-forestier (bois des Caures, forêt domaniale de Verdun, Meuse). *EchoGéo* **2016**, 1–22. [[CrossRef](#)]
64. Krasinski, K.E.; Wygal, B.T.; Wells, J.; Martin, R.L.; Seager-Boss, F. Detecting Late Holocene cultural landscape modifications using LiDAR imagery in the Boreal Forest, Susitna Valley, Southcentral Alaska. *J. Field Archaeol.* **2016**, *41*, 255–270. [[CrossRef](#)]
65. Roman, A.; Ursu, T.-M.; Lăzărescu, V.-A.; Opreanu, C.H.; Fărcaș, S. Visualization techniques for an airborne laser scanning-derived digital terrain model in forested steep terrain: Detecting archaeological remains in the subsurface. *Geoarchaeology* **2017**, *32*, 549–562. [[CrossRef](#)]
66. Holata, L.; Plzák, J.; Světlík, R.; Fonte, J.; Holata, L.; Plzák, J.; Světlík, R.; Fonte, J. Integration of Low-Resolution ALS and Ground-Based SfM Photogrammetry Data. A Cost-Effective Approach Providing an 'Enhanced 3D Model' of the Hound Tor Archaeological Landscapes (Dartmoor, South-West England). *Remote Sens.* **2018**, *10*, 1357. [[CrossRef](#)]
67. Stott, D.; Kristiansen, S.M.; Lichtenberger, A.; Raja, R. Mapping an ancient city with a century of remotely sensed data. *Proc. Natl. Acad. Sci. USA* **2018**, 201721509. [[CrossRef](#)] [[PubMed](#)]

68. Williams, R.; Byer, S.; Howe, D.; Lincoln-Owyang, J.; Yap, M.; Bice, M.; Ault, J.; Aygun, B.; Balakrishnan, V.; Brereton, F.; et al. *Photoshop CS5*; Adobe Systems Incorporated: San Jose, CA, USA, 2010.
69. Valentine, S. *The Hidden Power of Blend Modes in Adobe Photoshop*; Adobe Press: Berkeley, CA, USA, 2012.
70. ISO 32000-1:2008. *Document Management—Portable Document Format—Part 1: PDF 1.7*; ISO: Geneva, Switzerland, 2008; p. 747.
71. Lidar Data Acquired by Plate Boundary Observatory by NCALM, USA. PBO Is Operated by UNAVCO for EarthScope and Supported by the National Science Foundation (No. EAR-0350028 and EAR-0732947). 2008. Available online: <http://opentopo.sdsc.edu/datasetMetadata?otCollectionID=OT.052008.32610.1> (accessed on 22 March 2019).
72. Lidar Data Acquired by the NCALM at the University of Houston and the University of California, Berkeley, on behalf of David E. Haddad (Arizona State University) as Part of an NCALM Graduate Student Seed Grant: Geologic and Geomorphic Characterization of Precariously Balanced Rocks. 2009. Available online: <http://opentopo.sdsc.edu/datasetMetadata?otCollectionID=OT.102010.26912.1> (accessed on 22 March 2019).
73. Grohmann, C.H.; Sawakuchi, A.O. Influence of cell size on volume calculation using digital terrain models: A case of coastal dune fields. *Geomorphology* **2013**, *180–181*, 130–136. [[CrossRef](#)]
74. Wong, B. Points of view: Color coding. *Nat. Methods* **2010**, *7*, 573. [[CrossRef](#)] [[PubMed](#)]
75. Lindsay, J.B.; Cockburn, J.M.H.; Russell, H.A.J. An integral image approach to performing multi-scale topographic position analysis. *Geomorphology* **2015**, *245*, 51–61. [[CrossRef](#)]
76. Guyot, A.; Hubert-Moy, L.; Lorho, T.; Guyot, A.; Hubert-Moy, L.; Lorho, T. Detecting Neolithic Burial Mounds from LiDAR-Derived Elevation Data Using a Multi-Scale Approach and Machine Learning Techniques. *Remote Sens.* **2018**, *10*, 225. [[CrossRef](#)]
77. Niccoli, M. Geophysical tutorial: How to evaluate and compare color maps. *Lead Edge* **2014**, *33*, 910–912. [[CrossRef](#)]
78. Zhou, L.; Hansen, C.D. A Survey of Colormaps in Visualization. *IEEE Trans. Vis. Comput. Graph.* **2015**, *22*, 2051–2069. [[CrossRef](#)] [[PubMed](#)]
79. Ware, C. Color sequences for univariate maps: Theory, experiments and principles. *IEEE Comput. Graph. Appl.* **1988**, *8*, 41–49. [[CrossRef](#)]
80. Banaszek, L.; Cowley, D.C.; Middleton, M. Towards National Archaeological Mapping. Assessing Source Data and Methodology—A Case Study from Scotland. *Geosciences* **2018**, *8*, 272. [[CrossRef](#)]
81. Cowley, D.C. In with the new, out with the old? Auto-extraction for remote sensing archaeology. In *Proceedings of the SPIE 8532*; Bostater, C.R., Mertikas, S.P., Neyt, X., Nichol, C., Cowley, D., Bruyant, J.-P., Eds.; SPIE: Edinburgh, UK, 2012; p. 853206.
82. Bennett, R.; Cowley, D.; Laet, V.D. The data explosion: Tackling the taboo of automatic feature recognition in airborne survey data. *Antiquity* **2014**, *88*, 896–905. [[CrossRef](#)]
83. Kramer, I.C. An Archaeological Reaction to the Remote Sensing Data Explosion. Reviewing the Research on Semi-Automated Pattern Recognition and Assessing the Potential to Integrate Artificial Intelligence. Master's Thesis, University of Southampton, Southampton, UK, 2015.
84. Trier, Ø.D.; Zortea, M.; Tonning, C. Automatic detection of mound structures in airborne laser scanning data. *J. Archaeol. Sci. Rep.* **2015**, *2*, 69–79. [[CrossRef](#)]
85. Traviglia, A.; Cowley, D.; Lambers, K. Finding common ground: Human and computer vision in archaeological prospection. *AARGnews* **2016**, *53*, 11–24.
86. Grammer, B.; Draganits, E.; Gretscher, M.; Muss, U. LiDAR-guided Archaeological Survey of a Mediterranean Landscape: Lessons from the Ancient Greek Polis of Kolophon (Ionia, Western Anatolia). *Archaeol. Prospect.* **2017**, *24*, 311–333. [[CrossRef](#)] [[PubMed](#)]



© 2019 by the authors. Licensee MDPI, Basel, Switzerland. This article is an open access article distributed under the terms and conditions of the Creative Commons Attribution (CC BY) license (<http://creativecommons.org/licenses/by/4.0/>).

Article

# Integrating Remote Sensing, Machine Learning, and Citizen Science in Dutch Archaeological Prospection

Karsten Lambers <sup>1,\*</sup>, Wouter B. Verschoof-van der Vaart <sup>1,2</sup> and Quentin P. J. Bourgeois <sup>1</sup>

<sup>1</sup> Faculty of Archaeology, Leiden University, P.O. Box 9514, 2300 RA Leiden, The Netherlands; w.b.verschoof@arch.leidenuniv.nl (W.B.V.-v.d.V.); q.p.j.bourgeois@arch.leidenuniv.nl (Q.P.J.B.)

<sup>2</sup> Data Science Research Programme (Leiden Centre of Data Science), Leiden University, P.O. Box 9505, 2300 RA Leiden, The Netherlands

\* Correspondence: k.lambers@arch.leidenuniv.nl; Tel.: +31-71-527-6510

Received: 1 March 2019; Accepted: 29 March 2019; Published: 3 April 2019

**Abstract:** Although the history of automated archaeological object detection in remotely sensed data is short, progress and emerging trends are evident. Among them, the shift from rule-based approaches towards machine learning methods is, at the moment, the cause for high expectations, even though basic problems, such as the lack of suitable archaeological training data are only beginning to be addressed. In a case study in the central Netherlands, we are currently developing novel methods for multi-class archaeological object detection in LiDAR data based on convolutional neural networks (CNNs). This research is embedded in a long-term investigation of the prehistoric landscape of our study region. We here present an innovative integrated workflow that combines machine learning approaches to automated object detection in remotely sensed data with a two-tier citizen science project that allows us to generate and validate detections of hitherto unknown archaeological objects, thereby contributing to the creation of reliable, labeled archaeological training datasets. We motivate our methodological choices in the light of current trends in archaeological prospection, remote sensing, machine learning, and citizen science, and present the first results of the implementation of the workflow in our research area.

**Keywords:** airborne laser scanning; archaeological prospection; deep learning; citizen science; The Netherlands

## 1. Introduction

### 1.1. Remote Sensing in Archaeological Prospection

The importance of remote sensing as a data source for archaeological prospection has grown exponentially in recent years [1,2]. Remotely sensed data from terrestrial, aerial, and spaceborne sensors are today a key element of local and regional scale archaeological research, as well as heritage management [3]. A recent study from Scotland [4] even advocates the primary reliance on remotely sensed data as part of a national archaeological mapping strategy. This is in line with the growing importance of non-invasive research strategies that enable the preservation of archaeological heritage [5–7].

While most terrestrial [8] and some aerial [9,10] remotely sensed data used in archaeological prospection are generated specifically for archaeological purposes, most aerial and all spaceborne remotely sensed data are produced for either non-archaeological applications or for general purposes [11]. Consequently, a broad range of computational methods and tools for the analysis of remotely sensed data have been developed outside of archaeology [12,13], e.g., for object detection [14], a task akin to archaeological prospection (see Section 2.1). However, in archaeology, the acceptance

and use of these computational approaches were initially limited, since archaeology tends to rely on its own domain-specific toolbox [15].

Archaeologists have used aerial photographs for decades to detect and map archaeological traces in the landscape [16]. Thus, they initially tended to apply familiar protocols of aerial photograph analysis and interpretation to new types of remotely sensed data, e.g., by visually observing and manually marking potential archaeological objects [17] in single-frame 2D images of a given landscape, one image at a time (In the field of Computer Vision the term ‘feature’ refers to the properties of an image, while an ‘object’ refers to real-world entities [17]). This human-scale approach has obvious limitations [18]: 1) It cannot handle the sheer quantity of available remotely sensed data, which is growing exponentially; 2) it does not do justice to the quality of remotely sensed data, the dimensionality and resolution of which is often beyond the processing capacity of the human visual system; and 3) the inherent biases of the traditional approach [16,19] are not overcome but rather reproduced on a larger scale.

Thus, after initial attempts in the 1990s that had little effect, in the mid-2000s, archaeologists started in earnest to develop computational approaches to remote sensing-based archaeological prospection (see references in Reference [20] and overview in Reference [21]). While the history of this endeavor is thus short, clear patterns and trends have emerged. Referring to research undertaken by ourselves and others, we here follow the useful classification by Chen and Han ([14]; Figure 1), who identify four main classes of object detection methods in (optical) remotely sensed data that are based on either Template Matching, Knowledge, (Geographic) Object-based Image Analysis ((GE)OBIA), or Machine Learning.

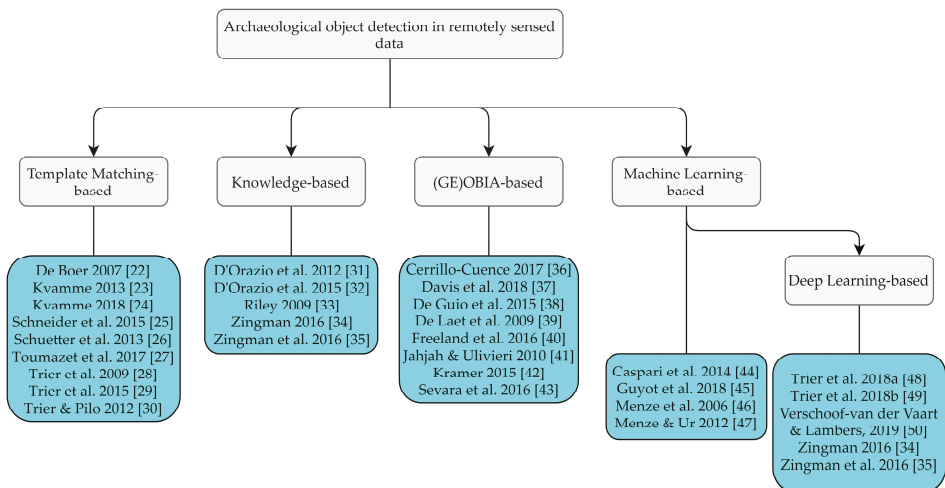


**Figure 1.** Classification of research on archaeological object detection in remotely sensed data, following Reference [14].

### 1.2. Archaeological Object Detection

In archaeological object detection, most available (custom) algorithms are based on Template Matching (e.g., [22–30]). Their continuous success is due to the fact that simple geometric shapes such as circles and rectangles are common in the archaeological record but rare in nature [23]. Knowledge-based algorithms (e.g., [31–35]) require detailed knowledge about the expected objects and their surroundings. They tend to be highly case-specific and are rarer in archaeology. (GE)OBIA-based approaches using image segmentation are more flexible and thus more common and have proven useful in various case studies (e.g., [36–43]). These first three classes of object detection methods (as opposed to the fourth class, machine learning, e.g., [44–50], see below) all build on explicit prior

knowledge of the properties of the expected archaeological objects. They thus relate easily to common archaeological practice that relies on a detailed recording and study of the archaeological record informed, in large parts, by prior discoveries. However, multiple case studies using these ‘traditional’ methods have revealed complications with their implementation: 1) The often handcrafted algorithms are specialized in specific object categories and data sources, which restrict their use in different contexts and limits their usability in general for archaeological prospection; 2) templates and characteristic spatial attributes are often difficult to define for heterogeneous archaeological objects, especially if these have been ‘transformed’ by various natural and anthropogenic processes over time [45]; and 3) these approaches are predominantly complex algorithms that can require a high level of expertise, and are regularly dependent on expensive software. All this results in a limited user-friendly implementation (see also Reference [51]).

The fourth class of object detection methods defined by Chen and Han [14], machine learning, is a rather new approach in archaeological applications. It is conceptually different from the other classes in that it does not require any explicit knowledge of the properties of the expected objects or their surroundings, nor any rules for finding them. Rather, the computer learns from many known positive (and negative) instances of the expected object class(es) without making the relevant object properties explicit. Machine learning using Random Forests has been used in a number of archaeological case studies [44–47]. To date, the most frequently used algorithms within deep learning [52], a subfield of machine learning, are Convolutional Neural Networks (CNNs) [53]. In essence, a CNN is an image-classifier that is loosely inspired by the (human) visual cortex [51]. A deep convolutional neural network, from which the term deep learning is derived, consists of multiple layers that together comprise a feature extractor and classifier. The layers in a CNN are, in sequence: 1) An input layer, 2) a varying number of alternating convolutional and pooling layers, and 3) an output layer. In the convolutional layers, various filters (kernels) are used to convolve (add values of a pixel within an image to its neighboring pixels based on a certain filter) the image into feature maps. The subsequent pooling layer reduces the dimensions of these feature maps. After the last pooling layer, there are several fully-connected layers that look at which particular class the produced feature maps most strongly correlates to, assign class labels and compute probabilities of a given class being present in the input image [51,54].

Comparable to other machine learning approaches, a CNN learns to generalize from given examples (normally a large set of labeled images) rather than relying on a human programmer to formulate rules or set parameters. While this has led to discussions about the ‘black box problem’ [55], the favorable results of CNN applications have outweighed most skeptical voices. For example, since 2015, neural networks have consistently outperformed humans in visual object recognition tasks [56]. In particular, the opportunities offered by transfer learning (or domain adaption; [57]) have opened up the use of so-called pre-trained CNNs to many fields that, up to now, were restricted by the (small) size of available datasets, e.g., archaeology. CNNs have recently successfully been implemented in archaeology: On photographs and drawings [58], as well as on images from remote sensing surveys [34,35,48–50].

CNN-based machine learning thus seemed the most promising approach to analyze remotely sensed data of our research area in the central Netherlands for the purpose of archaeological prospection.

### 1.3. The Research Area and Current Research Strategy

The research area, known locally as the *Veluwe*, comprises a largely forested area of circa 1100 km<sup>2</sup> (Figure 2). The Veluwe consists of ice-pushed ridges formed in the Saale glacial period (circa 350,000 to 130,000 years ago), which were subsequently partially covered with cover sand deposits during the Weichselian glacial period (circa 115,000 to 10,000 years ago) [59]. From the Neolithic through to the Middle Ages the Veluwe area was covered by forest and heath in varying proportions [60], and surrounded by marshes and river valleys. Significant deforestation of the area, due to extending agricultural areas and charcoal production, took place in the second half of the Middle Ages (circa

1000 to 1500 AD). This most likely caused the emergence of drift sand (aeolian sand; [59]). Large parts of the research area were reforested in the first half of the 20th century [61] and the majority of the still extant archaeological objects are now in heathland or under forest cover. Nowadays, the Veluwe holds one of the densest concentrations of known archaeological objects in The Netherlands, including barrows, Celtic fields, charcoal kilns, hollow roads, and *landweren* (border barriers). While the location of the archaeological objects under forest cover has almost certainly contributed to their present-day preservation, this also hinders the investigation of these objects and especially the survey of the surrounding landscape for potential new archaeological objects (see also Reference [62]).

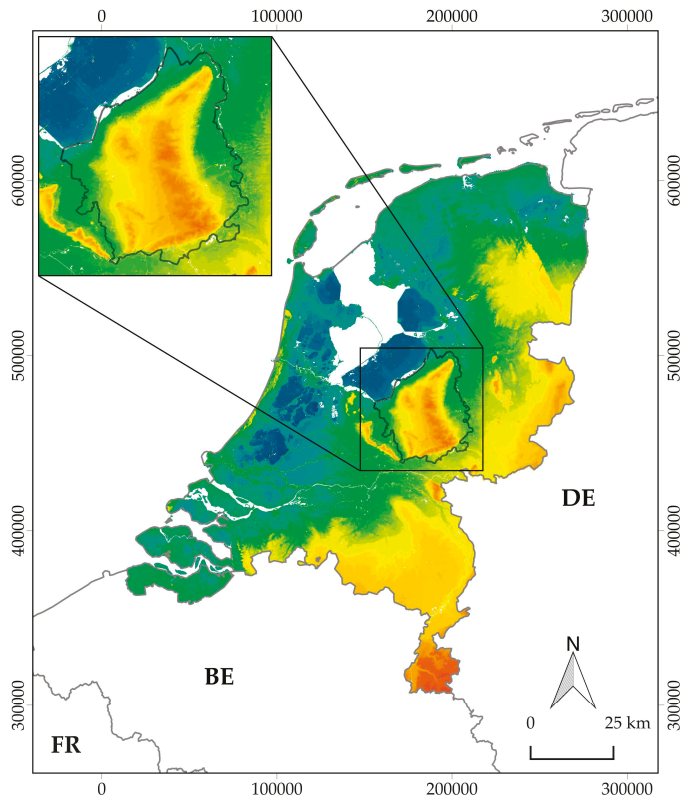


**Figure 2.** The research area on a height model of The Netherlands (source of the background image and height model: Reference [63]; coordinates in Amersfoort/RD New, EPSG: 28992).

Archaeological research on the Veluwe has mainly consisted of research-driven scientific studies, as opposed to development-driven commercial fieldwork. All this research involves, to a certain extent, the manual analysis of remotely sensed data. Recent research-driven excavations on the Veluwe have mainly focused on barrows (newly discovered in remotely sensed data) and their immediate surrounding landscape [64–66]. Recent large-scale surveys include the study of Celtic fields by Arnoldussen [67], the study of hollow ways and roads by Vletter and Van Lanen [68], and the research on barrow landscapes by Bourgeois [69]. The general research strategy in this area (and The Netherlands) consists of a stepped system of: 1) A desktop-survey; followed by 2) a field survey; and finally, 3) a (minimal) invasive survey, i.e., hand corings, test trenches, and excavations (Figure 3; see also Reference [70]). Recently, this research strategy has been successfully supplemented with geophysical surveys [71].



**Figure 3.** Recent barrow excavation at Apeldoorn—Echoput (Source: Reference [64]).

#### 1.4. Outline of This Paper

In this paper, we propose an integrated approach, incorporating and combining the analysis of remotely sensed data using deep learning and methods from citizen science with ‘traditional’ research methods, in order to conduct a survey of archaeological objects based on multiple data sources. In the next Section 2 these new data sources and methods are introduced. In Section 3 the integrated approach is presented, followed by an ongoing case study that incorporates this innovative workflow in the research area (Figure 2). In Section 4 the integrated approach as a whole, as well as the new additions to the current research strategy are discussed, followed by conclusions in Section 5.

## 2. New Data Sources and Methods

### 2.1. Multi-Class Object Detection in Remotely Sensed Data Using Deep Learning

In order to explore the possibilities of convolutional neural networks for archaeological object detection in remotely sensed data on the Veluwe, a workflow called WODAN (Workflow for Object Detection of Archaeology in The Netherlands) was developed [50]. For the initial experiments 437.5 km<sup>2</sup> of interpolated LiDAR data from the research area (Figure 2) was gathered (see [72,73] for information on LiDAR) (Interpolated LiDAR data of the entire Netherlands with a point density of 6–10 per m<sup>2</sup> and a 50 cm resolution is available from the online repository PDOK [62] or the *Actueel Hoogtebestand Nederland* [73]). The data was visualized with the Simple Local Relief Model (see [74]) from the *Relief Visualisation Toolbox* [75]. This LiDAR visualization enhances the local detail, while suppressing the large-scale terrain relief, making it very suitable to represent various archaeological objects present in the research area (Figure 4; see also Reference [76]). The images were entered into a geographic information system (GIS) environment [77] and dissected into sub-images of 1000 by 600 pixels (500 by 300 m). Archaeological objects, discernable in the LiDAR data, were compared with the locations of known archaeological objects [50]. The (geo)information of these known archaeological objects was derived from a multitude of databases, including the Dutch national archaeological database ArchIS [78], the Dutch archaeological monument registry AMR [79], and the results of different large-scale surveys of the research area [67–69]. Sub-images containing known archaeological objects were labeled and the necessary metadata was created in order to use the images for our deep learning approach.

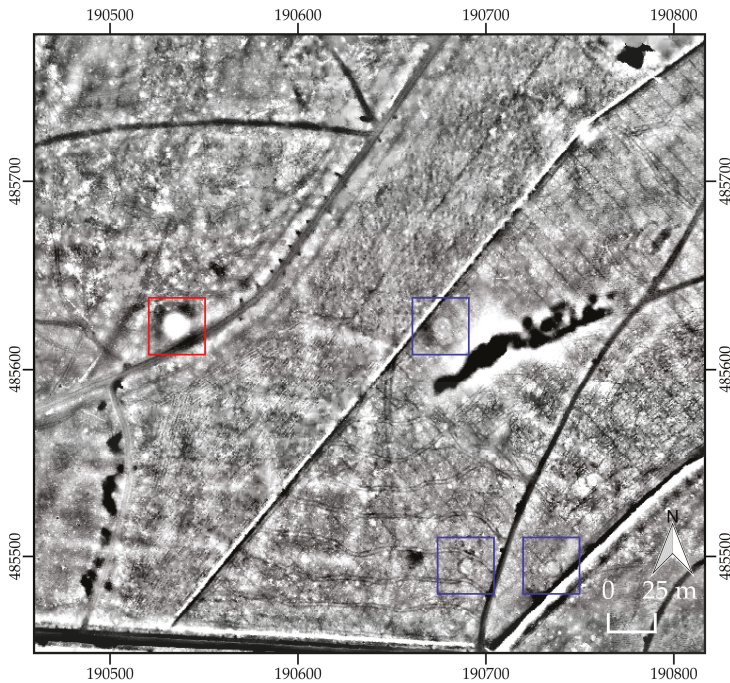


**Figure 4.** Sample of LiDAR data (source: Reference [63]; coordinates in Amersfoort/RD New, EPSG: 28992), visualized with Simple Local Relief Model, from the research area, showing a potential new barrow (red) and charcoal kilns (blue) amidst a Celtic field (white checkerboard pattern).

At the start of the development of WODAN, it was recognized that for archaeological prospection, obtaining the exact position of objects in the wider landscape (i.e., localizing) is as important as characterizing them (i.e., classifying, the typical task of a neural network). This combination of localizing and classifying—referred to as object detection in deep learning—is handled by a specialized type of neural networks, so called R-CNNs (Region-based CNNs or Regions with CNN features; [80]). These networks are able to localize and classify multiple objects within a larger image, as opposed to ‘normal’ CNNs that classify the entire input image [54]. The basic concept of the R-CNN model is: 1) To utilize the Selective Search algorithm [81] to produce object proposals; 2) to use a CNN to extract features for every object proposal; 3) to feed these features into a support vector machine (SVM) classifier to decide whether a proposal contains an object of interest; and finally, 4) to use a linear regressor to tighten the bounding box to fit the true dimensions of the object [80]. The successor of R-CNN (Fast R-CNN) improved on its predecessor by speeding up the feature extraction and classification step and by joining the CNN, SVM, and linear regressor into one CNN model [82]. Further improvements were made to speed up the object proposal step, resulting in the Faster R-CNN model [83]. The WODAN workflow therefore incorporates an adapted version of the Faster R-CNN model.

WODAN has been trained and tested on part of the research area (see Section 1.3) to detect barrows and Celtic fields in LiDAR images. The workflow served as a proof of concept, to demonstrate that by implementing deep learning techniques it was possible to create a multi-class detector for archaeological objects. WODAN (Figure 5) consists of three parts: A preprocessing part, an object detection part, and a post-processing part. For a comprehensive overview of WODAN see Reference [50]. The preprocessing part converts interpolated LiDAR data into input images that meet the requirements of the object detection model. In the second part, the actual object detection by

the adapted Faster R-CNN model is performed. The post-processing part converts the results of the prior step into geographical vectors, directly usable in a GIS environment. This final step improves the usability of the object detection results for archaeological prospection.

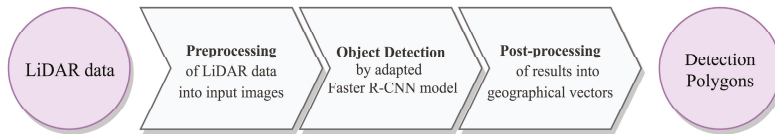


**Figure 5.** Simplified representation of WODAN (Workflow for Object Detection of Archaeology in The Netherlands; for a comprehensive overview see Reference [50]).

## 2.2. Creation of (Training) Datasets

During the development of WODAN, two major challenges were encountered: The absence of large datasets with labeled archaeological objects and the presence of hitherto unknown archaeological objects that have to be validated within the datasets.

In order to successfully train Faster R-CNN—or any machine learning object detection model—training-, validation-, and testing datasets containing a large number of labeled archaeological objects are needed. Unfortunately, at the outset of the development of WODAN no such datasets were available, and therefore had to be created. This manual creation of the necessary datasets is a labor-intensive process, which is susceptible to bias, inaccuracies, and errors, largely depending on the (number of) interpreters or ‘taggers’ [84,85].

During the creation of the dataset it was noted that many images contained prospective archaeological objects that were previously unknown (Figure 4). At the moment of writing, 739 potential barrows (on average 1.7 new potential barrows per km<sup>2</sup>) and 415 potential charcoal kilns (on average 0.95 new potential charcoal kilns per km<sup>2</sup>) have been discovered in an area of 437.5 km<sup>2</sup>. Based on these numbers, a rough extrapolation can be made for the amount of new potential barrows and charcoal kilns in the entire research area (circa 1100 km<sup>2</sup>). We expect about 1750 new potential barrows (including the previously mentioned 739) and about 1000 new potential charcoal kilns (including the previously mentioned 415) in the research area. In this we have considered the amount of archaeology in ‘high potential’ zones, with an abundance of forest and/or heathland cover and therefore good preservation conditions, and ‘low potential’ zones, with large areas of agricultural- and/or built-up cover. Validating circa 2750 new potential archaeological objects would take more than six years of continuous (field)work, following the present-day research strategy (see Section 1.3), without any additional data analysis.

These challenges caused us to contemplate whether the systematic involvement of volunteers (i.e., citizen science) could possibly be an answer to the non-existence of large, labeled datasets, as well as the validation of newly discovered archaeological objects either during the creation of datasets or as the result of automated object detection methods.

## 2.3. Citizen Science

The definition of citizen science can be very broad [86,87], but essentially it boils down to volunteer (non-professional) scientists, generally called citizen researchers [87], helping with a scientific inquiry. Within archaeology, this has long been a recurrent practice, especially during fieldwork where community engagement is prevalent [88]. However, directly involving citizens in the collection and/or interpretation of datasets, in order to cope with the so-called professional bottleneck [89], is less common.

In recent years a few large-scale online citizen science projects have been launched successfully within archaeology (e.g., [90,91]). One of the more successful projects is the crowdsourced search for Genghis Khan’s tomb by National Geographic [92]. Over 10,000 online volunteers contributed

30,000 hours (3.4 years), examining 6000 km<sup>2</sup> of high-resolution satellite images of a region in Mongolia. This generated 2.3 million potential archaeological objects, including Bronze Age and Mongol period burial mounds, so-called “deer stone” megaliths, and ancient city fortifications. An example of a more small-scale project is the Cotswold Escarpment project, in which six volunteers examined LiDAR data of an area of 100 km<sup>2</sup> in South West England and identified over 260 archaeological objects [93].

The success of some of these projects already highlights their potential for our current approach. However, online citizen science projects face specific challenges [94,95]. Previous research has shown that the majority of the contributions in such projects are made by a relatively small group of volunteers [94,95]. Thus, recruiting a critical mass of citizen researchers and ensuring they are kept engaged throughout the project is one of the biggest challenges such a project would face.

A further challenge, in particular related to archaeological projects, is that the quality of the contributions is difficult to assess (beforehand). The weeding out of false positives, especially in the case of the interpretation and classification of remotely sensed data, is a critical aspect [96]. In this respect, we envision that the results of machine learning approaches can be validated against the results of citizen science approaches and vice-versa. The feedback between these two datasets will inform us on the quality of both.

An added benefit of using citizen science in the interpretation of remotely sensed data, is that citizen researchers will also be able to detect objects they have not been instructed to detect [97]. Machine learning approaches can only detect objects similar to known ones of which enough examples are available, yet finding potential new types of archaeology requires a human perspective. For example, in the specific case of the Veluwe, already one potential Roman marching camp has been discovered by human interpreters. As the number of known Roman marching camps in The Netherlands (and continental Europe) is very low [98], finding these will require a human perspective.

Both the citizen science and machine learning datasets will generate specific locations where archaeological objects are expected. Gauging the quality of these predictions often requires field observations [70]. As highlighted above, the sheer number of expected archaeological objects makes such a fieldwork project a daunting task through regular means. Therefore, we aim to also combine this fieldwork with a citizen science approach, where citizen researchers can participate in a dedicated fieldwork campaign. Citizen researchers can easily take most of the initial steps needed to rule out false positives in the field. For example, in our Veluwe case study a simple visual inspection can quickly differentiate between a potential barrow or a stack of fodder next to a farm, both of which will generate the same pattern on a LiDAR image. Nevertheless, recognizing different object classes in the landscape and distinguishing archaeological objects from natural or modern ones is difficult and requires training and experience.

We argue that the combination and integration of all three approaches—machine learning-based object detection, citizen science-based online data interpretation and revision, and a citizen science fieldwork campaign—will provide an integrated approach that will be beneficial to all three elements. Finally, the added benefit of the citizen science approach is that it will help generate awareness and better protection of the archaeological relics in the area directly through the involvement of the citizen researchers [93].

### 3. Implementation and Results

Based on the results and challenges presented by automated object detection techniques, the opportunities offered by citizen science, and the current research strategy for validating new potential archaeological objects from remotely sensed data, we propose an innovative integrated workflow to generate datasets for machine learning approaches and to validate new potential archaeological objects. This integrated approach (Figure 6) incorporates the aforementioned new data sources and methods in the existing research strategy, with a clear focus on the participation of a wide range of different interest groups, including citizen researchers, data scientists, heritage managers, and academic researchers.

In the following Section 3.1, the separate steps within the integrated approach are presented, followed by an overview of their implementation in our research area (Section 3.2).

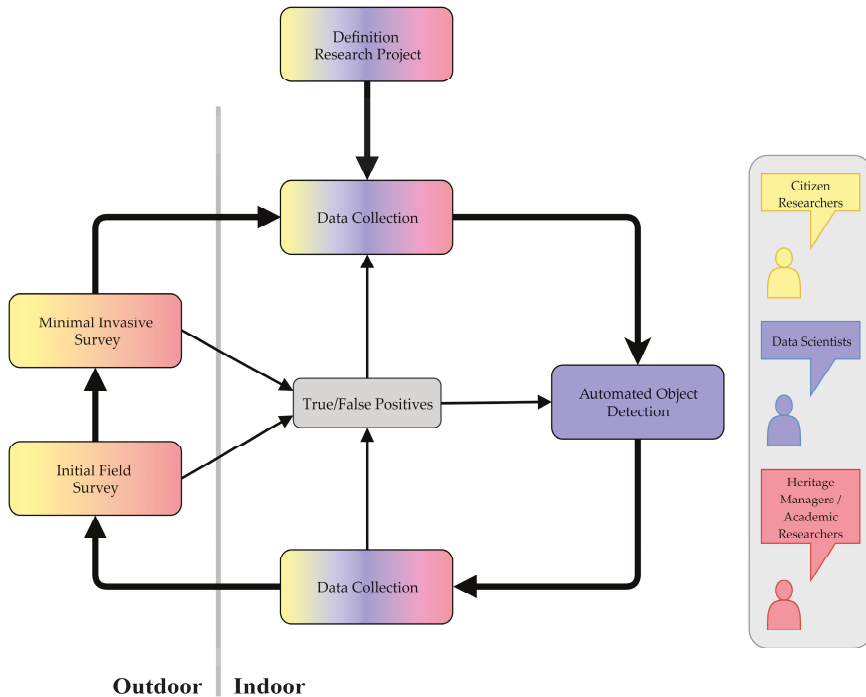


**Figure 6.** The integrated approach as proposed in this paper with colors depicting the involvement of different interest groups (see box on right).

### 3.1. An Integrated Approach for Dataset Generation and Validation

The start of the integrated approach (Figure 6) lies in the definition of the overall research project, including a research area, a central research problem, and associated research questions. Our intention is that all above-mentioned groups can and should participate in the formulation of the research project. While the interests and questions may differ between these groups, they can all contribute to a common goal. For example, local citizen researchers might be interested in the history of their home region, data scientists in the development of accurate training datasets for machine learning methods, heritage managers in the exact location and preservation of archaeological objects within their region of influence, and academic researchers in (the physical residue of) social processes through time in a certain area. All these questions have in common that answering them requires the detection, localization and classification of archaeological objects in the defined research area.

#### 3.1.1. Data Collection and Automated Object Detection Steps

Following the formulation of the specifics of the research project, a continuous, iterative process of data generation and validation starts. The first step in this process involves the collection of (remotely sensed and archaeological) data, predominantly to generate training datasets for the next step in the approach. This collection of data will be extended and updated constantly, based on the validation of detections later on in the process. It is presumed that new potential archaeological objects are discovered already during this step in the process, especially when new data sources are used or when the defined research area has not been extensively researched in the past (see Section 2.2). This step,

as well as the subsequent desktop survey step, present opportunities for using online platforms to include and involve a wide audience of (citizen) researchers. Spreading the workload of data collection among a large group of individuals can prove to be a solution to the professional labor bottleneck encountered in training dataset generation [89].

The result of the first step is a substantial collection of data containing (geo)information about known and newly discovered archaeological objects. This training dataset can be used for automated object detection using deep learning or other machine learning approaches. Given enough training examples, deep learning approaches have proven to be able to localize and classify new examples of the archaeological object(s) in question (e.g., [49]). Therefore, just like the prior step in the process, these object detection schemes will generate detections of new potential archaeological objects.

### 3.1.2. Validation Steps

Following the data collection and automated object detection step, the new potential archaeological objects will be validated in three consecutive steps (Figure 6), closely following the current Dutch research strategy (see Section 1.3) of desktop survey, initial field survey, and minimal invasive survey. These validation steps can be conducted by different groups of citizen researchers in cooperation with or assisted by (local) heritage managers and/or academic researchers. A clear distinction can be made between the first step of the validation process, i.e., desktop survey, and the subsequent two steps, i.e., initial field survey and minimal invasive survey. The desktop survey is an indoor and digital activity that is not impeded by the distance between the citizen researcher and the research area. Therefore, this step can include a wide group of contributors on the national and even international level. On the other hand, the second and third validation steps have a distinct local and outdoor character. These steps involve the active participation of citizen researchers at the actual location of the detections. Thus, there may or may not be an overlap between the two groups of citizen researchers involved in the desktop and field surveys, respectively.

In the desktop survey the results of the prior steps (especially the automated object detection step) will first undergo a data quality control. Thereafter, the results are compared with digital (geo)information sources, such as historical, geo(morpho)logical, and topographic maps, (historical) aerial photographs, and other remotely sensed data. This will lead to the discernment of false positives. More importantly, this step can lead to new insights in the relation between certain archaeological object classes and particular topographic and/or geological parameters. This relational information can be used in subsequent iterations of the process.

In the initial field survey, the newly discovered potential archaeological objects will be investigated in the field. (Citizen) researchers will be asked to record a predefined set of characteristics such as dimensions, height, position in the landscape, etc. for every new potential archaeological object. This validation step will, in addition to identifying false positives, lead to the recognition of important parameters of the archaeological objects in question. Furthermore, by recording natural and anthropogenic disturbances to the archaeological object such as toppled trees, burrows, excavations, etc., a first indication can be gained on the preservation of the archaeological object and further steps can be undertaken by heritage managers to conserve the object.

The third and last validation step involves the investigation of new potential archaeological objects through minimal invasive techniques, such as hand corings or test trenches. This step is specifically to validate those new potential archaeological objects that could not be confirmed nor discarded in the two preceding validation steps.

The validation steps within the integrated approach lead to the determination of true and false positives, the determination of important parameters of the archaeological objects in question, and the identification of potential new data sources. These results will be used to update the data collection and automated object detection and can thus be exploited at a subsequent iteration of the process. This integrated approach will result in large reliable datasets, better automated object detection models that can rely on these large reliable datasets, a complete picture of the occurrence of the archaeological

object classes within the research area, and more knowledge of the archaeological objects in question. This, in turn, will lead to new insights into the number, distribution, and state of preservation of the archaeological objects in question, and the potential for better preserving and monitoring of these objects, thus answering the different research questions of the different interest groups.

### 3.2. Case Study: Using the Integrated Approach in Studying Archaeological Landscapes on the Veluwe

The integrated approach to archaeological prospection proposed here (Figure 6) is currently being implemented in the research area (Figure 2), where it enables us to create and validate datasets of archaeological objects, namely three typical, abundantly present classes: Barrows, Celtic fields, and charcoal kilns (Figure 4). The citizen science elements of our project have been designed and are being conducted in collaboration with the regional heritage agency, *Erfgoed Gelderland*. The iterative nature of our approach leads to a continuous generation of data. We here present the results of the initial project phase.

#### 3.2.1. Data Collection and Object Detection: The Zooniverse and WODAN

In order to analyze the LiDAR data, our primary data source, of the entire Veluwe, we use the Zooniverse, a web-based platform that offers opportunities for citizen science projects or ‘people-powered research’ [99]. The concept of the Zooniverse is that users do not need any specialized background, training, or expertise to participate in any project on that platform. In our Zooniverse project, named *Heritage Quest* [100] (*Heritage Quest* will officially be launched on 10 May 2019 and be available online at Reference [100] from that date onwards), participants are asked to mark every potential barrow, Celtic field and charcoal kiln within a small LiDAR image of 300 m by 300 m (Figure 7). The participant has the option to switch between different LiDAR visualizations (currently shaded relief and Simple Local Relief Model; see Reference [76]) in order to assist them in their classification. In order to allow international citizen researchers to participate in the data collection step, the user interface of *Heritage Quest* is bilingual Dutch/English. Every individual LiDAR image will be classified by at least eight different users, therefore guaranteeing minimal inter-analyst variability and furthermore presenting possibilities to explore inter-rater agreement [101]. The monitoring of user engagement, feedback and online support will be provided by a dedicated staff member at our regional collaboration partner, *Erfgoed Gelderland*, who knows the study region first-hand.

The automated object detection workflow WODAN [50] will be used on the same areas as the *Heritage Quest* project. The results of both will be compared with each other (see Section 2.3).

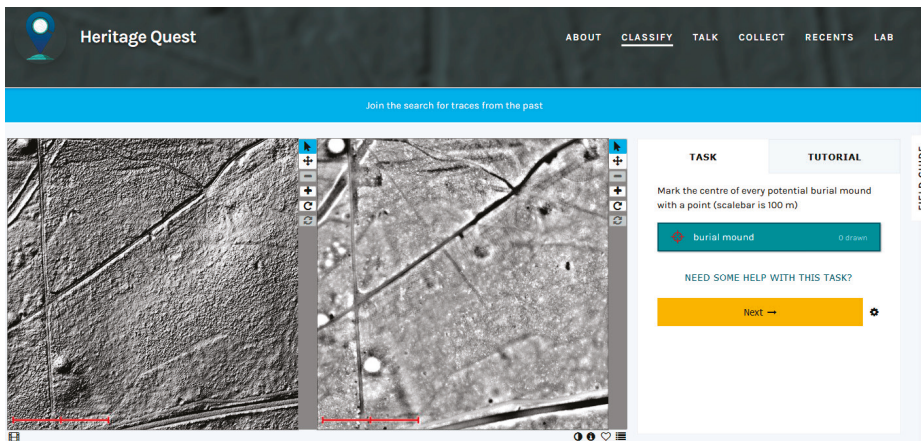


Figure 7. Classifying archaeological objects in LiDAR images in the *Heritage Quest* project [100].

### 3.2.2. Validation: Field Expeditions and Coring Campaigns

The new potential archaeological objects, discovered in the previous steps of the project, will be validated by the cooperation between citizen researchers and heritage managers and/or academic researchers. The initial field surveys will focus on the validation of new potential barrows and charcoal kilns, as tests have shown that Celtic fields are too difficult to recognize under vegetation cover in the field. These investigations can be conducted individually, or in larger groups in so-called field expeditions, organized at regular intervals during the year. The initial field surveys will be guided by a mobile WebGIS application, which incorporates a simplified GIS environment and a digital survey form. This program guides the user to the location of new potential archaeological objects and offers the possibility to collect and register a set of predefined characteristics directly in the application. Apart from the documentation of these characteristics, it offers the possibility to record natural and anthropogenic disturbances.

It is recognized that the last validation step within the process, involving minimal invasive techniques, is a complex affair, which requires a certain degree of experience (see Section 2.3). Furthermore, invasive archaeological research is strictly regulated and restricted to ‘professional archaeologists’ by Dutch heritage laws [102]. Therefore, this step within the validation will be conducted by heritage managers and/or academic researchers assisted by citizen researchers and/or students in so-called coring campaigns. After successful test runs in early 2019 (Figure 8), both the field expeditions and the coring campaigns will take place in summer and autumn, building on previous collaboration with regional heritage managers and citizen researchers in the Veluwe project.



**Figure 8.** The validation of a new potential barrow through hand corings in early 2019, from left to right: R. Kramer (*Erfgoed Gelderland*), M. Wispelwey (*Samenwerkingsverband Noord Veluwe*), G. Scheltema (*Archeologische Werkgroep Nederland*), Q.P.J. Bourgeois (*Leiden University*), W.B. Verschoof-van der Vaart (*Leiden University*), and K. Lambers (*Leiden University*) (Photograph by E. Kaptijn (*Erfgoed Gelderland*)).

After the initial iteration of the process the results will be incorporated in the training dataset of WODAN, which will lead to an improved performance in subsequent iterations [50]. New archaeological object classes can be added and new areas can be explored. The end result of the project will be a large reliable dataset of different archaeological object classes, a better understanding of the occurrence, distribution, and preservation of these archaeological object classes, and the engagement of citizen researchers with the cultural heritage of the Veluwe.

#### 4. Discussion

The integrated workflow that we introduce here and are currently employing in our Veluwe case study is a novel combination of methods from remote sensing, machine learning, and citizen science for the purpose of archaeological prospection. While these methods have been combined in different partial constellations in the past, our project on the Veluwe, although in its early stages, shows the benefits of a full integration.

Numerous studies in recent years have shown that a thorough analysis of remotely sensed data consistently leads to a significant increase in the number of potential archaeological objects in a given region (e.g., [4,46,93,103–105]). The quantity and complexity of—often high-resolution, multi-dimensional—remote sensing data requires an investment of labour far beyond traditional means. Apart from computational approaches, discussed below, this can either be achieved by having few people work on the task over a long period of time (e.g., [104]) or many people over a short period of time (e.g., [92,103]). In the latter case, those people are either trained project staff or citizen researchers. While trained staff can contribute to both object detection and validation [103], the employment of citizen researchers has so far been mostly limited to object detection [92,93]. As our workflow shows, citizen researchers can make important contributions on multiple levels (Figure 6): 1) In the research design step, by contributing their own research questions, 2) in the data collection step, detecting archaeological objects based on their own knowledge and/or training provided by heritage managers/academic researchers, and 3) in the data validation steps, by checking object detections made on remotely sensed data digitally and in the field. This is where we propose two related but separate citizen science projects: An online screening of remotely sensed data (our Heritage Quest project [100] on the Zooniverse) in which many citizen researchers on an international level can participate, and field observations in our research area by local citizen researchers, some of whom have collaborated with other archaeological projects on the Veluwe in the past. While there might be an overlap between the user populations of both projects, and we use one project to advertise the other, such an overlap is not required for the success of both projects.

Apart from the detection and validation of archaeological objects in our research area, both citizen science projects also contribute to the generation of large reliable training datasets of archaeological objects in remotely sensed data. These are required to improve our deep learning-based multi-class object detection workflow WODAN, but also other machine learning-based archaeological object detection methods can benefit from these. In fact, the generation of large training datasets is a prerequisite to make any machine learning approach work in archaeological contexts where reliable data is often sparse. Although strategies such as data augmentation [52] and transfer learning [57] have considerably lowered the required number of confirmed instances of archaeological objects for the training of deep learning-based algorithms, higher numbers will always improve their performance. The iterative nature of our integrated approach (Figure 6) ensures that any validation will feed directly into the training dataset, thus constantly improving the deep learning-based detection algorithm. We have started to exchange our training data with projects working in similar fields. Since most automation projects so far have been targeting a narrow range of typical, pervasive archaeological object classes such as barrows, charcoal kilns, mounds and pits (see Section 1), such an exchange is likely to lead to quick improvements of the different approaches. In the long run, we envision the creation of truly large archaeological training datasets that can be used in regular competitions not unlike the annual ImageNet challenges [106].

With this perspective in mind, we argue that deep learning and citizen science not only combine well, but depend on each other for the success of both. This has, in fact, been recently demonstrated by case studies in other domains, such as biology [107], medicine [108], and ecology [109], to name just a few. In archaeology, however, both approaches have so far been used alternatively instead of complementarily. Especially object validation has been left to trained project staff or professionals [4,103,110], in some cases explicitly favouring this option over any automation approach [103]. Our proposed workflow and its implementation in our Veluwe project shows that such a dichotomy between people-powered and computer-powered archaeological object detection does not exist and that we should indeed strive for an integration of both approaches.

In choosing CNN-based deep learning as a basis for our approach to archaeological object detection in the Veluwe project, we are aware of the criticism that this method faces (see Section 1 and discussion in Reference [111]). However, we are not just following the latest trends here but have based our decision on our own experience and learning curve in the field of automated archaeological object detection over more than a decade.

In the course of consecutive projects, the first author tested different approaches to automated archaeological object detection (e.g., Nasca geoglyphs in Peru [112,113] and livestock enclosures in the Alps [34,35,114]), moving from simple tools such as edge detectors to complex knowledge-based algorithms. While the detection results became more powerful and accurate over time, little efficiency was gained, and transferability was limited. Towards the end of our previous project we compared our custom detector of livestock enclosures with two common CNNs: AlexNet and VGG-f (see Reference [54]). The results were exciting and sobering at the same time. While our custom detector, hand-crafted over four years, performed best, the CNNs performed nearly as well after having been adapted to our case study within just a few weeks [34,35]. Thus, in terms of efficiency, common pre-trained neural networks clearly outperformed our custom algorithm. This—to our knowledge—first application of CNN-based deep learning approaches to archaeological object detection in remotely sensed data showed the great potential of transfer learning for archaeology, but also the necessity of a large training dataset.

In the present study, we are building on this experience and enhance the deep learning approach with a complementary citizen science approach, integrating them in an iterative workflow that yields benefits for both. In our Veluwe project, deep learning-based automated object detection already works, although there is clearly room for improvement [50]. Citizen science-based data collection and validation has been tested successfully and is likely to contribute to the project soon. A challenge here will be the retention of citizen researcher engagement during the project. Research has shown that regular feedback and support are necessary factors contributing to the success of long-term citizen science projects [94,95]. This will be true for the online desktop-based survey (Heritage Quest [100] on the Zooniverse), but will perhaps be even more critical for the dedicated fieldwork teams. As the recognition of archaeological objects is dependent on experience as well as training, the quality of the field inspections will be affected by the long-term engagement of the citizen researchers. In this respect, we will team up with national volunteer organizations such as the *Archeologische Werkgroep Nederland* (AWN) to provide training and information to prospective citizen researchers involved in fieldwork.

## 5. Conclusions

We have proposed an innovative integrated approach for archaeological object detection that draws on recent developments and own experiences in remote sensing, machine learning, and citizen science (Figure 6). This workflow is currently being employed in a long-standing investigation of the archaeological landscape of the Veluwe in the central Netherlands (Figure 2). In this case study, a key element of the integrated approach is a deep learning-based object detection workflow called WODAN [50], to our knowledge, the first functional multi-class detector of archaeological objects in remotely sensed data. In order to validate objects detected by WODAN and to add additional detections, we involve citizen researchers in different stages of the project, both through an online

survey of remotely sensed data (Heritage Quest [100]), and through dedicated fieldwork. These field observations are then fed back into the training dataset of WODAN, which in turn produces more accurate object detections for the next validation step. Over time, this iterative process will lead to a reliable database of validated archaeological objects of recurrent, pervasive classes, providing an excellent basis for archaeological research, heritage management and regional historiography.

At the same time, and beyond the scope of our Veluwe project, this database constitutes a growing dataset of labeled archaeological objects that is much needed to train machine learning-based approaches to archaeological object detection in this project and elsewhere [111]. The three recurrent archaeological object classes currently targeted, namely barrows, Celtic fields, and charcoal kilns, are present in other parts of Europe as well. For example barrows/burial mounds and—functionally different but morphologically similar—other earthen mounds are even a constitutive element of the archaeological record of many regions of the world (e.g., [37,44,115]) and are probably one of the most pervasive archaeological object classes worldwide. Combining training data from different projects is likely to enhance the performance and transferability of multiple detection algorithms that are currently under development in different contexts across Europe and beyond. While this research has so far been mainly driven by archaeologists and data scientists, our integrated workflow shows the crucial role that citizen researchers can play in this research endeavour.

**Author Contributions:** Conceptualization, K.L., W.B.V.-v.d.V. and Q.P.J.B.; formal analysis, W.B.V.V.; funding acquisition, K.L. and Q.P.J.B.; investigation, K.L., W.B.V.-v.d.V. and Q.P.J.B.; methodology, K.L., W.B.V.-v.d.V. and Q.P.J.B.; project administration, K.L. and Q.P.J.B.; resources, Q.P.J.B.; Software, W.B.V.-v.d.V.; visualization, W.B.V.-v.d.V. and Q.P.J.B.; writing—original draft, K.L., W.B.V.-v.d.V. and Q.P.J.B.; writing—review & editing, K.L., W.B.V.-v.d.V. and Q.P.J.B.

**Funding:** This research was partially funded by The Data Science Research Programme of Leiden University, The Netherlands Organisation for Scientific Research (NWO, project nr. 275-60-008), Lorentz Center (grant nr. 17071), Erfgoed Gelderland and the Province of Gelderland.

**Acknowledgments:** The workflow proposed in this paper was developed based on discussions at a workshop held in July 2018 at the Lorentz Center, Leiden University (<http://www.lorentzcenter.nl/lc/web/2018/1027/info.php?wsid=1027&venue=Snellius>), which brought together the different interest groups mentioned in Figure 6. We thank the Lorentz Center team and Dave Cowley, our co-host, for their help in organizing this workshop, and all participants for their valuable contributions. We are also grateful to Eva Kaptijn and Roel Kramer at *Erfgoed Gelderland*, and Sigrid van Rooode at *Provincie Gelderland* for their collaboration in developing and implementing the citizen science elements of our project.

**Conflicts of Interest:** The authors declare no conflict of interest.

## References

1. Bennett, R.; Cowley, C.; De Laet, V. The data explosion: Tackling the taboo of automatic feature recognition in airborne survey data. *Antiquity* **2014**, *88*, 896–905. [CrossRef]
2. Bevan, A. The data deluge. *Antiquity* **2015**, *89*, 1473–1484. [CrossRef]
3. Cowley, D. *Remote Sensing for Archaeological Heritage Management*; Europae Archaeologia Consilium: Brussels, Belgium, 2011; ISBN 9789639911208.
4. Banaszek, .; Cowley, D.C.; Middleton, M. Towards national archaeological mapping. Assessing source data and methodology—A case study from Scotland. *Geosciences* **2018**, *8*, 272. [CrossRef]
5. Corsi, C.; Slapšak, B.; Vermeulen, F. *Good Practice in Archaeological Diagnostics: Non-invasive Survey of Complex Archaeological Sites*; Springer: Cham, Switzerland, 2013; ISBN 9783319017839.
6. Doneus, M. *Die hinterlassene Landschaft—Prospektion und Interpretation in der Landschaftsarchäologie*; Austrian Academy of Sciences: Vienna, Austria, 2013; ISBN 9783700171973.
7. Sarris, A. *Best Practices of Geoinformatic Technologies for the Mapping of Archaeological Landscapes*; Archaeopress: Oxford, UK, 2015; ISBN 9781784911621.
8. Trinks, I.; Hinterleitner, A.; Neubauer, W.; Nau, E.; Löcker, K.; Wallner, M.; Gabler, M.; Filzwieser, R.; Wilding, J.; Schiel, H.; et al. Large-area high-resolution ground-penetrating radar measurements for archaeological prospect. *Archaeol. Prospect.* **2018**, *25*, 171–195. [CrossRef]

9. Musson, C.; Palmer, R.; Campana, S. *Flights into the Past: Aerial Photography, Photo Interpretation and Mapping for Archaeology*; Aerial Archaeology Research Group and Universitätsbibliothek Heidelberg: Heidelberg, Germany, 2013; ISBN 9783000444791. Available online: <http://nbn-resolving.de/urn:nbn:de:bsz:16-propylaeumdok-20096> (accessed on 26 February 2019).
10. Verhoeven, G.J. Are we there yet? A review and assessment of archaeological passive airborne optical imaging approaches in the light of landscape archaeology. *Geosciences* **2017**, *7*, 86. [CrossRef]
11. Lillesand, T.M.; Kiefer, R.W.; Chipman, J.W. *Remote Sensing and Image Interpretation*, 7th ed.; Wiley: Hoboken, NJ, USA, 2015; ISBN 9781118343289.
12. Richards, J.A. *Remote Sensing Digital Image Analysis*, 5th ed.; Springer: Berlin/Heidelberg, Germany, 2013; ISBN 9783642300615.
13. Jensen, J.R. *Introductory Digital Image Processing: A Remote Sensing Perspective*, 4th ed.; Pearson: Glenview, IL, USA, 2015; ISBN 9780134058160.
14. Chen, G.; Han, J. A survey on object detection in optical remote sensing images. *ISPRS J. Photogramm. Remote Sens.* **2016**, *117*, 11–18. [CrossRef]
15. De Laet, V.; Lambers, K. Archaeological prospecting using high-resolution digital satellite imagery: Recent advances and future prospects—A session held at the Computer Applications and Quantitative Methods in Archaeology (CAA) conference, Williamsburg, USA, March 2009. *AARGnews—Newsl. Aer. Archaeol. Res. Group* **2009**, *39*, 9–17. Available online: <http://nbn-resolving.de/urn:nbn:de:bsz:352-opus-100818> (accessed on 26 February 2019).
16. Brophy, K.; Cowley, D. *From the Air: Understanding Aerial Archaeology*; Tempus: Stroud, UK, 2005; ISBN 9780752431307.
17. Traviglia, A.; Cowley, D.; Lambers, K. Finding common ground: Human and computer vision in archaeological prospection. *AARGnews—Newsl. Aer. Archaeol. Res. Group* **2016**, *53*, 11–24. Available online: <http://hdl.handle.net/1887/43751> (accessed on 1 October 2018).
18. Cowley, D.C. In with the new, out with the old? Auto-extraction for remote sensing archaeology. *Proc. SPIE* **2012**, *8532*, 853206. [CrossRef]
19. Cowley, D.C. What do the patterns mean? Archaeological distributions and bias in survey data. In *Digital Methods and Remote Sensing in Archaeology: Archaeology in the Age of Sensing*; Forte, M., Campana, S., Eds.; Springer: Cham, Switzerland, 2016; pp. 147–170, ISBN 9783319406565.
20. Lambers, K.; Traviglia, A. Automated detection in remote sensing archaeology: A reading list. *AARGnews—Newsl. Aer. Archaeol. Res. Group* **2016**, *53*, 25–29. Available online: <http://hdl.handle.net/1887/43750> (accessed on 26 February 2019).
21. Lambers, K. Airborne and spaceborne remote sensing and digital image analysis in archaeology. In *Digital Georchaology: New Techniques for Interdisciplinary Human-Environmental Research*; Siart, C., Forbriger, M., Bubenzer, O., Eds.; Springer: Cham, Switzerland, 2018; pp. 109–122, ISBN 9783319253145.
22. De Boer, A. Using pattern recognition to search LIDAR data for archaeological sites. In *The World Is in Your Eyes: Proceedings of the XXXIII Computer Applications and Quantitative Methods in Archaeology Conference (March 2005—Tomar, Portugal)*; Figueiredo, A., Velho, G., Eds.; CAAPortugal: Tomar, Portugal, 2007; pp. 245–254, ISBN 97898995313.
23. Kvamme, K.L. An examination of automated archaeological feature recognition in remotely sensed imagery. In *Computational Approaches to Archaeological Spaces*; Bevan, A., Lake, M., Eds.; Left Coast Press: Walnut Creek, CA, USA, 2013; pp. 53–68, ISBN 9781611323467.
24. Kvamme, K.L. Experiments in the automatic detection of archaeological features in remotely sensed data from Great Plains villages, USA. In *CAA2016: Oceans of Data. Proceedings of the 44th Conference on Computer Applications and Quantitative Methods in Archaeology*; Matsumoto, M., Uleberg, E., Eds.; Archaeopress: Oxford, UK, 2018; pp. 173–184, ISBN 9781784917302.
25. Schneider, A.; Takla, M.; Nicolay, A.; Raab, A.; Raab, T. A template-matching approach combining morphometric variables for automated mapping of charcoal kiln sites. *Archaeol. Prospect.* **2015**, *22*, 45–62. [CrossRef]
26. Schuetter, J.; Goel, P.; McCorrison, J.; Park, J.; Senn, M.; Harrower, M. Autodetection of ancient Arabian tombs in high-resolution satellite imagery. *Int. J. Remote Sens.* **2013**, *34*, 6611–6635. [CrossRef]
27. Toumazet, J.; Vautier, F.; Roussel, E.; Dousteysier, B. Automatic detection of complex archaeological grazing structures using airborne laser scanning data. *J. Archaeol. Sci. Rep.* **2017**, *12*, 569–579. [CrossRef]

28. Trier, Ø.D.; Larsen, S.; Solberg, R. Automatic detection of circular structures in high-resolution satellite images of agricultural land. *Archaeol. Prospect.* **2009**, *16*, 1–15. [[CrossRef](#)]
29. Trier, Ø.D.; Zortea, M.; Tønning, C. Automatic detection of mound structures in airborne laser scanning data. *J. Archaeol. Sci. Rep.* **2015**, *2*, 69–79. [[CrossRef](#)]
30. Trier, Ø.D.; Pilø, L.H. Automatic detection of pit structures in airborne laser scanning data. *Archaeol. Prospect.* **2012**, *19*, 103–121. [[CrossRef](#)]
31. D’Orazio, T.; Palumbo, F.; Guaragnella, C. Archaeological trace extraction by a local directional active contour approach. *Pattern Recognit.* **2012**, *45*, 3427–3438. [[CrossRef](#)]
32. D’Orazio, T.; Da Pelo, P.; Marani, R.; Guaragnella, C. Automated extraction of archaeological traces by a modified variance analysis. *Remote Sens.* **2015**, *7*, 3565–3587. [[CrossRef](#)]
33. Riley, M.A. Automated Detection of Prehistoric Conical Burial Mounds from Lidar Bare-Earth Digital Elevation Models. Master’s Thesis, Northwest Missouri State University, Maryville, MO, USA, April 2009.
34. Zingman, I. Semi-Automated Detection of Fragmented Rectangular Structures in High Resolution Remote Sensing Images with Application in Archaeology. Ph.D. Thesis, University of Konstanz, Konstanz, Germany, 7 October 2016. Available online: <http://nbn-resolving.de/urn:nbn:de:bsz:352-0-386546> (accessed on 28 September 2018).
35. Zingman, I.; Saupe, D.; Penatti, O.A.B.; Lambers, K. Detection of fragmented rectangular enclosures in very high resolution remote sensing images. *IEEE Trans. Geosci. Remote Sens.* **2016**, *54*, 4580–4593. [[CrossRef](#)]
36. Cerrillo-Cuenca, E. An approach to the automatic surveying of prehistoric barrows through LiDAR. *Quat. Int.* **2017**, *435*, 135–145. [[CrossRef](#)]
37. Davis, D.S.; Sanger, M.C.; Lipo, C.P. Automated mound detection using lidar and object-based image analysis in Beaufort County, South Carolina. *Southeast. Archaeol.* **2018**, *38*, 23–37. [[CrossRef](#)]
38. De Guio, A.; Magnini, L.; Bettineschi, C. GeOBIA approaches to remote sensing of fossil landscapes: Two case studies from Northern Italy. In *Across Space and Time: Papers from the 41st Conference on Computer Applications and Quantitative Methods in Archaeology, Perth, Australia, 25–28 March 2013*; Traviglia, A., Ed.; Amsterdam University Press: Amsterdam, The Netherlands, 2015; pp. 45–53, ISBN 9789089647153.
39. De Laet, V.; Paulissen, E.; Meuleman, K.; Waelkens, M. Effects of image characteristics on the identification and extraction of archaeological features from Ikonos-2 and Quickbird-2 imagery: Case study Sagalassos (southwest Turkey). *Int. J. Remote Sens.* **2009**, *30*, 5655–5668. [[CrossRef](#)]
40. Freeland, T.; Heung, B.; Burley, D.V.; Clark, G.; Knudby, A. Automated feature extraction for prospection and analysis of monumental earthworks from aerial LiDAR in the Kingdom of Tonga. *J. Archaeol. Sci.* **2016**, *69*, 64–74. [[CrossRef](#)]
41. Jahjah, M.; Ulivieri, C. Automatic archaeological feature extraction from satellite VHR images. *Acta Astronaut.* **2010**, *66*, 1302–1310. [[CrossRef](#)]
42. Kramer, I.C. An Archaeological Reaction to the Remote Sensing Data Explosion. Reviewing the Research on Semi-automated Pattern Recognition and Assessing the Potential to Integrate Artificial Intelligence. Master’s Thesis, University of Southampton, Southampton, UK, 2015.
43. Sevara, C.; Pregeßbauer, M.; Doneus, M.; Verhoeven, G.; Trinks, I. Pixel versus object—A comparison of strategies for the semi-automated mapping of archaeological features using airborne laser scanning data. *J. Archaeol. Sci. Rep.* **2016**, *5*, 485–498. [[CrossRef](#)]
44. Caspari, G.; Balz, T.; Gang, L.; Wang, X.; Liao, M. Application of Hough Forests for the detection of grave mounds in high-resolution satellite imagery. *IEEE IGARSS* **2014**, 906–909. [[CrossRef](#)]
45. Guyot, A.; Hubert-Moy, L.; Lorho, T. Detecting Neolithic burial mounds from LiDAR-derived elevation data using a multi-scale approach and machine learning techniques. *Remote Sens.* **2018**, *10*, 225. [[CrossRef](#)]
46. Menze, B.H.; Ur, J.A.; Sherratt, A.G. Detection of ancient settlement mounds: Archaeological survey based on the SRTM terrain model. *Photogramm. Eng. Remote Sens.* **2006**, *72*, 321–327. [[CrossRef](#)]
47. Menze, B.H.; Ur, J.A. Mapping patterns of long-term settlement in Northern Mesopotamia at a large scale. *Proc. Natl. Acad. Sci. USA* **2012**, *109*, 778–787. [[CrossRef](#)]
48. Trier, Ø.D.; Cowley, D.C.; Waldeland, A.U. Using deep neural networks on airborne laser scanning data: Results from a case study of semi-automatic mapping of archaeological topography on Arran, Scotland. *Archaeol. Prospect.* **2018**, 1–11. [[CrossRef](#)]

49. Trier, Ø.D.; Salberg, A.-B.; Pilø, L.H. Semi-automatic mapping of charcoal kilns from airborne laser scanning data using deep learning. In *CAA2016: Oceans of Data. Proceedings of the 44th Conference on Computer Applications and Quantitative Methods in Archaeology*; Matsumoto, M., Uleberg, E., Eds.; Archaeopress: Oxford, UK, 2018; pp. 219–231, ISBN 9781784917302.
50. Verschoof-van der Vaart, W.B.; Lambers, K. Learning to look at LiDAR. The use of R-CNN in the automated detection of archaeological objects in LiDAR data from The Netherlands. *J. Comput. Appl. Archaeol.* **2019**, *2*, 31–40. [[CrossRef](#)]
51. Ball, J.E.; Anderson, D.T.; Chan, C.S. Comprehensive survey of deep learning in remote sensing: Theories, tools, and challenges for the community. *J. Appl. Remote Sens.* **2017**, *11*, 042609. [[CrossRef](#)]
52. Goodfellow, I.; Bengio, Y.; Courville, A. *Deep Learning*; MIT: Cambridge, MA, USA, 2016; ISBN 9780262035613.
53. Krizhevsky, A.; Sutskever, I.; Hinton, G.E. ImageNet classification with deep convolutional neural networks. *Adv. Neural Inf. Process. Syst.* **2012**, *25*, 1106–1114. [[CrossRef](#)]
54. Guo, Y.; Liu, Y.; Oerlemans, A.; Lao, S.; Wu, S.; Lew, M.S. Deep learning for visual understanding: A review. *Neurocomputing* **2016**, *187*, 27–48. [[CrossRef](#)]
55. Castelvechi, D. Can we open the black box of AI? *Nature* **2016**, *538*, 20–23. [[CrossRef](#)] [[PubMed](#)]
56. Shoham, Y.; Perrault, R.; Brynjolfsson, E.; Clark, J. *Artificial Intelligence Index—2017 Annual Report*. 2017. Available online: <http://cdn.aiindex.org/2017-report.pdf> (accessed on 28 September 2018).
57. Razavian, A.S.; Azizpour, H.; Sullivan, J.; Carlsson, S. CNN features off-the-shelf: An astounding baseline for recognition. *IEEE CVPRW* **2014**, 806–813. [[CrossRef](#)]
58. Hohl, S. *Neural Network Based Image Classification in the Context of Archaeology*. Master's Thesis, Hochschule für Technik und Wirtschaft Berlin, Berlin, Germany, 29 March 2016.
59. Berendsen, H.J.A. *De Vorming van het Land. Inleiding in de Geologie en de Geomorfologie*, 4th ed.; Koninklijke van Gorcum: Assen, The Netherlands, 2004; ISBN 9023240758.
60. Doorenbosch, M. *Ancestral Heaths. Reconstructing the Barrow Landscape in the Central and Southern Netherlands*, 2nd ed.; Sidestone Press: Leiden, The Netherlands, 2013; ISBN 9789088901928.
61. Bleumink, H.; Neeffes, J. *Kroondomein het Loo*; Matrijs: Utrecht, The Netherlands, 2010; ISBN 9789053454138.
62. Kenzler, H.; Lambers, K. Challenges and perspectives of woodland archaeology across Europe. In *Concepts, Methods and Tools. Proceedings of the 42nd Annual Conference on Computer Applications and Quantitative Methods in Archaeology*; Giligny, F., Djindjian, F., Costa, L., Moscati, P., Robert, S., Eds.; Archaeopress: Oxford, UK, 2015; pp. 73–80, ISBN 9781784911003.
63. PDOK. Available online: <https://www.pdok.nl/> (accessed on 22 February 2019).
64. Fontijn, D.R.; Bourgeois, Q.P.J.; Louwen, A. *Iron Age Echoes. Prehistoric Land Management and the Creation of a Funerary Landscape—The “Twin Barrows” at the Echoput in Apeldoorn*; Sidestone Press: Leiden, The Netherlands, 2012; ISBN 9789088900730.
65. Louwen, A.; Fontijn, D.R. *Death Revisited. The Excavation of Three Bronze Age Barrows and Surrounding Landscape at Apeldoorn-Wieselseweg*; Sidestone Press: Leiden, The Netherlands, 2019; in press; ISBN 9789088905803.
66. Amkreutz, L.; Bourgeois, Q.; Schreurs, J.; Vossen, N. Verstoep op de Veluwe. Speuren naar een immens ritueel landschap uit de prehistorie. *Archeol. Mag.* **2017**, *1*, 16–20. Available online: [https://www.academia.edu/31941676/Verstoep\\_op\\_de\\_Veluwe\\_Speuren\\_naar\\_een\\_immens\\_ritueel\\_landschap\\_uit\\_de\\_prehistorie?auto=download](https://www.academia.edu/31941676/Verstoep_op_de_Veluwe_Speuren_naar_een_immens_ritueel_landschap_uit_de_prehistorie?auto=download) (accessed on 27 February 2019).
67. Arnoldussen, S. The fields that outlived the Celts: The use-histories of later prehistoric field systems (Celtic Fields or Raattakkers) in The Netherlands. *Proc. Prehist. Soc.* **2018**, *84*, 303–327. [[CrossRef](#)]
68. Vletter, W.F.; van Lanen, R.J. Finding vanished routes: Applying a multi-modelling approach on lost route and path networks in the Veluwe region, The Netherlands. *Rural Landsc. Soc. Environ. Hist.* **2018**, *5*, 1–19. [[CrossRef](#)]
69. Bourgeois, Q. *Monuments on the Horizon: The Formation of the Barrow Landscape throughout the 3rd and 2nd Millennium BC*; Sidestone Press: Leiden, The Netherlands, 2013; ISBN 9789088901041.
70. Lauwerier, R.C.G.M.; Eerden, M.C.; Groenewoudt, B.J.; Lascaris, M.A.; Rensink, E.; Smit, B.I.; Speleers, B.P.; van Doesburg, J. (Eds.) *Knowledge for Informed Choices. Tools for More Effective and Efficient Selection of Valuable Archaeology in The Netherlands*; Nederlandse Archeologische Rapporten 55; Cultural Heritage Agency of The Netherlands: Amersfoort, The Netherlands, 2017; ISBN 9789057992773.

71. Lambers, L.; Fassbinder, J.W.E.; Lambers, K.; Bourgeois, Q. The Iron-Age burial mounds of Epe-Niersen, The Netherlands: Results from magnetometry in the range of  $\pm 1.0$  nT. In Proceedings of the 12th International Conference of Archaeological Prospection, Bradford, UK, 12–16 September 2017; Jennings, B., Gaffney, C., Sparrow, T., Gaffney, S., Eds.; Archaeopress: Oxford, UK, 2017; pp. 132–134, ISBN 978 1784916770.
72. Crutchley, S.; Crow, P. *Using Airborne Lidar in Archaeological Survey: The Light Fantastic*, 2nd ed.; Historic England: Swindon, UK, 2018. Available online: <https://historicengland.org.uk/images-books/publications/using-airborne-lidar-in-archaeological-survey/> (accessed on 5 September 2018).
73. Actueel Hoogtebestand Nederland (AHN). Available online: <https://ahn.arcgisonline.nl/ahnviewer/> (accessed on 22 February 2019).
74. Hesse, R. LiDAR-derived Local Relief Models—A new tool for archaeological prospection. *Archaeol. Prospect.* **2010**, *17*, 67–72. [CrossRef]
75. Relief Visualisation Toolbox (RVT). Available online: <https://iaps.zrc-sazu.si/en/rvt#v> (accessed on 26 October 2018).
76. Kokalj, Ž.; Hesse, R. *Airborne Laser Scanning Raster Data Visualization: A Guide to Good Practice*; Založba ZRC: Ljubljana, Slovenia, 2017; ISBN 9789612549848.
77. QGIS Geographic Information System. Available online: <https://qgis.org> (accessed on 14 February 2019).
78. Archeologisch Informatie Systeem (ArchIS). Available online: <https://archis.cultureelerfgoed.nl/#/login> (accessed on 13 November 2018).
79. Archeologisch Monumenten Register (AMR). Available online: <https://cultureelerfgoed.nl/monumentenregister> (accessed on 13 November 2018).
80. Girshick, R.; Donahue, J.; Darrell, T.; Malik, J. Rich feature hierarchies for accurate object detection and semantic segmentation. *IEEE CVPR* **2014**, 580–587. [CrossRef]
81. Uijlings, J.R.R.; van de Sande, K.E.A.; Gevers, T.; Smeulders, A.W.M. Selective search for object recognition. *Int. J. Comput. Vis.* **2013**, *104*, 154–171. [CrossRef]
82. Girshick, R. Fast R-CNN. *IEEE ICCV* **2015**. [CrossRef]
83. Ren, S.; He, K.; Girshick, R.; Sun, J. Faster R-CNN: Towards real-time object detection with regional proposal networks. *IEEE TPAMI* **2017**, *39*, 1137–1149. [CrossRef] [PubMed]
84. Quintus, S.; Day, S.S.; Smith, N.J. The efficacy and analytical importance of manual feature extraction using lidar datasets. *Adv. Archaeol. Pract.* **2017**, *5*, 351–364. [CrossRef]
85. Sadr, K. The impact of coder reliability on reconstructing archaeological settlement patterns from satellite imagery: A case study from South Africa. *Archaeol. Prospect.* **2016**, *23*, 45–54. [CrossRef]
86. Curtis, V. *Online Citizen Science and the Widening of Academia: Distributed Engagement with Research and Knowledge Production*; Palgrave Macmillan: Cham, Switzerland, 2018; ISBN 9783319776637.
87. Eitzel, M.V.; Cappadonna, J.L.; Santos-Lang, C.; Duerr, R.E.; Virapongse, A.; West, S.E.; Kyba, C.C.M.; Bowser, A.; Cooper, C.B.; Sforzi, A.; et al. Citizen science terminology matters: Exploring key terms. *Citiz. Sci. Theory Pract.* **2017**, *2*, 1–20. [CrossRef]
88. Van den Dries, M. Community archaeology in The Netherlands. *J. Community Archaeol. Herit.* **2014**, *1*, 68–88. [CrossRef]
89. Smith, M.L. Citizen science in archaeology. *Am. Antiq.* **2014**, *79*, 749–762. [CrossRef]
90. GlobalXplorer. Available online: <https://www.globalexplorer.org/> (accessed on 22 February 2019).
91. FossilFinder. Available online: <http://fossilfinder.org/> (accessed on 22 February 2019).
92. Lin, A.Y.-M.; Huynh, A.; Lanckriet, G.; Barrington, L. Crowdsourcing the unknown: The satellite search for Genghis Khan. *PLoS ONE* **2014**, *9*, e114046. [CrossRef] [PubMed]
93. Duckers, G.L. Bridging the “geospatial divide” in archaeology: Community based interpretation of LiDAR data. *Internet Archaeol.* **2013**, *35*. [CrossRef]
94. West, S.; Pateman, R. Recruiting and retaining participants in citizen science: What can be learned from the volunteering literature? *Citiz. Sci. Theory Pract.* **2016**, *1*, 15. [CrossRef]
95. Wald, D.M.; Longo, J.; Dobell, A.R. Design principles for engaging and retaining virtual citizen scientists. *Conserv. Biol.* **2016**, *30*, 562–570. [CrossRef]
96. Conrad, C.C.; Hilchey, K.G. A review of citizen science and community-based environmental monitoring: Issues and opportunities. *Environ. Monit. Assess.* **2011**, *176*, 273–291. [CrossRef]

97. Lintott, C.J.; Schawinski, K.; Slosar, A.; Land, K.; Bamford, S.; Thomas, D.; Raddick, M.J.; Nichol, R.C.; Szalay, A.; Andreescu, D.; et al. Galaxy Zoo: Morphologies derived from visual inspection of galaxies from the Sloan Digital Sky Survey. *Mon. Not. R. Astron. Soc.* **2008**, *389*, 1179–1189. [CrossRef]
98. Hulst, R.S. *Het Romeins Marskamp bij Ermelo*; Matrijs: Utrecht, The Netherlands, 2007; ISBN 9789053453315.
99. The Zooniverse. Available online: <https://www.zooniverse.org/> (accessed on 25 February 2019).
100. Heritage Quest. Available online: <https://www.zooniverse.org/projects/evakap/heritage-quest> (accessed on 25 February 2019).
101. Lyman, R.L.; Van Pool, T.L. Metric data in archaeology: A study of intra-analyst and inter-analyst variation. *Am. Antiq.* **2009**, *74*, 485–504. [CrossRef]
102. Protocol 4003, Field Survey IVO (Soil). Available online: [https://www.sikb.nl/doc/BRL4000/Protocol%204003%20Inventariserend%20VeldOnderzoek-lb%204\\_1.pdf](https://www.sikb.nl/doc/BRL4000/Protocol%204003%20Inventariserend%20VeldOnderzoek-lb%204_1.pdf) (accessed on 19 February 2019).
103. Casana, J. Regional-scale archaeological remote sensing in the age of big data: Automated site discovery vs. brute force methods. *Adv. Archaeol. Pract.* **2014**, *2*, 222–233. [CrossRef]
104. Hesse, R. The changing picture of archaeological landscapes: Lidar prospection over very large areas as part of a cultural heritage strategy. In *Interpreting Archaeological Topography: 3D Data, Visualisation and Observation*; Opitz, R.S., Cowley, D.C., Eds.; Oxbow: Oxford, UK, 2013; pp. 171–183, ISBN 9781842175163.
105. Risbøl, O. Cultivating the ‘wilderness’—How lidar can improve archaeological landscape understanding. In *Interpreting Archaeological Topography: 3D Data, Visualisation and Observation*; Opitz, R.S., Cowley, D.C., Eds.; Oxbow: Oxford, UK, 2013; pp. 51–62, ISBN 9781842175163.
106. ImageNet Large Scale Visual Recognition Challenge (ILSVRC). Available online: <http://www.image-net.org/challenges/LSVRC/> (accessed on 26 February 2019).
107. Sullivan, D.P.; Winsnes, C.F.; Åkesson, L.; Hjelmare, M.; Wiking, M.; Schutten, R.; Campbell, L.; Leifsson, H.; Rhodes, S.; Nordgren, A.; et al. Deep learning is combined with massive-scale citizen science to improve large-scale image classification. *Nat. Biotechnol.* **2018**, *36*, 820–828. [CrossRef]
108. Keshavan, A.; Yeatman, J.; Rokem, A. *Combining Citizen Science and Deep Learning to Amplify Expertise in Neuroimaging*. 2018. Available online: <https://www.biorxiv.org/content/early/2018/07/06/363382.full.pdf> (accessed on 26 February 2019).
109. Willi, M.; Pitman, R.T.; Cardoso, A.W.; Locke, C.; Swanson, A.; Boyer, A.; Veldthuis, M.; Fortson, L. Identifying animal species in camera trap images using deep learning and citizen science. *Methods Ecol. Evol.* **2019**, *10*, 80–91. [CrossRef]
110. Kermit, M.; Reksten, J.H.; Trier, Ø.D. Towards a national infrastructure for semi-automatic mapping of cultural heritage in Norway. In *CAA2016: Oceans of Data. Proceedings of the 44th Conference on Computer Applications and Quantitative Methods in Archaeology*; Matsumoto, M., Uleberg, E., Eds.; Archaeopress: Oxford, UK, 2018; pp. 159–172, ISBN 9781784917302.
111. Opitz, R.; Herrmann, J. Recent trends and long-standing problems in archaeological remote sensing. *J. Comput. Appl. Archaeol.* **2018**, *1*, 19–41. [CrossRef]
112. Lambers, K. *The Geoglyphs of Palpa, Peru: Documentation, Analysis, and Interpretation*; Linden Soft: Aichwald, Germany, 2006; ISBN 9783929290325.
113. Sauerbier, M. *GIS-Based Management and Analysis of the Geoglyphs in the Palpa Region*; Institute of Geodesy and Photogrammetry, ETH Zurich: Zurich, Switzerland, 2009; ISBN 9783906467856.
114. Lambers, K.; Zingman, I. Towards detection of archaeological objects in high-resolution remotely sensed images: The Silvretta case study. In *Archaeology of the Digital Era, Volume II. e-Papers from the 40th Conference of Computer Applications and Quantitative Methods in Archaeology (CAA), Southampton, 26–30 March 2012*; Earl, G., Sly, T., Chrysanthi, A., Murrieta-Flores, P., Papadopoulos, C., Romanowska, I., Wheatley, D., Eds.; Amsterdam University Press: Amsterdam, The Netherlands, 2013; pp. 781–791, ISBN 9789048527281.
115. Evans, D. Airborne laser scanning as a method for exploring long-term socio-ecological dynamics in Cambodia. *J. Archaeol. Sci.* **2016**, *74*, 164–175. [CrossRef]



© 2019 by the authors. Licensee MDPI, Basel, Switzerland. This article is an open access article distributed under the terms and conditions of the Creative Commons Attribution (CC BY) license (<http://creativecommons.org/licenses/by/4.0/>).



Article

# Towards a Satellite System for Archaeology? Simulation of an Optical Satellite Mission with Ideal Spatial and Temporal Resolution, Illustrated by a Case Study in Scotland

Ciara N. McGrath <sup>1,\*</sup>, Charlie Scott <sup>2</sup>, Dave Cowley <sup>3</sup> and Malcolm Macdonald <sup>1</sup>

<sup>1</sup> Department of Electronic and Electrical Engineering, University of Strathclyde, Royal College Building, 204 George Street, Glasgow G1 1XW, UK; malcolm.macdonald.102@strath.ac.uk

<sup>2</sup> Department of Mechanical and Aerospace Engineering, University of Strathclyde, 75 Montrose Street, Glasgow G1 1XJ, UK; charlie.scott.2016@uni.strath.ac.uk

<sup>3</sup> Historic Environment Scotland, John Sinclair House, 16 Bernard Terrace, Edinburgh EH8 9NX, UK; dave.cowley@hes.scot

\* Correspondence: ciara.mcgrath@strath.ac.uk

Received: 28 August 2020; Accepted: 11 December 2020; Published: 15 December 2020

**Abstract:** Applications of remote sensing data for archaeology rely heavily on repurposed data, which carry inherent limitations in their suitability to help address archaeological questions. Through a case study framed around archaeological imperatives in a Scottish context, this work investigates the potential for existing satellite systems to provide remote sensing data that meet defined specifications for archaeological prospection, considering both spatial and temporal resolution, concluding that the availability of commercial data is currently insufficient. Tasking a commercial constellation of 12 spacecraft to collect images of a 150 km<sup>2</sup> region in Scotland through the month of July 2020 provided 26 images with less than 50% cloud cover. Following an analysis of existing systems, this paper presents a high-level mission architecture for a bespoke satellite system designed from an archaeological specification. This study focuses on orbit design and the number of spacecraft needed to meet the spatial and temporal resolution requirements for archaeological site detection and monitoring in a case study of Scotland, using existing imaging technology. By exploring what an ideal scenario might look like from a satellite mission planning perspective, this paper presents a simulation analysis that foregrounds archaeological imperatives and specifies a satellite constellation design on that basis. High-level design suggests that a system of eight 100 kg spacecraft in a 581 km altitude orbit could provide coverage at a desired temporal and spatial resolution of two-weekly revisit and <1 m ground sampling distance, respectively. The potential for such a system to be more widely applied in regions of similar latitude and climate is discussed.

**Keywords:** archaeological remote sensing; satellite mission design; satellite archaeology; archaeological survey

## 1. Introduction

Significant challenges exist in the application of remote sensing data for archaeological prospection and monitoring at a landscape scale. There is a heavy reliance on re-purposed datasets such as aerial photographs, satellite imagery and airborne laser scanning collected for reasons such as cartography, military intelligence and infrastructure planning. This repurposing of data for archaeological purposes is unsurprising as it is expensive to acquire. However, it also brings limitations because the data acquisition was not specified with archaeological imperatives in mind. This paper is a contribution to the discussion of how heritage applications of satellite data might be developed, seeking to reframe the

common question of an archaeologist repurposing remote sensing data who might ask ‘how can data collected for other purposes be best used to address archaeological questions?’. Rather, the approach taken here is to ask ‘what might a satellite system for archaeology look like?’, specifically for a constellation of optical satellites. This exercise has been attempted to explore what an ideal scenario might be—a simulation analysis that foregrounds archaeological survey questions and specifies a satellite system design on that basis. The analysis is framed within imperatives drawn from a specification for imagery in Scotland, which nevertheless illustrates factors that require consideration in specifying such a system anywhere.

Specifying ‘a satellite for archaeology’ is of course a complex multi-faceted process, but the focus here is primarily on mission architecture, considering the number of spacecraft and appropriate orbit selection to deliver the desired spatial resolution and revisit times. While recognising that platforms, sensors, and workflows, to name but a few, are all fundamental aspects of a specification, these are out of the scope of this paper. By exploring mission architecture as one aspect of the design of satellite systems, this paper aims to provide an understanding of the impacts of these factors that will be informative to all users of satellite data.

This contribution is framed by the widespread leveraging of satellite remote sensing for archaeology (e.g., [1–10])—and that the trajectory for development is witnessing increasing spatial, spectral and temporal resolution, the potential to task data collection, and the proliferation of available data. While this is not yet a panacea for a range of reasons, including costs and, for example, the difficulties in calibrating and integrating different datasets from a range of Earth observation sensors [11], the rate of development is startling. Nevertheless, while recognising this trajectory, the lack of archaeological imperatives in the specification of data acquisition means that there are inherent compromises in primary survey data (see [12] for a comprehensive discussion of these factors for passive optical imaging).

A central issue here is the capacity of remote sensing data to provide systematic and reliable data for archaeological management and research questions. This depends on many factors, not least of which is the ability to specify data acquisitions. Thus, while the capacity to image large areas with sub-metre ground sampling distance (GSD) optical sensors, to revisit regularly, and to specify conditions for acquisitions are all important, this remains largely beyond the reach of archaeology. Rather, archaeologists rely on using what is available in the market (inherently random, usually too expensive), what is possible to collect oneself (limited in coverage with inherent user bias), or what is freely available (medium to high spatial resolution or not specified for archaeology). Working with these available datasets, archaeologists have demonstrated that relevant information can be extracted from a range of remotely sensed data, including satellite data, at a variety of spatial and temporal resolutions for prospection, condition monitoring and land-use change [6,7]. This, correspondingly begs the questions: ‘what could be achieved with an ideal, bespoke remote sensing system?’ and ‘what would this ideal system comprise?’.

The analysis presented below attempts to explore the parameters for a constellation of optical satellites against this background, using Scotland as a case study area to define the mission requirements. The design primarily focuses on the number of spacecraft and orbits required to provide the necessary temporal and spatial resolution. This design is presented not so much in the expectation that a satellite system for archaeology will be launched, but, by outlining the high-level features of such an ideal system, to contribute to the further development of this data source for the discipline.

## 2. Scope: Specifying a Satellite for Archaeology

In considering the question of what a satellite for archaeology might look like, a scope has been defined for a specific form of archaeological prospection. This is used as a device to help consider the relationships between archaeological imperatives and satellite system design, recognising that, even with a theoretical question, an element of feasibility is required and that a ‘do everything’ approach would over-complicate the issues. As such, sensors, platforms, and data processing and

interpretation workflows remain out of scope for the paper, without wishing to underplay their importance. Instead, by focusing on the orbital mechanics of the system, this work presents a mission architecture that could meet the spatial and temporal resolution requirements for archaeological prospection with existing imaging technology.

At a high level, the scope is defined with the need to cover the whole of Scotland (c. 80,000 km<sup>2</sup>), with regular revisit periods and GSD of <1 m in multi-spectral data. Such data could be expected to inform a range of activities, including archaeological prospection, condition monitoring, and landscape-scale change detection. The required GSD is specified at <1 m to enable clear identification of archaeological features at a scale of 1 m and smaller, where a higher GSD would result in insufficient spatial resolving power to do so (Figure 1). A core objective is to contribute to the creation of systematic national data [13,14], and because of this aspiration to deal with very large areas, solutions like UAVs or localised survey methods do not provide the necessary data coverage. Within this general framework, a specific aspect of scope focusses on those otherwise buried archaeological remains that are expressed through crop proxies. The emergence of cropmarking is dependent on climatic conditions, soil properties and land-use patterns which introduce considerable variation in the timing and potential for formation [15]. These factors necessitate regular revisit periods, as crop development across even relatively small areas is not uniform through the summer and is thus time critical. Crop proxies are used for archaeological prospection across the European continent and Scotland is selected as a study region with the understanding that the presented method of space system architecture design could be applied to other regions. It should be noted, however, that the latitude, prevailing weather and timing of the crop season in the region of interest will impact the solution obtained.

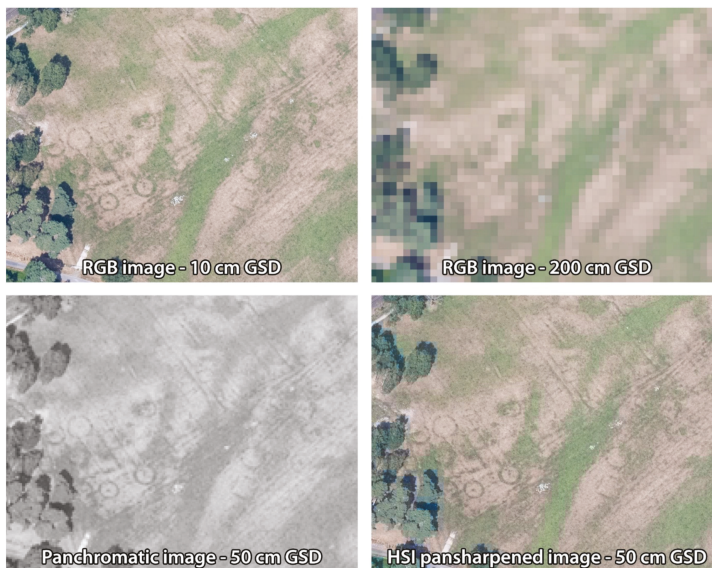


**Figure 1.** Many archaeological sites in Scotland, and indeed elsewhere in Europe, are composed of relatively small discrete features, as this example of an early medieval cemetery at Croftgowan in Highland illustrates. The discrete features that make up the site are characterised by ditches often <1 m across and small burial pits. The scale of expected features requires a GSD of <1 m to enable clear identification of archaeological features. Graphic: Geert Verhoeven; Source image DP281499 © Historic Environment Scotland.

In Scotland, the distributions of soils that are conducive to cropmark formation and appropriate land use (mainly arable crops, but in extreme droughts also pasture) are largely in the east and south

of the country (Figure 2), so this represents a specific area of interest. Archaeological prospection in these areas is currently dependent on a light aircraft-based observer-directed survey, informed by broad-brush soil moisture deficit data as a proxy for areas of likely crop stress. On this basis, prospection is undertaken relying on visual identification of cropmarking and selective imaging, in an approach that is recognised as introducing significant bias in what is observed and recorded [16–19]. This ‘cropmark survey’ then is a central focus for the specification of our satellite for archaeology, alongside monitoring of designated archaeological sites for which multi-temporal high-resolution imaging is required. This specification is discussed in further detail below.

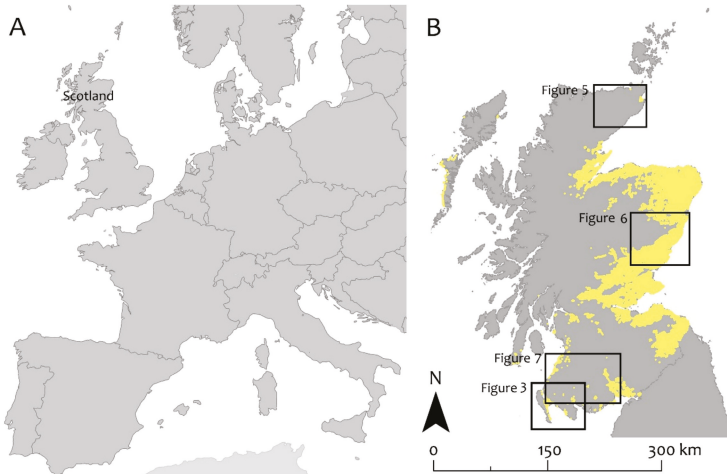


**Figure 2.** (A) The location of the study area in north-west Europe. (B) Map of Scotland, with yellow tone indicating the generalised extent of arable ground, which is a specific focus of interest for repeat imaging. The locations of Figures 3, 5, 6 and 7 are shown, referring to issues discussed below.

Using the priorities defined above, the following engineering specification was generated for a satellite system for archaeology:

- Coverage must extend to all of Scotland;
- For eastern and southern Scotland (Figure 2) the maximum revisit time should be three weeks, with a two-week revisit interval desirable, to ensure cropmark formation, which is time variant, can be captured;
- A GSD of <1 m is required, with 0.5 m desirable, in recognition of the scale of anticipated features;
- Imagery should be multi-spectral (including at least Red, Green, Blue and Near-Infra-Red bands);
- The system must operate for a minimum of five years, to allow for observations during both wet and dry years;
- Usability in regions of similar climate/land environment is desirable.

Based on the engineering specification, some high-level system requirements are identified that will constrain the space system design. Firstly, the requirement to provide a GSD of <1 m requires a low-Earth orbiting (LEO) spacecraft, as spacecraft in low altitude orbits will produce lower GSD data. LEO spacecraft are generally defined as having mean orbit altitudes of 300–1000 km and will orbit the Earth with a period of approximately 90 min. Geosynchronous and geostationary spacecraft have an orbit period that is the same as the Earth’s speed of rotation about its axis, allowing for continuous observations over a given longitude. However, these spacecraft operate at approximately 36,000 km altitude, and hence would be unable to provide the GSD required. Furthermore, an imager with a low GSD will generally have a small field of view, meaning that it may be necessary to use a constellation

of spacecraft to achieve the desired revisit times. A greater number of spacecraft would tend to imply a higher cost system, and so the space system design discussed below will attempt to reduce costs by employing the minimum number of spacecraft. However, space system cost depends on a range of factors and is challenging to estimate due to the limited public availability of past mission costs. As such, any cost estimates will be subject to significant uncertainties.

On the basis of the defined requirements, existing space systems are firstly assessed against the specification (Section 3), which is followed by discussion of a bespoke space system design (Section 4).

### 3. Existing Space Systems

Of the multitude of Earth observing (EO) spacecraft currently in operation (as of 26 June 2020), only a small number can provide the appropriate GSD, multi-spectral imagery necessary for the archaeological purposes outlined in Sections 1 and 2. These systems are summarised in Table 1, where GSD given are the maximum attainable (normally at nadir). In all cases panchromatic multi-spectral images are available at the stated panchromatic spatial resolution. While the listing of eleven systems (Table 1), with often daily revisit intervals, suggests that suitable data should be readily available, this is not the case. Firstly, the majority of these systems are commercial; as such, not all data are publicly available, and most of the data are certainly not freely available. Moreover, the revisit rates listed indicate the frequency with which a region of the Earth can be observed, but the actual data collection frequency is much lower. This is because the stated revisit time includes the ability of the spacecraft to slew and point their instrument off-nadir. As such, the revisit time represents the time in which any one region of the Earth could be imaged; it does not represent the time in which imagery of the entire Earth can be collected. As the spacecraft can only point at one location at a time, the limiting factor for the complete imaging of a region is the instrument swath width (i.e., the width of the spacecraft imager field of view on the Earth's surface) and, as noted in Section 2, a lower GSD generally corresponds to a smaller field of view.

For visual imagery, the images must be taken during daytime and at times of limited cloud cover, further compounding these difficulties. For Scotland, the average cloud cover in May, June and July is 70%, though it may be lower on the east coast of the country [20]. Assuming an equal chance of cloud being present at any time, this indicates that only 30% of daytime satellite passes over the region of interest are likely to be useable. These factors highlight the reality behind the headline figures of revisit rates, and the potential difficulties of securing imagery of given locations at specified periods.

Conspicuously absent from Table 1 are the Sentinel-2 spacecraft, part of the EU Copernicus programme, and NASA's Landsat spacecraft, as, in spite of their frequent revisits over Europe (five days for Sentinel-2 A and B combined and eight days for Landsat 7 and 8 combined) and previous use in archaeological prospection and condition monitoring [6,7], they cannot provide the GSD necessary for the purposes outlined in Section 2.

In order to assess the suitability of existing satellite systems for archaeological purposes as defined in the scope (Section 2), an approximately 150 km<sup>2</sup> region in Scotland is examined as a sample site (Figure 3). For each of the eleven systems listed in Table 1, the availability of recent data is assessed for the periods from 1 May 2016 to 31 July 2016 and from 1 May 2018 to 31 July 2018. These periods were selected for the favourable cropmark formation conditions that prevailed during dry and hot summers that encouraged crop stress. For all the apparent likelihood of data availability on the basis of the large number of operational systems, for the sample area there are a total of eight images with <30% cloud cover for these two time periods, many of which provide <100% coverage of the area of interest. The low number of images available is striking, with a concomitant low number of time series of multiple overlapping images. The trends of image acquisition seen here reflect the priorities of most satellite data providers/consumers, with high demand, and hence high acquisition, generally focusing on urban areas. Failing a significant change in the global use of satellite data, such trends are likely to continue across all very high-resolution satellite data providers. Leaving aside the cost of procuring such commercial data (indicative costs for these products range from \$5 to \$50/km<sup>2</sup> [25]), this volume

of imagery is clearly insufficient as a primary source for the routine archaeological survey of the region specified above.

**Table 1.** Selection of existing very-high-resolution multi-spectral satellite imaging systems [21–24].

System	Operator	Multi-Spectral GSD	Panchromatic GSD	Approximate Revisit Time
Worldview-2	MAXAR/DigitalGlobe	1.84 m	0.46 m	1–4 days
Worldview-3	MAXAR/DigitalGlobe	1.24 m	0.31 m	1–4 days
GeoEye-1	MAXAR/DigitalGlobe	1.84 m	0.46 m	3 days
SkySat	Planet	1 m	0.5 m	<1 day
Pleiades-1A + 1B	AIRBUS Defence and Space	2 m	0.5 m	1 day
DMC3-TripleSat-1	DMCii	3.2 m	0.8 m	1 day
DMC3-TripleSat-3	DMCii	3.2 m	0.8 m	1 day
SuperView-1	Beijing Space View Technology	2 m	0.5 m	2 days
KOMPASAT-3	Korea Aerospace Research Institute	2.2 m	0.5 m	1.4 days
Gaofen-2	China National Space Administration	3.2 m	0.8 m	5 days
Deimos-2	UrtheCast	3 m	0.75 m	2 days

Through the European Space Agency Third Party Mission programme, access was granted to data obtained by the SkySat constellation of spacecraft (operated by Planet) to evaluate its use in detection and monitoring of archaeological sites. Through this, a request was made to Planet for one image to be collected of the study area (Figure 3) each week in July 2020 using the SkySat spacecraft. In order to satisfy this request Planet collected multiple images on almost every day in July. During the month of July, 150 images were collected, but only 26 of these have <50% cloud cover; this corresponds to just 17% of images. Furthermore, if the images are to be used for the detection of time varying cropmarking, multiple images collected on the same day are of limited value. While this data volume could be sufficient for the detection of crop proxies in summer, it has required dedicated daily collections from a total of 12 different spacecraft.



**Figure 3.** Stranraer area of interest [26]. Centred on 54° 52'27"N, 4° 58' 76"W; see Figure 2 for location.  
© Planet Labs Inc. 2020.

#### 4. Bespoke Space System Design

The discussion in Section 3 identifies that the ideal requirements for routine archaeological detection and monitoring in Scotland, as defined by the requirements outlined in Section 2, cannot be achieved by using satellite data acquired for general purposes, which is not to negate the potential utility of such data in other contexts (e.g., [1–10]). Tasking a constellation of 12 spacecraft did allow for suitable imagery to be collected of a small region of Scotland, but the competing needs of other customers imply that extending this to provide routine, systematic coverage of the entirety of Scotland would be challenging. This reinforces many of the limitations to the effectiveness of archaeological applications

of satellite data discussed in general terms in Section 1. From that position, a high-level design for a bespoke space system is developed and presented. It should be noted that this design is based on requirements derived for specific archaeological priorities in Scotland. As such, the space system specified may not be ideal for archaeological purposes elsewhere; however, the design methodology presented, and the general insights obtained, could be applied to any region.

4.1. Payload Selection

The key component of any spacecraft system is the payload, which must be selected or designed to meet the mission requirements. The function of the rest of the spacecraft, referred to as the spacecraft bus, is to ensure the successful operation of the payload. The potential variability in the payload, as a key variable in a system, is illustrated in a selection of existing multi-spectral imaging satellite systems with the required GSD (Table 2).

Table 2. Specifications for existing high-resolution satellite systems [21,27–29].

Spacecraft	Multi-Spectral GSD, m	Panchromatic GSD, m	Swath Width, km	Spacecraft Mass, kg	Altitude, km
Worldview-3	1.24	0.31	13.1	2800	617
SkySat 3-13	1	0.72	6.6	110	500
Pleides 1A/1B	2	0.5	20	1015	694
DubaiSat-2	4	1	12	300	600
Spot 6/7	8	2	30	720	694

The spacecraft system properties can be further expressed in the panchromatic GSD of each imager plotted against its swath width and the total mass of the host spacecraft (Figure 4). The mass of the spacecraft is indicative of the mission budget, as the launch cost, which often dominates the mission budget, will rise with increasing mass. In this respect, the SkySat 3-13 design is an attractive option as it offers high-resolution imagery for an extremely low spacecraft mass when compared to other systems. However, the corollary of this is that it has the smallest swath width of all the imagers considered, which will correspond to a longer revisit time as the ground covered on each orbit is concomitantly less.

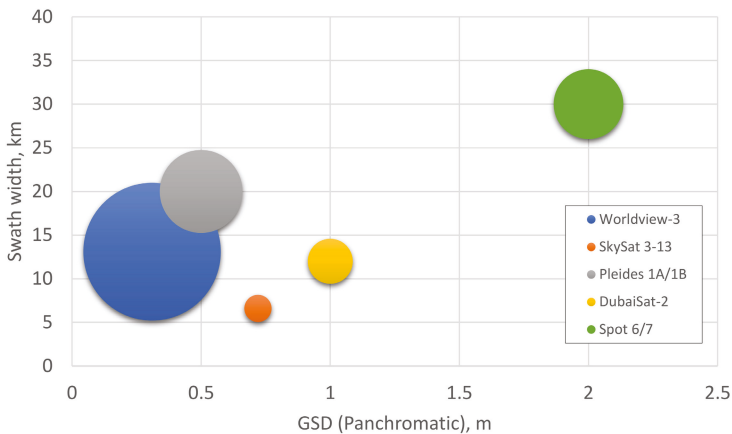


Figure 4. Panchromatic spatial resolution versus swath width for existing high-resolution satellite systems. Bubble size indicates spacecraft mass.

4.2. Orbit Design

The orbit selected for the spacecraft will greatly influence the coverage and revisit capabilities of the system. Using the SkySat parameters defined in Section 4.1 as a baseline, an orbit is selected with

the intent of maximising coverage of Scotland, and an estimation is made of the number of spacecraft required within this orbit to provide the desired revisit times. Circular orbits are assumed to be used due to ease of orbit insertion and operational maintenance.

Altitude is one of the most significant parameters for the orbit design as it will influence the spatial resolution and swath width of the payload instrument; a lower altitude will result in a higher resolution image, but a narrower swath width. Inclination, which describes the angle between the orbit plane and the Earth’s equator, is another critical parameter in orbit design. The inclination is critical for two primary reasons. Firstly, the most northerly and southerly latitude a spacecraft will pass over is defined by the orbit inclination such that the geodetic latitude,  $\delta$ , range of the spacecraft coverage can be defined as, where  $0 \leq \delta \leq \tan^{-1}\left(\frac{\tan i}{1-f(2-f)}\right)$ , where  $i$  is the orbit inclination in degrees and  $f$  is the Earth flattening factor to allow for conversion from geocentric to geodetic latitude [30]. It should be noted that depending on the swath width of the imager and the pointing capabilities of the spacecraft, it may be possible to view latitudes beyond this range. Secondly, spacecraft will have the shortest revisit period over regions at the most northerly and southerly viewable latitudes. The revisit time will generally increase as the latitude of the location of interest approaches the equator. The SkySat spacecraft operate in sun-synchronous orbits. A sun-synchronous orbit is a near-polar orbit where the average rate of nodal precession (i.e., the rate at which the spacecraft orbit rotates around the Earth’s axis of rotation) is the same as the Earth’s average rate of orbit around the sun. This synchronicity means that the relative time of day along the satellite’s ground track remains approximately the same for each orbit pass. This is especially useful for Earth observing satellites as it ensures consistent lighting conditions each time a region is observed. Furthermore, as a near-polar orbit it allows for the entirety of the Earth to be observed. However, sun-synchronous orbits generally have an inclination of  $96 \text{ deg} < i < 99 \text{ deg}$ , depending on the orbit altitude, and hence provide maximum coverage in the region of  $81 \text{ deg} < \delta < 84 \text{ deg}$ .

In order to estimate the revisit time for a satellite in a sun-synchronous orbit over the entirety of Scotland, the time to provide full coverage of the lowest latitude of interest is calculated, assuming no overlaps between passes. The southernmost point of Scotland is the Mull of Galloway, with a latitude of approximately 54.63 deg. The circumference of the circle defined by a given line of latitude,  $c_\delta$ , can be estimated as [31]

$$c_\delta = 2 \pi \frac{R_\oplus}{\sqrt{1 - \sin \delta [(1 - f)^2 - 1]}} \cos \delta \tag{1}$$

where  $R_\oplus$  is the Earth equatorial radius, taken as 6378 km,  $f$  is the Earth flattening factor and  $\delta$  is the geodetic latitude of interest. The circumference of the Earth at 54.63 deg latitude is hence estimated as 23135 km, assuming a flattening factor  $f$  of  $3.3528 \times 10^{-3}$  as given by the World Geodetic System 1984 [32].

The width of a latitude band covered by an inclined spacecraft in a single pass,  $W$ , with a swath width,  $s$ , will depend on the direction of motion of the spacecraft relative to the line of latitude at nadir. At the equator, the relative angle between the spacecraft direction of motion and that of the line of latitude,  $\beta$ , will be  $\beta = i$ , where  $i$  is the orbit inclination, while at a latitude  $\delta = i$ , there will be  $\beta = 0$ . This angle  $\beta$  can be calculated [33] as

$$\beta = \tan^{-1} \left( \frac{\sqrt{\sin^2 i - \sin^2 \delta}}{\cos i - \omega \cos^2 \delta} \right) \tag{2}$$

where  $\omega$  is the rotational rate of the Earth, taken as  $7.2921 \times 10^{-5}$  rad/s. The width of the latitude band covered in a single pass is then

$$W = \frac{s}{\sin \beta}. \tag{3}$$

It should be noted that as the latitude of interest,  $\delta$ , approaches the orbit inclination,  $i$ , the width covered will tend to infinite; as such the above approximation is not valid at latitudes close to  $i$ . For a swath width of 6.6 km, and a spacecraft inclined at 97 deg, this gives a width covered,  $W$ , at 54.63 deg latitude of 6.8 km, meaning 3417 passes would be required for full coverage at 54.63 deg latitude, assuming no overlap between passes.

The orbit period,  $T$ , of a spacecraft in a circular orbit is

$$T = 2\pi \sqrt{\frac{(R_E + h)^3}{\mu}} \quad (4)$$

where  $h$  is the orbit altitude,  $R_E$  is the mean Earth radius, taken as 6371 km, and  $\mu$  is the standard gravitational parameter of the Earth, taken as  $3.986 \times 10^5 \text{ m}^3/\text{s}^2$ . A spacecraft at an altitude of 500 km would have an orbit period of 94.47 min and therefore would require approximately 224 days to achieve 3417 passes; this gives a revisit time of approximately 224 days at 54.63 deg latitude. Assuming spacecraft could be distributed to provide no overlap in coverage, 16 spacecraft would hence be required to meet the desired revisit criteria of two weeks.

In order to minimise the revisit time of a spacecraft over a region, an inclination can be selected that is greater than, but close to, the most northerly latitude of interest. For Scotland, this is approximately 60 deg. For an orbit inclined at 60 deg, the width covered by a spacecraft with a swath of 6.6 km in a single pass at 54.63 deg increases to 13.1 km, as calculated using Equations (2) and (3), meaning 1761 passes are required to cover the full Earth's circumference at 54.63 deg latitude. This would take 116 days for a single spacecraft, using the orbit period calculated with Equation (4), and so nine spacecraft could meet the two-week requirement—a significant improvement in comparison to the sun-synchronous case.

Increasing the spacecraft altitude will increase the swath width but decrease the GSD; this provides an opportunity to fine-tune the performance of the space system to, potentially, further reduce the number of spacecraft required. The relationship between GSD, swath width,  $s$ , and spacecraft altitude,  $h$ , can be expressed as

$$\frac{p}{GSD} = \frac{L}{h} = \frac{w}{s} \quad (5)$$

where  $w$  is the sensor width,  $p$  is the photosite pitch and  $L$  is the instrument focal length [34]. Assuming the sensor parameters  $p$ ,  $L$ , and  $w$  remain constant, both the GSD and swath width vary linearly with altitude according to Equation (5). Estimating the GSD and swath width at a given altitude using Equation (5) gives the results shown in Table 3. The number of spacecraft that would be required to provide a two-week revisit of Scotland at each altitude for a 60 deg inclined orbit as calculated using Equations (2)–(4) are also given. Note that the number of spacecraft required is rounded up to the nearest whole and the values should be considered a minimum as eclipse periods, cloud cover, and tasking restrictions may impact the spacecraft performance. The general trend is that a higher altitude gives a reduction in the number of spacecraft required, with diminished returns at greater altitudes. If the upper limit on GSD is taken as 1 m, then the minimum number of spacecraft needed will be seven, at an altitude of <700 km.

**Table 3.** Estimated GSD, swath width, revisit times, and deorbit time as a function of altitude for a spacecraft baselined against the SkySat spacecraft.

Altitude, km	GSD, m	Swath Width, km	Width Covered at 54.63 deg Latitude, km	Time to Full Coverage for One s/c, days	No. of s/c for 2-Week Revisit	Time to Deorbit to 100 km, years
200	0.29	2.6	5.2	270.9	20	0.003
300	0.43	4.0	7.9	184.8	14	0.072
400	0.58	5.3	10.5	141.7	11	0.762
500	0.72	6.6	13.1	115.9	9	4.748
600	0.86	7.9	15.7	98.7	7	21.18
700	1.01	9.2	18.3	86.4	7	74.97
800	1.15	10.6	21.0	77.2	6	224.1
900	1.30	11.9	23.6	70.1	5	588.8
1000	1.44	13.2	26.2	64.4	5	1397.1

Orbit altitude will also directly impact the spacecraft on-orbit lifetime. A spacecraft in low-Earth orbit, that is with an altitude <1000 km, will experience drag due to the Earth’s atmosphere. Over time this will cause the spacecraft altitude to reduce, ultimately resulting in the spacecraft naturally deorbiting. A spacecraft orbit should be sufficiently high to ensure a suitable operational life for the spacecraft prior to deorbit, while also ideally complying with the UN Space Debris Mitigation Guideline to “limit the long-term presence of spacecraft and launch vehicle orbital stages in the low-Earth orbit (LEO) region after the end of their mission” [35]. Generally, this guideline is considered to be met if the spacecraft will naturally deorbit within 25 years of the end of the mission.

Assuming a power law fit to the 1976 standard atmosphere [36], the time for a spacecraft to naturally decay to a certain altitude,  $h_1$ , as a function of time can be defined as [37]

$$t = \frac{m}{C_D A \Lambda \sqrt{\mu R_{\oplus}}} \frac{\left( (h_0 - R_{\oplus})^{1+\gamma} - (h_1 - R_{\oplus})^{1+\gamma} \right)}{1 + \gamma} 1000^{-\gamma} \tag{6}$$

where  $h_0$  is the initial spacecraft altitude,  $C_D$  is the coefficient of drag, taken as 2.2, and  $\gamma$  and  $\Lambda$  are coefficients of the power law taken as 7.201 and  $10^7$ , respectively. For a spacecraft with a mass,  $m$ , of 100 kg and a cross-sectional area,  $A$ , of 1 m<sup>2</sup> (similar to those of SkySat), and with de-orbit assumed to occur at an altitude of 100 km, the time to deorbit from a range of possible orbit altitudes are shown in Table 3. A spacecraft in an orbit of 500 km or lower will deorbit naturally in less than five years, meaning that significant on-board propulsion would be required to maintain the spacecraft altitude and meet the requirement for a minimum operational life of five years. A 600 km orbit seems suitable as it requires the minimum number of spacecraft while still meeting the 25 year natural deorbit requirement and providing <1 m GSD.

#### 4.3. Detailed Constellation Design and Simulation

Based on the coverage estimates made in Section 4.2, a 600 km altitude, 60 deg inclined orbit is selected as a baseline for the constellation. In order to ensure a 14 day revisit over Scotland, a repeating ground-track (RGT) orbit is designed [38]. It is calculated that for a spacecraft in a 60 deg inclined orbit, an altitude of 581.077 km will give a repeat period of 207 orbits in 14 days. At this altitude, the width covered by a single spacecraft pass at 54.63 deg latitude, the lowest latitude of interest, is 15.3 km as calculated using Equations (2) and (3), meaning eight spacecraft would be required for full coverage in 14 days. To ensure an even distribution of coverage, the spacecraft should be organised in a ‘train formation’ such that one edge of the swath of the first spacecraft passing 54.63 deg latitude is aligned exactly with the opposite edge of the swath of the subsequent spacecraft [39]. The time for Earth to

rotate such that the surface at 54.63 deg latitude will move through a distance equal to the width seen by the spacecraft at the latitude of interest,  $W$ , can be estimated as

$$t_{sep} = \frac{2\pi W}{\omega c_\delta} \tag{7}$$

where  $\omega$  is the rotational rate of Earth, and  $c_\delta$  is the circumference of the circle of the latitude of interest. The spacecraft should then be separated through true anomaly (i.e., within the orbit plane) such that a following spacecraft will reach the true anomaly of the previous spacecraft in the time  $t_{sep}$ . This separation can be calculated, in radians, as

$$\theta_{sep} = \frac{2\pi t_{sep}}{T} \tag{8}$$

where  $T$  is the orbit period, as calculated using Equation (4). For spacecraft in a RGT orbit at 581.077 km, this gives a required true anomaly separation between spacecraft of approximately 3.556 deg.

An orbit propagator is used to estimate the coverage that could be expected from a constellation of eight spacecraft in a 581.077 km altitude, 60 deg inclined orbit, with a separation between spacecraft of 3.556 deg through true anomaly. Using Equation (5), the spacecraft are calculated to have a swath width of 7.7 km at 581.077 km altitude and the simulation is carried out for a 30 day period. The propagator uses the Gauss/Lagrange planetary equations [40] to calculate the change in the Keplerian orbit elements of the spacecraft over time.  $J_2$ , which is the perturbation due to an oblate central body, is the only perturbation included [41]. Drag and other forces acting on the satellite are disregarded as they are considered small when compared to the  $J_2$  effect. The satellite ground track and associated coverage is calculated assuming a spherical Earth. The constants and orbit parameters used in this analysis are given in Tables 4 and 5, respectively. The epoch date of 1 June 2020 is arbitrarily chosen for this example study. Sample sections of the north, east and south of Scotland are considered to reduce computational complexity, selected on the basis of the areas of interest (Figure 2 and Table 6).

**Table 4.** Simulation constants.

Parameter	Value	Unit
Gravitational parameter	$3.986 \times 10^{14}$	$\text{m}^3/\text{s}^2$
Mean Earth radius	6371	km
Coefficient of $J_2$ for Earth	0.0010827	-
Angular velocity of Earth	$7.29212 \times 10^{-5}$	rad/s

**Table 5.** Orbital parameters.

Parameter	Value	Unit
Time and date at epoch	00:00 1 June 2020	-
Number of spacecraft	8	-
Mean orbit altitude	581.077	km
Orbit inclination	60	deg
Right ascension of the ascending node (RAAN)	0	deg
True anomaly of lead spacecraft	0	deg
True anomaly spacing between spacecraft	3.556	deg

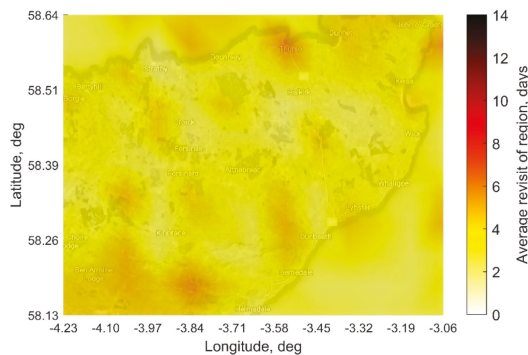
**Table 6.** Selected regions for coverage simulation.

Region	Maximum Latitude, deg	Minimum Latitude, deg	Maximum Longitude, deg	Minimum Longitude, deg	Area, km <sup>2</sup>
North	58.64	58.13	-3.06	-4.23	3832
East	57.15	56.56	-2.10	-3.37	5025
South	55.47	54.90	-3.60	-5.03	5675

The orbit simulation results are summarised in Table 7 and visualised in Figures 5–7. For each region selected, the average time between viewings (the average revisit time across all discrete points in the region) is less than seven days and each discrete point in the regions would be seen an average of 11–22 times, depending on latitude. 100% of the northern region, 99% of the eastern region, and 97% of the southern region are observed with a maximum revisit time of less than 14 days, though it should be noted that cloud cover and lighting conditions would mean that only a portion of the passes would be useable. There are a small number of points with maximum revisit times in excess of 14 days shown as grey regions in Figures 5–7. These points of high maximum revisit are likely a result of inaccuracies in the calculation of the RGT orbit altitude and satellite distribution and could be addressed through precision orbit design. It should also be noted that maintaining the precise RGT orbit altitude and spacecraft distribution would necessitate active orbit maintenance using on-board propulsion.

**Table 7.** Maximum and average coverage of selected regions of Scotland for a constellation of eight spacecraft in a 60 deg inclined RGT orbit.

Region	No. of S/C	Average Revisit, Days	Maximum Revisit, Days	Average Number of Passes	% Area with <14 Day Revisit
North	8	3.5	13.0	22	100%
East	8	4.2	15.0	18	99%
South	8	6.3	27.1	11	97%



(a)

**Figure 5.** Cont.

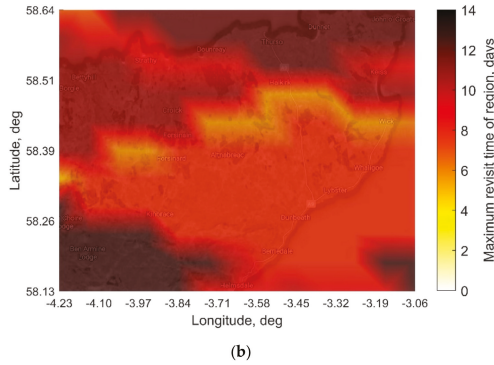


**Figure 5.** Maps of the north region of interest as described in Table 6 and indicated on Figure 2. The maps are oriented with north to the top and cover an area of approximately 57 km (N-S) × 68 km (E-W). The colours overlaid on the maps indicate the (a) average and (b) maximum revisit times of each location in the region after 30 days. Coverage is calculated at approximately 5 km intervals and interpolated to provide the coverage estimates for the full region of interest (Map data: Google, TerraMetrics, [www.google.com/maps](http://www.google.com/maps) [retrieved 16 March 2020]).

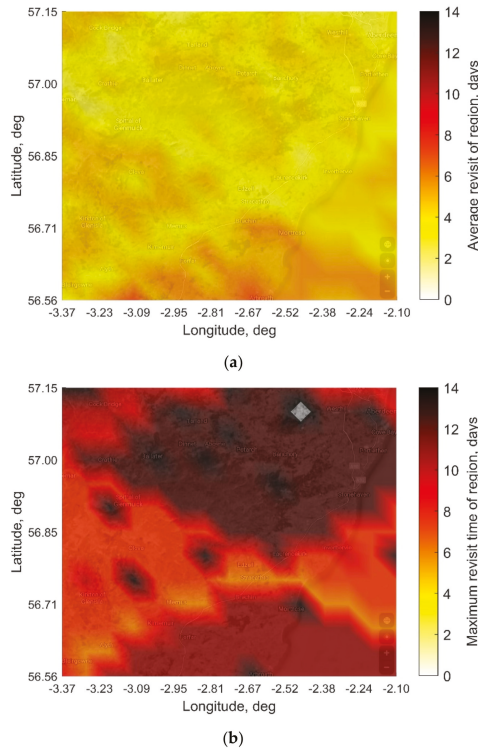


**Figure 6.** Maps of the east region of interest as described in Table 6 and indicated on Figure 2. The maps are oriented with north to the top and cover an area of approximately 65 km (N-S) × 77 km (E-W). The colours overlaid on the maps indicate the (a) average and (b) maximum revisit times of each location in the region after 30 days. Coverage is calculated at approximately 5 km intervals and interpolated to provide the coverage estimates for the full region of interest. (Map data: Google, TerraMetrics, [www.google.com/maps](http://www.google.com/maps) [retrieved 16 March 2020]).

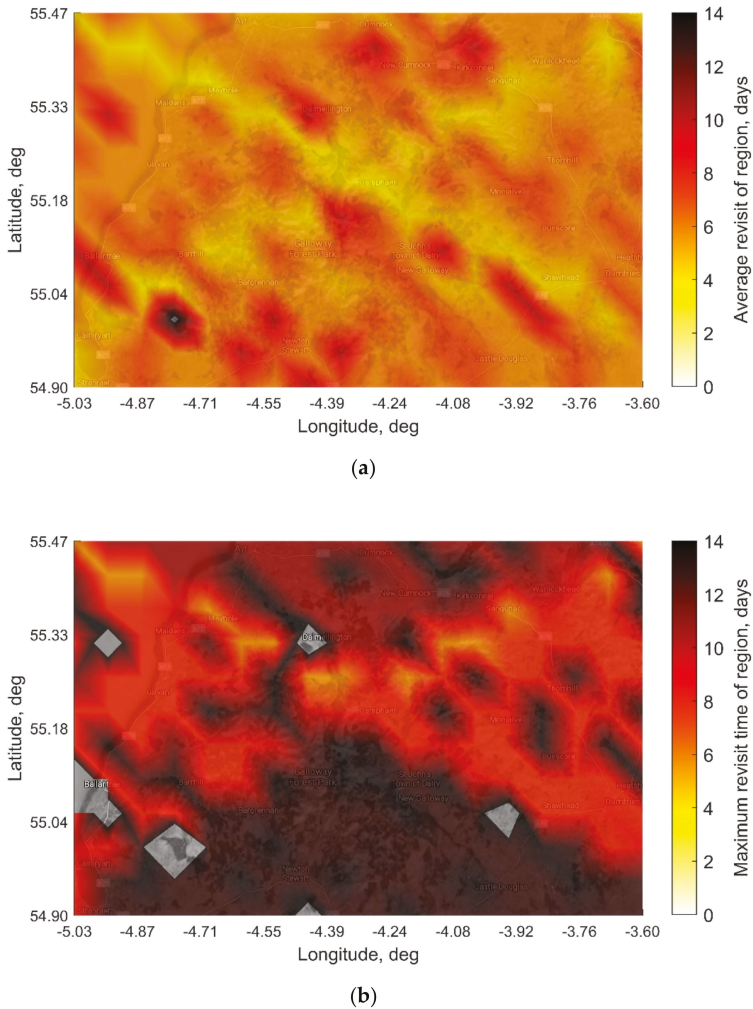


**Figure 7.** Maps of the south region of interest as described in Table 6 and indicated on Figure 2. The maps are oriented with north to the top and cover an area of approximately 63 km (N-S)  $\times$  90 km (E-W). The colours overlaid on the maps indicate the (a) average and (b) maximum revisit times of each location in the region after 30 days. Coverage is calculated at approximately 5 km intervals and interpolated to provide the coverage estimates for the full region of interest. (Map data: Google, TerraMetrics, [www.google.com/maps](http://www.google.com/maps) [retrieved 16 March 2020]).

## 5. Discussion

From an examination of appropriate currently operational multi-spectral imaging spacecraft, it is clear that the ideal requirements of the archaeological community, illustrated here with a case study of Scotland, would be challenging to meet using existing systems. What is readily available as a by-product of existing acquisitions may not be suitable, and even with expensive bespoke tasking there is no guarantee of acquiring the data required. Although the global revisit time of many of these systems appears sufficient (1–4 days), this only expresses the ability to view all areas of the globe, and does not correspond to the ability to image all areas. Tasking patterns, slewing and imaging constraints

mean that the useable imagery available of any area is collected at a much lower frequency than might be expected. For archaeological applications, the useable imagery collected is even lower because commercial imperatives mean that a high proportion of historical imagery is centred on urban areas. Considering eleven satellite systems (as described in Table 1) only eight appropriate archive images were identified of a 150 km<sup>2</sup> region of archaeological interest in Scotland over a six-month period during the summers of 2016 and 2018. This highlights the significant compromises inherent in archaeological applications of commercial satellite systems for site detection and monitoring, and the potential benefits of a bespoke system. When a constellation of 12 spacecraft were tasked with imaging this region in July 2020, 150 images were collected, though due to cloud cover only 17% of these images (a total of 26) were usable. This underlines the requirement for a system tasked consistently to improve the chances of securing the necessary imagery for archaeological observations. It also highlights the major impact of cloud cover, which is not further considered here, but is clearly a significant consideration in sensor choice and an imperative to developing uses of radar systems, for example. It is of note that the method of coverage analysis and orbit design presented in this paper is independent of sensor type, and the swath widths for very-high-resolution synthetic aperture radar (SAR) spacecraft are similar to those of the multi-spectral optical systems presented. For example, the recently launched ICEYE constellation can collect SAR imagery at <1 m GSD with a corresponding swath of 5 km [42] and Capella SAR offers <1 m GSD with a swath of approximately 10 km [43]. The spacecraft in both constellations have a mass of approximately 100 kg each, similar to the optical systems considered here. As such, a spaceborne SAR system designed to meet the outlined requirements would likely have similar parameters to the presented optical constellation. TerraSAR-X [44] and COSMO-SkyMed [45] are larger spacecraft, but both offer similar <1 m GSD SAR data and have been successfully used in archaeological prospection and cultural heritage monitoring, confirming the viability of this approach [7,45].

In designing a bespoke satellite for archaeology in Scotland, an inclined 60 deg orbit offers an increased revisit rate over a more common sun-synchronous orbit. The main drawback to this orbit is that even though there is a higher revisit rate, there may be issues with coverage due to the chance of passing over during eclipse, when an optical payload is ineffective. Using a 60 deg inclined orbit, it is estimated that full coverage of Scotland every two weeks could be achieved using eight spacecraft in repeating ground-track orbits, positioned to avoid any overlap in coverage. Such a system is estimated to provide an average revisit time across Scotland of 3–7 days, depending on the latitude. In the simulations performed, 97% of the areas of interest have a maximum revisit time of less than 14 days and it is expected that this could be extended to the full region with more precise orbit modelling.

The ground tracks of the satellite constellation would pass over various land masses across the globe. This presents a collaboration opportunity where research, development and costs could be shared with other countries in exchange for access to the system. The orbit characteristics recommended are designed to cover Scotland but could be adapted for better coverage across various countries. Land masses at a similar latitude to Scotland (56°) could be subject to a comparable coverage pattern and rate of revisit (Figure 8), provided that the satellites are capable of handling larger quantities of data. For example, Lithuania is at the same latitude as Glasgow (55°), allowing for similar results without changes to the existing orbit path. Due to the circular orbit selected, areas in the southern hemisphere of approximately −56° latitude (Figure 8) are subject to a similar coverage pattern and rate of revisit. However, this area is almost exclusively ocean. The use of an elliptical orbit could allow for longer dwell times in the northern hemisphere, reducing this impact, though this would require significant fuel for orbit maintenance.

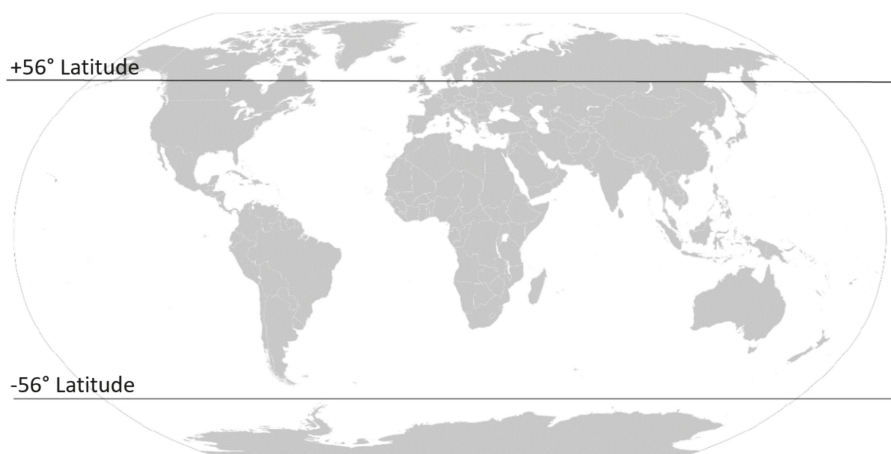


**Figure 8.** Robinson projection map of the world with lines of  $\pm 56^\circ$  latitude indicated. Regions of the Earth close to these latitudes would experience coverage similar to Scotland from the proposed satellite constellation.

## 6. Conclusions and Future Perspectives

This paper has presented an analysis of the requirements for a satellite system for archaeology based on a specification drawn up from ideal requirements in a Scottish context. The analysis highlights the extent to which existing satellite data, even against the recent proliferation of suitable systems, is not as readily available as might be expected. Thus, while tasking existing systems shows promise, a bespoke system should offer increased performance. The ‘satellite for archaeology’ simulation analysis presented here should contribute to assessment of the suitability of applications of satellite remote sensing for archaeology, drawing out the nature and reasons for the compromises that are routinely made in fundamental areas of source data collection. This study illustrates the extent to which archaeologists are most often ‘passive’ receivers of source data collected according to imperatives set by others. While this will remain largely inevitable, aspects of the analysis should be useful in promoting heritage concerns and specifications in future satellite system designs, and, at the very least, promoting a better understanding of the systems that produce their data amongst users of satellite derived data.

High-level design for a bespoke satellite for archaeology system suggests that eight 100 kg spacecraft at approximately 581 km altitude could meet the defined needs. While the bespoke nature of traditional space missions makes cost estimates challenging, based on the cost of the similar sized Carbonite-2 spacecraft, each spacecraft could be expected to cost in the region of \$6.3 million USD [46]. Rocket Lab USA provide dedicated launches for up to 150 kg to low-Earth orbit for an indicative cost of \$4.5 million USD [47]. Assuming one launch per spacecraft, this would give an estimated build and launch cost in the region of c. \$80–90 million USD. By heritage standards, this is a lot of money, but could be off-set by cost-sharing amongst countries at similar latitudes, with commercial tasking to subsidise costs and other social ventures offering further potential funding. Very-high-resolution multi-spectral satellite imagery with frequent revisit across Europe is expected to be valuable for many applications beyond cultural heritage. As such, a collaborative mission addressing a variety of compatible user needs could be envisioned, while additional imagery collection beyond the primary mission schedule could allow for repurposing and use by wider communities for many years into the future. It is beyond the scope of this paper to further explore these considerations, but they are raised here because of the potential they offer for archaeological considerations to be more directly taken account of in the design of future systems. This is especially pertinent as the trajectory of satellite development will continue to offer improved spatial resolution imagery from smaller spacecraft and reduced launch

costs, allowing similar performance to be achieved at a lower cost. Furthermore, development of satellite relay systems [48,49], inter-satellite links [48,50], responsively manoeuvrable spacecraft [51,52] and federated satellite systems [53] may allow for new methods of operation that could be suitable for archaeological applications, in particular due to the seasonal restrictions on observations. For example, the challenge of high cloud cover could, in future, be addressed through on-board autonomous agility. Forward-facing cloud-detection cameras for spacecraft are currently being developed, which would enable spacecraft to autonomously slew and plan data collection to mitigate the effects of cloud cover [54].

The focus of this study is explicitly on mission architecture, recognising that there are many other factors that require consideration, not least of which are sensor design (e.g., to deal with cloud cover issues), which would further influence system specifications, and processing and analysis workflows. Nevertheless, even with this focus, many attributes of satellite mission planning that are directly relevant to end users of derived data have been highlighted. These should promote the more informed use of that data, through a better understanding of the attributes and characteristics of source data. Published works promoting the application of satellite data for archaeology (e.g., [1–10,55]) focus extensively on the characteristics of data and imagery, but this paper represents, to the best of our knowledge, the first instance of a discussion of the influence on archaeological applications of mission architecture as a fundamental aspect of satellite system design with profound down-the-line implications. In the future development of reliable and systematic data sources to inform archaeological enquiry, we hope it will not be the last.

**Author Contributions:** Conceptualisation, C.N.M. and D.C.; methodology, C.N.M. and C.S.; software, C.N.M.; validation, C.N.M.; formal analysis, C.N.M. and C.S.; investigation, C.N.M. and C.S.; resources, M.M.; data curation, C.S.; writing—original draft preparation, C.S., C.N.M., and D.C.; writing—review and editing, C.N.M. and D.C.; visualisation, C.N.M. and C.S.; supervision, M.M.; project administration, D.C.; funding acquisition, M.M. All authors have read and agreed to the published version of the manuscript.

**Funding:** This research received no external funding.

**Acknowledgments:** This paper is based in large part on a thesis submitted in partial fulfilment of the requirements of 4th year BEng (Hons) Aero-Mechanical Engineering, University of Strathclyde, 2020 [56]. The authors would like to thank Athos Agapiou, Rog Palmer, Chris Sevara, Žiga Kokalj and Geert Verhoeven for comments on various iterations of this paper, and the anonymous reviewers who provided valuable input. SkySat data provided by the European Space Agency.

**Conflicts of Interest:** The authors declare no conflict of interest.

## References

1. Lasaponara, R.; Masini, N. *Satellite Remote Sensing. A New Tool for Archaeology*; Springer: New York, NY, USA, 2012.
2. Comer, D.; Harrower, M. *Mapping Archaeological Landscapes from Space*; Springer: New York, NY, USA, 2013.
3. Fowler, M.J. Satellite imagery and archaeology. In *Landscapes through the Lens. Aerial Photographs and Historic Environment*, 1st ed.; Cowley, D., Stranding, A., Abicht, M., Eds.; Oxbow: Oxford, UK, 2010; pp. 99–110.
4. Hammer, E.; Ur, J. Near eastern landscapes and declassified U2 aerial imagery. *Adv. Archaeol. Pract.* **2019**, *7*, 107–126. [[CrossRef](#)]
5. Lasaponara, R.; Masini, N. Detection of archaeological crop marks by using satellite QuickBird multispectral imagery. *J. Archaeol. Sci.* **2007**, *34*, 214–221. [[CrossRef](#)]
6. Lasaponara, R.; Masini, N. Satellite remote sensing in archaeology: Past, present and future perspectives. *J. Archaeol. Sci.* **2011**, *38*, 1995–2002. [[CrossRef](#)]
7. Luo, L.; Wang, X.; Guo, H.; Lasaponara, R.; Xin, Z.; Masini, N.; Wang, G.; Shi, P.; Khatteli, H.; Chen, F.; et al. Airborne and spaceborne remote sensing for archaeological and cultural heritage applications: A review of the century (1907–2017). *Remote Sens. Environ.* **2019**, *232*. [[CrossRef](#)]
8. Philip, G.; Donoghue, D.; Beck, A.; Galitsatos, N. CORONA satellite photography: An archaeological application from the Middle East. *Antiquity* **2002**, *76*, 109–118. [[CrossRef](#)]
9. Scardozzi, G. An introduction to satellite remote sensing in archaeology: State of the art, methods, and applications. In *Looking to the Future, Caring for the Past: Preventive Archaeology in Theory and Practice*, 1st ed.; Boschi, F., Ed.; Bologna University: Bologna, Italy, 2016; pp. 217–239.

10. Verhoeven, G.J.J. Satellite hyperspectral and multispectral imaging. In *The Encyclopedia of Archaeological Sciences*, 1st ed.; López Varela, S.L., Ed.; John Wiley & Sons: Hoboken, NJ, USA, 2018. [CrossRef]
11. Agapiou, A.; Alexakis, D.D.; Hadjimitsis, D.G. Potential of virtual earth observation constellations in archaeological research. *Sensors* **2019**, *19*, 4066. [CrossRef]
12. Verhoeven, G.J. Are we there yet? A review and assessment of archaeological passive airborne optical imaging approaches in the light of landscape archaeology. *Geosciences* **2017**, *7*, 86. [CrossRef]
13. Banaszek, Ł.; Cowley, D.; Middleton, M. Towards national archaeological mapping. Assessing source data and methodology—A case study from Scotland. *Geosciences* **2018**, *8*, 272. [CrossRef]
14. Cowley, D.; Banaszek, Ł.; Geddes, G.; Gannon, A.; Middleton, M.; Millican, K. Making LiGHT work of large area survey? Developing approaches to rapid archaeological mapping and the creation of systematic national-scaled heritage data. *J. Comput. Appl. Archaeol.* **2020**, *3*, 109–121. [CrossRef]
15. Evans, R.; Jones, R.J.A. Crop marks and soils at two archaeological sites in Britain. *J. Archaeol. Sci.* **1977**, *4*, 63–76. [CrossRef]
16. Cowley, D. A case study in the analysis of patterns of aerial reconnaissance in a lowland area of southwest Scotland. *Archaeol. Prospect.* **2003**, *9*, 255–265. [CrossRef]
17. Brophy, K.; Cowley, D. (Eds.) *From the Air: Understanding Aerial Archaeology*; Tempus: Stroud, UK, 2005.
18. Verhoeven, G.J.; Sevara, C. Trying to break new ground in aerial archaeology. *Remote Sens.* **2016**, *8*, 918. [CrossRef]
19. Cowley, D. Aerial photography and reconnaissance for archaeology in the 21st century: Achievements and challenges. *Archeol. Aerea* **2017**, *XI*, 9–15.
20. Met Office, Department for Business, Energy and Industrial Strategy. Access to UK Climate Datasets. Available online: <https://www.metoffice.gov.uk/research/climate/maps-and-data/data/index> (accessed on 21 December 2019).
21. Satellite Imaging Corporation. Satellite Sensors. Available online: <https://www.satimagingcorp.com/satellite-sensors/> (accessed on 30 June 2020).
22. European Space Agency. EO-CAT Web Client. Available online: <https://eocat.esa.int/> (accessed on 30 June 2020).
23. Earth Observing System. KOMPSAT 3/3A. Available online: <https://eos.com/kompsat-3-3a/> (accessed on 30 June 2020).
24. Deimos Imaging. Our Virtual Constellation Satellites. Available online: <https://www.deimos-imaging.com/our-satellites> (accessed on 30 June 2020).
25. European Space Agency. Newcomers Earth Observation Guide. Available online: <https://business.esa.int/newcomers-earth-observation-guide> (accessed on 30 June 2020).
26. Planet Team. Planet Application Program Interface: In Space for Life on Earth. Available online: <https://api.planet.com> (accessed on 30 June 2020).
27. Planet Labs Inc. *Planet Imagery Product Specifications*; Planet Labs Inc.: San Francisco, CA, USA, 2020.
28. European Space Agency. Earth Online—Third Party Missions: SkySat. Available online: <https://earth.esa.int/web/guest/missions/3rd-party-missions/current-missions/skysat> (accessed on 30 June 2020).
29. European Space Agency. EO Portal Directory: Satellite Missions Database. Available online: <https://directory.eoportal.org/web/eoportal/satellite-missions> (accessed on 28 July 2020).
30. Osborne, P. *The Mercator Projections*; Zenodo: Edinburgh, UK, 2013; pp. 88–90. [CrossRef]
31. Vallado, D.A.; McClain, W.D. Coordinate and time systems. In *Fundamentals of Astrodynamics and Applications*, 3rd ed.; Microcosm Press: Hawthorn, CA, USA; Springer: New York, NY, USA, 2007; pp. 142–149. ISBN 978-0-387-71831-6.
32. Decker, B.L. *World Geodetic System 1984*; Technical Report; Defense Mapping Agency Aerospace Center: St Louis, MO, USA, 1986.
33. Washburn, A.R. *Earth Coverage by Satellites in Circular Orbit*; Technical Report; Department of Operations Research Naval Postgraduate School: Monterey, CA, USA, 2004.
34. Verhoeven, G. Resolving some spatial resolution issues: Part 1: Between line pairs and sampling distance. *AARGNEWS* **2018**, *57*, 25–34. [CrossRef]
35. United Nations. *Space Debris Mitigation Guidelines of the Committee on the Peaceful Uses of Outer Space*; United Nations Office for Outer Space Affairs, United Nations: Vienna, Austria, 2010.
36. NASA. *U.S. Standard Atmosphere*; Technical Report No. NASA-TM-X-74335 [NOAA-ST 76-1562]; National Aeronautics and Space Administration (NASA): Washington, DC, USA, 1976.

37. Macdonald, M.; McInnes, C.; Lücking, C.; Visagie, L.; Lappas, V.J.; Erb, S. Needs assessment of gossamer structures in communications platform end-of-life disposal. In Proceedings of the AIAA Guidance, Navigation, and Control (GNC) Conference, Boston, MA, USA, 19–22 August 2013. [CrossRef]
38. Fu, X.; Wu, M.; Tang, Y. Design and maintenance of low-earth repeat-ground-track successive-coverage orbits. *J. Guid. Control Dyn.* **2012**, *35*, 686–691. [CrossRef]
39. Lowe, C.; Macdonald, M.; Greenland, S.; McKee, D. ‘Charybdis’—The next generation in ocean colour and biogeochemical remote sensing. In Proceedings of the 26th Annual AIAA/USU Conference on Small Satellites, Logan, UT, USA, 13–16 August 2012.
40. Vallado, D.A.; McClain, W.D. Initial orbit determination. In *Fundamentals of Astrodynamics and Applications*, 3rd ed.; Microcosm Press: Hawthorn, CA, USA; Springer: New York, NY, USA, 2007; pp. 615–633, 642–667. ISBN 978-0-387-71831-6.
41. Mishne, D. Formation control of satellites subject to drag variations and J2 perturbations. *J. Guid. Control Dyn.* **2004**, *27*, 685–692. [CrossRef]
42. ICEYE Data. Spotlight Imaging Mode. Available online: <https://www.iceye.com/sar-data/spotlight> (accessed on 2 October 2020).
43. Stringham, C.; Farquharson, G.; Castelletti, D.; Quist, E.; Riggi, L.; Eddy, D.; Soenen, S. The Capella X-band SAR constellation for rapid imaging. In Proceedings of the IEEE International Geoscience and Remote Sensing Symposium, Yokohama, Japan, 28 July–2 August 2019; pp. 9248–9251. [CrossRef]
44. Pitz, W.; Miller, D. The TerraSAR-X satellite. *IEEE Trans. Geosci. Remote Sens.* **2010**, *48*, 615–622. [CrossRef]
45. Tapete, D.; Cigna, F. COSMO-SkyMed SAR for detection and monitoring of archaeological and cultural heritage sites. *Remote Sens.* **2019**, *11*, 1326. [CrossRef]
46. Pultarova, T. UK military looking at smallsats to increase space resilience. Space News, 23 May 2018. Available online: <https://spacenews.com/uk-military-looking-at-smallsats-to-increase-space-resilience/> (accessed on 2 October 2020).
47. Wekerle, T.; Pessoa Filho, J.B.; Costa, L.E.V.L.D.; Trabasso, L.G. Status and trends of smallsats and their launch vehicles—An Up-to-date Review. *J. Aerosp. Technol. Manag.* **2017**, *9*, 269–286. [CrossRef]
48. Lowe, C.J.; Macdonald, M. Resource-considerate Data Routing through Satellite Networks. *J. Aerosp. Inf. Syst.* **2017**, *14*, 472–482. [CrossRef]
49. Troendle, D.C.; Rochow, C.; Martin Pimentel, P.; Heine, F.F.; Meyer, R.; Lutzer, M.; Benzi, E.; Sivac, P.; Krassenburg, M.; Shurmer, I. Optical LEO-GEO data relay: The in-orbit experience. In Proceedings of the AIAA SPACE 2015 Conference and Exposition, Pasadena, CA, USA, 31 August–2 September 2015. [CrossRef]
50. Heine, F.; Kämpfner, H.; Czichy, R.; Meyer, R.; Lutzer, M.; Meyer, R. Laser communication applied for EDRS, the european data relay system. *Ceas Space J.* **2011**, *2*, 85–90. [CrossRef]
51. McGrath, C.N.; Macdonald, M. General perturbation method for satellite constellation reconfiguration using low-thrust maneuvers. *J. Guid. Control. Dyn.* **2019**, *42*, 1676–1692. [CrossRef]
52. Legge, R.S., Jr. Optimization and Valuation of Reconfigurable Satellite Constellations under Uncertainty. Ph.D. Thesis, Massachusetts Institute of Technology, Cambridge, MA, USA, 2014.
53. Golkar, A.; i Cruz, I.L. The federated satellite systems paradigm: Concept and business case evaluation. *Acta Astronaut.* **2015**, *111*, 230–248. [CrossRef]
54. Greenland, S.; Ireland, M.; Kobayashi, C.; Mendham, P.; Post, M.; White, D. Development of a miniaturised forwards looking imager using deep learning for responsive operations. Presented at the 4S Symposium, Sorrento, Italy, 28 May–1 June 2018.
55. Parcak, S. *Satellite Remote Sensing for Archaeology*; Routledge: London, UK; New York, NY, USA, 2009.
56. Scott, C. Archaeology, but from Space! Ph.D. Thesis, Aero-Mechanical Engineering, University of Strathclyde, Glasgow, UK, 2020.

**Publisher’s Note:** MDPI stays neutral with regard to jurisdictional claims in published maps and institutional affiliations.



© 2020 by the authors. Licensee MDPI, Basel, Switzerland. This article is an open access article distributed under the terms and conditions of the Creative Commons Attribution (CC BY) license (<http://creativecommons.org/licenses/by/4.0/>).





## Article

# Cropmarks in Aerial Archaeology: New Lessons from an Old Story

Zoltán Czajlik <sup>1,\*</sup>, Máttyás Árvai <sup>2</sup>, János Mészáros <sup>2</sup>, Balázs Nagy <sup>3</sup>, László Rupnik <sup>4</sup> and László Pásztor <sup>2</sup>

- <sup>1</sup> Department of Archeometry, Archaeological Heritage and Methodology, Institute of Archaeological Sciences, Faculty of Humanities, Eötvös Loránd University, Múzeum krt. 4/B, 1088 Budapest, Hungary
- <sup>2</sup> Institute for Soil Sciences, Centre for Agricultural Research, Herman Ottó út 15, 1022 Budapest, Hungary; arvai.matyas@rissac.hu (M.Á.); meszaros.janos@rissac.hu (J.M.); pasztor@rissac.hu (L.P.)
- <sup>3</sup> Department of Physical Geography, Center of Geography, Faculty of Science, Eötvös Loránd University, Pázmány Péter sétány 1, 1117 Budapest, Hungary; nagybalazs@caesar.elte.hu
- <sup>4</sup> MTA-ELTE Research Group for Interdisciplinary Archaeology, Múzeum krt. 4/B, 1088 Budapest, Hungary; rupnik.laszlo@btk.elte.hu
- \* Correspondence: czajlik.zoltan@btk.elte.hu

**Abstract:** Cropmarks are a major factor in the effectiveness of traditional aerial archaeology. Identified almost 100 years ago, the positive and negative features shown by cropmarks are now well understood, as are the role of the different cultivated plants and the importance of precipitation and other elements of the physical environment. Generations of aerial archaeologists are in possession of empirical knowledge, allowing them to find as many cropmarks as possible every year. However, the essential analyses belong mostly to the predigital period, while the significant growth of datasets in the last 30 years could open a new chapter. This is especially true in the case of Hungary, as scholars believe it to be one of the most promising cropmark areas in Europe. The characteristics of soil formed of Late Quaternary alluvial sediments are intimately connected to the young geological/geomorphological background. The predictive soil maps elaborated within the framework of renewed data on Hungarian soil spatial infrastructure use legacy, together with recent remote sensing imagery. Based on the results from three study areas investigated, analyses using statistical methods (the Kolmogorov–Smirnov and Random Forest tests) showed a different relative predominance of pedological variables in each study area. The geomorphological differences between the study areas explain these variations satisfactorily.

**Keywords:** cropmarks; empirical knowledge; alluvial sediments; geomorphological/pedological background; soil spatial infrastructure; statistical methods



**Citation:** Czajlik, Z.; Árvai, M.; Mészáros, J.; Nagy, B.; Rupnik, L.; Pásztor, L. Cropmarks in Aerial Archaeology: New Lessons from an Old Story. *Remote Sens.* **2021**, *13*, 1126. <https://doi.org/10.3390/rs13061126>

Academic Editors: Geert Verhoeven, Dave Cowley and Arianna Travigla

Received: 31 December 2020

Accepted: 9 March 2021

Published: 16 March 2021

**Publisher’s Note:** MDPI stays neutral with regard to jurisdictional claims in published maps and institutional affiliations.



**Copyright:** © 2021 by the authors. Licensee MDPI, Basel, Switzerland. This article is an open access article distributed under the terms and conditions of the Creative Commons Attribution (CC BY) license (<https://creativecommons.org/licenses/by/4.0/>).

## 1. Introduction

In June 1998, one of the most prolific aerial archaeologists of the second half of the 20th century, René Goguy, arrived in Budapest from Paris on an Air France scheduled flight. While still at the airport, he commented that from an altitude of 20,000 feet it was clear to him that research into cropmarks on the Little Plain (Rába interfluvium) should begin immediately. Despite the previous several years’ lack of success, work was recommenced in this region, and a large number of good quality archaeological features visible as cropmarks were identified [1].

To understand the significance and the complexity of cropmarks in aerial archaeology, a brief summary of traditional ways of investigating them and a short presentation of the factors affecting their formation are required. Alluvial fans are ideal for studying the role of the different soils in the formation of cropmarks, and therefore, this introduction will also contain the geographical background of the alluvial fans and the relevant results of soil mapping in Hungary.

### 1.1. Cropmarks in Aerial Archaeology

What has been long recognized is the correlation between variations in vegetation on arable land (and, under certain conditions, on grazed and mowed areas) and the presence of traces of past human activities (along with many natural phenomena). Although there were indications of an understanding that vegetation might reveal the past in this way as early as around 1540 (John Leland), it was the work of O. G. S. Crawford in the UK beginning in 1914 that definitively linked variations in crop growth to the presence of buried archaeological features [2]. By the 1920s, this was already being applied in his research [3]. The development of aviation and aerial photography then led to similar insights in continental Europe, too. In Hungary, Sándor Neogrády, another experienced World War I aviator, was an aerial photographer and cartographer who started to collect what he termed “unnatural phenomena” from the 1920s [4]. Pioneer researchers began to organize them systematically, so Neogrády also described the role of darker, denser vegetation, which grows over filled-in ditches/pits, and the sparser, lighter vegetation over buried walls, introducing the distinction between positive and negative cropmarks as basic categories [4].

In addition to variations in color, differences in the height of crops and vegetation are also important (Figure 1), as illustrated in various studies [5,6]. Many cultivated plant species indicate anomalies very early in their growing season, but it is in the course of ripening that the greater part of variations may be detected [7,8].



**Figure 1.** Dabas—Öreg Országúti-dűlő (Pest County, Hungary) aerial archaeological site. The image is dominated by the positive cropmarks showing the color variations (marks of a green circular ditch and small pits) in yellow wheat. On the right side, mostly due to the barley's late harvest period, some further pits are visible (cf. Figure 2) owing to shadow effect of the cropmarks (Oblique aerial photograph, 12 June 2015, Zoltán Czajlik).

From the 1950s, first in France and Germany, later in Austria and Italy, and finally in the 1990s in Switzerland and the former socialist countries, the importance assigned to the identification of the cropmarks has grown. This, together with data gathered using traditional, analog aerial photography in archaeology, was summarized by Irwin Scollar in his work on archaeological prospection, which is still relevant today [9].

Beginning in the 2000s, the use of digital cameras and GPS for positioning images and navigation has greatly increased the efficiency of traditional aerial archaeological data collection. Images with reference points can be quickly rectified, and the interpretation and creation of photomaps has become much easier. Thanks to digital technology, it is now

possible to collect information not only from the visible spectrum, but also from the NIR and NUV domains, which (in a way similar to infrared films in the analog era) can increase the contrast between normal and stressed crops and improve the visibility of cropmarks following data enhancement [10].



**Figure 2.** Rectified oblique aerial photographs at Dabas—Öreg Országúti-dűlő (Pest County, Hungary, cf. Figure 1). Aerial photo polygons are generally related to the parcel-system. The “normal”/late harvest cropmarks are marked in different colors. Source: Zoltán Czajlik, 12 June 2015 and GE-imagery.

Nowadays, archaeological aerial photography has become part of airborne and spaceborne remote sensing (ASRS), in addition to those mentioned above, as well as the multi- and hyperspectral applications [11]. The programmed use of the latest UAV platform—as with non-traditional ASRS—makes (semi) automatic photography also possible. Thus, traditional aerial archaeology remains one of the last remote sensing techniques requiring an observer, so its overhaul is certainly justified [12,13]. However, this does not lead to the undervaluing or discarding of the experience and benefits that come from the observer being not only part of the learning process, but also being constantly present during data collection and influencing its quality and efficiency through decisions; all this represents a resource to be exploited. This is especially true in the case of such a complex phenomenon as cropmarks, which are to this day still understood on the basis, more or less, of empirical knowledge [14].

### 1.2. Factors Affecting the Formation of Cropmarks

As summarized above, the experiences of pioneers in this field show that what character and what quality of cropmarks become visible depends on when a photo is taken. Some of these factors are connected to agricultural activity: in which way the soil is cultivated, and above all, what species are grown, and in what proportion [15]. The significance of barley (*Hordeum vulgare*), wheat (*Triticum aestivum*), winter rape (*Brassica napus*) and alfalfa (*Medicago sativa*) in this area of research is well-documented. To varying degrees, maize (*Zea mays* L.), pea (*Pisum sativum* L.) and sun-flower (*Helianthus annuus* L.) may also reveal archaeological features [16]. On the basis of the personal experience of the authors of the present paper, triticale (Triticale) and poppy (*Papaver somniferum* L.) also have important regional roles [17]. The explanation for these observations is mainly related to

the sowing distance, structure (e.g., normal root length) and drought tolerance/resistance to high amounts of precipitation of the plants [18,19].

One of the most difficult natural factors to calculate is the weather, and the personal experience of both the aerial photographer-archaeologist and the pilot still plays an important role in dealing with this. As a general rule, droughts caused by dry weather can dramatically increase the number of detectable cropmarks, which is what happened in England in 1976. Too much rainfall, on the other hand, yields few cropmarks, while a lot of rain in early summer can ruin even what had earlier been regarded as promising cropmark development—this is what happened in Hungary in 2019, for example.

Taking all the above into account, the investigation of the correlation between infiltration/evaporation data and cropmarks requires the detailed analysis not only of data sets for late spring/early summer but also of long-term sets [20–23]. Furthermore, it should be noted here that while the analysis of precipitation-related factors is important, it is not in itself sufficient; temperature and even, in some cases wind, may also be of significance [24].

Among the geological factors, the role of gravel-rich subsurface layers or gravel covers and fluvial-dominated fan surfaces is of extraordinary importance [25,26]. On the basis of data from Bavaria, it would appear that even in moderately rainy years, good results can be achieved by researching these areas [5]. In Central Bohemia, in the Elbe Basin, 75% of the cropmarks identified between 1993 and 2009 are in gravel/sandy areas, and a further 22% in territories underlain by loess bedrock [16]. Such areas can be successfully investigated in Hungary as well, though in this case, the difference in favor of gravel/sand areas is not as remarkable [17,23].

While soil conditions are, naturally, not independent of the underlying geology, alluvial areas may, nonetheless, present a very diverse picture, making it difficult to recognize correlations with soil types. The effects of sub-soil archaeological features on the growth of crops and the related question of within-plot variability in soil properties has been studied in Central European agricultural landscapes by Czech researchers. Hejcman et al. (2013) [27] were able to demonstrate that variations in soil pH and nutrient availability were attributable to prehistoric settlement activities. They recorded substantially higher contents of organic matter, higher pH, and concentrations of plant-available P, Ca, Mg, Cu, and Zn in the sub-soil layer in cropmarks identified on spring barley as compared to their surroundings. In the arable layer, pH and concentrations of P, Ca and Mg were generally higher. Cropmarks were characterized by barley plants that grew to twice the height of those in the control group, and with significantly higher Ca, Mg and P concentrations. In Bohemia, the cropmarks were most visible on sandy soils, as the soil texture, water holding capacity, and nutrient availability between filled-in archaeological features and the surrounding sub-soil layers showed the greatest contrast. The soil properties differ significantly in areas with clayey soils, which may explain the almost complete absence of cropmarks in these zones [16,28,29]. According to Gojda and Hejcman, positive cropmarks may appear particularly noticeable above graves due to the phosphorus from the bodies [19]. On the basis of the experiences of the current authors, it should be noted that the identification of graves through cropmarks is more sensitive to weather/precipitation than is the case with other archaeological phenomena.

### 1.3. Geographical Background

The interior of the Carpathian Basin is dominated by lowlands derived from alluvial fans. The watercourses reaching the basin from the mountainous surroundings formed their vast alluvial fans with lengths of 10 km to 100 km, stretching out towards the deep-lying part of the giant basin during the Pleistocene [30]. The alluvial fans—representing a total area of more than 50,000 km<sup>2</sup>—are separated by low mountains and gentle hills. Elsewhere, however, interlinked alluvial fans underwent significantly different Late Pleistocene and Holocene development histories; in these cases, due to both tectonic and climatic processes, the watercourses gradually “slid down” (migrated) from the alluvial fans with gravel bases and silty and sandy sediment dominated upper layers [31].

On some of the alluvial fans—e.g., on the remnants of an alluvial fan flanked by a terraced valley edge—the movements of wind-blown sand and loess formation became dominant. The sand-formed topography is dominated by large blowout-residual ridge-hummock form assemblages that are extensive and adapt to the runoff direction(s) of the former alluvial fan surface.

In other cases, the tectonic fragmentation of former alluvial fans with thick loess and sand cover formed a tectonically controlled valley network. Their streams sharply divided the alluvial fan bodies: alluvial valleys were formed, with steep marginal slopes, above which extended flat plateaus with a geological past as alluvial fans but subsequently were covered with loess and/or sand.

At the edges of the alluvial fans, the rivers that migrated there formed wide floodplains. After their strong alluvial fan erosion activity, during the accumulation phase—which is also characteristic of the Holocene—they partially covered the marginal areas with their sediments, or they could even cover the entire surface of the smaller alluvial fan.

#### 1.4. Soil Mapping

The upper, weathered, solid mantle of the Earth, the pedosphere, results from the complex interplay of several soil forming factors and soil forming processes in the zone of interaction between the lithosphere, atmosphere, hydrosphere and biosphere. Soil is a multifunctional natural resource [32], one of its main functions is the conservation of natural and human heritages.

The goal of soil mapping is to reveal and visualize the spatial relationships of thematic knowledge concerning the soil mantle. Soil maps are thematic maps, whereby a theme is determined through specific information related to the soils [33]. These can be primary or secondary (derived), quantitative, or qualitative properties. There are two basic and apparently contradictory but in fact complementary concepts employed in the characterization of spatial variability in soils [34]. One approach essentially builds on similarity, and represents the soil mantle via the mapping of units of homogeneous composition. Its cartographic realization is classic soil maps, of which there is an extensive tradition [34]. The other approach emphasizes the continuous spatial variation of soil properties, and the mapped soil property is predicted using cells and the spatial resolution is determined by the cell size.

In Hungary, large amounts of soil information have been collected through soil surveys, observation and mapping. The goals and methodology of successive soil mapping projects differed, and as a consequence, very often it was dissimilar soil features that were highlighted. The maps were compiled at various scales, from farm to national level. Smaller scale, synthesized maps provide national coverage, while larger scale ones cover only parts of the country [35].

Recently, predictive soil maps in the form of digital soil maps have come to be considered the most effective representation of specific features of the soil mantle [36]. The evolution of digital soil mapping is closely related to the rising availability of spatially exhaustive, relatively low-cost data available in the form of satellite imagery covering wide time scales and spectra, and also digital elevation models originating from remote sensing, both of which provide efficient representations of various soil forming factors and processes [37]. In Hungary, the very recently elaborated DOSoReMI.hu is a collection of spatial soil information in the form of unique digital soil map products compiled to optimize the identification of specific soil features at the regional scale [38]. A significant part of these had never been mapped before, even nationally, at a high (~1 ha) spatial resolution. The new digital soil maps are compiled from specific spatial predictions based on (i) measured soil observation data, (ii) spatially exhaustive, environmental auxiliary variables, and (iii) sophisticated geostatistical and data mining methods for inferring the spatial and temporal variations of soil features. The inherent vagueness of spatial prediction is explicitly expressed through a proper accuracy assessment, and the newly produced

digital soil information and maps are therefore supplied with an estimation of the degree of both local and global uncertainty or reliability.

## 2. Materials and Methods

Studying cropmarks requires a special mixture of knowledge, as besides the technical factors, its efficiency depends on experience of the local setting, archaeological and geomorphological knowledge, and on environmental factors which are permanently changing with respect to one another. Among these dynamic factors, the role of precipitation is decisive, and the weather during the early summer time window can influence the results for better or for worse to a great extent. In the light of this, it is clear why methods may vary greatly in heritage management, but the greater the researcher's experience and the longer the research timescale, the greater the progress which can be made in reducing the impact of seasonal differences.

The primary spatial unit of the traditional archaeological approach is the archeological site. Official geoinformatics-based records rely on the sites being some kind of polygon clearly delimited in an area using field survey data. In the case of aerial archaeological sites, the greater part of the data concerns the archaeological features. This allows a much more detailed interpretation than the information from a field survey. Thanks to the detailed interpretation of aerial photos, defining the archaeological site boundaries is not necessary [39]. However, in aerial archaeology research, sites can be defined as territorial units reshaped by the imposition of modern borders, divisions, and changes in designation and use. Nevertheless, the density of aerial archaeological sites are usually marked on integrated maps with the help of simple coordinates/GPS tracks determined during flights or later in laboratory, meaning that there is no spatial data showing their true extent in most databases [8,17,40–42]. One important exception is the system operated by the University of Vienna for years, as they use both coordinates and polygons [26,29]. The method—in some aspects similar to the Austrian one—employed by the current authors is, with a few exceptions, adapted to the growth of cultivated field crops. In the presentation it is not aerial photograph coordinates which are used, but polygons. Aerial photo polygons do not show the boundaries of archaeological sites, but the plots planted with the same species, and any archaeological phenomena thus revealed. So, these are units which, thanks to the presence of homogenous conditions, theoretically all the important archeological phenomena should be visible.

Herein, the term cropmark plot (CMP) will be used for the areas covered by each polygon. In the absence of CMPs, the extent of all archaeological aerial photo sites should be determined in order to obtain comparable spatial data. Meanwhile, there may be often several, in some cases even 8–10 aerially identifiable archaeological sites within the area of a CMP (Figure 2).

The opposite is, of course, also true. Maps of various archaeological sites can be put together, just like pieces of a puzzle, based on aerial archaeological prospection conducted on different dates. In other words, the number of puzzle pieces—and the average size of the CMPs—depends on the pattern of land use. To meet these conditions, the CMPs are formed on the basis of the polygons determined by the parcel boundaries at the time when the photo is taken. As a result of further photography, CMPs can be merged or resized if the documented area expands.

The aim of the current research was to compare the pedological features of cropmark plots (CMP) and non-cropmark plots (nCMP) in order to identify demonstrable differences between them. For this purpose, the spatial soil information on primary soil properties provided by DOSoReML.hu was employed. To compensate for the inherent vagueness of spatial predictions, together with the fact that the definition of CMPs and nCMPs adopted here is somewhat indefinite, the comparisons were carried out using data-driven, statistical approaches.

## 2.1. Study Areas

To examine the utility of this method, areas subject to increased systematic research from 1993 onwards were selected, and 2017 was the last year processed. This does not, however, mean that the regular aerial archaeological prospecting of the areas has ceased. The sample areas also represent examples of all three characteristic alluvial fan evolution types (1, 2, 3). These distinct environment types also demonstrate different patterns in terms of cropmark appearance (Figure 3).

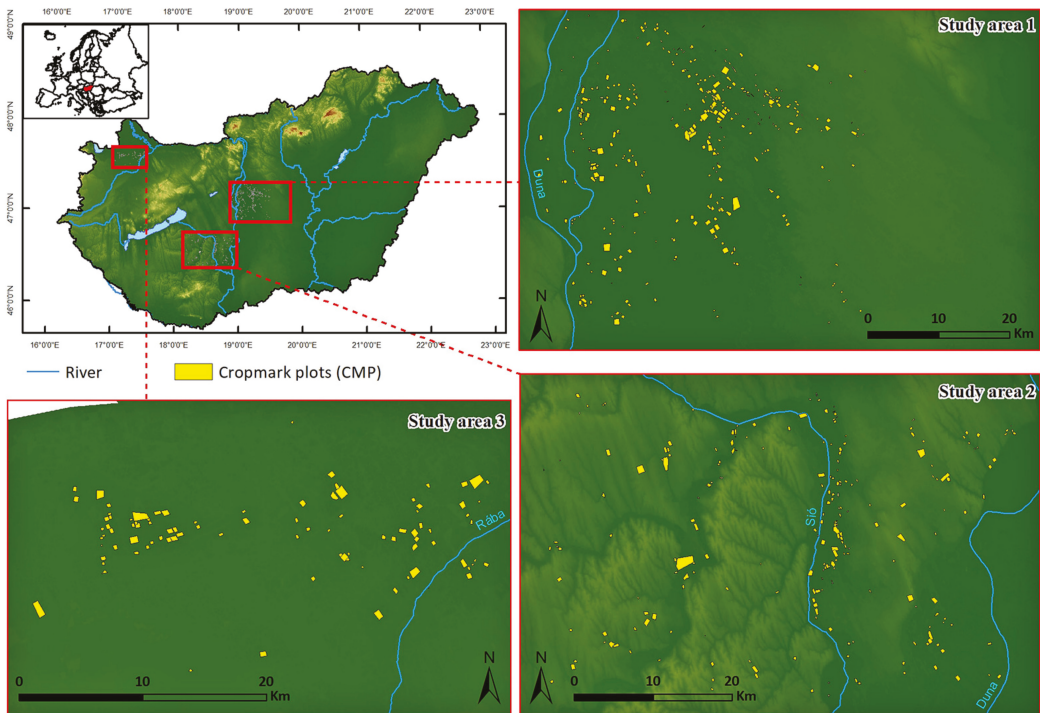


**Figure 3.** Location of the study areas. Cropmark plots (CMPs) are displayed in yellow.

### 1. The alluvial fan of the Danube-Tisza interfluvium (Study area 1)

This is a remnant of a huge alluvial fan of the paleo-Danube aligned in a NW-SE direction, and from which the river—for tectonic reasons—migrated to the West. In this new location, the Danube has created a wide floodplain extending 30–50 m below the top of the former alluvial fan. On the surface of the inactive alluvial fan there is a gravel-rich alluvial plain in the North but going southwards it is dominated by loess and sandy sediments, and due to aeolian processes (which were extremely significant in the Holocene as well), by sand ridges, hollows and dunes. A near-surface gravel presence occurs at the neck of the alluvial fan and on the terraces of the Danube as it cuts into its western margin.

### 2. Sió-Sárvíz valley (Study area 2)

The Carpathian Basin has been divided by fluvial activity (the paleo-Danube) and controlled by tectonic processes. This loess and sand region is markedly separated from the wide floodplain of the Danube due to its Pleistocene migration and even from the sandy surface of the wide alluvial fan of the Danube-Tisza interfluvium. In the Sió-Sárvíz valley, which deepens into a tectonically divided terrain, significant valley widening and

slope erosion took place. The area's classification as a lowland can be explained by the flat surface of the extensive loess and sandy plateaus that dominate the region.

### 3 Rába interfluvium (Study area 3)

The alluvial fans of the section of the paleo-Danube entering the Carpathian Basin and of the watercourses (e.g., Rába) coming from the eastern edge of the Alps developed into one of the sub-basins of the Carpathian Basin in the direction of the Győr Basin. The gravel-dominated alluvial fans were built on top of each other in this lowland depression. Their floodplain sedimentary cover also significantly thickened during the Holocene, covering the alluvial fan-derived basement.

All the three study areas were preprocessed for the analysis in four steps:

- A minimum bounding box was defined, covering the CMPs of the given site. Its extent is defined by the outermost CMPs. The distribution of CMPs within these rectangles is inhomogeneous.
- The countrywide soil property maps with 1 ha spatial resolution were clipped to the extent of the bounding rectangles.
- Non-croplands were masked out from the clipped soil property maps on the basis of the very recently elaborated, national, high resolution ecosystem-type map [43], which also represents land-use/landcover characteristics with a high degree of accuracy.
- Two sample populations were defined for each test site and each soil property, containing (1) the raster cells in CMPs and (2) the rest of the cells. These sample populations represented the two types of areas, which show cropmark features, or not, respectively.

#### 2.2. Spatial Soil Information

Traditionally, the spatial knowledge of soils is summarized chiefly in the form of soil type maps based on an appropriate classification system [44]. Generally, these maps are simply called soil maps, which in fact reflects their importance. Historically, soil mapping was done based on soil typology, and soil types have strong didactic significance. Soil type maps have also been created on different levels and according to different classification systems. In present study, the cartographically prepared (raster-vector transformed and generalized) version of the newly compiled nationwide soil type map (with harmonized legend and spatially consistent predictivity [45]), was used for the identification of the location of CMPs along main soil types.

In the quantitative investigations, optimized primary soil property maps with 1 ha spatial resolution were tested for their ability to reveal differences between CMPs and nCMPs. As with soil type, rooting depth refers to the whole soil profile (pedon), while particle size fractions (clay, sand and silt content), bulk density (BD), soil organic matter content (SOM), CaCO<sub>3</sub> content (CC), and pH are mapped for subsequent soil layers according to various partitions (Table 1). Each target variable was modelled using a sequence of spatial inference approaches (altering either methods or the reference and predictor data), which were always accompanied by a detailed accuracy assessment for the determination of the best performing set of soil data, method and auxiliary covariables for the given target variable [38]. The map products are published on the [www.dosoremi.hu](http://www.dosoremi.hu) website and are serviced in two different ways. The maps elaborated according to GSM specifications represent the Hungarian contribution to the GlobalSoilMap.net project.

**Table 1.** Summary of the primary soil property maps used for the comparison of the pedological features of CMPs and nCMPs.

Soil Properties Linked to Layers	GSM.net Depth Intervals [cm]						Equidistant Depths [cm]			Topsoil
	0–5	5–15	15–30	30–60	60–100	100–200	0–30	30–60	30–60	0–60
soil organic matter [%] (SOM)	x	x	x	x	x	x	x		x	
pH	x	x	x	x	x	x	x		x	
bulk density [g/cm <sup>3</sup> ] (BD)							x			
sand [%]	x	x	x	x	x	x	x	x	x	x
silt [%]	x	x	x	x	x	x	x	x	x	x
clay [%]	x	x	x	x	x	x	x	x	x	x
CaCO <sub>3</sub> [%] (CC)	x	x	x	x	x	x	x		x	
<b>Soil properties linked to soil profile</b>										
genetic soil type (traditional)										x
rooting depth [cm]										x

### 2.3. Statistical Methods

To identify their pedological differences, the two types of area underwent (i) testing using a traditional, non-parametric statistical test, namely the Kolmogorov–Smirnov (KS) homogeneity test and (ii) modelling using a recently “popularized” data mining method, namely Random Forest (RF). Despite their inherent differences, both methods are appropriate for revealing the hypothesized differences in the two types of areas on the basis of the available data.

#### 2.3.1. Kolmogorov–Smirnov Homogeneity Test

The two-sample Kolmogorov–Smirnov (KS) homogeneity test is used to test whether two samples come from the same distribution by comparing the cumulative distributions of the two data sets. A great advantage of this non-parametric test is that it does not assume that data are sampled from normal distributions. The null hypothesis is that both groups were sampled from populations with identical distributions. The KS test reports the maximum difference (D) between the two cumulative distributions and calculates a *p* value from that and the sample sizes. The *p* value shows what the chances are that the value of the Kolmogorov–Smirnov D statistic is as large, or larger than observed. If the *p* value is small, the two groups are sampled from populations with different distributions.

The distribution of raster values for the two sample populations was compared by KS for each soil property independently for the three pilot areas. The two distributions were considered statistically different at a 95% confidence level, then the soil properties with  $P < 0.05$  were ranked according to their D values. The higher the D value, the greater degree to which CMPs and nCMPs differ in their tested soil property.

#### 2.3.2. Random Forests

Random Forests (RF) are an ensemble data mining method for classification and/or regression. The RF algorithm depending on its settings and on the type of the dependent variable, generates a number of regression or classification trees. The model relies on averaging the result of the trees, which are grown independently of each other [46]. In the course of RF modelling, the number of trees was set at 500, the number of variables available for splitting at each tree node (mtry) was set at 7 ( $50^{1/2}$ ). RF models provide a variable rank, reflecting which co-variables play a more important role in the prediction model. According Hengl et al. (2017) [47], the main advantages of random forest over linear regression are: (i) it has no requirements in terms of the probability distribution of

the target variable; (ii) it can fit complex non-linear relationships in  $k+1$ -dimensional space (where  $k$  is the number of environmental covariates); and (iii) the correlation between the environmental covariates is not a limiting factor.

In the present study, the prediction of CMPs and nCMPs was tested using RF modelling. The test dataset was set up by using all raster values for each study areas, and a binary classification was carried out for the identification of CMPs and nCMPs. The variable degrees of importance provided by RF were used for the ranking of soil properties in the discrimination. RF was carried out once on genetic soil type and once only with merely quantitative predictors.

### 3. Results

Differences in geological/geomorphological background alone do not explain all anomalies. It was presumed that the recent state of soil formation, expressed by genetic soil type, water absorption and water holding as well as nutrition supply capacity, would play an essential role, too.

#### 3.1. Distribution of CMPs along Main Genetic Soil Types

As witnessed in the study areas, Chernozem and Meadow type soils are remarkably helpful in the formation of cropmarks, while the suitability of sandy soils is limited.

The eastern part of study area 1 (Figure 4, first panel) is dominated by an alluvial fan covered with sandy soils, and the amount of the detected CMPs decreases. Furthermore, in the case of the area derived from the fan, the CMPs were not recognizable on salt-affected soils. Only rarely do a few cropmarks show up on alluvial soils close to the riverbanks.

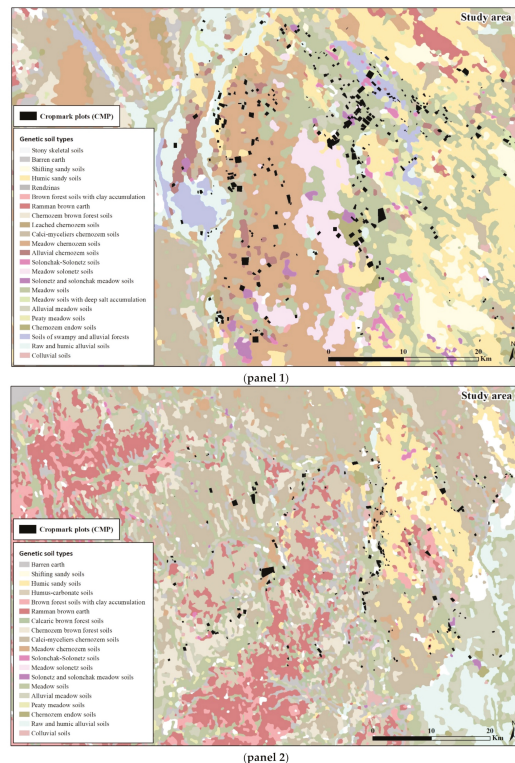
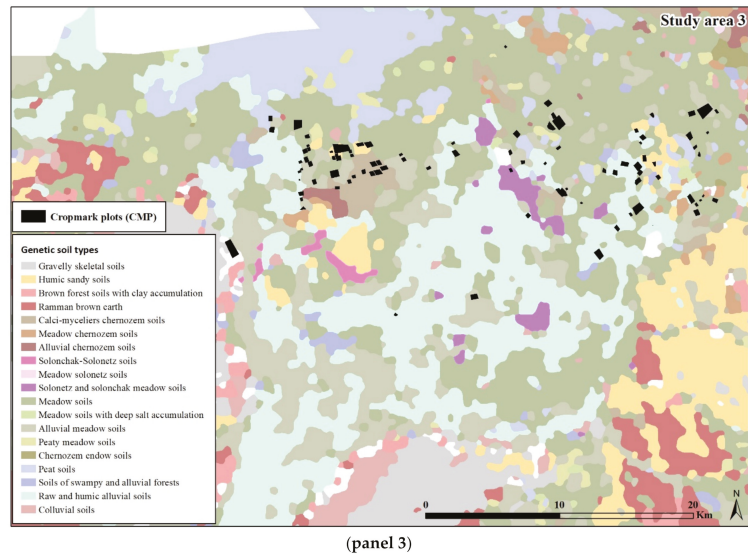


Figure 4. Cont.



**Figure 4. (panel 1–3).** Distribution of CMPs on the soil type map for the study areas.

Study area 2 (Figure 4, second panel) is the most geomorphologically determined area of the three study areas. The cropmarks fit in the typical soil types of valley floors, and in the vast majority of cases, the CMPs occur on Chernozem soils. As with previous study areas, only a few CMPs could be detected on sandy soils. Study area 3 (Figure 4, third panel) is the most heterogeneous area in relation to the distribution of soil types. The majority of CMPs occur on Meadow and Chernozem type soils. It is suggested that the detection of CMPs depends mainly on the weather and seasons.

### 3.2. Differences between Pedological Characteristics of CMPs and nCMPs as Revealed by the Kolmogorov–Smirnov Test

In the light of the two-sample Kolmogorov–Smirnov homogeneity tests, the three pilot areas display significant differences. The ranked soil properties are listed in Table S1. For each study area, the histogram of the raster cell values for the two data sets (CMPs and nCMPs) in the case of the most discriminating soil properties are displayed in Figure 5.

In the Rába interfluvial study area, CMPs and nCMPs mostly differ in the carbonate content of the upper layers. Particle size fractions (clay, sand and silt content) in subsoil (under 1m) and near-surface soil organic carbon also seem to be strong discriminating factors. As can be seen in Figure 5, the carbonate content of the 15–30 cm layer is shifted towards higher values in CMPs, with the distribution reaching a maximum in the 6–8% range; however, a second, local maximum is similarly situated for both data sets at about 13%.

In the Sió-Sárvíz study area CMPs and nCMPs differ mostly in the particle size fractions (clay, sand and silt content) of all layers; carbonate and soil organic matter content lag behind and seem to be rather weak discriminating factors. Despite the significant test result, the histograms in Figure 5 do not seem to differ to any great extent, except for the fact that for CMPs the maximum close range sand content of the 5–15 cm layer is wider, and at over 40% is still almost as high as at 30%.

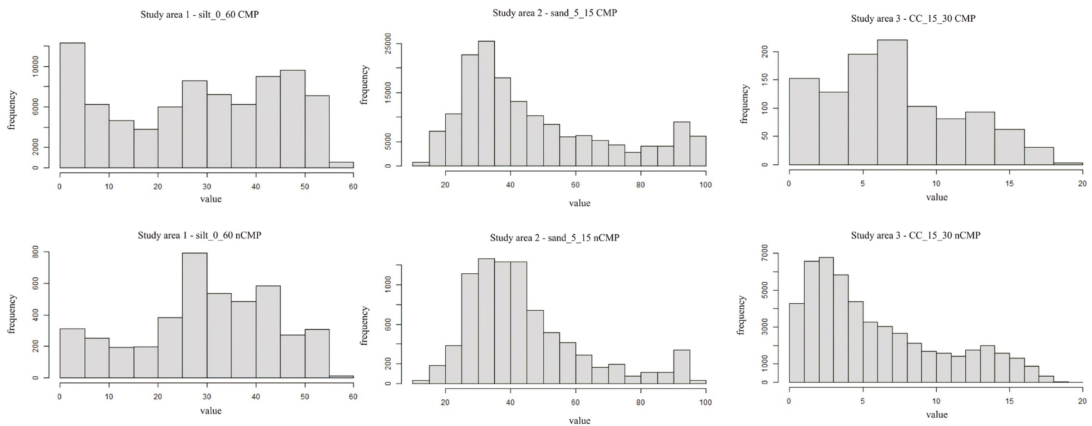


**Figure 5.** The histograms of the raster cell values for the two data sets (CMPs and nCMPs) in the case of the most discriminating soil properties for the three study areas.

In the Danube-Tisza interfluvium study area, CMPs and nCMPs also differ to a large extent in particle size fractions (clay, sand and silt content). However, deeper layers occur later in the ranking; carbonate and soil organic matter content even lag behind and seem to be rather loose discriminating factors. The two histograms in Figure 5 for the silt content of the 0–60 cm layer look rather different, while for CMPs the maximum is located at the lowest values and the overall distribution shows only slight fluctuations. For nCMPs the maximum is close to 30% and only one mode is visible.

It is an interesting fact that for all the three study areas rooting depth showed very weak discriminating power, while pH and bulk density did not provide any statistically valid test results despite their presupposed higher significance.

For all three study areas, the use of RF with genetic soil type as qualitative predictor provided the same results in relation to the importance of soil type, ranking it in the hindmost position. As a consequence, the result and discussion of the models excluding soil type alone form the focus of the discussion. Variable ranks are listed in Table S2. They are also displayed graphically for each study area in Figure S1 [48].

In the Rába interfluvium study area the most important soil properties in the prediction of CMPs and nCMPs are the soil organic matter content of the deeper layers, rooting depth, pH of the subsoil (under 1 m) and bulk density of the topsoil (0–30 cm).

In the Sió-Sárvíz valley study area, the most important soil properties in the prediction of CMPs and nCMPs are rooting depth, soil organic matter content of the deeper layers, pH of the subsoil (under 1 m), bulk density of the topsoil (0–30 cm).

In the Danube-Tisza interfluvium study area the most important soil properties in the prediction of CMPs and nCMPs are bulk density of the topsoil (0–30 cm), soil organic matter content of the topmost layers (0–5 and 5–15 cm), rooting depth, pH of the subsoil (under 1 m), the soil organic matter content of the deeper layers.

It is an interesting point that particle size fractions (clay, sand and silt content) lag behind in all three study areas, while in KS they were top ranked, and the least discriminating properties provided by KS became the determining factors in the RF based prediction of CMPs (Figure 6).

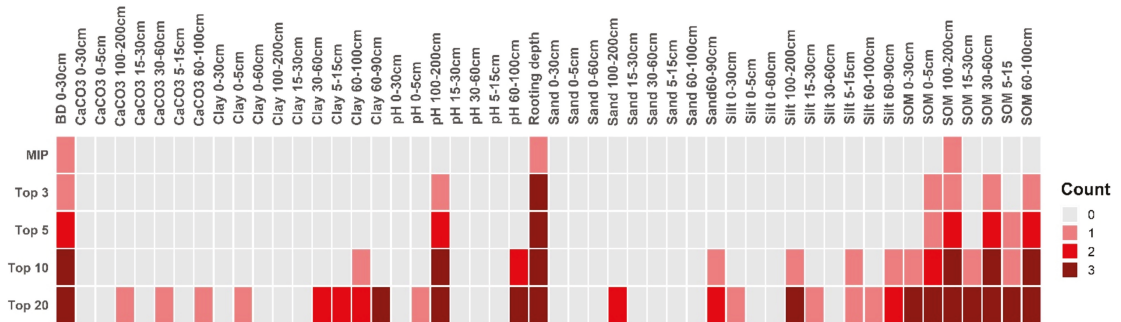


**Figure 6.** Importance of soil property covariates for predicting the indicators of CMPs and nCMPs. Abbreviations: BD: bulk density, SOM: soil organic matter content.

#### 4. Discussion

Although in the selection of the study areas, the aim was to match as many criteria as possible, it should be noted that it is not yet possible to guarantee the same level of analysis of the areas, and they thus cannot be compared with a perfect level of consistency in terms of cropmark formation conditions. This is primarily due to the weather factor, which shows considerable variations every year for the three study areas. While in the area of the Danube-Tisza interfluvial cropmarks can be detected every year, there are years when their discovery is not possible in the Rába interfluvial. The Sió/Sárvíz valley falls somewhere in between these two, as there are no completely unsuccessful years, but truly good ones are rare as well. A further weather-related observation is that the periods ideal for identifying cropmarks—the cropmark time-windows—are not of the same length in the case of each study area. In the Danube-Tisza interfluvial study area, there may be a relatively long period of up to two months, whereas this period is noticeably shorter in the Sió / Sárvíz valley, and only 1–2 weeks long in the Rába interfluvial. A further complicating factor in the case of the Sió / Sárvíz valley is that the maize/sunflower/rape trio plays a noticeably greater role in field crop production than in the other areas. This means that barley/wheat are grown less frequently in crop rotation than in the other two study areas. Finally, it should be noted that the research of the Danube-Tisza interfluvial is much cheaper due to its proximity to the bases of the researchers. Thus, even in the years of scarce funding, flights were guaranteed, while good years—like 2012—may have been missed in the other two areas (Table 2).

**Table 2.** Comparison of the cropmark investigation circumstances and the proportions of CMP/nCMP of the study areas.

	Danube–Tisza Interfluvial	Sió–Sárvíz Valley	Rába Interfluvial
<i>area (km<sup>2</sup>)</i>	2144	2824	809
<i>general time window</i>	8–10 weeks	5–6 weeks	1–2 weeks
<i>seasonal differences</i>	not significant	medium	significant
<i>total CMP [ha]</i>	4339	2440	1070
<i>total nCMP [ha]</i>	81303	170885	51469
<i>proportion CMP [ha]</i>	5.34	1.43	2.08
<i>proportion nCMP [ha]</i>	94.66	98.57	97.92

Also due to these differences, the proportion of areas covered by CMP is significantly higher in the Danube-Tisza interfluvial than in the other two study areas. It is possible that further flights will reduce the differences in representativeness between the study areas,

eventually making the results of the statistical analyses more coherent regardless of the study areas.

Although all three sample areas have alluvial fan origins, their sediment accumulation and surface evolution show distinct features. Their geologic and geomorphologic diversity makes it difficult to specify factors that influence the cropmark appearance clearly. Because of the different appearance of geomorphological/sedimentological fragmentation, determining soil-parameters can still be used to boost the effectiveness of identifying cropmarks.

Regarding the occurrence of CMP-nCMP, the topsoil bulk density and the grain-size composition can be definitive on areas of fluvially determined low angle fans with a complex recent geomorphologic history. On these surfaces diverse landforms are built up from sediments differing greatly in their water-balance, resulting in a mosaic of sand regions, wet meadows, terrace surfaces and floodplains (e.g., the Danube-Tisza interfluvium). As sand movement and fluvial land-forming have been active processes during the Holocene, [49] both the subsurface sediments and the topsoil display great spatial variability.

The situation/picture/ is different in areas where during the Late Quaternary surface evolution was governed by shallow valleys cutting into alluvial fans (e.g., the Sió-Sárvíz valley): in the dual fluvial system of floodplains and flood-free relief areas, the topsoil bulk density is also an important factor. But the dominant component yielding sediment and forming surfaces is sediment accumulation related to the recent flooding of active streams. This therefore results in significantly higher organic material and carbonate content as CMP-nCMP markers.

Regarding the CMP-nCMP analyses, the most problematic areas are completely flat plains with origins as alluvial fan. Considering sedimentation and buried paleo-landforms together, the area must be considered fragmented. These terrains covered in thick, alluvial sediments partially Holocene in origin are characterized by invariable reliefs [50]. The majority of paleochannels are completely buried by now (e.g., in the Rába interfluvium). As today's surface does not reflect the earlier, rougher terrain, and because of its covering alluvial sediment, higher organic material and carbonate content seem to be even more dominant factors in defining CMP and nCMP areas.

Pedological differences between CMPs and nCMPs can be detected by all the three approaches. The statistically identified differences, however, differ to a fair degree between the various approaches. Differences in the distribution of specific soil property values for CMPs and nCMPs (as opposed to the variable importance provided by RF for the prediction of the two types of areas) result in significantly different rankings of soil properties. This might be caused by the problem of representative sampling in the study areas.

In contrast to results for the Czech Republic [16,19], those presented here do not show the dominance of sandy soils in cropmarks.

The role of soil chemical properties in cropmarks revealed by Hejzman et al. (2013) [27] are, however, supported by the result in the present study that organic matter and carbonate as well as pH are important variables in RF models. However, nutrients available to plants have not been mapped in the frame of DOSoReMI.hu due to their dynamic nature and the lack of available observational data. Thus, their role in cropmarks is not considered in the present work. Nevertheless, the approach employed can reveal the more static pedological background where the spatial differences in nutrient status due to archeological sources may result in stronger effects on crop development, thus making plots more suitable for cropmarks.

## 5. Conclusions

The analyses of the factors behind the formation of cropmarks gave rather complex results, despite the fact that only the fixed elements of the system were examined. The importance of alluvial fans has also been prospected in Southern Germany, Switzerland, Austria, and the Czech Republic. However, the differences in cropmark between alluvial fan sub-types have been explained by analyzing Hungarian soil data. At the same time, this method could prove useful in the future for the analysis of areas with significantly

different geomorphological conditions—bearing in mind the important role of loess areas in the Czech Republic.

Based on the detailed statistical analysis of both the aerial archaeological and pedological data, different factors seem to be relevant to each study area. However, these differences can be sufficiently explained by the slightly different formation and landscape evolution processes of study areas with similar bedrock. While cropmarks correlate well with the results of traditional soil mapping, much more complex processes underlie the formation of cropmarks. This is probably due to the fact that in previous analyses, the role of some important factors (e.g., sandy soils) seems to have been more subordinate.

Since the 1990s, Hungary has been considered highly suitable for the prospection of cropmarks, thanks chiefly to the presence of large field monoculture grain corn production and also to early summer weather suitable for aerial archaeological research. Among a number of other factors, the favorable conditions can certainly be linked to a high-quality soil mantle. It is worth noting that by increasing the representativeness of archaeological prospecting, an even more accurate picture may hopefully be created in the future. One important objective of the methodological developments presented here is the creation of a predictive model in order to start mapping cropmarks during flights over micro-regions not previously researched, but in which the geomorphological / soil conditions seem to be favorable.

We also plan to explore the roles of changeable factors. The above described features' influence on cropmarks might be enhanced, decreased, or—in years of extreme weather—completely altered by weather conditions, especially by the amount of precipitation.

The use of cropmarks in aerial archaeology helps primarily the identification and the geomorphological analyses of sites, as well as the mapping of archaeological data. However, in order to understand the complex factors of cropmark formation better, new methods were needed. Asked in 2000 how much experience he needed truly to understand the nature and the research opportunities of cropmarks, René Goguy's answer was: "After 30 years work, I've started to realize". Now, 20 years later, progress seems possible on the basis of an approach which makes cropmark data suitable for statistical processing, together with analyses related to soil data systems based on remote sensing data sources and interpreted from a geomorphological point of view. It is the hope of the authors that the methodological experiments detailed here may make the technology of aerial archaeological prospecting, which has been somewhat sidelined in the last 10 years, more predictable, plannable and thereby more effective.

**Supplementary Materials:** The following are available online at <https://www.mdpi.com/2072-4292/13/6/1126/s1>, Table S1: Rank of primary soil property maps used for the comparison of the pedological features of CMPs and nCMPs in the case of the three study areas. The higher the D value, the greater the degree to which CMPs and nCMPs differed in their tested soil properties. Table S2: Variable importance rank of primary soil properties used in Random Forest modelling of CMPs and nCMPs in the case of the three study areas. The higher the importance value, the more informative is the given soil property in the discrimination of CMPs and nCMPs. Figure S1: Variable importance rank of primary soil properties used in Random Forest modelling of CMPs and nCMPs in the case of the three test sites.

**Author Contributions:** Conceptualization, Z.C. and L.P.; methodology, Z.C., B.N. and L.P.; software, M.Á. and J.M.; validation, Z.C., B.N. and L.P.; formal analysis, Z.C.; investigation, Z.C. and L.P.; resources, Z.C. and L.P.; data curation, M.Á., J.M. and L.R.; writing—original draft preparation, Z.C., B.N. and L.P.; writing—review and editing, Z.C., B.N. and L.P.; visualization, M.Á., J.M. and L.R.; supervision, Z.C. and L.P.; project administration, Z.C.; funding acquisition, Z.C. and L.P. All authors have read and agreed to the published version of the manuscript.

**Funding:** This research was funded by National Research Development and Innovation Office (Hungary), grant numbers NN-111058, K-131820 and SNN 134635, by the Higher Educational Institutional Excellence Program / the Thematic Excellence Program of the Eötvös Loránd University, and Momentum Mobility research project (Institute of Archaeology, Research Centre for the Humanities), granted by the Momentum Program of the Hungarian Academy of Sciences.

**Data Availability Statement:** The digital soil maps used in the present study were compiled in the “Digital Optimized Soil Related Maps and Information” framework and are published on the [www.dosoremi.hu](http://www.dosoremi.hu) website. The maps were elaborated according to GSM specifications, thus they also represent the Hungarian contribution to the GlobalSoilMap.net project. The CMPs are sensitive data containing archaeological site information indirectly.

**Acknowledgments:** The authors thank Á. Marton for his indispensable contribution. We are grateful to the editors and the six anonymous reviewers who provided valuable suggestions regarding the manuscript.

**Conflicts of Interest:** The authors declare no conflict of interest.

## References

- Goguey, R. *Traces dans la Grande Plaine... Photographies Aériennes de Hongrie. Exposition du 18 Avril au 2 Juin 2002*; Conseil Général du Rhône: Saint-Romain-en-Gal-Vienne, France, 2002.
- Barber, M. *A History of Aerial Photography and Archaeology. Mata Hari's Glass Eye and Other Stories*; English Heritage: Swindon, UK, 2011; ISBN 978-1-848020-36-8.
- Crawford, O.G.S. Air Survey and Archaeology. *Geogr. J.* **1923**, *61*, 342–360. [[CrossRef](#)]
- Neogrády, S. A légifénykép és az archeológiai kutatások [The aerial photo and the archaeological survey]. *Térképzéseti Közöny* **1950**, *7*, 283–332.
- Christlein, R.; Braasch, O. *Das Unterirdische Bayern. 7000 Jahre Geschichte und Archäologie im Luftbild*; Theiss: Stuttgart, Germany, 1990; ISBN 3-8062-0855-7.
- Cowley, D.C. Creating the Cropmark Archaeological Record in East Lothian, South-East Scotland. In *Prehistory without Borders. The Prehistoric Archaeology of the Tyne-Forth Region*; Crellin, R., Fowler, C., Tipping, R., Eds.; Oxbow Books: Oxford, UK, 2016; pp. 59–70. ISBN 978-1-78570-200-6.
- Dabas, M.; Delétang, H.; Ferdière, A.; Jung, C.; Zimmermann, W.H. *La Prospection*; Errance: Paris, France, 1998; ISBN 2-87772-160-4.
- Braasch, O. *Vom heiteren Himmel . . . Luftbildarchäologie*; Gesellschaft für Vor- und Frühgeschichte Württemberg und Hohenzollern e.V.: Esslingen, Germany, 2005; ISBN 3-9808926-1-1.
- Scollar, I. *Archaeological Prospecting and Remote Sensing*; Cambridge University Press: Cambridge, UK, 1990; ISBN 10: 052132050X.
- Verhoeven, G.J. Near-Infrared Aerial Crop Mark Archaeology: From its Historical Use to Current Digital Implementations. *J. Archaeol. Method Theory* **2012**, *19*, 132–160. [[CrossRef](#)]
- Luo, L.; Wang, X.; Guo, H.; Lasaponara, R.; Zong, X.; Masini, N.; Wang, G.; Shi, P.; Khatteli, H.; Chen, F.; et al. Airborne and spaceborne remote sensing for archaeological and cultural heritage applications: A review of the century (1907–2017). *Remote Sens. Environ.* **2019**, *232*, 111280. [[CrossRef](#)]
- Verhoeven, G.; Sevara, C. Trying to break new ground in aerial archaeology. *Remote Sens.* **2016**, *8*, 918. [[CrossRef](#)]
- Verhoeven, G.J. Are we there yet? A review and assessment of archaeological passive airborne optical imaging approaches in the light of landscape archaeology. *Geosciences* **2017**, *7*, 86. [[CrossRef](#)]
- Cowley, D.C. Aerial photographs and aerial reconnaissance for landscape studies. In *Detecting and Understanding Historical Landscapes*; Chavarria Arnau, A., Reynolds, A., Eds.; SAP Societ  Archeologica: Mantova, Italy, 2015; pp. 37–66. ISBN 978-88-87115-99-4.
- Cowley, D.C.; Stichelbaut, B.B. Historic Aerial Photographic Archives for European Archaeology. *Eur. J. Archaeol.* **2012**, *15*, 217–236. [[CrossRef](#)]
- Hejcman, M.; Smr z, Z. Cropmarks in stands of cereals, legumes and winter rape indicate sub-soil archaeological features in the agricultural landscape of Central Europe. *Agric. Ecosyst. Environ.* **2010**, *138*, 348–354. [[CrossRef](#)]
- Czajlik, Z. Les possibilit s de la prospection a rienne conventionnelle en Hongrie. In *Studia Celtica Classica et Romana Nicolae Szab  Septuagesimo Dedicata*; Pytheas: Budapest, Hungary, 2012; pp. 80–96. ISBN 978-963-9746-77-0.
- Leidorf, K. Luftbildarch ologie—Geschichte und Methode. In *Arch ologische Prospektion. Luftbildarch ologie und Geophysik. Arbeitshefte des Bayerischen Landesamtes f r die Denkmalpflege, Band 59*; Becker, H., Ed.; Bayerisches Landesamt f r Denkmalpflege: M nchen, Germany, 1996; pp. 33–44. ISBN 3-87490-541-1.
- Gojda, M.; Hejcman, M. Cropmarks in main field crops enable the identification of a wide spectrum of buried features on archaeological sites in Central Europe. *J. Archaeol. Sci.* **2012**, *39*, 1655–1664. [[CrossRef](#)]
- Stanjek, H.; Fa sbinder, J.W.E. Soil aspects affecting archaeological details in aerial photographs. *Archaeol. Prospect.* **1995**, *2*, 91–101. [[CrossRef](#)]
- Evans, R.; Jones, R.J.A. Crop marks and soils at two archaeological sites in Britain. *J. Archaeol. Sci.* **1977**, *4*, 63–76. [[CrossRef](#)]
- Braasch, O.; Kaufmann, D. Zum Beginn arch ologischer Flugprospektion in Sachsen-Anhalt. *Ausgrab. Funde* **1992**, *4*, 186–205.
- Czajlik, Z.; B d cs, A. The Effectiveness of Aerial Archaeological Research—An Approach from the GIS Perspective. In *Moments in Time. Papers Presented to P l Raczky on His 60th Birthday*; l’Harmattan: Budapest, Hungary, 2013; pp. 873–883. ISBN 978-963-236-346-2.

24. Linck, R.; Abandowitz, S.; Leidorf, K. Mitten im Mais: Rekordsommer enthüllt Grabenwerke mittels Luftbildarchäologie. *Das archäologische Jahr Bayern* **2018**, *38*, 163–166.
25. Leckebusch, J.; Nagy, P. *Propektionsmethoden in der Archäologie*; Stiftung für die Erforschung des Üetlibergs: Zürich, Switzerland, 1991.
26. Doneus, M. Luftbildarchäologie und Photogrammetrie am Institut für Ur-und Frühgeschichte in Wien. In *Luftbildarchäologie in Ost-und Mitteleuropa. Aerial Archaeology in Eastern and Central Europe. Internationales Symposium 26.–30. September 1994 Kleinmachnow. Land Brandenburg, Forschungen zur Archäologie im Land Brandenburg 3*; Verlag Brandenburgisches Landesmuseum für Ur-und Frühgeschichte: Potsdam, Germany, 1995; pp. 123–132.
27. Hejzman, M.; Součková, K.; Gojda, M. Prehistoric settlement activities changed soil pH, nutrient availability, and growth of contemporary crops in Central Europe. *Plant Soil* **2013**, *369*, 131–140. [[CrossRef](#)]
28. Evans, R. The weather and other factors controlling the absence of crop marks on clay and „difficult“ soils. In *Populating Clay Landscapes*; Tempus: Stroud, UK, 2007; pp. 16–27.
29. Doneus, M. *Die hinterlassene Landschaft—Prospektion und Interpretation in der Landschaftsarchäologie. Mitteilungen der Prähistorischen Kommission Band 78*; Österreichisch Akademie der Wissenschaften: Wien, Austria, 2013; ISBN 978-3-7001-7197-3.
30. Gábris, G.; Nádor, A. Long-term fluvial archives in Hungary: Response of the Danube and Tisza rivers to tectonic movements and climatic changes during the Quaternary: A review and new synthesis. *Quat. Sci. Rev.* **2007**. [[CrossRef](#)]
31. Gábris, G.; Nagy, B. Climate and tectonically controlled river style changes on the Sajó-Hernád alluvial fan (Hungary). In *Alluvial Fans: Geomorphology, Sedimentology, Dynamics—Introduction. A Review of Alluvial-Fan Research*; Geological Society: London, UK, 2005; pp. 61–67.
32. Vogel, H.J.; Bartke, S.; Daedlow, K.; Helming, K.; Kögel-Knabner, I.; Lang, B.; Rabot, E.; Russell, D.; Stöfel, B.; Weller, U.; et al. A systemic approach for modeling soil functions. *Soil* **2018**, *4*, 83–92. [[CrossRef](#)]
33. Miller, B.A.; Schaetzl, R.J. The historical role of base maps in soil geography. *Geoderma* **2014**, *230–231*, 329–339. [[CrossRef](#)]
34. Heuvelink, G.B.M.; Webster, R. Modelling soil variation: Past, present, and future. *Geoderma* **2001**, *100*, 269–301. [[CrossRef](#)]
35. Várallyay, G. Soil mapping in Hungary. *Agrokémia Talajt* **1989**, *38*, 696–714.
36. Minasny, B.; McBratney, A.B. Digital soil mapping: A brief history and some lessons. *Geoderma* **2016**. [[CrossRef](#)]
37. McBratney, A.B.; Mendonça Santos, M.L.; Minasny, B. On Digital Soil Mapping. *Geoderma* **2003**, *117*, 3–52. [[CrossRef](#)]
38. Pásztor, L.; Laborcz, A.; Takács, K.; Illés, G.; Szabó, J.; Szatmári, G. Progress in the elaboration of GSM conform DSM products and their functional utilization in Hungary. *Geoderma Reg.* **2020**, *21*, e00269. [[CrossRef](#)]
39. Whimster, R. *The Emerging Past. Air Photography and the Buried Landscape*; Royal Commission on the Historical Monuments of England: Abingdon, UK, 1989; ISBN 095072369.
40. Cowley, D.; Gilmour, S.M.D. Some observations on the nature of aerial survey. In *From the Air: Understanding Aerial Archaeology*; Tempus Publishing: Stroud, UK, 2005; pp. 50–63. ISBN 0-7524-3130-7.
41. Hanson, W.S. Sun, sand and see: Creating bias in the archaeological record. In *From the Air: Understanding Aerial Archaeology*; Tempus Publishing: Stroud, UK, 2005; pp. 73–85. ISBN 0-7524-3130-7.
42. Szabó, M. *Archaeology from Above*; Archaeolingua: Budapest, Hungary, 2016; ISBN 978-963-9911-86-4.
43. Tanács, E.; Belényesi, M.; Lehoczki, R.; Pataki, R.; Petrik, O.; Standovár, T.; Pásztor, L.; Laborcz, A.; Szatmári, G.; Molnár, Z.; et al. Országos, nagyfelbontású ökoszisztéma-alaptérkép: Módszertan, validáció és felhasználási lehetőségek. *Természetvédelmi Közlemények* **2019**, *25*, 34–58. [[CrossRef](#)]
44. Brevik, E.C.; Calzolari, C.; Miller, B.A.; Pereira, P.; Kabala, C.; Baumgarten, A.; Jordán, A. Soil mapping, classification, and pedologic modeling: History and future directions. *Geoderma* **2016**. [[CrossRef](#)]
45. Pásztor, L.; Laborcz, A.; Bakacsi, Z.; Szabó, J.; Illés, G. Compilation of a national soil-type map for Hungary by sequential classification methods. *Geoderma* **2018**. [[CrossRef](#)]
46. Breiman, L. Random forests. *Mach. Learn.* **2001**. [[CrossRef](#)]
47. Hengl, T.; De Jesus, J.M.; Heuvelink, G.B.M.; Gonzalez, M.R.; Kilibarda, M.; Blagotić, A.; Shangguan, W.; Wright, M.N.; Geng, X.; Bauer-Marschallinger, B.; et al. SoilGrids250m: Global gridded soil information based on machine learning. *PLoS ONE* **2017**, *12*, e0169748. [[CrossRef](#)] [[PubMed](#)]
48. Szatmári, G.; Bakacsi, Z.; Laborcz, A.; Petrik, O.; Pataki, R.; Tóth, T.; Pásztor, L. Elaborating Hungarian Segment of the Global Map of Salt-Affected Soils (GSSmap): National Contribution to an International Initiative. *Remote Sens.* **2020**, *12*, 4073. [[CrossRef](#)]
49. Gábris, G.; Horváth, E.; Novothny, Á.; Ruzsiczay-Rüdiger, Z. Fluvial and aeolian landscape evolution in Hungary—Results of the last 20 years research. *Geol. en Mijnbouw/Neth. J. Geosci.* **2012**. [[CrossRef](#)]
50. Czajlik, Z.; Rupnik, L.; Losonczi, M.; Timár, L. Aerial archaeological survey of a buried landscape: The Tóköz project. In *Remote Sensing for Archaeological Heritage Management, Proceedings of the 11th EAC Heritage Management Symposium, Reykjavik, Iceland, 25–27 March 2010*; Archaeolingua: Brussels, Belgium, 2011; pp. 235–241. ISBN 978-963-9911-20-8.



MDPI  
St. Alban-Anlage 66  
4052 Basel  
Switzerland  
Tel. +41 61 683 77 34  
Fax +41 61 302 89 18  
[www.mdpi.com](http://www.mdpi.com)

*Remote Sensing* Editorial Office  
E-mail: [remotesensing@mdpi.com](mailto:remotesensing@mdpi.com)  
[www.mdpi.com/journal/remotesensing](http://www.mdpi.com/journal/remotesensing)





MDPI  
St. Alban-Anlage 66  
4052 Basel  
Switzerland

Tel: +41 61 683 77 34  
Fax: +41 61 302 89 18

[www.mdpi.com](http://www.mdpi.com)



ISBN 978-3-0365-1376-8